



الجامعة الإسلامية بالمدينة المنورة
ISLAMIC UNIVERSITY OF MADINAH

The Islamic University Journal of Applied Sciences (JESC)

Refereed periodical scientific journal

Volume: VI Issue: I Year: 2024

بِسْمِ اللَّهِ الرَّحْمَنِ الرَّحِيمِ

Paper version

Filed at the King Fahd National Library No. 8742/1439 on 17/09/1439 AH
International serial number of periodicals (ISSN) 1658-7936

Online version

Filed at the King Fahd National Library No. 8742/1439 on 17/09/1439 AH
International Serial Number of Periodicals (e-ISSN) 1658-7944

The Journal's Website

<https://jesc.iu.edu.sa>

The papers are sent in the name of the Editor-in-Chief of the Journal to
this E-mail address

jesc@iu.edu.sa

(The views expressed in the published papers reflect the views of the
researchers only, and do not necessarily reflect the opinion of the journal)

Publication Rules at the Journal (*)

❖ General rules:

- Report original scientific research (the main results and conclusions must not have been published or submitted elsewhere).
- Fit with the topics of the journal.
- Report novel results, innovative work and show a new scientific contribution.
- Not to bear similarity of more than 25% of a previously published work of the same author(s).
- Follow the rules, regulation and authentic research methodologies.
- Fulfill the required items and the format of the journal provided in appendix below related to the guide for author.
- Opinions expressed in published articles commit the authors themselves only and not necessarily the opinion of the journal.

❖ For all articles:

- The exclusive right to publish and distribute an article, and to grant rights to others, including commercial purposes.
- For open access articles, IU will apply the relevant third-party user license where IU publishes the article on its online platforms.
- The right to provide the article in all forms and media so the article can be used on the latest technology even after publication.
- The authority to enforce the rights in the article, on behalf of an author, against third parties, for example in the case of plagiarism or copyright infringement.

(*) These general rules are explained in details along with other rules for Author's guide in the journal's website: <https://jesc.iu.edu.s>

The Editorial Board

Ahmad B. Alkhodre

Editor-in-Chief
Professor, Computer Science,
Islamic University of Madinah,
Saudi Arabia.

Fazal Noor

Managing Editor
Professor, Computer science and
engineering, Islamic University of
Madinah. Saudi Arabia

Tomita Kentaro

Associate Professor, Division of
Quantum Science and Engineering,
Graduate School of Engineering,
Hokkaido University, Japan

Fayez Gebali

Professor, Electrical and Computer
Engineering, University of Victoria,
Victoria, B.C., Canada

Saad Talal Alharbi

Professor in Computer Science,
Human Computer Interaction,
Faculty of Computers, Taibah
University, Saudi Arabia

Abdul Qadir Bhatti

Professor, Civil Engineering, Faculty
of Engineering, Islamic University of
Madinah.
Saudi Arabia

Essam Ramadan Shaaban

Professor, Physics, Al-Azhar University,
Assiut Branch, Egypt

Yazed Alsaawy

Associate Professor, Computer and
information systems, Islamic
University of Madinah. Saudi Arabia

M. M. Khader

Professor, Numerical Analysis,
Alimam University, Riyadh.
Saudi Arabia

**Reda Mohamed Awad El-
Shishtawy**

Professor, Organic Chemistry,
Chemistry Department Faculty of
Science - King Abdulaziz
University, Saudi Arabia

Basem R. Alamri

Associate Professor of Electrical Power
Engineering, Taif University

Shamsuddin Ahmed

Professor, Industrial Engineering, The
Faculty of Computer and Information
Systems Islamic University of
Madinah

Editorial Secretary: **Ahmad Ziad Al-Zuhaily**

The Advisory Board

Hussein T. Mouftah
Professor, Electrical
Engineering and Computer
Science, University of Ottawa,
Ottawa, ON, Canada

Canada Research Chair in
Wireless Sensor Networks

Distinguished University
Professor, University of Ottawa

**Sultan T. Abu-Orabi
Aladwan**
Professor, Organic Chemistry,
Jordan

Kamal Mansour Jambi
Professor, Computer and
Information Systems, King
Abdel-Aziz University, Jeddah,
Saudi Arabia

Diaa Khalil
Professor, Electrical Engineering,
and Vice-Dean, Ain-Shams
University, Cairo, Egypt

A. Ghafoor
Professor, Mechanical Engineering,
National University of Science and
Technology, Pakistan

Mahmoud Abdel-Aty
Professor, Applied
Mathematics, Egypt

Claus Haetinger
Professor, Mathematics, Brazil

Ameen Farouq Fahmy
Professor, Chemistry,
Egypt

The Islamic University Journal of Applied Sciences

Issued By

Islamic University of Madinah, Madinah, Saudi Arabia

Table of Contents

Article	Page
Geometry of Quasi bi-slant conformal Submersions from Kenmotsu manifold	10
Central generalized bi-semi-derivations on semiprime rings	38
An Adaptive Model for Distributing and Balancing Air Conditioning in Crowded Places	50
Vibration Assignment, B3pw91 Calculation and Conformational Analysis of Antimicrobial 5-Amino -3-(Methylthio)-1-(1,3,4Thiadiazol -2-Yl)-1H-Pyrazole-4-Carbonitrile	64
Multiple sources of big data are used to create a method for protecting computer networks	92
Separation of yttrium y(iii) from rubidium rb(i) using poly hydroxamic acid	114
Investigation of levels and human health risk of heavy metals in tea samples marketed in Jazan, Saudi Arabia	131
Design And Development of a Feeding Unit for Medical Devices Implanted Inside Human Body Using Artificial Intelligence Theories	151
Investigating Artificial Intelligence Systems Through the Use of Constrained Deep Neural Networks	168
Computer simulation for optimizing mining waste recycling in cement raw meals	198

Geometry of Quasi bi-slant conformal Submersions from Kenmotsu manifold

Fahad Sikander

Department of Basic Sciences, College of Science and Theoretical Studies,
Saudi Electronic University, Jeddah, K.S.A

email:f.sikander@seu.edu.sa

Tanveer Fatima

Department of Mathematics and Statistics, College of Sciences,
Taibah University. Yanbu, K.S.A.

email: tansari@taibahu.edu.sa

Mohammad Shuaib

Department of Mathematics, Lovely Professional University, Punjab, India.

email: shuaibyouf6@gmail.com

Abstract

In this study, we examine Quasi bi-slant conformal submersions originating from a Kenmotsu manifold, focusing on the vertical Reeb vector field ξ . Initially, we explore the integrability conditions for the distributions defined by quasi-bi-slant submersions. Furthermore, we delve into the geometry of the associated leaves. The research concludes by presenting two intriguing observations regarding the pluriharmonicity of Quasi Bi-Slant Conformal Submersions and includes several non-trivial examples of such submersions.

keywords

Kenmotsu manifold, Riemannian submersions, Conformal bi-slant submersions, quasi bi-slant submersions.

هندسة الغمرات المتطابقة شبه الثنائية المائلة من مشعب كينموتسو

الملخص: في هذه الدراسة، قمنا بدراسة الغمرات المتطابقة شبه ثنائية المائل الناشئة عن مشعب كينموتسو، مع التركيز على مجال ناقل الريب الرأسي ξ . في البداية، قمنا باستكشاف شروط التكامل للتوزيعات المحددة بواسطة الغمر شبه ثنائي المائل. علاوة على ذلك، فإننا نتعمق في هندسة الأوراق المرتبطة. ويختتم البحث بتقديم ملاحظتين مثيرتين للاهتمام فيما يتعلق بتعدد التناغم في الغمرات المتطابقة شبه الثنائية المائلة، ويتضمن عدة أمثلة غير تافهة لمثل هذه الغمرات.

1 Introduction

Immersion and submersions play crucial roles in differential geometry, with slant submersions being a particularly intriguing subject in the fields of differential, complex, and contact geometry. The study of Riemannian submersions between Riemannian manifolds was first explored by O'Neill [24] and Gray [12], independently, and subsequently led to investigations of Riemannian submersions between almost Hermitian manifolds, known as almost Hermitian submersions, by Watson in 1976 [38]. Riemannian submersions have many applications in mathematics and physics, especially in Yang-Mills theory ([7], [39]) and Kaluza-Klein theory ([18], [22]).

Semi-invariant submersions, a generalization of holomorphic submersions and anti-invariant submersions, were introduced by Sahin in 2013 [32]. In 2016, Tatsan, Sahin, and Yanan studied hemi-slant Riemannian submersions from almost Hermitian manifolds onto Riemannian manifolds, and presented several decomposition theorems for them [37]. R. Prasad et al. further examined quasi bi-slant submersions from almost contact metric manifolds onto Riemannian manifolds [26], as well as from Kenmotsu manifolds [27], which represents a step forward in the study of Riemannian submersions.

Since then, many authors have explored different types of Riemannian submersions, including anti-invariant submersions ([4], [31]), slant submersions [10], [33], semi-slant submersions ([16], [25]), and hemi-slant submersions ([36], [1]), from both almost Hermitian manifolds and almost contact metric manifolds. These studies have greatly expanded our understanding of the geometrical structures of Riemannian manifolds.

The concept of almost contact Riemannian submersions from almost contact manifold was introduced by Chinea in [8]. Chinea also examined the fibre space, base space and total space using a differential geometric perspective. To generalize Riemannian submersions, Gundmundsson and Wood [14, 15] presented horizontally conformal submersion, defined as: Let (M_1, g_1) and (M_2, g_2) be two Riemannian manifolds of dimension m_1 and m_2 , respectively. A smooth map $J: (M_1, g_1) \rightarrow (M_2, g_2)$ is called a horizontally conformal submersion, if there is a positive function λ such that

$$\lambda^2 g_1(X_1, X_2) = g_2(J_*X_1, J_*X_2), \tag{1.1}$$

for all $X_1, X_2 \in \Gamma(\ker J)^\perp$. Thus, Riemannian submersion is a particular horizontally conformal submersion with $\lambda = 1$. Later on, Fuglede [13] and Ishihara [20] separately studied horizontally conformal submersions. Additionally various other kind of submersions such as, conformal slant submersions [3], conformal anti-invariant submersions [34], conformal semi-slant submersions [2], conformal semi-invariant submersions [5] and conformal anti-invariant submersions [27] have been studied by Akyol and Sahin and R. Prasad et al [28]. Furthermore, Shuaib and Fatima recently explored conformal hemi-slant Riemannian submersions from almost product manifolds onto Riemannian manifolds [35].

In this paper, we study quasi bi-slant conformal submersions from Kenmotsu manifold onto a Riemannian manifold considering the Reeb vector field ξ vertical. This paper is divided into six sections. Section 2 contains definitions of almost contact metric manifolds and, in particular, Kenmotsu manifolds. In section 3, fundamental results for quasi bi-slant conformal submersion are investigated, which are necessary our main results. The conditions of integrability and totally geodesicness of distributions are explored in Section 4. Section 5 provides some condition under which a Riemannian submersion becomes totally geodesic as well as some decomposition theorems for quasi bi-slant conformal submersion are obtained. The last section discusses ϕ -pluriharmonicity.

Note: Throughout the paper, we will consider abbreviations as follows: Riemannian submersion- RS, Riemannian Manifold- RM, Almost contact metric manifold-ACM manifold, Quasi bi-slant conformal submersion- \mathcal{QBSCS} , gradient- G.

2 Preliminaries

Let M be a $(2n + 1)$ -dimensional almost contact manifold with almost contact structures (ϕ, ξ, η) , where a $(1, 1)$ tensor field ϕ , a vector field ξ and a 1-form η satisfying

$$\phi^2 = -I + \eta \otimes \xi, \quad \phi\xi = 0, \quad \eta \circ \phi = 0, \quad \eta(\xi) = 1, \quad (2.2)$$

where I is the identity tensor. The almost contact structure is said to be normal if $N + d\eta \otimes \xi = 0$, where N is the Nijenhuis tensor of ϕ . Suppose that a Riemannian metric tensor g is given in M and satisfies the condition

$$g(\phi\hat{U}, \phi\hat{V}) = g(\hat{U}, \hat{V}) - \eta(\hat{U})\eta(\hat{V}), \quad \eta(\hat{U}) = g(\hat{U}, \xi). \quad (2.3)$$

Then (ϕ, ξ, η, g) -structure is called an almost contact metric structure. Define a tensor field Φ of type $(0, 2)$ by $\Phi(\hat{X}, \hat{Y}) = g(\phi\hat{X}, \hat{Y})$. If $d\eta = \Phi$, then an almost contact metric structure is said to be normal contact metric structure. Let Φ be the fundamental 2-form on M , i.e, $\Phi(\hat{U}, \hat{V}) = g(\hat{U}, \phi\hat{V})$. If $\Phi = d\eta$, M is said to be a contact manifold. If ξ is a Killing vector field with respect to g , the contact metric structure is called a K -contact structure.

S.Tanno [30], who categorized connected, almost contact metric manifolds with the largest automorphism groups. The sectional curvature of a plane section containing ξ for such a manifold is a constant c . This classification includes classes of warped products with $c < 0$ is $R \times_f C^n$. The tensorial equation of these manifolds are:

$$(\nabla_{\hat{U}}\phi)\hat{V} = g(\phi\hat{U}, \hat{V})\xi - \eta(\hat{V})\phi\hat{U}. \quad (2.4)$$

Kenmotsu [21], investigated a few basic differential geometric features of these spaces, giving rise to the name Kenmotsu manifolds. It is also apparent on a Kenmotsu manifold M that

$$\nabla_{\widehat{U}}\xi = -\phi^2\widehat{U} = \widehat{U} - \eta(\widehat{U})\xi, \quad (2.5)$$

The covariant derivative of ϕ is defined by

$$(\nabla_{\widehat{U}_1}\phi)\widehat{V}_1 = \nabla_{\widehat{U}_1}\phi\widehat{V}_1 - \phi\nabla_{\widehat{U}_1}\widehat{V}_1, \quad (2.6)$$

for any vector fields $\widehat{U}_1, \widehat{V}_1 \in \Gamma(TM)$. Now we outline conformal submersion and examine several relevant results that assist us attain our major goals.

Definition 2.1 [6] Let J be a Riemannian submersion (RS) from an ACM manifold $(\bar{B}_1, \phi, \xi, \eta, g_1)$ onto a Riemannian manifold (RM) (\bar{B}_2, g_2) . Then J is called a horizontally conformal submersion, if there is a positive function λ such that

$$g_1(\widehat{U}_1, \widehat{V}_1) = \frac{1}{\lambda^2}g_2(J_*\widehat{U}_1, J_*\widehat{V}_1), \quad (2.7)$$

for any $\widehat{U}_1, \widehat{V}_1 \in \Gamma(\ker J_*)^\perp$. It is obvious that every RS is a particularly horizontally conformal submersion with $\lambda = 1$.

Let $J : (\bar{B}_1, \phi, \xi, \eta, g_1) \rightarrow (\bar{B}_2, g_2)$ be a RS. A vector field \widehat{X} on \bar{B}_1 is called a basic vector field if $\widehat{X} \in \Gamma(\ker J_*)^\perp$ and J -related with a vector field \widehat{X} on \bar{B}_2 i.e $J_*(\widehat{X}(q)) = \widehat{X}(q)$ for $q \in \bar{B}_1$.

The formulas provide the two $(1, 2)$ tensor fields \mathcal{T} and \mathcal{A} by O'Neill are

$$\mathcal{A}_{E_1}F_1 = \mathcal{H}\nabla_{\mathcal{H}E_1}\mathcal{V}F_1 + \mathcal{V}\nabla_{\mathcal{H}E_1}\mathcal{H}F_1, \quad (2.8)$$

$$\mathcal{T}_{E_1}F_1 = \mathcal{H}\nabla_{\mathcal{V}E_1}\mathcal{V}F_1 + \mathcal{V}\nabla_{\mathcal{V}E_1}\mathcal{H}F_1, \quad (2.9)$$

for any $E_1, F_1 \in \Gamma(T\bar{B}_1)$ and ∇ is Levi-Civita connection of g_1 . Note that a RS $J : (\bar{B}_1, \phi, \xi, \eta, g_1) \rightarrow (\bar{B}_2, g_2)$ has totally geodesic fibers if and only if \mathcal{T} vanishes identically. From equations (2.8) and (2.9), we can deduce

$$\nabla_{\widehat{U}_1}\widehat{V}_1 = \mathcal{T}_{\widehat{U}_1}\widehat{V}_1 + \mathcal{V}\nabla_{\widehat{U}_1}\widehat{V}_1 \quad (2.10)$$

$$\nabla_{\widehat{U}_1}\widehat{X}_1 = \mathcal{T}_{\widehat{U}_1}\widehat{X}_1 + \mathcal{H}\nabla_{\widehat{U}_1}\widehat{X}_1 \quad (2.11)$$

$$\nabla_{\widehat{X}_1}\widehat{U}_1 = \mathcal{A}_{\widehat{X}_1}\widehat{U}_1 + \mathcal{V}_1\nabla_{\widehat{X}_1}\widehat{U}_1 \quad (2.12)$$

$$\nabla_{\widehat{X}_1}\widehat{Y}_1 = \mathcal{H}\nabla_{\widehat{X}_1}\widehat{Y}_1 + \mathcal{A}_{\widehat{X}_1}\widehat{Y}_1 \quad (2.13)$$

for any vector fields $\widehat{U}_1, \widehat{V}_1 \in \Gamma(\ker J_*)$ and $\widehat{X}_1, \widehat{Y}_1 \in \Gamma(\ker J_*)^\perp$ [11].

It is obvious that \mathcal{T} and \mathcal{A} are skew-symmetric, that is

$$g(\mathcal{A}_{\hat{X}}E_1, F_1) = -g(E_1, \mathcal{A}_{\hat{X}}F_1), g(\mathcal{T}_{\hat{V}}E_1, F_1) = -g(E_1, \mathcal{T}_{\hat{V}}F_1), \quad (2.14)$$

for any vector fields $E_1, F_1 \in \Gamma(T_p\bar{B}_1)$.

Definition 2.2 A horizontally conformally submersion $J: \bar{B}_1 \rightarrow \bar{B}_2$ is called horizontally homothetic if the gradient (G) of its dilation λ is vertical, i.e.,

$$H(G\lambda) = 0, \quad (2.15)$$

at $p \in TM_1$, where H is the complement orthogonal distribution to $\nu = \ker J_*$ in $\Gamma(T_pM)$.

The second fundamental form of smooth map J is provided by the formula

$$(\nabla J_*)(\hat{U}_1, \hat{V}_1) = \nabla_{\hat{U}_1}^J J_* \hat{V}_1 - J_* \nabla_{\hat{U}_1} \hat{V}_1, \quad (2.16)$$

and the map be totally geodesic if $(\nabla J_*)(\hat{U}_1, \hat{V}_1) = 0$ for all $\hat{U}_1, \hat{V}_1 \in \Gamma(T_pM)$ where ∇ and ∇J_* are Levi-Civita and pullback connections.

Lemma 2.1 Let $J: \bar{B}_1 \rightarrow \bar{B}_2$ be a horizontal conformal submersion. Then, we have

$$(i) (\nabla J_*)(\hat{X}_1, \hat{Y}_1) = \hat{X}_1(\ln\lambda)J_*(\hat{Y}_1) + \hat{Y}_1(\ln\lambda)J_*(\hat{X}_1) - g_1(\hat{X}_1, \hat{Y}_1)J_*(\text{grad } \ln\lambda),$$

$$(ii) (\nabla J_*)(\hat{U}_1, \hat{V}_1) = -J_*(\mathcal{T}_{\hat{U}_1} \hat{V}_1),$$

$$(iii) (\nabla J_*)(\hat{X}_1, \hat{U}_1) = -J_*(\nabla_{\hat{X}_1} \hat{U}_1) = -J_*(\mathcal{A}_{\hat{X}_1} \hat{U}_1)$$

for any horizontal vector fields \hat{X}_1, \hat{Y}_1 and vertical vector fields \hat{U}_1, \hat{V}_1 [6].

3 Quasi bi-slant conformal submersions

Definition 3.1 Let $(\bar{B}_1, \phi, \xi, \eta, g_1)$ be a ACM manifold and (\bar{B}_2, g_2) a Riemannian manifold. A RS $J: \bar{B}_1 \rightarrow \bar{B}_2$ is called quasi bi-slant conformal submersion (\mathcal{QBSCS}) if there exists mutually orthogonal distributions $\mathcal{D}, \mathcal{D}_{\theta_1}$ and \mathcal{D}_{θ_2} with $\ker J_* = \mathcal{D} \oplus \mathcal{D}_{\theta_1} \oplus \mathcal{D}_{\theta_2}$ where, \mathcal{D} is invariant under ϕ . i.e., $\phi\mathcal{D} = \mathcal{D}$, for the slant distributions $\phi\mathcal{D}_{\theta_1} \perp \mathcal{D}_{\theta_1}$, $\phi\mathcal{D}_{\theta_2} \perp \mathcal{D}_{\theta_2}$ and for any non-zero vector field $\hat{V}_i \in (\mathcal{D}_{\theta_i})_{p_i}$, $p_i \in \bar{B}_i$ the angle θ_i between $(\mathcal{D}_{\theta_i})_{p_i}$ and $\phi\hat{V}_i$ is constant and independent of the choice of the point p_i and $\hat{V}_i \in (\mathcal{D}_{\theta_i})_{p_i}$, for $i = 1, 2$, where θ_1 and θ_2 are called the slant angles of submersion.

If we suppose m_1, m_2 and m_3 are the dimensions of $\mathcal{D}, \mathcal{D}_{\theta_1}$ and \mathcal{D}_{θ_2} respectively, then we have the following:

- (i) If $m_1 \neq 0, m_2 = 0$ and $m_3 = 0$, then J is an invariant submersion.
- (ii) If $m_1 \neq 0, m_2 \neq 0, 0 < \theta_1 < \frac{\pi}{2}$ and $m_3 = 0$, then J is a proper semi-slant submersion.
- (iii) If $m_1 = 0, m_2 = 0$ and $m_3 \neq 0, 0 < \theta_2 < \frac{\pi}{2}$, then J is a slant submersion with slant angle θ_2 .
- (iv) If $m_1 = 0, m_2 \neq 0, 0 < \theta_1 < \frac{\pi}{2}$ and $m_3 \neq 0, \theta_2 = \frac{\pi}{2}$, then J proper hemi-slant submersion.
- (v) If $m_1 = 0, m_2 \neq 0, 0 < \theta_1 < \frac{\pi}{2}$ and $m_3 \neq 0, 0 < \theta_2 < \frac{\pi}{2}$, then J is proper bi-slant submersion with slant angles θ_1 and θ_2 .
- (vi) If $m_1 \neq 0, m_2 \neq 0, 0 < \theta_1 < \frac{\pi}{2}$ and $m_3 \neq 0, 0 < \theta_2 < \frac{\pi}{2}$, then J is proper quasi bi-slant submersion with slant angles θ_1 and θ_2 . ”

Let J be a \mathcal{QBSCS} from an ACM manifold $(\bar{B}_1, \phi, \xi, \eta, g_1)$ onto a RM (\bar{B}_2, g_2) . Then, for any $U \in (kerJ_*)$, we have

$$\hat{U} = P_1\hat{U} + P_2\hat{U} + P_3\hat{U} \tag{3.17}$$

where P_1, P_2 and P_3 are the projections morphism onto $\mathcal{D}, \mathcal{D}_{\theta_1}$, and \mathcal{D}_{θ_2} . Now, for any $\hat{U} \in (kerJ_*)$, we have

$$\phi\hat{U} = \omega\hat{U} + \chi\hat{U} \tag{3.18}$$

where $\omega\hat{U} \in \Gamma(kerJ_*)$ and $\chi\hat{U} \in \Gamma(kerJ_*)^\perp$. From equations (3.17) and (3.18), we have

$$\begin{aligned} \phi\hat{U} &= \phi(P_1\hat{U}) + \phi(P_2\hat{U}) + \phi(P_3\hat{U}) \\ &= \omega(P_1\hat{U}) + \chi(P_1\hat{U}) + \omega(P_2\hat{U}) + \chi(P_2\hat{U}) + \omega(P_3\hat{U}) + \chi(P_3\hat{U}). \end{aligned}$$

Since $\phi\mathcal{D} = \mathcal{D}$ and $\chi(P_1\hat{U}) = 0$, we have

$$\phi\hat{U} = \omega(P_1\hat{U}) + \omega(P_2\hat{U}) + \chi(P_2\hat{U}) + \omega(P_3\hat{U}) + \chi(P_3\hat{U}).$$

Hence we have the decomposition as :

$$\phi(kerJ_*) = \omega\mathcal{D} \oplus \omega\mathcal{D}_{\theta_1} \oplus \omega\mathcal{D}_{\theta_2} \oplus \chi\mathcal{D}_{\theta_1} \oplus \chi\mathcal{D}_{\theta_2}. \tag{3.19}$$

From equations (3.19), we have the following decomposition

$$(kerJ_*)^\perp = \chi\mathcal{D}_{\theta_1} \oplus \chi\mathcal{D}_{\theta_2} \oplus \mu, \tag{3.20}$$

where μ is the orthogonal complement to $\chi\mathcal{D}_{\theta_1} \oplus \chi\mathcal{D}_{\theta_2}$ in $(kerJ_*)^\perp$ such that $\mu = (\phi\mu) \oplus \langle \xi \rangle$ and μ is invariant with respect to ϕ . Now, for any $\hat{X} \in \Gamma(kerJ_*)^\perp$, we have

$$\phi\hat{X} = t\hat{X} + n\hat{X} \tag{3.21}$$

where $t\hat{X} \in \Gamma(\ker J_*)$ and $n\hat{X} \in \Gamma(\ker J_*)^\perp$.

Lemma 3.1 Let $(\bar{B}_1, \phi, \xi, \eta, g_1)$ be an ACM manifold and (\bar{B}_2, g_2) be a RM. If $J : \bar{B}_1 \rightarrow \bar{B}_2$ is a \mathcal{QBSCS} , then we have

$$-\hat{U} + \eta(\hat{U})\xi = \omega^2\hat{U} + t\chi\hat{U}, \quad \chi\omega\hat{U} + n\chi\hat{U} = 0,$$

$$-\hat{X} = \chi t\hat{X} + n^2\hat{X}, \quad \omega t\hat{X} + tn\hat{X} = 0,$$

for $\hat{U} \in \Gamma(\ker J_*)$ and $\hat{X} \in \Gamma(\ker J_*)^\perp$.

Proof. On using equations (2.2), (3.18) and (3.21), we get the desired results. Since $J : \bar{B}_1 \rightarrow \bar{B}_2$ is a \mathcal{QBSCS} , Then let us provide some helpful findings that will be utilise throughout the paper.

Lemma 3.2 Let J be a \mathcal{QBSCS} from an ACM manifold $(\bar{B}_1, \phi, \xi, \eta, g_1)$ onto a RM (\bar{B}_2, g_2) , then we have

$$(i) \quad \omega^2\hat{U} = -\cos^2\theta_1\hat{U},$$

$$(ii) \quad g_1(\omega\hat{U}, \omega\hat{V}) = \cos^2\theta_1 g_1(\hat{U}, \hat{V}),$$

$$(iii) \quad g(\chi\hat{U}, \chi\hat{V}) = \sin^2\theta_1 g_1(\hat{U}, \hat{V}),$$

for any vector fields $\hat{U}, \hat{V} \in \Gamma(\mathcal{D}_{\theta_1})$.

Lemma 3.3 Let J be a \mathcal{QBSCS} from an ACM manifold $(\bar{B}_1, \phi, \xi, \eta, g_1)$ onto a RM (\bar{B}_2, g_2) , then we have

$$(i) \quad \omega^2\hat{Z} = -\cos^2\theta_2\hat{Z},$$

$$(ii) \quad g_1(\omega\hat{Z}, \omega\hat{W}) = \cos^2\theta_2 g_1(\hat{Z}, \hat{W}),$$

$$(iii) \quad g_1(\chi\hat{Z}, \chi\hat{W}) = \sin^2\theta_2 g_1(\hat{Z}, \hat{W}),$$

for any vector fields $\hat{Z}, \hat{W} \in \Gamma(\mathcal{D}_{\theta_2})$.

Proof. The proof of the preceding Lemmas is identical to the proof of Theorem (2.2) of [9]. As a result, we omit the proofs.

Let us suppose that (\bar{B}_2, g_2) be a Riemannian manifold and $(\bar{B}_1, \phi, \xi, \eta, g_1)$ be a Kenmotsu manifold. We now analyse how the Kenmotsu structure on \bar{B}_1 influences the tensor fields \mathcal{T} and \mathcal{A} of $\mathcal{QBSCS} J : (\bar{B}_1, \phi, \xi, \eta, g_1) \rightarrow (\bar{B}_2, g_2)$.

Lemma 3.4 Let J be a \mathcal{QBSCS} from Kenmotsu manifold $(\bar{B}_1, \phi, \xi, \eta, g_1)$ onto a RM (\bar{B}_2, g_2) , then we have

$$\mathcal{A}_{\hat{X}}n\hat{Y} + \mathcal{V}\nabla_{\hat{X}}t\hat{Y} = t\mathcal{H}\nabla_{\hat{X}}\hat{Y} + \omega\mathcal{A}_{\hat{X}}\hat{Y} + g_1(\phi\hat{X}, \hat{Y})\xi \quad (3.22)$$

$$\mathcal{H}\nabla_{\hat{X}}n\hat{Y} + \mathcal{A}_{\hat{X}}t\hat{Y} = n\mathcal{H}\nabla_{\hat{X}}\hat{Y} + \chi\mathcal{A}_{\hat{X}}\hat{Y} \quad (3.23)$$

$$\mathcal{V}\nabla_{\hat{X}}\omega\hat{V} + \mathcal{A}_{\hat{X}}\chi\hat{V} = t\mathcal{A}_{\hat{X}}\hat{V} + \omega\mathcal{V}\nabla_{\hat{X}}\hat{V} + g_1(t\hat{X}, \hat{U})\xi - \eta(\hat{U})t\hat{X} \quad (3.24)$$

$$\mathcal{A}_{\hat{X}}\omega\hat{V} + \mathcal{H}\nabla_{\hat{X}}\chi\hat{V} = n\mathcal{A}_{\hat{X}}\hat{V} + \chi\mathcal{V}\nabla_{\hat{X}}\hat{V} - \eta(\hat{U})n\hat{X} \quad (3.25)$$

$$\mathcal{V}\nabla_{\hat{V}}t\hat{X} + \mathcal{T}_{\hat{V}}n\hat{X} = \omega\mathcal{T}_{\hat{V}}\hat{X} + t\mathcal{H}\nabla_{\hat{V}}\hat{X} + g_1(\hat{X}, \phi\hat{V})\xi \quad (3.26)$$

$$\mathcal{T}_{\hat{V}}t\hat{X} + \mathcal{H}\nabla_{\hat{V}}n\hat{X} = \chi\mathcal{T}_{\hat{V}}\hat{X} + n\mathcal{H}\nabla_{\hat{V}}\hat{X} \quad (3.27)$$

$$\mathcal{V}\nabla_{\hat{U}}\omega\hat{V} + \mathcal{T}_{\hat{U}}\chi\hat{V} - \omega\mathcal{V}\nabla_{\hat{U}}\hat{V} = t\mathcal{T}_{\hat{U}}\hat{V} + g_1(\phi\hat{U}, \hat{V})\xi - \eta(\hat{V})\omega\hat{U} \quad (3.28)$$

$$\mathcal{T}_{\hat{U}}\omega\hat{V} + \mathcal{H}\nabla_{\hat{U}}\chi\hat{V} = n\mathcal{T}_{\hat{U}}\hat{V} + \chi\mathcal{V}\nabla_{\hat{U}}\hat{V} - \eta(\hat{V})\chi\hat{U}, \quad (3.29)$$

for any vector fields $\hat{U}, \hat{V} \in \Gamma(\ker J_*)$ and $\hat{X}, \hat{Y} \in \Gamma(\ker J_*)^\perp$.

Proof. From (3.21), (2.13) and (2.6), we obtained the conditions (3.22) and (3.23). Again using equations (3.18), (3.21), (2.10)-(2.13) and (2.6), finish the result. We will now go through some key conclusions that can be utilized to examine the geometry of $\mathcal{QBSCS} J : \bar{B}_1 \rightarrow \bar{B}_2$. From the direct calculations, we can conclude the following:

$$(\nabla_{\hat{U}}\omega)\hat{V} = \mathcal{V}\nabla_{\hat{U}}\omega\hat{V} - \omega\mathcal{V}\nabla_{\hat{U}}\hat{V} \quad (3.30)$$

$$(\nabla_{\hat{U}}\chi)\hat{V} = \mathcal{H}\nabla_{\hat{U}}\chi\hat{V} - \chi\mathcal{V}\nabla_{\hat{U}}\hat{V} \quad (3.31)$$

$$(\nabla_{\hat{X}}t)\hat{Y} = \mathcal{V}\nabla_{\hat{X}}t\hat{Y} - t\mathcal{H}\nabla_{\hat{X}}\hat{Y} \quad (3.32)$$

$$(\nabla_{\hat{X}}n)\hat{Y} = \mathcal{H}\nabla_{\hat{X}}n\hat{Y} - n\mathcal{H}\nabla_{\hat{X}}\hat{Y}, \quad (3.33)$$

for any vector fields $\hat{U}, \hat{V} \in \Gamma(\ker J_*)$ and $\hat{X}, \hat{Y} \in \Gamma(\ker J_*)^\perp$.

Lemma 3.5 Let $(\bar{B}_1, \phi, \xi, \eta, g_1)$ be a Kenmotsu manifold and (\bar{B}_2, g_2) be a RM. If $J : \bar{B}_1 \rightarrow \bar{B}_2$ is a \mathcal{QBSCS} , then we have

$$(\nabla_{\hat{U}}\omega)\hat{V} = t\mathcal{T}_{\hat{U}}\hat{V} - \mathcal{T}_{\hat{U}}\chi\hat{V} + g_1(\phi\hat{U}, \hat{V})\xi - \eta(\hat{V})\omega\hat{U}$$

$$(\nabla_{\hat{U}}\chi)\hat{V} = n\mathcal{T}_{\hat{U}}\hat{V} - \mathcal{T}_{\hat{U}}\omega\hat{V} - \eta(\hat{V})\chi\hat{U}$$

$$(\nabla_{\hat{X}}t)\hat{Y} = \omega\mathcal{A}_{\hat{X}}\hat{Y} - \mathcal{A}_{\hat{X}}n\hat{Y} + g_1(\phi\hat{X}, \hat{Y})\xi$$

$$(\nabla_{\hat{X}}n)\hat{Y} = \chi\mathcal{A}_{\hat{X}}\hat{Y} - \mathcal{A}_{\hat{X}}t\hat{Y},$$

for all vector fields $\hat{U}, \hat{V} \in \Gamma(\ker J_*)$ and $\hat{X}, \hat{Y} \in \Gamma(\ker J_*)^\perp$.

Proof. From some basic facts and taking account the fact from equations (2.6), (2.10)-(2.13) and equations (3.30)-(3.33), we can obtained the results. The tensor fields ω and χ , if they are parallel with regard to the connection ∇ of \bar{B}_1 , then we obtain

$${}^t\mathcal{T}_{\hat{U}}\hat{V} = \mathcal{T}_{\hat{U}}\chi\hat{V}, \quad n\mathcal{T}_{\hat{U}}\hat{V} = \mathcal{T}_{\hat{U}}\omega\hat{V}$$

for any vector fields $\hat{U}, \hat{V} \in \Gamma(T\bar{B}_1)$.

4 Integrability and totally geodesicness of distributions

Since $(\bar{B}_1, \phi, \xi, \eta, g_1)$ stands for a Kenmotsu manifold and (\bar{B}_2, g_2) for a Riemannian manifold such that $J : \bar{B}_1 \rightarrow \bar{B}_2$ is a \mathcal{LBSCS} . Three mutually orthogonal distributions, including an invariant distribution \mathcal{D} and a pair of slant distributions \mathcal{D}_{θ_1} and \mathcal{D}_{θ_2} , are assured by the theory of \mathcal{LBSCS} . The integrability of slant distribution is assessed to begin the debate on distributions integrability in the following manner.

Theorem 4.1 *Let J be a \mathcal{LBSCS} from Kenmotsu manifold $(\bar{B}_1, \phi, \xi, \eta, g_1)$ onto a RM (\bar{B}_2, g_2) . Then slant distribution \mathcal{D}_{θ_1} is integrable if and only if*

$$\begin{aligned} & \frac{1}{\lambda^2} \{g_2(-\nabla_{\hat{U}_1}^J J_*\chi\hat{V}_1 + \nabla_{\hat{V}_1}^J J_*\chi\hat{U}_1, J_*\chi P_3\hat{Z})\} \\ &= \frac{1}{\lambda^2} \{g_2((\nabla J_*)(\hat{U}_1, \chi\hat{V}_1) + (\nabla J_*)(\hat{V}_1, \chi\hat{U}_1), J_*\chi P_3\hat{Z})\} \\ & \quad - g_1(\nabla_{\hat{V}_1}\chi\omega\hat{U}_1 - \nabla_{\hat{U}_1}\chi\omega\hat{V}_1, \hat{Z}) - g_1(\mathcal{T}_{\hat{U}_1}\chi\hat{V}_1 - \mathcal{T}_{\hat{V}_1}\chi\hat{U}_1, \phi P_1\hat{Z} + \omega P_3\hat{Z}), \end{aligned} \tag{4.34}$$

for any $\hat{U}_1, \hat{V}_1 \in \Gamma(\mathcal{D}_{\theta_1})$ and $\hat{Z} \in \Gamma(\mathcal{D} \oplus \mathcal{D}_{\theta_2} \oplus \langle \xi \rangle)$.

Proof. For all $\hat{U}_1, \hat{V}_1 \in \Gamma(\mathcal{D}_{\theta_1})$ and $\hat{Z} \in \Gamma(\mathcal{D} \oplus \mathcal{D}_{\theta_2} \oplus \langle \xi \rangle)$ with using equations (2.3), (2.6), (2.4) and (3.18), we get

$$\begin{aligned} g_1([\hat{U}_1, \hat{V}_1], \hat{Z}) &= g_1(\nabla_{\hat{U}_1}\omega\hat{V}_1, \phi\hat{Z}) + g_1(\nabla_{\hat{U}_1}\chi\hat{V}_1, \phi\hat{Z}) - g_1(\nabla_{\hat{V}_1}\omega\hat{U}_1, \phi\hat{Z}) \\ & \quad - g_1(\nabla_{\hat{V}_1}\chi\hat{U}_1, \phi\hat{Z}). \end{aligned}$$

By using equations (2.6), (2.4) and (3.18), we have

$$\begin{aligned} g_1([\hat{U}_1, \hat{V}_1], \hat{Z}) &= -g_1(\nabla_{\hat{U}_1}\omega^2\hat{V}_1, \hat{Z}) - g_1(\nabla_{\hat{U}_1}\chi\omega\hat{V}_1, \hat{Z}) + g_1(\nabla_{\hat{V}_1}\omega^2\hat{U}_1, \hat{Z}) \\ & \quad + g_1(\nabla_{\hat{V}_1}\chi\omega\hat{U}_1, \hat{Z}) + g_1(\nabla_{\hat{U}_1}\chi\hat{V}_1, \phi P_1\hat{Z} + \omega P_3\hat{Z} + \chi P_3\hat{Z}) \\ & \quad - g_1(\nabla_{\hat{V}_1}\chi\hat{U}_1, \phi P_1\hat{Z} + \omega P_3\hat{Z} + \chi P_3\hat{Z}). \end{aligned}$$

Taking account the fact of Lemma 3.2 with equation (2.11), we get

$$\begin{aligned} g_1([\widehat{U}_1, \widehat{V}_1], \widehat{Z}) &= \cos^2 \theta_1 g_1([\widehat{U}_1, \widehat{V}_1], \widehat{Z}) + g_1(\nabla_{\widehat{V}_1} \chi \omega \widehat{U}_1 - \nabla_{\widehat{U}_1} \chi \omega \widehat{V}_1, \widehat{Z}) \\ &\quad + g_1(\mathcal{F}_{\widehat{U}_1} \chi \widehat{V}_1 - \mathcal{F}_{\widehat{V}_1} \chi \widehat{U}_1, \phi P_1 \widehat{Z} + \omega P_3 \widehat{Z}) \\ &\quad + g_1(\mathcal{H} \nabla_{\widehat{U}_1} \chi \widehat{V}_1 - \mathcal{H} \nabla_{\widehat{V}_1} \chi \widehat{U}_1, \chi P_3 \widehat{Z}). \end{aligned}$$

On using equation (2.7), formula (2.16) with Lemma 2.1, we finally get

$$\begin{aligned} &\sin^2 \theta_1 g_1([\widehat{U}_1, \widehat{V}_1], \widehat{Z}) \\ &= \frac{1}{\lambda^2} \{g_2((\nabla J_*)(\widehat{U}_1, \chi \widehat{V}_1), J_* \chi P_3 \widehat{Z}) + g_2((\nabla J_*)(\widehat{V}_1, \chi \widehat{U}_1), J_* \chi P_3 \widehat{Z})\} \\ &\quad + g_1(\mathcal{F}_{\widehat{U}_1} \chi \widehat{V}_1 - \mathcal{F}_{\widehat{V}_1} \chi \widehat{U}_1, \phi P_1 \widehat{Z} + \omega P_3 \widehat{Z}) + g_1(\nabla_{\widehat{V}_1} \chi \omega \widehat{U}_1 - \nabla_{\widehat{U}_1} \chi \omega \widehat{V}_1, \widehat{Z}) \\ &\quad \frac{1}{\lambda^2} \{g_2(\nabla_{\widehat{U}_1}^J J_* \chi \widehat{V}_1 - \nabla_{\widehat{V}_1}^J J_* \chi \widehat{U}_1, J_* \chi P_3 \widehat{Z})\}. \end{aligned}$$

The condition of integrability for \mathfrak{D}_{θ_2} can be determined in the same way, as shown below:

Theorem 4.2 Let $J : (\bar{B}_1, \phi, \xi, \eta, g_1) \rightarrow (\bar{B}_2, g_2)$ be a \mathcal{QBSCS} , where $(\bar{B}_1, \phi, \xi, \eta, g_1)$ a Kenmotsu manifold and (\bar{B}_2, g_2) a RM. Then slant distribution \mathfrak{D}_{θ_2} is integrable if and only if

$$\begin{aligned} &-\frac{1}{\lambda^2} \{g_2((\nabla J_*)(\widehat{U}_2, \chi \widehat{V}_2) - (\nabla J_*)(\widehat{V}_2, \chi \widehat{U}_2), J_* \chi P_2 \widehat{Z})\} \\ &= g_1(\mathcal{F}_{\widehat{V}_2} \chi \omega \widehat{U}_2 - \mathcal{F}_{\widehat{U}_2} \chi \omega \widehat{V}_2, \widehat{Z}) + g_1(\mathcal{F}_{\widehat{U}_2} \chi \widehat{V}_2 - \mathcal{F}_{\widehat{V}_2} \chi \widehat{U}_2, \phi P_1 \widehat{Z} + \omega P_2 \widehat{Z}) \\ &\quad + \frac{1}{\lambda^2} \{g_2(\nabla_{\widehat{U}_2}^J J_* \chi \widehat{V}_2 - \nabla_{\widehat{V}_2}^J J_* \chi \widehat{U}_2, J_* \chi P_2 \widehat{Z})\}, \end{aligned}$$

for any $\widehat{U}_2, \widehat{V}_2 \in \Gamma(\mathfrak{D}_{\theta_2})$ and $\widehat{Z} \in \Gamma(\mathfrak{D} \oplus \mathfrak{D}_{\theta_1} \oplus \langle \xi \rangle)$.

Proof. On using equations (2.3), (2.4), (2.6) and (3.18), we have

$$\begin{aligned} g_1([\widehat{U}_2, \widehat{V}_2], \widehat{Z}) &= g_1(\nabla_{\widehat{V}_2} \omega^2 \widehat{U}_2, \widehat{Z}) + g_1(\nabla_{\widehat{V}_2} \chi \omega \widehat{U}_2, \widehat{Z}) - g_1(\nabla_{\widehat{U}_2} \omega^2 \widehat{V}_2, \widehat{Z}) \\ &\quad - g_1(\nabla_{\widehat{U}_2} \chi \omega \widehat{V}_2, \widehat{Z}) + g_1(\nabla_{\widehat{U}_2} \chi \widehat{V}_2 - \nabla_{\widehat{V}_2} \chi \widehat{U}_2, \phi \widehat{Z}), \end{aligned}$$

for any $\widehat{U}_2, \widehat{V}_2 \in \Gamma(\mathfrak{D}_{\theta_2})$ and $\widehat{Z} \in \Gamma(\mathfrak{D} \oplus \mathfrak{D}_{\theta_1} \oplus \langle \xi \rangle)$. From equation (2.11) and Lemma 3.3, we get

$$\begin{aligned} \sin^2 \theta_2 g_1([\widehat{U}_2, \widehat{V}_2], \widehat{Z}) &= g_1(\mathcal{F}_{\widehat{V}_2} \chi \omega \widehat{U}_2 - \mathcal{F}_{\widehat{U}_2} \chi \omega \widehat{V}_2, \widehat{Z}) + g_1(\mathcal{F}_{\widehat{U}_2} \chi \widehat{V}_2 - \mathcal{F}_{\widehat{V}_2} \chi \widehat{U}_2, \phi P_1 \widehat{Z} + \omega P_2 \widehat{Z}) \\ &\quad + g_1(\mathcal{H} \nabla_{\widehat{U}_2} \chi \widehat{V}_2 - \mathcal{H} \nabla_{\widehat{V}_2} \chi \widehat{U}_2, \chi P_2 \widehat{Z}). \end{aligned}$$

Since J is \mathcal{QBSCS} , using conformality condition with equations (2.7) and (2.16), we finally get

$$\begin{aligned} \sin^2 \theta_2 g_1([\widehat{U}_2, \widehat{V}_2], \widehat{Z}) &= g_1(\mathcal{T}_{\widehat{V}_2} \chi \omega \widehat{U}_2 - \mathcal{T}_{\widehat{U}_2} \chi \omega \widehat{V}_2, \widehat{Z}) + g_1(\mathcal{T}_{\widehat{U}_2} \chi \widehat{V}_2 - \mathcal{T}_{\widehat{V}_2} \chi \widehat{U}_2, \phi P_1 \widehat{Z} + \omega P_2 \widehat{Z}) \\ &+ \frac{1}{\lambda^2} \{g_2((\nabla J_*)(\widehat{U}_2, \chi \widehat{V}_2) - (\nabla J_*)(\widehat{V}_2, \chi \widehat{U}_2), J_* \chi P_2 \widehat{Z})\} \\ &+ \frac{1}{\lambda^2} \{g_2(\nabla_{\widehat{U}_2}^J J_* \chi \widehat{V}_2 - \nabla_{\widehat{V}_2}^J J_* \chi \widehat{U}_2, J_* \chi P_2 \widehat{Z})\}. \end{aligned}$$

This completes the proof of the theorem.

Given that slant distributions and the invariant distribution are mutually orthogonal. This inspired us to look into the prerequisites for the integrability of the invariant distribution \mathfrak{D} .

Theorem 4.3 *Let $J : (\bar{B}_1, \phi, \xi, \eta, g_1) \rightarrow (\bar{B}_2, g_2)$ be a \mathcal{QBSCS} , where $(\bar{B}_1, \phi, \xi, \eta, g_1)$ a Kenmotsu manifold and (\bar{B}_2, g_2) a RM. Then the invariant distribution \mathfrak{D} is integrable if and only if*

$$\begin{aligned} &g_1(\mathcal{T}_{\widehat{U}} \omega P_1 \widehat{V} - \mathcal{T}_{\widehat{V}} \omega P_1 \widehat{U}, \chi P_2 \widehat{Z} + \chi P_3 \widehat{W}) \\ &= -g_1(\mathcal{V} \nabla_{\widehat{U}} \omega P_1 \widehat{V} - \mathcal{V} \nabla_{\widehat{V}} \omega P_1 \widehat{U}, \omega P_2 \widehat{Z} + \omega P_3 \widehat{Z}), \end{aligned} \tag{4.35}$$

for any $\widehat{U}, \widehat{V} \in \Gamma(\mathfrak{D})$ and $\widehat{Z} \in \Gamma(\mathfrak{D}_{\theta_1} \oplus \mathfrak{D}_{\theta_2} \oplus \langle \xi \rangle)$.

Proof. For all $\widehat{U}, \widehat{V} \in \Gamma(\mathfrak{D})$ and $\widehat{Z} \in \Gamma(\mathfrak{D}_{\theta_1} \oplus \mathfrak{D}_{\theta_2} \oplus \langle \xi \rangle)$ with using equations (2.3), (2.4), (2.10) and decomposition (3.17), we have

$$g_1([\widehat{U}, \widehat{V}], \widehat{Z}) = g_1(\nabla_{\widehat{U}} \omega P_1 \widehat{V}, \phi P_2 \widehat{Z} + \phi P_3 \widehat{Z}) - g_1(\nabla_{\widehat{V}} \omega P_1 \widehat{U}, \phi P_2 \widehat{Z} + \phi P_3 \widehat{Z}).$$

On using equation (3.18), we finally have

$$\begin{aligned} g_1([\widehat{U}, \widehat{V}], \widehat{Z}) &= g_1(\mathcal{T}_{\widehat{U}} \omega P_1 \widehat{V} - \mathcal{T}_{\widehat{V}} \omega P_1 \widehat{U}, \chi P_2 \widehat{Z} + \chi P_3 \widehat{Z}) \\ &+ g_1(\mathcal{V} \nabla_{\widehat{U}} \omega P_1 \widehat{V} - \mathcal{V} \nabla_{\widehat{V}} \omega P_1 \widehat{U}, \omega P_2 \widehat{Z} + \omega P_3 \widehat{Z}). \end{aligned}$$

This completes the proof of theorem.

After describing the necessary conditions for distributions integrability, we will move on to the necessary and sufficient conditions that must also exist in order for distributions to be totally geodesic. We begin by looking into the prerequisites and criteria for totally geodesic distributions.

Theorem 4.4 *Let $J : (\bar{B}_1, \phi, \xi, \eta, g_1) \rightarrow (\bar{B}_2, g_2)$ be \mathcal{QBSCS} from a Kenmotsu manifold onto a Riemannian manifold. (\bar{B}_2, g_2) . Then \mathfrak{D} is not defines totally geodesic foliation on \bar{B}_1 .*

Proof. Taking the vector fields $\widehat{Z}, \widehat{V} \in \Gamma(\mathfrak{D})$ and since \widehat{V} and ξ are orthogonal, we have

$$g(\nabla_{\widehat{U}} \widehat{V}, \xi) = -g(\widetilde{\nabla}, \nabla_{\widehat{U}} \xi)$$

By considering equation (2.8), we get

$$g(\nabla_{\widehat{U}}\widehat{V}, \xi) = -g(\widehat{U}, \widehat{V}).$$

For $\widehat{U}, \widehat{V} \in \Gamma(\mathfrak{D})$, $g(\widehat{U}, \widehat{V}) \neq 0$, that is $g(\nabla_{\widehat{U}}\widehat{V}, \xi) \neq 0$. Hence, the distribution is not totally geodesic. Since, the invariant distribution is not defines totally geodesic foliation on \bar{B}_1 , therefore, we discuss the geometry of leaf of distribution $\mathfrak{D} \oplus \langle \xi \rangle$.

Theorem 4.5 Let $J : (\bar{B}_1, \phi, \xi, \eta, g_1) \rightarrow (\bar{B}_2, g_2)$ be a \mathcal{DBSCS} , where $(\bar{B}_1, \phi, \xi, \eta, g_1)$ a Kenmotsu manifold and (\bar{B}_2, g_2) a RM. Then invariant distribution $\mathfrak{D} \oplus \langle \xi \rangle$ defines totally geodesic foliation on \bar{B}_1 if and only if

$$(i) \lambda^{-2}g_2\{((\nabla J_*)(\widehat{U}, \phi\widehat{V}), J_*\chi\widehat{Z})\} = g_1(\mathcal{V}\nabla_{\widehat{U}}\phi\widehat{V}, \omega\widehat{Z})$$

$$(ii) \lambda^{-2}\{g_2((\nabla J_*)(\widehat{U}, \phi\widehat{V}), J_*n\widehat{X})\} = g_1(\mathcal{V}\nabla_{\widehat{U}}\phi\widehat{V}, t\widehat{X}),$$

for any $\widehat{U}, \widehat{V} \in \Gamma(\mathfrak{D} \oplus \langle \xi \rangle)$ and $\widehat{Z} \in \Gamma(\mathfrak{D}_{\theta_1} \oplus \mathfrak{D}_{\theta_2})$, $\widehat{X} \in \Gamma(KerJ_*)^\perp$.

Proof. For any $\widehat{U}, \widehat{V} \in \Gamma(\mathfrak{D})$ and $\widehat{Z} \in \Gamma(\mathfrak{D}_{\theta_1} \oplus \mathfrak{D}_{\theta_2})$ with using equations (2.3), (2.4), (2.6) and (3.18), we may write

$$g_1(\nabla_{\widehat{U}}\widehat{V}, \widehat{Z}) = g_1(\mathcal{V}\nabla_{\widehat{U}}\phi\widehat{V}, \omega\widehat{Z}) + g_1(\mathcal{T}_{\widehat{U}}\phi\widehat{V}, \chi\widehat{Z}).$$

On using the conformality of J with equation (2.7) and (2.16), we get

$$g_1(\nabla_{\widehat{U}}\widehat{V}, \widehat{Z}) = g_1(\mathcal{V}\nabla_{\widehat{U}}\phi\widehat{V}, \omega\widehat{Z}) - \lambda^{-2}g_2((\nabla J_*)(\widehat{U}, \phi\widehat{V}), J_*\chi\widehat{Z}).$$

On the other hand, using equations (2.3), (2.4), (2.6) with conformality of J with $\widehat{X} \in \Gamma(KerJ_*)^\perp$, we finally have

$$g_1(\nabla_{\widehat{U}}\widehat{V}, \widehat{X}) = g_1(\mathcal{V}\nabla_{\widehat{U}}\phi\widehat{V}, t\widehat{X}) - \lambda^{-2}g_2((\nabla J_*)(\widehat{U}, \phi\widehat{V}), J_*n\widehat{X}),$$

from which we get the desired result.

Theorem 4.6 Let $J : (\bar{B}_1, \phi, \xi, \eta, g_1) \rightarrow (\bar{B}_2, g_2)$ be \mathcal{DBSCS} from a Kenmotsu manifold onto a Riemannian manifold. (\bar{B}_2, g_2) . Then \mathfrak{D}_{θ_1} is not defines totally geodesic foliation on \bar{B}_1 .

Proof. Taking the vector fields $\widehat{X}, \widehat{Y} \in \Gamma(\mathfrak{D}_{\theta_1})$ and since \widehat{Y} and ξ are orthogonal, we have

$$g(\nabla_{\widehat{X}}\widehat{Y}, \xi) = -g(\widehat{Y}, \nabla_{\widehat{X}}\xi)$$

By considering equation (2.8), we get

$$g(\nabla_{\widehat{X}}\widehat{Y}, \xi) = -g(\widehat{X}, \widehat{Y}).$$

For $\widehat{X}, \widehat{Y} \in \Gamma(\mathfrak{D}_{\theta_1})$, $g(\widehat{X}, \widehat{Y}) \neq 0$, that is $g(\nabla_{\widehat{X}}\widehat{Y}, \xi) \neq 0$. Hence, the distribution is not totally geodesic.

In same manner, we can examine the geometry of leaves of $\mathfrak{D}_{\theta_1} \oplus \xi$ as follows:

Theorem 4.7 *Let J be a \mathcal{LBSCS} from Kenmotsu manifold $(\bar{B}_1, \phi, \xi, \eta, g_1)$ onto a RM (\bar{B}_2, g_2) . Then slant distribution $\mathfrak{D}_{\theta_1} \oplus \xi$ defines totally geodesic foliation on \bar{B}_1 if and only if*

$$\begin{aligned} & \frac{1}{\lambda^2}g_2(\nabla_{\widehat{Z}}^J J_*\chi P_2\widehat{W}, J_*\chi P_3\widehat{W}) \\ &= \cos^2\theta_1g_1(\nabla_{\widehat{Z}}P_2\widehat{W}, \widehat{U}) - g_1(\mathcal{F}_{\widehat{Z}}\chi\omega P_2\widehat{W}, \widehat{U}) + g_1(\mathcal{F}_{\widehat{Z}}\chi\omega P_2\widehat{W}, \phi P_1\widehat{U}) \\ &+ g_1(\mathcal{F}_{\widehat{Z}}\chi P_2\widehat{W}, \omega P_3\widehat{U}) - \frac{1}{\lambda^2}g_2((\nabla J_*)(\chi P_2\widehat{W}, \widehat{Z}), J_*P_3\widehat{U}) - g_1(\phi\widehat{Z}, \widehat{U})\eta(P_2\widehat{W}). \end{aligned} \quad (4.36)$$

and

$$\begin{aligned} & \lambda^{-2}\{g_2(\nabla_{\widehat{Z}}^J J_*\chi\omega P_2\widehat{W}, J_*\widehat{X})\} + \eta(P_2\widehat{W})g_1(\phi\widehat{Z}, \widehat{X}) \\ &= \frac{1}{\lambda^2}g_2((\nabla J_*)(\widehat{Z}, \chi\omega P_2\widehat{W}), J_*\widehat{X}) - \frac{1}{\lambda^2}g_2((\nabla J_*)(\widehat{Z}, \chi\omega P_2\widehat{W}), J_*n\widehat{X}) \\ &+ \cos^2\theta_1g_1(\nabla_{\widehat{Z}}P_2\widehat{W}, \widehat{X}) + g_1(\mathcal{F}_{\widehat{Z}}\chi\omega P_2\widehat{W}, t\widehat{X}) - g_2(\nabla_{\widehat{Z}}^J J_*\chi\omega P_2\widehat{W}, J_*n\widehat{X}), \end{aligned} \quad (4.37)$$

for any $\widehat{Z}, \widehat{W} \in \Gamma(\mathfrak{D}_{\theta_1} \oplus \xi)$, $\widehat{U} \in \Gamma(D \oplus \mathfrak{D}_{\theta_2})$ and $\widehat{X} \in \Gamma(\ker J_*)^\perp$.

Proof. By using equations (2.3), (2.6), (2.4) and (3.18), we get

$$g_1(\nabla_{\widehat{Z}}\widehat{W}, \widehat{U}) = g_1(\nabla_{\widehat{Z}}\chi P_2\widehat{W}, \phi(P_1\widehat{U} + P_3\widehat{U})) - g_1(\phi\nabla_{\widehat{Z}}\omega P_2\widehat{W}, \widehat{U}),$$

for $\widehat{Z}, \widehat{W} \in \Gamma(\mathfrak{D}_{\theta_1} \oplus \xi)$ and $\widehat{U} \in \Gamma(D \oplus \mathfrak{D}_{\theta_2})$. Again using equations (2.3), (2.6), (2.4), (3.18), (2.11) with Lemma 3.2, we may write

$$\begin{aligned} g_1(\nabla_{\widehat{Z}}\widehat{W}, \widehat{U}) &= \cos^2\theta_1g_1(\nabla_{\widehat{Z}}P_2\widehat{W}, \widehat{U}) - g_1(\mathcal{F}_{\widehat{Z}}\chi\omega P_2\widehat{W}, \widehat{U}) + g_1(\mathcal{F}_{\widehat{Z}}\chi\omega P_2\widehat{W}, \phi P_1\widehat{U}) \\ &+ g_1(\mathcal{F}_{\widehat{Z}}\chi P_2\widehat{W}, \omega P_3\widehat{U}) + g_1(\mathcal{H}\nabla_{\widehat{Z}}\chi P_2\widehat{W}, \chi P_3\widehat{U}) - g_1(\phi\widehat{Z}, \widehat{U})\eta(P_2\widehat{W}). \end{aligned}$$

Since, J is conformal, using Lemma 2.1 with equations (2.7) and (2.16), we have

$$\begin{aligned} g_1(\nabla_{\widehat{Z}}\widehat{W}, \widehat{U}) &= \cos^2\theta_1g_1(\nabla_{\widehat{Z}}P_2\widehat{W}, \widehat{U}) - g_1(\mathcal{F}_{\widehat{Z}}\chi\omega P_2\widehat{W}, \widehat{U}) + g_1(\mathcal{F}_{\widehat{Z}}\chi\omega P_2\widehat{W}, \phi P_1\widehat{U}) \\ &+ g_1(\mathcal{F}_{\widehat{Z}}\chi P_2\widehat{W}, \omega P_3\widehat{U}) - \frac{1}{\lambda^2}g_2(\nabla_{\widehat{Z}}^J J_*\chi P_2\widehat{W}, J_*\chi P_3\widehat{W}) \\ &- \frac{1}{\lambda^2}g_2((\nabla J_*)(\chi P_2\widehat{W}, \widehat{Z}), J_*P_3\widehat{U}) - g_1(\phi\widehat{Z}, \widehat{U})\eta(P_2\widehat{W}). \end{aligned} \quad (4.38)$$

On the other hand, for $\widehat{Z}, \widehat{W} \in \Gamma(\mathfrak{D}_{\theta_1} \oplus \xi)$ and $\widehat{X} \in \Gamma(\ker J_*)^\perp$, with using equations (2.3), (2.6), (2.4) and (3.18), we get

$$g_1(\nabla_{\widehat{Z}}\widehat{W}, \widehat{X}) = g_1(\nabla_{\widehat{Z}}\omega P_2\widehat{W}, \phi\widehat{X}) + g_1(\nabla_{\widehat{Z}}\chi P_2\widehat{W}, \phi\widehat{X}) + \eta(P_2\widehat{W})g_1(\phi\widehat{Z}, \widehat{X}).$$

From Lemma 3.2 with equations (2.11) and (3.21), the above equation takes the form

$$g_1(\nabla_{\widehat{Z}}\widehat{W}, \widehat{X}) = \cos^2\theta_1 g_1(\nabla_{\widehat{Z}}P_2\widehat{W}, \widehat{X}) - g_1(\mathcal{H}\nabla_{\widehat{Z}}\chi\omega P_2\widehat{W}, \widehat{X}) + \eta(P_2\widehat{W})g_1(\phi\widehat{Z}, \widehat{X}) \\ + g_1(\mathcal{T}_{\widehat{Z}}\chi\omega P_2\widehat{W}, t\widehat{X}) + g_1(\mathcal{H}\nabla_{\widehat{Z}}\chi\omega P_2\widehat{W}, n\widehat{X}).$$

Since J is conformal and from equations (2.7) and (2.16), we have

$$g_1(\nabla_{\widehat{Z}}\widehat{W}, \widehat{X}) = \cos^2\theta_1 g_1(\nabla_{\widehat{Z}}P_2\widehat{W}, \widehat{X}) + g_1(\mathcal{T}_{\widehat{Z}}\chi\omega P_2\widehat{W}, t\widehat{X}) - \eta(P_2\widehat{W})g_1(\phi\widehat{Z}, \widehat{X}) \\ + \frac{1}{\lambda^2}g_2((\nabla J_*)(\chi\omega P_2\widehat{W}, \widehat{Z}), J_*\widehat{X}) - \frac{1}{\lambda^2}g_2(\nabla_{\widehat{Z}}^J J_*\chi\omega P_2\widehat{W}, J_*\widehat{X}) \\ - \frac{1}{\lambda^2}g_2((\nabla J_*)(\chi\omega P_2\widehat{W}, \widehat{Z}), J_*n\widehat{X}) + \frac{1}{\lambda^2}g_2(\nabla_{\widehat{Z}}^J J_*\chi\omega P_2\widehat{W}, J_*n\widehat{X}),$$

from which we get the result.

Theorem 4.8 Let $J : (\bar{B}_1, \phi, \xi, \eta, g_1) \rightarrow (\bar{B}_2, g_2)$ be \mathcal{DBSCS} from a Kenmotsu manifold onto a Riemannian manifold. (\bar{B}_2, g_2) . Then \mathfrak{D}_{θ_2} is not defines totally geodesic foliation on \bar{B}_1 .

Proof. Taking the vector fields $\widehat{X}, \widehat{Y} \in \Gamma(\mathfrak{D}_{\theta_2})$ and since \widehat{Y} and ξ are orthogonal, we have

$$g(\nabla_{\widehat{X}}\widehat{Y}, \xi) = -g(\widehat{Y}, \nabla_{\widehat{X}}\xi)$$

By considering equation (2.8), we get

$$g(\nabla_{\widehat{X}}\widehat{Y}, \xi) = -g(\widehat{X}, \widehat{Y}).$$

For $\widehat{X}, \widehat{Y} \in \Gamma(\mathfrak{D}_{\theta_2}), g(\widehat{X}, \widehat{Y}) \neq 0$, that is $g(\nabla_{\widehat{X}}\widehat{Y}, \xi) \neq 0$. Hence, the distribution is not totally geodesic.

In the following theorem, we study the necessary and sufficient conditions for slant distribution \mathfrak{D}_{θ_2} to be totally geodesic.

Theorem 4.9 Let $J : (\bar{B}_1, \phi, \xi, \eta, g_1) \rightarrow (\bar{B}_2, g_2)$ be a \mathcal{DBSCS} , where $(\bar{B}_1, \phi, \xi, \eta, g_1)$ a Kenmotsu manifold and (\bar{B}_2, g_2) a RM. Then slant distribution $\mathfrak{D}_{\theta_2} \oplus \langle \xi \rangle$ defines totally geodesic

foliation on \bar{B}_1 if and only if

$$\begin{aligned} & \frac{1}{\lambda^2} g_2(\nabla_{\hat{Z}}^J J_* \chi P_2 \hat{W}, J_* \chi P_3 \hat{V}) \\ &= \cos^2 \theta_1 g_1(\nabla_{\hat{Z}} P_2 \hat{W}, \hat{V}) - g_1(\mathcal{T}_{\hat{Z}} \chi \omega P_2 \hat{W}, \hat{V}) + g_1(\mathcal{T}_{\hat{Z}} \chi \omega P_2 \hat{W}, \phi P_1 \hat{V}) \\ &+ g_1(\mathcal{T}_{\hat{Z}} \chi P_2 \hat{W}, \omega P_3 \hat{V}) - \frac{1}{\lambda^2} g_2((\nabla J_*)(\chi P_2 \hat{W}, \hat{Z}), J_* P_3 \hat{V}) - g_1(\phi \hat{Z}, \hat{V}) \eta(P_2 \hat{W}). \end{aligned} \quad (4.39)$$

and

$$\begin{aligned} & \lambda^{-2} \{g_2(\nabla_{\hat{Z}}^J J_* \chi \omega P_3 \hat{W}, J_* \hat{Y}) - g_2(\nabla_{\hat{Z}}^J J_* \chi \omega P_3 \hat{W}, J_* n \hat{Y})\} + \eta(P_2 \hat{W}) g_1(\phi \hat{Z}, \hat{Y}) \\ &= \frac{1}{\lambda^2} g_2((\nabla J_*)(\hat{Z}, \chi \omega P_3 \hat{W}), J_* \hat{Y}) - \frac{1}{\lambda^2} g_2((\nabla J_*)(\hat{Z}, \chi \omega P_3 \hat{W}), J_* n \hat{Y}) \\ &+ \cos^2 \theta_2 g_1(\nabla_{\hat{Z}} P_3 \hat{W}, \hat{Y}) + g_1(\mathcal{T}_{\hat{Z}} \chi \omega P_3 \hat{W}, t \hat{Y}) + \eta(\hat{W}) g_1(\hat{Z}, t \hat{Y}), \end{aligned} \quad (4.40)$$

for any $\hat{Z}, \hat{W} \in \Gamma(D_{\theta_2} \oplus \langle \xi \rangle)$, $\hat{V} \in \Gamma(D \oplus D_{\theta_1})$ and $\hat{Y} \in \Gamma(\ker J_*)^\perp$.

Proof. The proof of above theorem is similar to the proof of Theorem 4.7.

Since, J is \mathcal{QBSCS} , having $(\ker J_*)$ and $(\ker J_*)^\perp$ are vertical and horizontal distributions, respectively. We now investigate the conditions under which distributions define totally geodesic foliation on \bar{B}_1 . In terms of vertical distribution's total geodesicness, we have

Theorem 4.10 Let $J : (\bar{B}_1, \phi, \xi, \eta, g_1) \rightarrow (\bar{B}_2, g_2)$ be a \mathcal{QBSCS} , where $(\bar{B}_1, \phi, \xi, \eta, g_1)$ a Kenmotsu manifold and (\bar{B}_2, g_2) a RM. Then $\ker J_*$ defines totally geodesic foliation on \bar{B}_1 if and only if

$$\begin{aligned} & \frac{1}{\lambda^2} \{g_2(\nabla_{\hat{U}}^J J_* \chi \omega P_2 \hat{V} + \nabla_{\hat{U}}^J J_* \chi \omega P_3 \hat{V}, J_* \hat{X})\} \\ &= g_1(\mathcal{T}_{\hat{U}} P_1 \hat{V} + \cos^2 \theta_1 \mathcal{T}_{\hat{U}} P_2 \hat{V} + \cos^2 \theta_2 \mathcal{T}_{\hat{U}} P_3 \hat{V}, \hat{X}) + g_1(\mathcal{T}_{\hat{U}} \chi \hat{V}, t \hat{X}) \\ &+ \frac{1}{\lambda^2} \{g_2((\nabla J_*)(\hat{U}, \chi \omega P_2 \hat{V}) - (\nabla J_*)(\hat{U}, \chi \omega P_3 \hat{V}), J_* \hat{X})\} \\ &+ \frac{1}{\lambda^2} \{g_2(\nabla_{\hat{U}}^J J_* \chi \hat{V} - (\nabla J_*)(\hat{U}, \chi \hat{V}), J_* n \hat{X})\}. \end{aligned} \quad (4.41)$$

for any $\hat{U}, \hat{V} \in \Gamma(\ker J_*)$ and $\hat{X} \in \Gamma(\ker J_*)^\perp$.

Proof. For any $\hat{U}, \hat{V} \in \Gamma(\ker J_*)$ and $\hat{X} \in \Gamma(\ker J_*)^\perp$ with using equations (2.3), (2.6), (2.4) with decomposition (3.17), we get

$$g_1(\nabla_{\hat{U}} \hat{V}, \hat{X}) = g_1(\nabla_{\hat{U}} \phi P_1 \hat{V}, \phi \hat{X}) + g_1(\nabla_{\hat{U}} \phi P_2 \hat{V}, \phi \hat{X}) + g_1(\nabla_{\hat{U}} \phi P_3 \hat{V}, \phi \hat{X}).$$

On using equation (3.18) with Lemma 3.2 and Lemma 3.3, we have

$$\begin{aligned} g_1(\nabla_{\hat{U}}\hat{V},\hat{X}) &= g_1(\nabla_{\hat{U}}P_1\hat{V},\hat{X}) + \cos^2\theta_1g_1(\nabla_{\hat{U}}P_2\hat{V},\hat{X}) + \cos^2\theta_2g_1(\nabla_{\hat{U}}P_3\hat{V},\hat{X}) \\ &\quad + g_1(\nabla_{\hat{U}}\chi P_2\hat{V},\phi\hat{X}) - g_1(\nabla_{\hat{U}}\chi\omega P_2\hat{V},\hat{X}) - g_1(\nabla_{\hat{U}}\chi\omega P_3\hat{V},\hat{X}) \\ &\quad + g_1(\nabla_{\hat{U}}\chi P_3\hat{V},\phi\hat{X}) - \eta(P_2\hat{V})g_1(\chi\hat{U},\hat{X}). \end{aligned}$$

From equations (2.10), (2.11) and (3.21), we may yields

$$\begin{aligned} g_1(\nabla_{\hat{U}}\hat{V},\hat{X}) &= g_1(\mathcal{T}_{\hat{U}}P_1\hat{V} + \cos^2\theta_1\mathcal{T}_{\hat{U}}P_2\hat{V} + \cos^2\theta_2\mathcal{T}_{\hat{U}}P_3\hat{V},\hat{X}) \\ &\quad - g_1(\mathcal{H}\nabla_{\hat{U}}\chi\omega P_2\hat{V} + \mathcal{H}\nabla_{\hat{U}}\chi\omega P_3\hat{V},\hat{X}) + g_1(\mathcal{T}_{\hat{U}}\chi P_2\hat{V} + \mathcal{T}_{\hat{U}}\chi P_3\hat{V},t\hat{X}) \\ &\quad + g_1(\mathcal{H}\nabla_{\hat{U}}\chi P_2\hat{V} + \mathcal{H}\nabla_{\hat{U}}\chi P_3\hat{V},n\hat{X}) - \eta(P_2\hat{V})g_1(\chi\hat{U},\hat{X}). \end{aligned}$$

From decomposition (3.17), the above equation takes the form

$$\begin{aligned} g_1(\nabla_{\hat{U}}\hat{V},\hat{X}) &= g_1(\mathcal{T}_{\hat{U}}P_1\hat{V} + \cos^2\theta_1\mathcal{T}_{\hat{U}}P_2\hat{V} + \cos^2\theta_2\mathcal{T}_{\hat{U}}P_3\hat{V},\hat{X}) + g_1(\mathcal{T}_{\hat{U}}\chi\hat{V},t\hat{X}) \\ &\quad - g_1(\mathcal{H}\nabla_{\hat{U}}\chi\omega P_2\hat{V} + \mathcal{H}\nabla_{\hat{U}}\chi\omega P_3\hat{V},\hat{X}) + g_1(\mathcal{H}\nabla_{\hat{U}}\chi\hat{V},n\hat{X}) \\ &\quad - \eta(P_2\hat{V})g_1(\chi\hat{U},\hat{X}). \end{aligned}$$

Using the conformality of J with equations (2.7) and (2.16), we have

$$\begin{aligned} g_1(\nabla_{\hat{U}}\hat{V},\hat{X}) &= g_1(\mathcal{T}_{\hat{U}}P_1\hat{V} + \cos^2\theta_1\mathcal{T}_{\hat{U}}P_2\hat{V} + \cos^2\theta_2\mathcal{T}_{\hat{U}}P_3\hat{V},\hat{X}) + g_1(\mathcal{T}_{\hat{U}}\chi\hat{V},t\hat{X}) \\ &\quad + \frac{1}{\lambda^2}\{g_2((\nabla J_*)(\hat{U},\chi\omega P_2\hat{V}) - (\nabla J_*)(\hat{U},\chi\omega P_3\hat{V}),J_*\hat{X})\} \\ &\quad - \frac{1}{\lambda^2}\{g_2(\nabla_{\hat{U}}^J J_*\chi\omega P_2\hat{V} + \nabla_{\hat{U}}^J J_*\chi\omega P_3\hat{V},J_*\hat{X})\} \\ &\quad + \frac{1}{\lambda^2}\{g_2(\nabla_{\hat{U}}^J J_*\chi\hat{V} - (\nabla J_*)(\hat{U},\chi\hat{V}),J_*n\hat{X})\} \\ &\quad - \eta(P_2\hat{V})g_1(\chi\hat{U},\hat{X}). \end{aligned}$$

This completes the proof of the theorem.

Now we can discuss the geometry of the horizontal distribution's leaves. The necessary and sufficient conditions under which horizontal distribution totally geodesic foliation on \bar{B}_1 are presented in the following theorem.

Theorem 4.11 *Let J be a \mathcal{DBSCS} from Kenmotsu manifold $(\bar{B}_1, \phi, \xi, \eta, g_1)$ onto a RM (\bar{B}_2, g_2) .*

Then $(kerJ_*)^\perp$ defines totally geodesic foliation on \bar{B}_1 if and only if

$$\begin{aligned}
 & -\frac{1}{\lambda^2}g_2(\nabla_{\hat{X}}^J J_* n\hat{Y}, J_* \chi Z) + \frac{1}{\lambda^2}g_2(\nabla_{\hat{X}}^J J_* \hat{Y}, J_* \chi \omega P_2 Z) \\
 & = \cos^2 \theta_1 g_1(\mathcal{A}_{\hat{X}} \hat{Y}, P_2 Z) + \cos^2 \theta_2 g_1(\mathcal{A}_{\hat{X}} \hat{Y}, P_3 Z) \\
 & \quad + g_1(\mathcal{V} \nabla_{\hat{X}} t\hat{Y}, \omega P_1 Z) + g_1(\mathcal{A}_{\hat{X}} n\hat{Y}, \omega P_1 Z) + g_1(\mathcal{A}_{\hat{X}} t\hat{Y}, \chi Z) \\
 & \quad + \frac{1}{\lambda^2}g_2(\hat{X}(\ln \lambda) J_* n\hat{Y} + n\hat{Y}(\ln \lambda) J_* \hat{X} - g_1(\hat{X}, n\hat{Y}) J_*(G \ln \lambda), J_* \chi Z) \\
 & \quad + \frac{1}{\lambda^2}g_2(\hat{X}(\ln \lambda) J_* \hat{Y} + \hat{Y}(\ln \lambda) J_* \hat{X} - g_1(\hat{X}, \hat{Y}) J_*(G \ln \lambda), J_* \chi \omega P_2 Z) \\
 & \quad + \frac{1}{\lambda^2}g_2(\hat{X}(\ln \lambda) J_* \hat{Y} + \hat{Y}(\ln \lambda) J_* \hat{X} - g_1(\hat{X}, \hat{Y}) J_*(G \ln \lambda), J_* \chi \omega P_3 Z) \\
 & \quad + \frac{1}{\lambda^2}g_2(\nabla_{\hat{X}}^J J_* \hat{Y}, J_* \chi \omega P_3 Z)
 \end{aligned} \tag{4.42}$$

for any $\hat{X}, \hat{Y} \in \Gamma(kerJ_*)^\perp$ and $\hat{Z} \in \Gamma(kerJ_*)$.

Proof. For any $\hat{X}, \hat{Y} \in \Gamma(kerJ_*)^\perp$ and $\hat{Z} \in \Gamma(kerJ_*)$ with using equations (2.3), (2.4), (2.6) with decomposition (3.17), we get

$$g_1(\nabla_{\hat{X}} \hat{Y}, \hat{Z}) = g_1(\nabla_{\hat{X}} \phi \hat{Y}, \phi P_1 \hat{Z}) + g_1(\nabla_{\hat{X}} \phi \hat{Y}, \phi P_2 \hat{Z}) + g_1(\nabla_{\hat{X}} \phi \hat{Y}, \phi P_3 \hat{Z}).$$

From equations (3.18) and (2.12) with Lemma 3.2, we have

$$\begin{aligned}
 & g_1(\nabla_{\hat{X}} \hat{Y}, \hat{Z}) \\
 & = g_1(\mathcal{V} \nabla_{\hat{X}} t\hat{Y}, \omega P_1 Z) + g_1(\mathcal{A}_{\hat{X}} n\hat{Y}, \omega P_1 Z) + g_1(\phi \nabla_{\hat{X}} \phi \hat{Y}, \phi \omega P_2 Z) \\
 & \quad + g_1(\nabla_{\hat{X}} t\hat{Y}, \chi P_2 Z) + g_1(\nabla_{\hat{X}} n\hat{Y}, \chi P_2 Z) + g_1(\phi \nabla_{\hat{X}} \phi \hat{Y}, \phi \omega P_3 Z) \\
 & \quad + g_1(\nabla_{\hat{X}} t\hat{Y}, \chi P_3 Z) + g_1(\nabla_{\hat{X}} n\hat{Y}, \chi P_3 Z) + g_1(\mathcal{H} \nabla_{\hat{X}} n\hat{Y} + \mathcal{A}_{\hat{X}} t\hat{Y}, \chi P_2 \hat{Z}).
 \end{aligned}$$

Since $\chi P_2 Z + \chi P_3 Z = \chi Z$ and with using the equations (3.18) and (2.13), we get

$$\begin{aligned}
 & g_1(\nabla_{\hat{X}} \hat{Y}, \hat{Z}) \\
 & = g_1(\mathcal{V} \nabla_{\hat{X}} t\hat{Y}, \omega P_1 Z) + g_1(\mathcal{A}_{\hat{X}} n\hat{Y}, \omega P_1 Z) + g_1(\mathcal{A}_{\hat{X}} t\hat{Y}, \chi Z) \\
 & \quad + g_1(\mathcal{H} \nabla_{\hat{X}} n\hat{Y}, \chi Z) - g_1(\mathcal{H} \nabla_{\hat{X}} \hat{Y}, \chi \omega P_2 Z) - g_1(\mathcal{H} \nabla_{\hat{X}} \hat{Y}, \chi \omega P_3 Z) \\
 & \quad + \cos^2 \theta_1 \{g_1(\mathcal{A}_{\hat{X}} \hat{Y}, P_2 Z)\} + \cos^2 \theta_2 \{g_1(\mathcal{A}_{\hat{X}} \hat{Y}, P_3 Z)\} + g_1(\mathcal{H} \nabla_{\hat{X}} n\hat{Y} + \mathcal{A}_{\hat{X}} t\hat{Y}, \chi P_2 \hat{Z}).
 \end{aligned}$$

From formula (2.7) and (2.16), which yields that

$$\begin{aligned}
 & g_1(\nabla_{\widehat{X}}\widehat{Y}, \widehat{Z}) \\
 &= g_1(\mathcal{V}\nabla_{\widehat{X}}t\widehat{Y}, \omega P_1Z) + g_1(\mathcal{A}_{\widehat{X}}n\widehat{Y}, \omega P_1Z) + g_1(\mathcal{A}_{\widehat{X}}t\widehat{Y}, \chi Z) \\
 &+ \frac{1}{\lambda^2}g_2(\nabla_{\widehat{X}}^J J_*n\widehat{Y}, J_*\chi Z) - \frac{1}{\lambda^2}g_2((\nabla J_*)(\widehat{X}, n\widehat{Y}), J_*\chi Z) \\
 &- \frac{1}{\lambda^2}g_2(\nabla_{\widehat{X}}^J J_*\widehat{Y}, J_*\chi \omega P_2Z) + \frac{1}{\lambda^2}g_2((\nabla J_*)(\widehat{X}, \widehat{Y}), J_*\chi \omega P_2Z) \\
 &- \frac{1}{\lambda^2}g_2(\nabla_{\widehat{X}}^J J_*\widehat{Y}, J_*\chi \omega P_3Z) + \frac{1}{\lambda^2}g_2((\nabla J_*)(\widehat{X}, \widehat{Y}), J_*\chi \omega P_3Z) \\
 &+ \cos^2 \theta_1 \{g_1(\mathcal{A}_{\widehat{X}}\widehat{Y}, P_2Z)\} + \cos^2 \theta_2 \{g_1(\mathcal{A}_{\widehat{X}}\widehat{Y}, P_3Z)\} + g_1(\mathcal{H}\nabla_{\widehat{X}}n\widehat{Y} + \mathcal{A}_{\widehat{X}}t\widehat{Y}, \chi P_2\widehat{Z}).
 \end{aligned}$$

Since J is conformal submersion, then we finally get

$$\begin{aligned}
 & g_1(\nabla_{\widehat{X}}\widehat{Y}, \widehat{Z}) \\
 &= \cos^2 \theta_1 g_1(\mathcal{A}_{\widehat{X}}\widehat{Y}, P_2Z) + \cos^2 \theta_2 g_1(\mathcal{A}_{\widehat{X}}\widehat{Y}, P_3Z) + g_1(\mathcal{H}\nabla_{\widehat{X}}n\widehat{Y} + \mathcal{A}_{\widehat{X}}t\widehat{Y}, \chi P_2\widehat{Z}) \\
 &+ g_1(\mathcal{V}\nabla_{\widehat{X}}t\widehat{Y} + \mathcal{A}_{\widehat{X}}n\widehat{Y}, \omega P_1Z) + g_1(\mathcal{A}_{\widehat{X}}t\widehat{Y}, \chi Z) + \frac{1}{\lambda^2}g_2(\nabla_{\widehat{X}}^J J_*\widehat{Y}, J_*\chi \omega P_3Z) \\
 &+ \frac{1}{\lambda^2}g_2(\widehat{X}(\ln \lambda)J_*n\widehat{Y} + n\widehat{Y}(\ln \lambda)J_*\widehat{X} - g_1(\widehat{X}, n\widehat{Y})J_*(G \ln \lambda), J_*\chi Z) \\
 &+ \frac{1}{\lambda^2}g_2(\widehat{X}(\ln \lambda)J_*\widehat{Y} + \widehat{Y}(\ln \lambda)J_*\widehat{X} - g_1(\widehat{X}, \widehat{Y})J_*(G \ln \lambda), J_*\chi \omega P_2Z) \\
 &+ \frac{1}{\lambda^2}g_2(\widehat{X}(\ln \lambda)J_*\widehat{Y} + \widehat{Y}(\ln \lambda)J_*\widehat{X} - g_1(\widehat{X}, \widehat{Y})J_*(G \ln \lambda), J_*\chi \omega P_3Z) \\
 &+ \frac{1}{\lambda^2}g_2(\nabla_{\widehat{X}}^J J_*n\widehat{Y}, J_*\chi Z) - \frac{1}{\lambda^2}g_2(\nabla_{\widehat{X}}^J J_*\widehat{Y}, J_*\chi \omega P_2Z).
 \end{aligned}$$

This completes the proof of theorem.

5 ϕ -Pluriharmonicity of Quasi bi-slant Conformal ξ^\perp -Submersion

In [23], Y. Ohnita constructed J -pluriharmonicity from a almost hermitian manifold. We expand the idea of ϕ -pluriharmonicity to almost contact metric manifolds in this section.

Let J be a \mathcal{QBSCS} from Kenmotsu manifold $(\bar{B}_1, \phi, \xi, \eta, g_1)$ onto a RM (\bar{B}_2, g_2) with slant angles θ_1 and θ_2 . Then \mathcal{QBSCS} submersion is ϕ -pluriharmonic, \mathfrak{D} - ϕ -pluriharmonic, \mathfrak{D}^{θ_i} - ϕ -pluriharmonic, $(\mathfrak{D} - \mathfrak{D}^{\theta_i})$ - ϕ pluriharmonic (where $i = 1, 2$), $ker J_*$ - ϕ -pluriharmonic, $(ker J_*)^\perp$ - ϕ -pluriharmonic and $((ker J_*)^\perp - ker J_*)$ - ϕ -pluriharmonic if

$$(\nabla J_*)(\widehat{U}, \widehat{V}) + (\nabla J_*)(\phi \widehat{U}, \phi \widehat{V}) = 0, \tag{5.43}$$

for any $\widehat{U}, \widehat{V} \in \Gamma(\mathfrak{D})$, for any $\widehat{U}, \widehat{V} \in \Gamma(\mathfrak{D}^{\theta_i})$, for any $\widehat{U} \in \Gamma(\mathfrak{D}), \widehat{V} \in \Gamma(\mathfrak{D}^{\theta_i})$ (where $i = 1, 2$), for

any $\widehat{U}, \widehat{V} \in \Gamma(\ker J_*)$, for any $\widehat{U}, \widehat{V} \in \Gamma(\ker J_*)^\perp$ and for any $\widehat{U} \in \Gamma(\ker J_*)^\perp, \widehat{V} \in \Gamma(\ker J_*)$.

Theorem 5.1 Let J be a \mathcal{QBSCS} from Kenmotsu manifold $(\bar{B}_1, \phi, \xi, \eta, g_1)$ onto a RM (\bar{B}_2, g_2) with slant angles θ_1 and θ_2 . Suppose that J is \mathfrak{D}_{θ_1} - ϕ -pluriharmonic. Then \mathfrak{D}_{θ_1} defines totally geodesic foliation \bar{B}_1 if and only if

$$\begin{aligned} & J_*(\chi \mathcal{T}_{\omega \widehat{U}} \chi \omega \widehat{V} + n \mathcal{H} \nabla_{\omega \widehat{U}} \chi \omega \widehat{V}) - J_*(\mathcal{A}_{\chi \widehat{U}} \omega \widehat{V} + \mathcal{H} \nabla_{\omega \widehat{U}} \chi \widehat{V}) \\ &= \cos^2 \theta_1 J_*(n \mathcal{T}_{\omega \widehat{U}} \widehat{V} + \chi \mathcal{V} \nabla_{\omega \widehat{U}} \widehat{V}) + \nabla_{\omega \widehat{U}}^J J_* \phi \widehat{V} \\ & \quad - \chi \widehat{U} (\ln \lambda) J_* \chi \widehat{V} - \chi \widehat{V} (\ln \lambda) J_* \chi \widehat{U} + g_1(\chi \widehat{U}, \chi \widehat{V}) J_*(G \ln \lambda) \end{aligned}$$

for any $\widehat{U}, \widehat{V} \in \Gamma(\mathfrak{D}_{\theta_1})$.

Proof. For any $\widehat{U}, \widehat{V} \in \Gamma(\mathfrak{D}_{\theta_1})$ and since, J is \mathfrak{D}_{θ_1} - ϕ -pluriharmonic, then by using equation (2.10) and (2.16), we have

$$\begin{aligned} 0 &= (\nabla J_*)(\widehat{U}, \widehat{V}) + (\nabla J_*)(\phi \widehat{U}, \phi \widehat{V}) \\ J_*(\nabla_{\widehat{U}} \widehat{V}) &= -J_*(\nabla_{\phi \widehat{U}} \phi \widehat{V}) + \nabla_{\phi \widehat{U}}^J J_*(\phi \widehat{V}) \\ &= -J_*(\mathcal{A}_{\chi \widehat{U}} \omega \widehat{V} + \mathcal{V} \nabla_{\chi \widehat{U}} \omega \widehat{V} + \mathcal{T}_{\omega \widehat{U}} \chi \widehat{V} + \mathcal{H} \nabla_{\omega \widehat{U}} \chi \widehat{V}) \\ & \quad + (\nabla J_*)(\chi \widehat{U}, \chi \widehat{V}) - \nabla_{\chi \widehat{U}}^J J_* \chi \widehat{V} + \nabla_{\phi \widehat{U}}^J J_* \phi \widehat{V} \\ & \quad + J_*(\phi \nabla_{\omega \widehat{U}} \phi \omega \widehat{V}) \end{aligned}$$

On using equations (3.18), (3.21) with Lemma 2.1 and Lemma 3.2, the above equation finally takes the form

$$\begin{aligned} J_*(\nabla_{\widehat{U}} \widehat{V}) &= -\cos^2 \theta_1 J_*(P \mathcal{T}_{\omega \widehat{U}} \widehat{V} + n \mathcal{T}_{\omega \widehat{U}} \widehat{V} + \omega \mathcal{V} \nabla_{\omega \widehat{U}} \widehat{V} + \chi \mathcal{V} \nabla_{\omega \widehat{U}} \widehat{V}) \\ & \quad + J_*(\omega \mathcal{T}_{\omega \widehat{U}} \chi \omega \widehat{V} + \chi \mathcal{T}_{\omega \widehat{U}} \chi \omega \widehat{V} + P \mathcal{H} \nabla_{\omega \widehat{U}} \chi \omega \widehat{V} + n \mathcal{H} \nabla_{\omega \widehat{U}} \chi \omega \widehat{V}) \\ & \quad - J_*(\mathcal{A}_{\chi \widehat{U}} \omega \widehat{V} + \mathcal{V} \nabla_{\chi \widehat{U}} \omega \widehat{V} + \mathcal{T}_{\omega \widehat{U}} \chi \widehat{V} + \mathcal{H} \nabla_{\omega \widehat{U}} \chi \widehat{V}) \\ & \quad + \chi \widehat{U} (\ln \lambda) J_* \chi \widehat{V} + \chi \widehat{V} (\ln \lambda) J_* \chi \widehat{U} - g_M(\chi \widehat{U}, \chi \widehat{V}) J_*(grad \ln \lambda) \\ & \quad - \nabla_{\chi \widehat{U}}^J J_* \chi \widehat{V} + \nabla_{\phi \widehat{U}}^J J_* \phi \widehat{V}. \end{aligned}$$

from which we get the desired result.

Theorem 5.2 Let \vec{f} be a \mathcal{QBSCS} from Kenmotsu manifold $(\bar{B}_1, \phi, \xi, \eta, g_1)$ onto a RM (\bar{B}_2, g_2) with slant angles θ_1 and θ_2 . Suppose that J is \mathfrak{D}_{θ_2} - ϕ -pluriharmonic. Then \mathfrak{D}_{θ_2} defines totally geodesic foliation \bar{B}_1 if and only if

$$\begin{aligned} & J_*(\chi \mathcal{T}_{\omega \widehat{Z}} \chi \omega \widehat{W} + n \mathcal{H} \nabla_{\omega \widehat{Z}} \chi \omega \widehat{W}) - J_*(\mathcal{A}_{\chi \widehat{Z}} \omega \widehat{W} + \mathcal{H} \nabla_{\omega \widehat{Z}} \chi \widehat{W}) \\ &= \cos^2 \theta_2 J_*(n \mathcal{T}_{\omega \widehat{Z}} \widehat{W} + \chi \mathcal{W} \nabla_{\omega \widehat{Z}} \widehat{W}) + \nabla_{\omega \widehat{Z}}^J J_* \phi \widehat{W} \\ & \quad - \chi \widehat{Z} (\ln \lambda) J_* \chi \widehat{W} - \chi \widehat{W} (\ln \lambda) J_* \chi \widehat{Z} + g_M(\chi \widehat{Z}, \chi \widehat{W}) J_*(grad \ln \lambda) \end{aligned}$$

for any $\widehat{Z}, \widehat{W} \in \Gamma(\mathfrak{D}_{\theta_2})$.

Proof. Theorem 5.1 proof is the same to this theorem's proof.

Theorem 5.3 Let \vec{f} be a \mathcal{QBSCS} from Kenmotsu manifold $(\bar{B}_1, \phi, \xi, \eta, g_1)$ onto a RM (\bar{B}_2, g_2) with slant angles θ_1 and θ_2 . Suppose that J is $((\ker J_*)^\perp - \ker J_*)$ - ϕ -pluriharmonic. Then the following assertion are equivalent.

(i) The horizontal distribution $(\ker J_*)^\perp$ defines totally geodesic foliation on \bar{B}_1 .

$$\begin{aligned} \text{(ii)} \quad & (\cos^2 \theta_1 + \cos^2 \theta_2) J_* \{ n \mathcal{T}_{i\widehat{X}} \omega P_1 \widehat{U} + \chi \mathcal{V} \nabla_{i\widehat{X}} \omega P_1 \widehat{U} + n \mathcal{A}_{n\widehat{X}} \omega P_1 \widehat{U} + \chi \mathcal{V} \nabla_{n\widehat{X}} \omega P_1 \widehat{U} \} \\ & + J_* \{ \chi \mathcal{A}_{n\widehat{X}} \chi \omega P_2 \widehat{U} + \chi \mathcal{A}_{n\widehat{X}} \chi \omega P_3 \widehat{U} - \mathcal{H} \nabla_{i\widehat{X}} \chi \widehat{U} \} + \nabla_{n\widehat{X}}^J J_* \chi \omega P_2 \widehat{U} + \nabla_{n\widehat{X}}^J J_* \chi \omega P_3 \widehat{U} \\ & = J_* \{ n \mathcal{T}_{i\widehat{X}} \omega P_1 \widehat{U} + \chi \mathcal{V} \nabla_{i\widehat{X}} \omega P_1 \widehat{U} + n \mathcal{A}_{n\widehat{X}} \omega P_1 \widehat{U} + \chi \mathcal{H} \nabla_{n\widehat{X}} \omega P_1 \widehat{U} \} \\ & - J_* \{ \chi \mathcal{T}_{i\widehat{X}} \chi \omega P_2 \widehat{U} + n \mathcal{H} \nabla_{i\widehat{X}} \chi \omega P_2 \widehat{U} + \chi \mathcal{T}_{i\widehat{X}} \chi \omega P_3 \widehat{U} + n \mathcal{H} \nabla_{i\widehat{X}} \chi \omega P_3 \widehat{U} \} \\ & + n \widehat{X} (\ln \lambda) J_* \chi \omega P_2 \widehat{U} + \chi \omega P_2 \widehat{U} (\ln \lambda) J_* n \widehat{X} - g_1(n \widehat{X}, \chi \omega P_2 \widehat{U}) J_* (\text{grad } \ln \lambda) \\ & + n \widehat{X} (\ln \lambda) J_* \chi \omega P_3 \widehat{U} + \chi \omega P_3 \widehat{U} (\ln \lambda) J_* n \widehat{X} - g_1(n \widehat{X}, \chi \omega P_3 \widehat{U}) J_* (\text{grad } \ln \lambda) \\ & + J_*(\nabla_{\widehat{X}} \widehat{U}) + \nabla_{\phi \widehat{X}}^J J_* \chi \widehat{U} + g_1(P \widehat{X}, \omega \widehat{U}) J_* \xi. \end{aligned}$$

for any $\widehat{X} \in \Gamma(\ker J_*)^\perp$ and $\widehat{U} \in \Gamma(\ker J_*)$

Proof. For any $\widehat{X} \in \Gamma(\ker J_*)^\perp$ and $\widehat{U} \in \Gamma(\ker J_*)$, since J is $((\ker J_*)^\perp - \ker J_*)$ - ϕ -pluriharmonic, then by using (2.16), (3.18) and (3.21), we get

$$J_*(\nabla_{n\widehat{X}} \chi \widehat{U}) = -J_*(\nabla_{i\widehat{X}} \omega \widehat{U} + \nabla_{i\widehat{X}} \chi \widehat{U} + \nabla_{n\widehat{X}} \omega \widehat{U}) + J_*(\nabla_{\widehat{X}} \widehat{U}) + \nabla_{\phi \widehat{X}}^J J_* \chi \widehat{U}.$$

Taking account the fact from (2.2) and (2.11), we have

$$\begin{aligned} J_*(\nabla_{n\widehat{X}} \chi \widehat{U}) &= -J_*(\mathcal{T}_{i\widehat{X}} \chi \widehat{U} + \mathcal{H} \nabla_{i\widehat{X}} \chi \widehat{U}) + J_*(\nabla_{\widehat{X}} \widehat{U}) + \nabla_{\phi \widehat{X}}^J J_* \chi \widehat{U} \\ &+ J_* \{ \phi \nabla_{i\widehat{X}} \phi \omega \widehat{U} \} + J_* \{ \phi \nabla_{n\widehat{X}} \phi \omega \widehat{U} \}. \end{aligned}$$

Now on using decomposition (3.17), Lemma 3.2, Lemma 3.3 with equations (3.18), we may yields

$$\begin{aligned} J_*(\nabla_{n\widehat{X}} \chi \widehat{U}) &= J_* \{ \phi \nabla_{i\widehat{X}} \omega P_1 \widehat{U} - \cos^2 \theta_1 \phi \nabla_{i\widehat{X}} \omega \widehat{U} - \cos^2 \theta_2 \phi \nabla_{i\widehat{X}} \omega \widehat{U} \\ &+ J_* \{ \phi \nabla_{n\widehat{X}} \omega P_1 \widehat{U} - \cos^2 \theta_1 \phi \nabla_{n\widehat{X}} \omega \widehat{U} - \cos^2 \theta_2 \phi \nabla_{n\widehat{X}} \omega \widehat{U} \\ &+ J_* \{ \phi \nabla_{i\widehat{X}} \chi \omega P_2 \widehat{U} + \phi \nabla_{i\widehat{X}} \chi \omega P_3 \widehat{U} + \phi \nabla_{n\widehat{X}} \chi \omega P_2 \widehat{U} + \phi \nabla_{n\widehat{X}} \chi \omega P_3 \widehat{U} \} \\ &- J_*(\mathcal{H} \nabla_{i\widehat{X}} \chi \widehat{U}) + J_*(\nabla_{\widehat{X}} \widehat{U}) + \nabla_{\phi \widehat{X}}^J J_* \chi \widehat{U}. \end{aligned}$$

From equations (2.10)-(2.13) and after simple calculation, we may write

$$\begin{aligned}
 J_*(\nabla_{n\hat{X}}\chi\hat{U}) &= -(cos^2\theta_1 + cos^2\theta_2)J_*\{n\mathcal{T}_{i\hat{X}}\omega P_1\hat{U} + \chi\mathcal{V}\nabla_{i\hat{X}}\omega P_1\hat{U} + n\mathcal{A}_{n\hat{X}}\omega P_1\hat{U} \\
 &\quad + \chi\mathcal{V}\nabla_{n\hat{X}}\omega P_1\hat{U}\} - J_*\{\chi\mathcal{A}_{n\hat{X}}\chi\omega P_2\hat{U} + \chi\mathcal{A}_{n\hat{X}}\chi\omega P_3\hat{U} - \mathcal{H}\nabla_{i\hat{X}}\chi\hat{U}\} \\
 &\quad + J_*\{n\mathcal{T}_{i\hat{X}}\omega P_1\hat{U} + \chi\mathcal{V}\nabla_{i\hat{X}}\omega P_1\hat{U} + n\mathcal{A}_{n\hat{X}}\omega P_1\hat{U} + \chi\mathcal{H}\nabla_{n\hat{X}}\omega P_1\hat{U}\} \\
 &\quad - J_*\{\chi\mathcal{T}_{i\hat{X}}\chi\omega P_2\hat{U} + n\mathcal{H}\nabla_{i\hat{X}}\chi\omega P_2\hat{U} + \chi\mathcal{T}_{i\hat{X}}\chi\omega P_3\hat{U} + n\mathcal{H}\nabla_{i\hat{X}}\chi\omega P_3\hat{U}\} \\
 &\quad - J_*(n\mathcal{H}\nabla_{n\hat{X}}\chi\omega P_2\hat{U} + n\mathcal{H}\nabla_{n\hat{X}}\chi\omega P_3\hat{U}) + J_*(\nabla_{\hat{X}}\hat{U}) + \nabla_{\phi\hat{X}}^J J_*\chi\hat{U}.
 \end{aligned}$$

Since J is conformal Riemannian submersion, the by using equations (2.16) and from Lemma 2.1, we finally have

$$\begin{aligned}
 &J_*(\nabla_{n\hat{X}}\chi\hat{U}) \\
 &= -(cos^2\theta_1 + cos^2\theta_2)J_*\{n\mathcal{T}_{i\hat{X}}\omega P_1\hat{U} + \chi\mathcal{V}\nabla_{i\hat{X}}\omega P_1\hat{U} + n\mathcal{A}_{n\hat{X}}\omega P_1\hat{U} + \chi\mathcal{V}\nabla_{n\hat{X}}\omega P_1\hat{U}\} \\
 &\quad + J_*\{n\mathcal{T}_{i\hat{X}}\omega P_1\hat{U} + \chi\mathcal{V}\nabla_{i\hat{X}}\omega P_1\hat{U} + n\mathcal{A}_{n\hat{X}}\omega P_1\hat{U} + \chi\mathcal{H}\nabla_{n\hat{X}}\omega P_1\hat{U}\} \\
 &\quad - J_*\{\chi\mathcal{T}_{i\hat{X}}\chi\omega P_2\hat{U} + n\mathcal{H}\nabla_{i\hat{X}}\chi\omega P_2\hat{U} + \chi\mathcal{T}_{i\hat{X}}\chi\omega P_3\hat{U} + n\mathcal{H}\nabla_{i\hat{X}}\chi\omega P_3\hat{U}\} \\
 &\quad + n\hat{X}(\ln\lambda)J_*\chi\omega P_2\hat{U} + \chi\omega P_2\hat{U}(\ln\lambda)J_*n\hat{X} - g_1(n\hat{X}, \chi\omega P_2\hat{U})J_*(grad\ln\lambda) \\
 &\quad + n\hat{X}(\ln\lambda)J_*\chi\omega P_3\hat{U} + \chi\omega P_3\hat{U}(\ln\lambda)J_*n\hat{X} - g_1(n\hat{X}, \chi\omega P_3\hat{U})J_*(grad\ln\lambda) \\
 &\quad - J_*\{\chi\mathcal{A}_{n\hat{X}}\chi\omega P_2\hat{U} + \chi\mathcal{A}_{n\hat{X}}\chi\omega P_3\hat{U} - \mathcal{H}\nabla_{i\hat{X}}\chi\hat{U}\} \\
 &\quad + J_*(\nabla_{\hat{X}}\hat{U}) + \nabla_{\phi\hat{X}}^J J_*\chi\hat{U} - \nabla_{n\hat{X}}^J J_*\chi\omega P_2\hat{U} - \nabla_{n\hat{X}}^J J_*\chi\omega P_3\hat{U},
 \end{aligned}$$

which completes the proof of theorem.

6 Decomposition Theorems

The following conclusion from [29] is recalled in this section, and other decomposition theorem is discussed utilizing earlier proof. Let's say that on the manifold $M = \bar{B}_1 \times \bar{B}_2$, g is a Riemannian metric. Then

- (i) $M = \bar{B}_1 \times_{\lambda} \bar{B}_2$ is a locally product if and only if \bar{B}_1 and \bar{B}_2 are totally geodesic foliations,
- (ii) a warped product $\bar{B}_1 \times_{\lambda} \bar{B}_2$ if and only if \bar{B}_1 is a totally geodesic foliation and \bar{B}_2 is a spherics foliation, i.e., it is umbilic and its mean curvature vector field is parallel,
- (ii) $M = \bar{B}_1 \times_{\lambda} \bar{B}_2$ is a twisted product if and only if \bar{B}_1 is a totally geodesic foliation and \bar{B}_2 is a totally umbilic foliation.

The fact that $J : (\bar{B}_1, \phi, \xi, \eta, g_1) \rightarrow (\bar{B}_2, g_2)$ is \mathcal{LBSCS} ensures the existence of three orthogonal complementary distributions \mathfrak{D} , \mathfrak{D}_{θ_1} , and \mathfrak{D}_{θ_2} , all of which meet the previously stated

characteristics of being integrable and totally geodesic. The logical next step is to search for the circumstances in which the total space \bar{B}_1 transforms into locally twisted product manifolds. We now present the following outcome.

Theorem 6.1 *Let J be a \mathcal{LBSCS} from Kenmotsu manifold $(M, \phi, \xi, \eta, g_1)$ onto a RM (M_2, g_2) . Then \bar{B}_1 is locally twisted product of the form $\bar{B}_{1(\ker J_*)} \times \bar{B}_{1(\ker J_*)^\perp}$ if and only if*

$$\begin{aligned} \frac{1}{\lambda^2} g_2((\nabla f_*)(\hat{U}, \chi \hat{V}), f_* n \hat{X}) &= g_1(\mathcal{T}_{\hat{U}} \omega \hat{V}, n \hat{X}) + g_1(\mathcal{V} \nabla_{\hat{U}} \omega \hat{V} + \mathcal{T}_{\hat{U}} \chi \hat{V}, t \hat{X}) \\ &+ \frac{1}{\lambda^2} g_2(\nabla_U^J \chi \hat{V}, J_* n \hat{X}) \end{aligned} \quad (6.44)$$

and

$$\begin{aligned} g(\hat{X}, \hat{Y})H &= -t \mathcal{A}_{\hat{X}} t \hat{Y} - \omega \nabla_{\hat{X}} t \hat{Y} - \omega \mathcal{A}_{\hat{X}} n \hat{Y} - \phi J_*(\nabla_{\hat{X}}^J J_* n \hat{Y}) + \hat{X}(\ln \lambda) t n \hat{Y} \\ &+ n \hat{Y}(\ln \lambda) t \hat{X} - t(G \ln \lambda) g(\hat{X}, n \hat{Y}) - \eta(\hat{U}) g_1(\hat{X}, \hat{Y}), \end{aligned} \quad (6.45)$$

where H is a mean curvature vector and for any $\hat{U}, \hat{V} \in \Gamma(\ker J_*)$ and $\hat{X}, \hat{Y} \in \Gamma(\ker J_*)^\perp$.

Proof. For any $\hat{X} \in \Gamma(\ker J_*)^\perp$ and $\hat{U}, \hat{V} \in \Gamma(\ker J_*)$ and using equations (2.3), (2.6), (2.4), (2.12) and (2.13), we have

$$g_1(\nabla_{\hat{U}} \hat{V}, \hat{X}) = g_1(\mathcal{T}_{\hat{U}} \omega \hat{V}, n \hat{X}) + g_1(\mathcal{V} \nabla_{\hat{U}} \omega \hat{V} + \mathcal{T}_{\hat{U}} \chi \hat{V}, t \hat{X}) - g_1(\mathcal{H} \nabla_{\hat{U}} \chi \hat{V}, n \hat{X})$$

From using formula (2.7), (2.16) and with conformality of RS J , the above equation finally takes the form

$$\begin{aligned} g_1(\nabla_{\hat{U}} \hat{V}, \hat{X}) &= g_1(\mathcal{T}_{\hat{U}} \omega \hat{V}, n \hat{X}) + g_1(\mathcal{V} \nabla_{\hat{U}} \omega \hat{V} + \mathcal{T}_{\hat{U}} \chi \hat{V}, t \hat{X}) \\ &- \frac{1}{\lambda^2} g_2((\nabla f_*)(\hat{U}, \chi \hat{V}), f_* n \hat{X}) + \frac{1}{\lambda^2} g_2(\nabla_U^J \chi \hat{V}, J_* n \hat{X}) \end{aligned}$$

It follows that the equation (6.44) satisfies if and only if $\bar{B}_{1(\ker J_*)}$ is totally geodesic. On the other hand, for $\hat{U} \in \Gamma(\ker J_*)$ and $\hat{X}, \hat{Y} \in \Gamma(\ker J_*)^\perp$ with using equations (2.3), (2.4), (2.6) and (3.21), we get

$$g_1(\nabla_{\hat{X}} \hat{Y}, \hat{U}) = g_1(\nabla_{\hat{X}} P \hat{Y}, \phi \hat{U}) + g_1(\mathcal{A}_{\hat{X}} n \hat{Y}, \omega \hat{U}) + g_1(\mathcal{H} \nabla_{\hat{X}} n \hat{Y}, \chi \hat{U}) - \eta(\hat{U}) g_1(\hat{X}, \hat{Y}).$$

By using the equation (2.16) with definition of conformality of J , we deduce that

$$\begin{aligned} g_1(\nabla_{\hat{X}} \hat{Y}, \hat{U}) &= -\frac{1}{\lambda^2} g_2((\nabla J_*)(\hat{X}, n \hat{Y}), J_* \chi \hat{U}) + \frac{1}{\lambda^2} g_2(\nabla_{\hat{X}}^J J_* n \hat{Y}, J_* \chi \hat{U}) \\ &+ g_1(\nabla_{\hat{X}} P \hat{Y}, \phi \hat{U}) + g_1(\mathcal{A}_{\hat{X}} n \hat{Y}, \omega \hat{U}) - \eta(\hat{U}) g_1(\hat{X}, \hat{Y}). \end{aligned}$$

Considering the (i) part of Lemma 2.1, above equation turns in to

$$g_1(\nabla_{\hat{X}}\hat{Y}, \hat{U}) = \frac{1}{\lambda^2}g_2(\nabla_{\hat{X}}^J J_* n\hat{Y}, J_* \chi\hat{U}) + g_1(\nabla_{\hat{X}} t\hat{Y}, \phi\hat{U}) + g_1(\mathcal{A}_{\hat{X}} n\hat{Y}, \omega\hat{U}) \\ - g_1(G \ln \lambda, \hat{X})g_1(n\hat{Y}, \chi\hat{U}) - g_1(G \ln \lambda, n\hat{Y})g_1(\hat{X}, \chi\hat{U}) \\ + g_1(G \ln \lambda, \chi\hat{U})g_1(\hat{X}, n\hat{Y}) - \eta(\hat{U})g_1(\hat{X}, \hat{Y}).$$

By direct calculation, finally we get

$$g_1(\hat{X}, \hat{Y})H = -t\mathcal{A}_{\hat{X}} t\hat{Y} - \omega\nabla_{\hat{X}} t\hat{Y} - \omega\mathcal{A}_{\hat{X}} n\hat{Y} - \phi J_*(\nabla_{\hat{X}}^J J_* n\hat{Y}) + \hat{X}(\ln \lambda)tn\hat{Y} \\ + n\hat{Y}(\ln \lambda)t\hat{X} - t(G \ln \lambda)g_1(\hat{X}, n\hat{Y}) + \eta(\hat{U})g_1(\phi\hat{X}, \hat{Y}).$$

From the above equation we conclude that $\bar{B}_{1(\ker J_*)^\perp}$ is totally umbilical if and only if equation (6.45) satisfied.

Declaration and Statement:

Conflict of Interest:

The authors declare that there is no conflict of interest.

Acknowledgement The authors extend their appreciation to the Deanship of Scientific Research at Saudi Electronic University for funding this research (9502).

References

- [1] M. A. Akyol and Y. Gunduzalp., Hemi-slant submersions from almost product Riemannian manifolds, Gulf J. Math., 4(3) (2016), 15-27.
- [2] M. A. Akyol., Conformal semi-slant submersions, International Journal of Geometric Methods in Modern Physics, 14(7) (2017), 1750114.
- [3] M. A. Akyol and B. Sahin., Conformal slant submersions, Hacettepe Journal of Mathematics and Statistics, 48(1) (2019), 28-44.
- [4] M. A. Akyol and B. Sahin., Conformal anti-invariant submersions from almost Hermitian manifolds, Turkish Journal of Mathematics, 40 (2016), 43-70.
- [5] M. A. Akyol and B. Sahin., Conformal semi-invariant submersions, Communications in Contemporary Mathematics, 19 (2017), 1650011.

- [6] P. Baird and J. C. Wood., *Harmonic Morphisms Between Riemannian Manifolds*, London Mathematical Society Monographs, 29, Oxford University Press, The Clarendon Press. Oxford, (2003).
- [7] J.-P. Bourguignon and H. B. Lawson., Jr., *Stability and isolation phenomena for YangMills fields*, *Comm. Math. Phys.*, 79 (1981), no. 2, 189–230. <http://projecteuclid.org/euclid.cmp/1103908963>.
- [8] D. Chinea., *Almost contact metric submersions*, *Rend. Circ. Mat. Palermo*, 34(1) (1985), 89-104.
- [9] J. L. Cabrerizo, A. Carriazo, L. M. Fernandez and M. Fernandez., *Slant submanifolds in Sasakian manifolds*, *Glasg. Math. J.*, 42 (1) (2000), 125-138.
- [10] I. K. Erken and C. Murathan., *On slant Riemannian submersions for cosymplectic manifolds*, *Bull. Korean Math. Soc.*, 51(6) (2014), 1749-1771.
- [11] M. Falcitelli, S. Ianus and A. M. Pastore., *Riemannian submersions and Related Topics*, World Scientific, River Edge, NJ, (2004).
- [12] A. Gray., *Pseudo-Riemannian almost product manifolds and submersions*, *J. Math. Mech.*, 16 (1967), 715–737.
- [13] B. Fuglede., *Harmonic morphisms between Riemannian manifolds*, *Annales de l’institut Fourier (Grenoble)*, 28 (1978), 107-144.
- [14] S. Gudmundsson., *The geometry of harmonic morphisms*, Ph.D. thesis, University of Leeds, (1992).
- [15] S. Gudmundsson and J. C. Wood, *Harmonic morphisms between almost Hermitian manifolds*, *Boll. Un. Mat. Ital. B (7) 11* (1997), no. 2, suppl., 185–197.
- [16] Y. Gunduzalp., *Semi-slant submersions from almost product Riemannian manifolds*, *Demonstratio Mathematica*, 49(3) (2016), 345-356.
- [17] Y. Gunduzalp and M. A. Akyol., *Conformal slant submersions from cosymplectic manifolds*, *Turkish Journal of Mathematics*, 48 (2018), 2672-2689.
- [18] S. Ianuș and M. Vișinescu., *Space-time compactification and Riemannian submersions*, In: Rassias, G.(ed.) *The Mathematical Heritage of C. F. Gauss*, World Scientific, River Edge (1991), 358-371.

- [19] S. Ianuș and M. Vișinescu., Kaluza-Klein theory with scalar fields and generalised Hopf manifolds, *Classical Quantum Gravity*, 4 (1987), no. 5, 1317–1325. <http://stacks.iop.org/0264-9381/4/1317>.
- [20] T. Ishihara., A mapping of Riemannian manifolds which preserves harmonic functions, *Journal of Mathematics of Kyoto University*, 19 (1979), 215-229.
- [21] Kenmotsu, K. (1972). A class of almost contact Riemannian manifolds. *Tohoku Math.*, 24, 93-103.
- [22] M. T. Mustafa., Applications of harmonic morphisms to gravity, *J. Math. Phys.*, 41 (2000), 6918-6929.
- [23] Y. Ohnita., On pluriharmonicity of stable harmonic maps, *J. London Math. Soc. (2)* 2 (1987), 563-568. 2.2
- [24] B. O’Neill., The fundamental equations of a submersion, *Michigan Math. J.*, 13 (1966), 459–469. <http://projecteuclid.org/euclid.mmj/1028999604>.
- [25] K. S. Park and R. Prasad., Semi-slant submersions, *Bull. Korean Math. Soc.* 50(3) (2013), 951-962.
- [26] R. Prasad, S. S. Shukla and S. Kumar., On Quasi bi-slant submersions, *Mediterr. J. Math.*, 16 (2019), 155. <https://doi.org/10.1007/s00009-019-1434-7>.
- [27] R. Prasad, M. A. Akyol, P. K. Singh and S. Kumar., On Quasi bi-slant submersions from Kenmotsu manifolds onto any Riemannian manifolds, *Journal of Mathematical Extension*, 8(16) (2021).
- [28] R. Prasad and S. Kumar., Conformal anti-invariant submersions from nearly Kaehler Manifolds, *Palestine Journal of Mathematics*, 8(2) (2019).
- [29] R. Ponge and H. Reckziegel., Twisted products in pseudo-Riemannian geometry, *Geom. Dedicata*, (1993), 48(1):15-25.
- [30] Tanno, S. (1069). The automorphism groups of almost contact metric manifolds. *Tohoku Math.*, J. 21, 21-38.
- [31] B. Sahin., Anti-invariant Riemannian submersions from almost Hermitian manifolds, *Central European J. Math.*, 3 (2010), 437-447.
- [32] B. Sahin., Semi-invariant Riemannian submersions from almost Hermitian manifolds, *Canad. Math. Bull.*, 56 (2013), 173-183.

- [33] B. Şahin, Slant submersions from almost Hermitian manifolds, Bull. Math. Soc. Sci. Math. Roumanie. 1 (2011) 93-105.
- [34] B.Sahin, M. A. Akyol Conformal Anti-Invariant Submersion From Almost Hermitian Manifolds, Turk J Math (2016) 40: 43 – 70
- [35] M. Shuaib and T. Fatima. A note on conformal hemi-slant submersions, Afr. Mat. 34, 4 (2023).
- [36] Sumeet Kumar et al., Conformal hemi-slant submersions from almost hermitian manifolds, Commun. Korean Math. Soc., 35 (2020), No. 3, pp. 999–1018 <https://doi.org/10.4134/CKMS.c190448> pISSN: 1225-1763 / eISSN: 2234-3024.
- [37] H. M. Tastan, B. Şahin and Ş. Yanan, Hemi-slant submersions, Mediterr. J. Math. 13(4) (2016) 2171-2184.
- [38] B. Watson., Almost Hermitian submersions, J. Differential Geometry, vol. 11, no. 1, pp. (1976), 147–165. <http://projecteuclid.org/euclid.jdg/1214433303>
- [39] B. Watson., G, G' -Riemannian submersions and nonlinear gauge field equations of general relativity, In: Rassias, T. (ed.) Global Analysis - Analysis on manifolds, dedicated M. Morse. Teubner-Texte Math., 57 (1983), 324-349, Teubner, Leipzig.

Central generalized bi-semi-derivations on semiprime rings

Faiza Shujat

Department of Mathematics, Faculty of Science, Taibah University, Madinah, K.S.A.
fullahkhan@taibahu.edu.sa, faiza.shujat@gmail.com

and

Abu Zaid Ansari

Department of Mathematics, Faculty of Science, Islamic University of Madinah, K.S.A.
ansari.abuzaid@gmail.com, ansari.abuzaid@iu.edu.sa

Abstract

In this research, our goal is to characterize the structure of central generalized bi-semiderivation δ on ring. Infact, we obtain a few commutativity observations for bi-semi-derivations that commute on prime and semiprime ring. A non-commutative version of some results is also investigated with the help of algebraic identities in which δ will acting as left centralizer.

keywords

Semiprime (prime) ring; algebraic identities; generalized bi-semi-derivation.

الاشتقاقات شبه المركزية المعممة على الحلقات شبه الأولية

المخلص: في هذا البحث، هدفنا هو توصيف بنية شبه الاشتقاق الثنائي المركزي المعمم δ على الحلقة. في الواقع، حصلنا على بعض الملاحظات التبادلية للمشتقات شبه الثنائية التي تنتقل على الحلقة الأولية وشبه الأولية. يتم أيضاً فحص نسخة غير تبادلية لبعض النتائج بمساعدة الهويات الجبرية التي ستعمل فيها δ كمركز مركزي أيسر.

1 Introduction

A mapping D from $R \times R$ to R is considered to be symmetric if $D(a, b) = D(b, a)$ for each $a, b \in R$. If D is additive within both slots, it is referred to as bi-additive. We are discussing the conceptual framework of symmetric bi-derivations, as seen in [1], it follows: A mapping $D : R \times R \rightarrow R$ is referred as bi-derivation if D is bi-additive and for every $a \in R$, the map $b \mapsto D(a, b)$ as well as for every $b \in R$, the map $a \mapsto D(a, b)$ is a derivation of R . For ideational reading in the related matter one can turn to [1]. For a symmetric biadditive mapping D , a map h on R identified as $h(j) = D(j, j)$, for every j in R is commonly referred to the trace of D .

Bergen [2] outlined the idea of semi-derivations on ring R . If a function $g : R \rightarrow R$ is in existence such that $f(ce) = f(c)g(e) + cf(e) = f(c)e + g(c)f(e)$ and $f(g(e)) = g(f(e))$ for any additive mapping f on R , then such map f is termed a semi-derivation. for each $e, c \in R$. Every semiderivations connected to g are manifestly typical derivations, if g is an identity map of R .

A function $\vartheta : R \times R \rightarrow R$ with symmetry and bi-additivity is termed as symmetric bi-semi-derivation linked with the function f from R to R , if ϑ and f fulfilling the requirements listed below

$$\vartheta(ei, c) = \vartheta(e, c)f(i) + e\vartheta(i, c) = \vartheta(e, c)i + f(e)\vartheta(i, c)$$

$$\vartheta(c, de) = \vartheta(c, d)f(e) + d\vartheta(c, e) = \vartheta(c, d)e + f(d)\vartheta(c, e)$$

and $\vartheta(f) = f(\vartheta)$ for all $d, e, i, c \in R$.

Example 1.1 Assume that S is a ring after matrix addition and multiplication are applied, where

$$S = \left\{ \begin{pmatrix} l & k \\ 0 & 0 \end{pmatrix} \mid l, k \in R \right\} \text{ and a commutative ring } R. \text{ Define } \vartheta : S \times S \rightarrow S \text{ such that}$$

$$\vartheta \left(\begin{pmatrix} l & k \\ 0 & 0 \end{pmatrix}, \begin{pmatrix} i & j \\ 0 & 0 \end{pmatrix} \right) = \begin{pmatrix} 0 & kj \\ 0 & 0 \end{pmatrix} \quad \text{and} \quad f : S \rightarrow S \quad \text{by}$$

$$f \left(\begin{pmatrix} l & k \\ 0 & 0 \end{pmatrix} \right) = \begin{pmatrix} l & 0 \\ 0 & 0 \end{pmatrix}. \text{ From this, } \vartheta \text{ refers to the bi-semi-derivation on } S \text{ with associated function } f.$$

Assume that f is a semi-derivation of R having an associated function g , an endomorphism. A generalized semiderivation is the additive map F on R if $F(ce) = F(c)e + g(c)f(e) = F(c)g(e) + cf(e)$ and $F(g) = g(F)$, for every c, e in R . There is a generalized semiderivation for every given semi-derivation. Furthermore, any generalized semi-derivations connected to g are just generalized derivations of R , if g is acting as identity on R . The most natural example of generalized semi-derivation, we consider a semi-derivation \mathcal{F} on a ring R joint with a function \mathcal{G} and define the two map as $F(l) = \mathcal{F}(l) - l$ and $H(l) = \mathcal{F}(l) + l$, l in R . With such construction the generalized

semiderivations on R are represented by F and H joint with \mathcal{G} .

Motivated by all above definitions and references includes in [3, 4, 2, 5, 6, 7], we deliver the concept of generalized bi-semiderivation on ring in [8] as follows: Consider the maps $\delta, \vartheta : R \times R \longrightarrow R$ and f from R to R . Now describe if for every $l \in R, b \mapsto \delta(l, b)$ and for every $b \in R, l \mapsto \delta(l, b)$ are generalized semi-derivation of R with associated function ϑ, f (defined as above), and satisfying $\delta(f) = f(\delta)$, then δ will be called generalized bi-semi-derivation on R . More precisely, δ, ϑ, f satisfying the following:

1. $\delta(lv, c) = \delta(l, c)f(v) + l\vartheta(v, c) = \delta(l, c)v + f(l)\vartheta(v, c)$
2. $\delta(l, wc) = \delta(l, w)f(c) + w\vartheta(l, c) = \delta(l, w)c + f(w)\vartheta(l, c)$
3. $f(\delta) = \delta(f)$ for every $l, v, c, w \in R$.

We present the example of generalized bi-semiderivation to understand the concept well.

Example 1.2 Consider the set $\mathcal{R} = \left\{ \begin{pmatrix} l & j \\ u & q \end{pmatrix} \mid j, l, u, q \in 2\mathbb{Z}_8 \right\}$. Then \mathcal{R} represents a ring under matrix addition and matrix multiplication. Define $\delta, \vartheta : \mathcal{R} \times \mathcal{R} \longrightarrow \mathcal{R}$ such as

$$\delta \left(\begin{pmatrix} l & j \\ u & q \end{pmatrix}, \begin{pmatrix} e & k \\ g & h \end{pmatrix} \right) = \begin{pmatrix} 0 & jk \\ ug & 0 \end{pmatrix},$$

$$\vartheta \left(\begin{pmatrix} a & b \\ c & d \end{pmatrix}, \begin{pmatrix} e & k \\ g & h \end{pmatrix} \right) = \begin{pmatrix} 0 & 0 \\ 0 & dh \end{pmatrix}$$

and $f : \mathcal{R} \longrightarrow \mathcal{R}$ by $f \left(\begin{pmatrix} a & b \\ c & d \end{pmatrix} \right) = \begin{pmatrix} a & 0 \\ 0 & 0 \end{pmatrix}$. Therefore, δ is a generalized bi-semiderivation with associated function ϑ and f on \mathcal{R} . In above defined concept of generalized bi-semiderivation, we easily observe that δ will be considered as bi-semiderivation, if we assume $\delta = \vartheta$.

Several mathematicians have identified a connection between the behavior of mappings observing algebraic identities involving prime (semiprime) rings and their subsets. The prime ring's R structure possessing a nonzero derivation \mathcal{D} that allows the values of \mathcal{D} to commute, or for which $\mathcal{D}(k)\mathcal{D}(j) = \mathcal{D}(j)\mathcal{D}(k)$ for each $k, j \in R$, was found by Herstein [6]. In this note, author determine the structure of commuting derivation on ring.

In [4], authors goal is to provide commutativity results for rings and show that if I is a nonzero ideal of R and R is a 2-torsion free semiprime ring, then a derivation d of R is commuting on I if one of the following rules is true: (i) $d(x)d(y) = xy$ (ii) $d(x)d(y) = yx$ (iii) $d(x)d(y) = -xy$ (iv)

$d(x)d(x) = x^2$ for all $x, y \in I$. Further, if $d(I) \neq 0$, then R has a nonzero, central ideal. Encouraged by each work of examined literature, we investigate the central generalized bi-semiderivations and it's related identities on semiprime ring.

Lastly, we show by some examples that the limitations placed on the hypothesis of the different theorems are not redundant.

2 Main Results

With the following lemmas, we get started.

Lemma 2.1 [9] *Let R be a semiprime ring, then:*

- (1) *There are no non-zero nilpotent elements in the center of R .*
- (2) *If for all $u, v \in R$ and a nonzero prime ideal J of R such that $uRv \subseteq J$, then either $u \in J$ or $v \in J$.*

Lemma 2.2 [10] *The center of a one sided (non-zero) ideal exists in the center of R , if R is a semiprime ring. Each commutative ideal (one-sided) is therefore always included in the center of R .*

Theorem 2.1 *Let R be a semiprime ring possessing 2 torsion freeness and δ be a generalized bi-semiderivation on R with associated surjective function f and bi-semiderivation ρ . If $\delta(r, r) \subseteq Z(R)$ for every r in R , then either $\rho = 0$ or R contains a central nonzero ideal.*

Proof: We have given that $\delta(r, r) \subseteq Z(R)$, for each r in R . So,

$$[\delta(r, r), s] = 0 \text{ for every } r, s \in R. \quad (1)$$

On linearization of above equation in r and utilize the torsion of R , we observe that

$$[\delta(r, p), s] = 0 \text{ for every } r, p, s \in R. \quad (2)$$

Now, put pt in place of p in (2) to find

$$\delta(r, p)[f(t), s] + p[\rho(r, t), s] + [p, s]\rho(r, t) = 0 \text{ for each } r, t, p, s \in R. \quad (3)$$

Surjectivity of f enable us to put q for $f(t)$, $q \in R$ in (3) and we get

$$\delta(r, p)[q, s] + p[\rho(r, t), s] + [p, s]\rho(r, t) = 0 \text{ for every } r, q, p, s, t \in R. \quad (4)$$

Reinstate (4) after putting ps for s and applying (4) to bring out

$$\delta(r, p)[q, p]s + p[\rho(r, t), p]s = 0 \text{ for each } r, p, t, q, s \in R. \quad (5)$$

At instance, we can find from (5)

$$p[\rho(r, t), p]s = 0 \text{ for every } t, p, s, r \in R. \quad (6)$$

Now make use of semiprimeness of R to obtain $[\rho(r, t), p] = 0$, for every $p, r, t \in R$. Therefore, $\rho(R, R) \subseteq Z(R)$. We conclude our claim by Lemma 2.2 in [11].

Theorem 2.2 *Suppose that I is a nonzero ideal of R and that R is a semiprime ring. If δ is a symmetric generalized bi-semiderivation on R with associated bi-semiderivation ρ and associated function f such that $[\delta(l, l), j] \mp [l, j] = 0$ for all $l, j \in R$, then δ is central. Moreover, either $\rho = 0$ or R contains a central (nonzero) ideal.*

Proof: In accordance to the stated hypothesis, we have

$$[\delta(l, l), j] \mp [l, j] = 0 \text{ for each } l, j \in I. \quad (7)$$

As a result of linearization in l of (7)

$$[\delta(l, l), j] + [\delta(q, q), j] + 2[\delta(l, q), j] \mp [l, j] \mp [q, j] = 0 \text{ for any } l, j, q \in I. \quad (8)$$

Comparing (7) and (8), we obtain

$$[\delta(l, q), j] = 0 \text{ for all } l, j, q \in I. \quad (9)$$

Replace rj in (25) to get $[\delta(l, q), r]j = 0$ for each $l, q, j \in I$ and $r \in R$. This implies that Hence $\delta(l, q) \subseteq Z(R)$. Applying Theorem 2.1, to conclude the proof.

Theorem 2.3 *Let a ring R be prime possessing characteristic not 2. If δ is a symmetric generalized bi-semiderivation on R with associated bi-semiderivation ρ and associated function f such that $[\delta(x, x), y] \mp (x \circ y) = 0$ for all $x, y \in R$, then δ is central δ is central. Moreover, either $\rho = 0$ or R contains a central nonzero ideal.*

Proof: The proof of this theorem is similar as that of above theorem.

Theorem 2.4 *Let R be a semiprime ring and $I \neq (0)$ be an ideal of R . If δ is a symmetric generalized bi-semiderivation on R with associated function f such that $\delta(p, p) \circ y - [p, y] = 0$ for $p, y \in R$, then δ is central. Moreover, either $\rho = 0$ or R contains a central nonzero ideal.*

Proof: In accordance to the stated hypothesis, we have

$$\delta(p, p) \circ y - [p, y] = 0 \text{ for each } p, y \in I. \quad (10)$$

Substitution of yz in place of y in (10) gives that

$$[\delta(p, p), y]z + y(\delta(p, p) \circ z) - [p, y]z - y[p, z] = 0 \text{ for each } y, p, z \in I. \quad (11)$$

Analyzing the last pair of equations, we have

$$[\delta(p, p), y]z - [p, y]z = 0 \text{ for each } y, p, z \in I. \quad (12)$$

Rewrite last expression by putting yx for y to find

$$y[\delta(x, x), x]z = 0 \text{ for each } x, y, z \in I. \quad (13)$$

R 's semiprimeness indicates that $[\delta(x, x), x] = 0$, for every $x \in R$. Hence $\delta(x, z) \subseteq Z(I) \subseteq Z(R)$, utilizing the property that the center of R contains the center of a nonzero ideal by Lemma 2.1.

Theorem 2.5 *Let a semiprime ring be R possessing 2-torsion freeness and $I \neq 0$ be an ideal of R . If δ is a symmetric generalized bi-semiderivation on R with associated function f and associated bi-semiderivation ρ such that $\delta(x, x)\delta(y, y) = xy \forall y, x \in R$, then ρ is central. Moreover, either $\rho = 0$ or R contains a central nonzero ideal.*

Proof: We have given that

$$\delta(x, x)\delta(y, y) = xy \text{ for each } x, y \in I. \quad (14)$$

Linearizing (14) in x yields that

$$\delta(x, z)\delta(y, y) = 0 \text{ for every } x, z, y \in I. \quad (15)$$

A similar way of linearization of (14) in y give us Linearizing (14) in x yields that

$$\delta(x, x)\delta(y, u) = 0 \text{ for each } x, u, y \in I. \quad (16)$$

Substitute xr for x in (15) to get

$$\delta(x, z)r\delta(y, y) + f(x)\rho(r, z)\delta(y, y) = 0 \text{ for every } x, z, y \in I, r \in R. \quad (17)$$

Multiply (17) by $\delta(w, w)$ from left and use (16) to find

$$\delta(w, w)f(x)\rho(r, z)\delta(y, y) = 0 \text{ for every } w, z, y \in I, r \in R. \quad (18)$$

Applying the surjectivity of f , the last equation can be seen as

$$\delta(w, w)t\rho(r, z)\delta(y, y) = 0 \text{ for each } w, z, y \in I, r \in R \text{ and } f(x) = t \in R. \quad (19)$$

This expressly implies that

$$\rho(r, z)\delta(w, w)t\rho(r, z)\delta(w, w) = 0 \text{ for every } w, z \in I, r, t \in R. \quad (20)$$

We obtain by R 's semiprimeness

$$\rho(r, z)\delta(w, w) = 0 \text{ for every } w, z \in I, r \in R. \quad (21)$$

Multiply above equation by $\delta(u, u)$ from right and use (14) to find

$$\rho(r, z)wu = 0 \text{ for each } w, u, z \in I, r \in R. \quad (22)$$

A suitable replacement in the last equation enable us to write $[\rho(r, z), u] = 0 \forall r \in R$ and $u, z \in I$. On implementing Lemma 2.2, $\rho(z, z) \subseteq Z(R)$, and hence ρ is central.

Another claim that either $\rho = 0$ or R contains a central nonzero ideal can conclude by Lemma 2.2 in [11], if ρ is central.

Theorem 2.6 *Let a ring R be semiprime having 2-torsion freeness and $I \neq 0$ be an ideal of R . If δ is a symmetric generalized bi-semiderivation on R linked with function f and associated bi-semiderivation ρ such that $\delta(x, x)\delta(y, y) = -yx \forall y, x \in R$, then ρ is central. Moreover, either $\rho = 0$ or R contains a central nonzero ideal.*

Proof: The proof of this theorem is obtained by following the identical approach as in the previous theorem.

The non-commutative version of our previous investigation can be seen as below result, in which we observe that δ will be acting as left centralizer. The detailed concept of left (right) centralizers can be found in [12].

Corollary 2.1 *Letting R be a prime ring that is non-commutative with $\text{char}(R) \neq 2$. If δ is a symmetric generalized bi-semiderivation on R with associated function f and associated bi-*

semiderivation ρ such that $\delta(x,x)\delta(y,y) = xy$ for all $x,y \in R$, then $\rho = 0$. In this case, δ will acting as left centralizer.

Theorem 2.7 Let a ring R be prime having characteristic not 2. If δ is a symmetric generalized bi-semiderivation on R with associated function f such that $[\delta(k,k),u] \mp [\rho(u,u),k] = 0 \forall u,k \in R$, then δ is central. Moreover, either $\rho = 0$ or R contains a central nonzero ideal.

Proof: From stated hypothesis, we have

$$[\delta(k,k),u] \mp [\rho(u,u),k] = 0 \text{ for every } u,k \in I. \quad (23)$$

Linearize in k (23) yields that

$$[\delta(k,k),u] + [\delta(v,v),u] + 2[\delta(k,v),u] \mp [\rho(u,u),k] \mp [\rho(u,u),v] = 0 \text{ for every } u,k,v \in I. \quad (24)$$

Comparing (23) and (24) and applying characteristic condition, we obtain

$$[\delta(k,v),u] = 0 \text{ for each } v,u,k \in I. \quad (25)$$

Hence $\delta(k,v) \subseteq Z(I) \subseteq Z(R)$, as follows from Lemma 2.1.

Theorem 2.8 Let R be a 2-torsion free semiprime ring. If ϑ is a symmetric bi-semiderivation on R such that $\vartheta(\vartheta(u,u),u) = 0$ for all $u \in R$, then $\vartheta = 0$.

Proof: We are given that by hypothesis

$$\vartheta(\vartheta(u,u),u) = 0 \text{ for all } u \in R. \quad (26)$$

Linearize (26) to obtain

$$\begin{aligned} &\vartheta(\vartheta(u,u),u) + \vartheta(\vartheta(v,v),u) + 2\vartheta(\vartheta(u,v),u) + \vartheta(\vartheta(u,u),v) \\ &+ \vartheta(\vartheta(v,v),v) + 2\vartheta(\vartheta(u,v),v) = 0 \text{ for every } v,u \in R. \end{aligned} \quad (27)$$

From (26) and (27), we get

$$\vartheta(\vartheta(v,v),u) + 2\vartheta(\vartheta(u,v),u) + \vartheta(\vartheta(u,u),v) + 2\vartheta(\vartheta(u,v),v) = 0 \text{ for each } v,u \in R. \quad (28)$$

Put $-u$ in place of u in(28) to find

$$-\vartheta(\vartheta(v,v),u) + 2\vartheta(\vartheta(u,v),u) + \vartheta(\vartheta(u,u),v) - 2\vartheta(\vartheta(u,v),v) = 0 \text{ for every } v,u \in R. \quad (29)$$

Analyzing (28) and (29) to obtain by using torsion of R

$$2\vartheta(\vartheta(u, v), v) + \vartheta(\vartheta(v, v), u) = 0 \text{ for every } v, u \in R. \quad (30)$$

Rewrite (30) after swapping u by tu , we have

$$\begin{aligned} &2t\vartheta(\vartheta(u, v), v) + 2\vartheta(\vartheta(t, v), v)u + 2\vartheta(t, v)\vartheta(u, v) + 2\vartheta(t, v)\vartheta(u, v) \\ &+ \vartheta(\vartheta(v, v), tu) + t\vartheta(\vartheta(v, v), u) = 0 \text{ for every } u, t, v \in R. \end{aligned} \quad (31)$$

Using (30), (31) becomes

$$4\vartheta(t, v)\vartheta(u, v) = 0 \text{ for every } u, t, v \in R. \quad (32)$$

Torsion restriction on R yields that $\vartheta(t, v)\vartheta(u, v) = 0$ for each $v, t, u \in R$. In particular, last expression can be written as $\vartheta(t, v)\vartheta(t, v) = 0$ for each $v, t \in R$. This implies that $(\vartheta(t, v))^2 = 0 \forall t, v \in R$, that is, ϑ is nilpotent with index 2. Use Lemma 2.1 to observe $\vartheta(t, v) = 0$ for each $t, v \in R$. Hence $\vartheta = 0$.

Example 2.1 Consider the set $R = \left\{ \begin{pmatrix} s & c \\ t & 0 \end{pmatrix} \mid s, c, t \in \mathbb{Z}_8 \right\}$ and $I = \left\{ \begin{pmatrix} l & 0 \\ j & 0 \end{pmatrix} \mid l, j \in \mathbb{Z}_8 \right\}$. When performing “+” and “.” in matrices of R , R denotes a ring.

and I will be a left ideal of R . Define $\delta : R \times R \rightarrow R$ such that $\delta \left(\begin{pmatrix} s & c \\ t & 0 \end{pmatrix}, \begin{pmatrix} u & f \\ g & 0 \end{pmatrix} \right) = \begin{pmatrix} su & 0 \\ 0 & 0 \end{pmatrix}$, $\vartheta \left(\begin{pmatrix} s & c \\ t & 0 \end{pmatrix}, \begin{pmatrix} u & f \\ g & 0 \end{pmatrix} \right) = \begin{pmatrix} 0 & 0 \\ tg & 0 \end{pmatrix}$ and $f : R \rightarrow R$ by $f \left(\begin{pmatrix} s & c \\ t & 0 \end{pmatrix} \right) = \begin{pmatrix} 0 & 0 \\ t & 0 \end{pmatrix}$. Therefore, δ is a generalized bi-semiderivation with associated function ϑ and associated map f on I . We easily observe that the maps δ, ϑ, f satisfying the condition of Theorem 2.7 and 2.8 but neither δ is central nor $\vartheta = 0$. Hence the Semiprimeness (Primeness) of ring is the essential requirement of the hypothesis.

References

- [1] G. Maksa, “A remark on symmetric biadditive functions having non-negative diagonalization,” *Glasnik. Mat.*, vol. 15, no. 35, pp. 279–282, 1980.
- [2] J. Bergen, “Derivations in prime rings,” *Canad. Math. Bull.*, vol. 26, no. 8, pp. 267–270, 1983.

- [3] A. Ali, D. V., and F. Shujat, "Results concerning symmetric generalized biderivations of prime and semiprime rings," *Matematiqki Vesnik*, vol. 66, no. 4, pp. 410–417, 2014.
- [4] S. Ali and H. Shuliang, "On derivations in semiprime rings," *Algebr. Represent. Theory*, vol. 15, no. 0, pp. 1023–1033, 2012.
- [5] J. C. Chang, "On semiderivations of prime rings," *Chinese J. Math.*, vol. 12, pp. 255–262, 1984.
- [6] I. N. Herstein, "A note on derivations ii," *Canad. Math. Bull.*, vol. 22, pp. 509–511, 1979.
- [7] N. Rehman and A. Z. Ansari, "On lie ideals with symmetric bi-additive maps in rings," *Palestine J. Math.*, vol. 2, pp. 14–21, 2013.
- [8] F. Shujat, "On symmetric generalized bi-semiderivations of prime rings," *Bol. Soc. Paran. Mat.*, vol. 42, pp. 1–5, 2024.
- [9] T. Lam, "A first course in noncommutative rings," *Graduate Texts in Mathematics*, 2001.
- [10] I. N. Herstein, "Rings with involution," *University of Chicago Press*, 1976.
- [11] F. Shujat, "Additive multipliers and bi-semiderivations on rings," *Ann. Math. Comp. Sci.*, vol. 4, pp. 1–6, 2021.
- [12] B. Zalar, "On centralizers of semiprime rings," *Comment. Math. Univ. Carol.*, vol. 32, pp. 609–614, 1991.

An Adaptive Model for Distributing and Balancing Air Conditioning in Crowded Places

Ahmed Alshafut

**Department of Information Technology, Faculty of Computing and Information,
Al-Baha University, AlBaha, Saudi Arabia.
a.alshafut@bu.edu.sa**

Abstract: This paper studies how the Heating, Ventilation, & Air conditioning (HVAC) systems can be optimized in response to global heat and energy demand rises. We advocate a performance-based framework geared towards high-density sites such as terminals and malls to obtain energy efficiency without sacrificing operational function. The model combines cutting-edge sensors, control and variable components, and feedback loops to continuously adapt HVAC usage in response to temperature, humidity data, and occupancy levels. An important feature of the model is its use of Internet-of-Things (IoT) technology to make networked devices able to share information automatically. Those types of integration include power consumption, network dynamics, load forecasting, and even user perception, making the model so resilient and scalable. The method is intended to be adaptable as situations arise based on changes in incident weather and room usage. A major consideration has been including potential users (especially older people). The goal is to improve occupant comfort, save energy, and encourage sustainable management of HVAC systems in crowded spaces. Experimental results show that there can be a high energy saving if certain scenarios are considered without compromising the comfort of living.

Keywords: HVAC, Energy Efficiency, Air Conditioning, Adaptive Systems, Environmental Sustainability.

نموذج تكيفي لتوزيع وموازنة تكيف الهواء في الأماكن المزدحمة

المخلص: تتناول هذه الورقة كيفية تحسين أنظمة التدفئة والتهوية وتكييف الهواء (HVAC) للاستجابة لارتفاع الطلب العالمي على الحرارة والطاقة. وذلك باقتراح إطار عمل قائم على الأداء موجه نحو المواقع عالية الكثافة مثل المحطات والمراكز التجارية للحصول على كفاءة طاقة دون التضحية بالوظيفة التشغيلية. يجمع النموذج أحدث أنظمة الاستشعار والتحكم والمكونات المتغيرة وحلقات التغذية المرتدة لتكيف استخدام هذه التقنية باستمرار الاستجابة لبيانات درجة الحرارة والرطوبة ومستويات الإشغال. ميزة مهمة للنموذج هي استخدام تقنية إنترنت الأشياء لجعل الأجهزة المتصلة بالشبكة قادرة على تبادل المعلومات تلقائيًا. تشمل أنواع الدمج هذه استهلاك الطاقة ، وديناميكيات الشبكة ، وتوقع الاحمال ، وحتى إدراك المستخدم ، مما يجعل النموذج متين وقابل للتطوير. الهدف من هذه الطريقة هو أن تكون قابلة للتكيف مع الظروف المتغيرة بناءً على التغيرات في الأحوال الجوية والاستخدام. كان أحد الاعتبارات الرئيسية هو إشراك المستخدمين المحتملين من مختلف الفئات العمرية للاستفادة من هذا النموذج. أيضا بتحسين راحة الشاغلين وتوفير الطاقة وتشجيع الإدارة المستدامة لهذه الأنظمة في الأماكن المزدحمة. تُظهر النتائج التجريبية أنه يمكن تحقيق توفير كبير في الطاقة إذا تم مراعاة بعض السيناريوهات دون المساس براحة المكان.

1. Introduction

Increases in global heat and energy consumption issues have concerned system designers in several disciplines. The solutions provided should consider productivity in addition to handling energy issues in most countries. Heating, ventilating, and air-conditioning (HVAC) have gathered much attention to improving the services at different places. Implementing efficient optimization and control mechanisms has been identified as one crucial way to help reduce and shift HVAC systems' energy consumption to save economic costs and foster improved integration with renewables [1]. Several attentions have attempted to balance energy consumption and enable more comfort for human needs. Moreover, as the electrical load continues to grow, it is highly interesting for power utilities to reduce the system peak demand and increase the utilization of electricity infrastructure with minimal investment in power generation and delivery systems [2]. However, more electricity consumption can occur when following incorrect behaviors. Thus, next-generation solutions should balance needs and energy efficiency.

In recent years, the demand for effective air conditioning systems in crowded environments has significantly grown in different scopes. With the rise in urbanization and the increase in population density, optimizing the balance and distribution of air conditioning has become a crucial aspect of providing a comfortable and healthy indoor climate. This paper focuses on the key concepts and strategies for balancing and distributing air conditioning in crowded places. These places include public transportation points, huge shopping malls, and large event halls [3]. Many considerations should be given to all visitors to these crowded places to meet individual needs. Future work should consider the well-being of all visitors in terms of environmental quality, including temperature, humidity, and air balancing. The main issue in this scope can be summarized as the varying thermal comfort needs of the different visitors within the same space [4]. Furthermore, another issue is balancing the visitor needs and managing the energy consumption increases [5].

Several attempts were mainly focused on developing advanced air conditioning systems. These attempts were considered from several eras, such as engineering, research, and industry. These combinations from different specializations are because these systems employ various technologies such as sensor advancement, data analytics, and intelligent algorithms. All cooperated efforts are to maintain the optimal environmental needs as well as to minimize energy consumption [6]. On the other hand, renewable energy sources with smart technologies have promised to develop sustainable AC systems, ensuring reduced greenhouse gas production [7]. All the previous considerations show the importance of quarrying new and sustainable solutions for these issues in crowded places. Nevertheless, energy consumption has recently become a critical issue. This was due to the importance of energy saving and its impact on the environment. However, it is known that electronic devices in the residential, industrial, and commercial sectors have the highest usage of energy consumption [8].

These devices affect energy consumption due to different factors, such as energy management techniques, power efficiency levels, and device operation conditions [9]. Thus, researchers have initially focused on deploying energy efficiency on the devices from the manufacturing phase [10]. More issues are focused on the sustainability of solutions to reduce carbon emissions worldwide [11].

2. Intelligent Applications of Air Conditioning

Recently, many attempts have been made to manage air conditioning systems. Also, energy consumption is greatly considered in these systems. For instance, the fuzzy logic-based AC system model is used to control the AC in specific buildings [12, 13]. This model focuses on factors such as indoor and outdoor temperature, user-preferred conditions, and humidity. This model focuses on adjusting the AC levels by considering all the previous factors. It has improved energy consumption compared to traditional AC systems [14].

Moreover, an artificial neural network-based AC system uses different models to manage AC balancing modes. This model uses artificial neural networks (ANNs) to control air conditioning systems. It uses input variables to train the ANN control AC condition systems. Then, the trained ANN predicts the appropriate settings based on the current input variables. It has shown improvement in energy efficiency compared to other models [15, 16]. They are moving forward to predictive control-based AC systems that adjust the condition settings using the prediction controls. Mainly, this model uses different factors when predicting to be used even for future settings.

When the behavior is predicted, the controller helps modify the settings accordingly to achieve the desired comfort level. This model could leverage the minimizing of energy consumption. It can be shown that this model would manage both energy consumption and raise indoor comfort levels [17, 18, 19, 20]. Furthermore, another model has been developed using the reinforcement learning-based AC system [21]. This model focuses on the interactions between the AC system and the environment [22]. These interactions can determine the optimal AC conditions. Similar factors in this model are considered to state the correct levels of AC settings. Also, this model has shown an improvement in energy consumption minimization [23, 24, 25].

3. The Proposed Model

This model is initially proposed to enable an adaptive approach for AC balancing, especially in crowded places. For this reason, it focuses on choosing an adaptive algorithm for adjusting the system's settings (Algorithm 1). Several factors are considered, starting from the phase design of this model. There are several components are involved in this model, including:

3.1 The involved components

- 3.1.1. **Sensors:** Such devices can monitor and generate readings from the surrounding environment, assisting in generating the needed data. Several technologies can be applied to sensors to minimise cost and energy consumption. Internet of Things applications can be used in this phase to link devices, as shown in figure 1.
- 3.1.2. **Control Algorithms:** In this phase, optimal settings are maintained for processing data efficiently. Past performance logs are used for future calculations, which assists in minimizing energy consumption and maximizing service quality.
- 3.1.3. **Variable components:** Control systems would be used to classify the AC scenarios, allowing for more comfort in indoor halls. They can be adjusted to achieve optimal performance. Changing conditions will be considered to reach the desired level of comfort.
- 3.1.4. **Feedback loop:** This model relies on the feedback loop for continuous learning from feedback. This would allow for continued enhancement of real-time decision-making based on the data received from sensors.

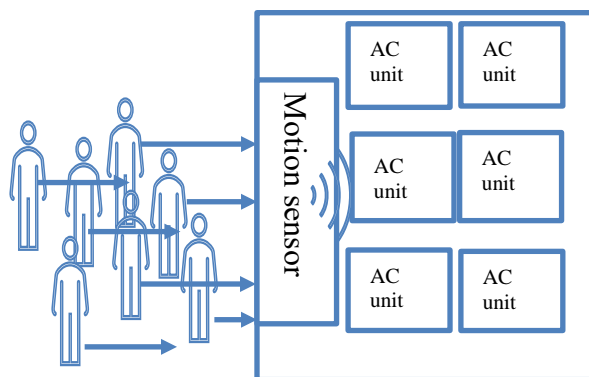


Figure 1: Motion Sensors

Different scenarios are considered for meeting the requirements of this model as shown below.

1. Initialization
Set initial thresholds: $T_{init}, H_{init}, O_{init}$
Initialize sensors $S_{temp}, S_{hum}, S_{occ}$
2. Data Collection
Collect real-time data $D_t = \{ T_t, H_t, O_t \}$.
3. Data Processing
Normalize data: $D'_t = \text{normalize}(D_t)$.
4. Occupancy Detection
Classify occupancy:
$O_{class}(t) = \begin{cases} Low & \text{if } O_t < O_{low} \\ Medium & \text{if } O_{low} < O_t < O_{high} \\ High & \text{if } O_t > O_{high} \end{cases}$
5. Environmental Analysis
Compute deviations: $\Delta T_t = T_t - T_{opt}, \Delta H_t = H_t - H_{opt}$.
6. Adaptive Control
Adjust HVAC: $HVAC_t = f(O_{class}(t), \Delta T_t, \Delta H_t)$
Predict future conditions: $\bar{O}_{(t+k)} = \text{ML_model}(D_{\{t-n:t\}})$
7. Feedback Loop
Monitor and adjust: $\text{Adjust}_t = g(\text{desired}_t - \text{actual}_t)$
8. Energy Optimization
Minimize energy consumption: $\min E_t$ subject to comfort constraints
9. Fault Tolerance and Scalability
Detect and mitigate faults: $\text{Fault}_t = \{ 1 \text{ if fault detected; } 0 \text{ otherwise } \}$
10. User Comfort
Personalize settings: $\text{Comfort}_t = h(\text{user preferences}, D_t)$
11. Logging and Reporting
Log activities $L_t = \{ D_t, HVAC_t, \text{Error}_t, \text{Adjust}_t \}$
12. Continuous Improvement
Evaluate and optimize: $\text{Optimize} = \text{Evaluate}(L_{\{t-n:t\}})$

Algorithm 1: Adaptive Algorithm

4. Effective Factors

Several factors have influenced this model regarding specifications and determining the priority for each sole requirement. Such considerations are considered from the beginning of the model design. Desired characteristics are well maintained to meet the model requirements. The main features are listed below:

4.1 Power consumption: This issue is handled by balancing individual and group request loads. Power requirements are considered when managing different devices or systems. Chosen algorithms can assist in distributing the loads with power consumption considerations. This approach would minimize energy waste.

4.2. Load characteristics: Different load characteristics are considered in this model for scalability purposes. Thus, this model maintains several requirements, such as response time, despite various load needs. Also, quality of service is considered by classifying the load by the priority levels. This feature can ensure that critical and time-sensitive loads receive the resources they need.

4.3. Network conditions: the current state of the network can affect the load balancing and other requirements. Thus, load distributions should be considered despite the various conditions to enable intelligent load balancing.

4.4. Prediction modes: The chosen algorithms consider the load balancing and predictive modes of future load patterns. Analyzing historical data can be achieved by using machine learning algorithms for future data estimations. This consideration can help in optimally allocating resources.

4.5. Fault tolerance: Multiple load-balancing algorithms ensure high availability and reliability. This can be achieved by mitigating the impact of maintenance activities or minimizing failures.

4.6. Scalability: Scalability is a vital factor when choosing load balancing models. Increasing loads should be considered to adjust the load distribution and meet scalability needs. Thus, changing system conditions should be considered when using provision techniques for load balancing strategies.

4.7. Cost optimization: The chosen model considers cost optimization and user preferences. In this factor, both resource utilization and user preferences are considered for enabling the best of the resources based on the needs of users. For example, when certain users or applications may have specific levels of requirements or priorities, the model can handle this issue based on the previous quality of service patterns.

5. Balancing Scenarios

Adaptive models for crowded places are vital solutions for managing air-conditioning systems. However, this depends on the algorithms chosen to handle this issue. As mentioned earlier, different factors play critical roles when applying chosen algorithms. The main purpose of our model is to enable balancing scenarios for crowded places. So, different users can be served, enabling instant decision-making features. For example, when elderly people visit this place, they will be directly guided to appropriate places within the hall. Otherwise, others will be directed to other places that suit their circumstances. This would ensure both the efficiency of the adaptive air conditioning model and the highest level of comfort for all users. Thus, dynamic adjusting for location-based decisions will be managing airflow and temperature in crowded places.

Our important goal is to determine the best places for each coming person with real-time decisions for adjustment and guidance for all coming people. Also, this model would maintain the best level of comfort for all current occupants. All generated data would assist our model in choosing the optimal situations in all the parts of the hall. Furthermore, identifying the various needs of occupants would enhance the possible solutions for future usability demands. Also, users' profile and needs for be saved for future decision making. This model depends on the personalized determination to enhance the user's comfort. Thus, it will help to enable good environmental conditions for all users. Also, energy saving is considered in this model to balance both occupant's comfort and resource allocations. Overall, the implementation of this system would manage between various factors in order to allow for optimal experience for all occupants in crowded places.

Users need to address their issues earlier for more usability scenarios. However, due to the mentioned factor above, it is needed to address different circumstances. These circumstances include the weather changes, user needs and the number of occupants in crowded places. The user needs are classified based on the age, gender, and the health status. The weather changes must be considered when applying this model, for example at the time of the day or night. Also, the season plays a vital role in determining appropriate temperature rates based on the model. Furthermore, other geographical matters are considered for the type of area, e.g., costal, mountainous, and desert places.

6. Experimental Setup and Results

Adaptability, energy efficiency, and user comfort were investigated in the experimental evaluations of an adaptive air conditioning system across five scenarios. When there is low occupancy (Scenario 1), where the occupancy level is just 20%, the system produces an air temperature of 22.5 degrees Celsius and 45 percent RH, consuming only 5.0 kW. It had a low response time of 2.0 seconds, yielding a human comfort level of 95% and an energy efficiency rate of 80%. This showed that the company scaled operations according to demand and yet provided comfortability. The experimental results are detailed in Table 1.

The second scenario is where there was high occupancy at approximately 80 percent. The temperature went up, though marginally, to 23.0°C and a relative humidity of 50%. This increased the power consumed up to 10.0kW and caused a longer response time of 3.5 seconds. This reduced the energy efficiency to 75%, and the system still had a 90% comfort feeling. It showed that the system could accommodate extra heat load, although it meant lower energy consumption.

The Evening Peak scenario (scenario 3) with medium occupancy (50%) effectively controlled a room temperature of 21.0°C and a humidity level of 60%, utilizing 8.0 kw electricity and a delay time of 2. Comfort level was 92% and the energy efficiency was 78%. This illustrated the flexibility of the system under peak demand providing comfortable users and saving energy.

Under Extreme Weather Scenario Four, when occupancy was 85%, the system struggled to achieve acceptable temperatures. The humidity level was lower at 25.0°C, and the temperature was 5% higher. The response time was lower at 4.0 seconds, while power consumption peaked at 12.0 KW. The comfort level decreased to 85% while maintaining the minimum level of energy efficiency at 70%. It pointed out areas where enhancements could be made to system robustness and resource management under stressed conditions.

Lastly, Scenario 5, Elderly Priority, stressed elderly comfort, where a medium occupancy room is maintained at 24.0°C and 55% humidity. It consumed a power of 9.0 kW and had a response time of 3.0 seconds, with a 93% satisfaction rate and 77% energy efficiency rating. In this way, it proved that the system is able to provide individualized atmospheric control, taking into account the specific needs of sensitive groups with minimal overall energy consumption.

Results from an experimental evaluation of research on adaptive AC systems are useful for life and developmental technologies. Additionally, the studies display impressive breakthroughs in energy conservation by monitoring power utilization that varies depending on presence and absence. The aspect is also very critical towards minimising unwanted energy consumption in buildings which have been taken up as part of urbanisation concerns.

Furthermore, it enhances indoor Environmental Quality (IEQ), contributing to health and comfort in schools, homes, and workplaces. The integration of IoT with adaptive algorithms makes today's HVAC systems modern. Now, it is ready for tomorrow's smart and efficient climate control solutions.

According to international goals that aim at creating a sustainable environment in the future, the study is sustainable because it deals with the challenges related to environmental protection. The system ensures that air conditioning has a low carbon footprint by enhancing energy efficiency and minimizing energy utilization. This is exemplified by the Elderly Priority scenario, where one has to recognize that climate control systems ought to be tailored based on particular demands for various sectors for improved livability. The implication of this research with regard to intelligent building technology is that adaptive systems are able to make effective use of real-time data for high-performance integrated building management. The study could help develop policies and build construction and maintenance standards to make them more environmentally friendly and convenient and promote wider sustainability across the board. In summary, the study seeks answers to some of the issues involved in building management and technology as a means for better environment.

Table 1: Results Obtained Used Different Scenarios

Test Scenario	Avg. temperature (°C)	Avg. Humidity (%)	Occupancy Level	Power Consumption (kW)	Response Time (s)	User Comfort Level (%)	Energy Efficiency (%)
Scenario 1: Low Occupancy	22.5	45	Low (20%)	5	2	95	80
Scenario 2: High Occupancy	23	50	High (80%)	10	3.5	90	75
Scenario 3: Evening Peak	21	60	Medium (50%)	8	2.5	92	78
Scenario 4: Extreme Weather	25	40	High (85%)	12	4	85	70
Scenario 5: Elderly Priority	24	55	Medium (55%)	9	3	93	77

7. Conclusion

This study introduces an adaptable framework for the distribution and regulation of air conditioning in densely populated locations, with a particular focus on regions with high population density such as terminals and malls. The suggested approach utilizes contemporary sensors, control systems, feedback loops, and Internet-of-Things (IoT) technology to enhance the efficiency of HVAC systems. Our methodology seeks to enhance occupant comfort, conserve energy, and encourage sustainable HVAC management by dynamically adjusting HVAC consumption in response to real-time temperature, humidity, and occupancy data. The model's usefulness was shown by our testing findings in five different scenarios: low occupancy, high occupancy, nighttime peak, bad weather, and elderly priority. The system successfully achieved substantial energy save while maintaining comfort, demonstrating its flexibility and ability to be expanded. For example, when there were few people present, the model was able to keep 95% of users comfortable while using 80% less energy. On the other hand, when there were many people present, the model was able to handle the extra heat without a significant drop in energy efficiency. Our adaptive approach was found to have advantages over existing HVAC control methods in comparative studies. Our concept differs from standard fuzzy logic or ANN-based systems by including real-time feedback and predictive capabilities, resulting in improved fault tolerance and scalability. This feature renders it especially well-suited for dynamic and densely populated areas. this work represents a notable advancement in the progress of creating environmentally friendly and highly efficient HVAC systems. Our concept promotes global sustainability goals and offers a strong foundation for future HVAC advances by minimizing energy waste and enhancing indoor environmental quality. This research has the potential to provide valuable insights for policy makers and contribute to the creation of new construction standards that focus on environmental sustainability.

References

- [1] A. Adegbenro, M. Short, and C. Angione, "An integrated approach to adaptive control and supervisory optimisation of hvac control systems for demand response applications," *Energies*, vol. 14, no. 8, 2021, doi: 10.3390/en14082078.
- [2] X. Kou et al., "Model-based and data-driven HVAC control strategies for residential demand response," *IEEE Open Access J. Power Energy*, vol. 8, pp. 186–197, 2021, doi: 10.1109/OAJPE.2021.3075426.
- [3] A. Mishra, S. Ram, and B. P. Singh, "Indoor Environment Quality and Energy Performance of Air-conditioned Buildings: A Critical Review," *Energy and Buildings*, vol. 160, pp. 107-130, 2018. [Online]. Available: <https://doi.org/10.1016/j.enbuild.2017.11.077>
- [4] H. Zhang, "Human Thermal Comfort and the HVAC System," *Procedia Engineering*, vol. 121, pp. 136-142, 2015. [Online]. Available: <https://doi.org/10.1016/j.proeng.2015.08.1089>
- [5] T. Hong, S. C. Taylor-Lange, D. D'Oca, W. J. N. Turner, and C. F. R. Corgnati, "Advances in Research and Applications of Energy-Related Occupant Behavior in Buildings," *Energy and Buildings*, vol. 116, pp. 694-702, 2016. [Online]. Available: <https://doi.org/10.1016/j.enbuild.2015.11.052>
- [6] M. F. Abdeen, M. A. M. Rasheed, and S. M. S. Ismail, "A Review on Building Energy Management System: Artificial Intelligence-based Methodologies and Techniques," *Energy and Buildings*, vol. 235, 110647, 2021. [Online]. Available: <https://doi.org/10.1016/j.enbuild.2021.110647>
- [7] H. Lund, B. V. Mathiesen, D. Connolly, and P. A. Østergaard, "Smart Energy and Smart Energy Systems," *energy*, vol. 137, pp. 556-565, 2017. [Online]. Available: <https://doi.org/10.1016/j.energy.2017.05.123>
- [8] International Energy Agency (IEA), "World Energy Outlook 2020," IEA, Paris, 2020.
- [9] A. Chandrakasan, S. Sheng, and R. W. Brodersen, "Low-power CMOS digital design," *IEEE Journal of Solid-State Circuits*, vol. 27, no. 4, pp. 473-484, Apr. 1992.
- [10] M. Pedram and Q. Wu, "Design Technologies for Energy-Efficient Computer Systems," *Proceedings of the IEEE*, vol. 107, no. 7, pp. 1281-1300, July 2019.
- [11] C. Schillaci, Jones, A., Vieira, D., Munafò, M., & Montanarella, L. (2023). Evaluation of the United Nations Sustainable Development Goal 15.3. 1 indicator of land degradation in the European Union. *Land Degradation & Development*, 34(1), 250-268.
- [12] E. M. El-Kholy, S. M. Ahmed, and M. A. El-Sayed. "Design and implementation of a motion sensor-based air conditioning control system" In 2017 IEEE International Conference on Electro/Information Technology (EIT), pp. 152-157.
- [13] J. H. Kim, J. H. Cha, and S. H. Kim. "Smart air conditioning control based on human presence detection using infrared sensors" In 2015 IEEE International Conference on Consumer Electronics (ICCE), pp. 409-410.
- [14] H. Vahidi, M. R. Jahed-Motlagh, "A fuzzy logic-based air conditioning control system for energy efficiency improvement," *Energy and Buildings*, vol. 42, no. 11, pp. 2037-2044, 2010.

- [15] A. A. El-Sebakhy, M. A. El-Shorbagy, and M. M. Osman, "Artificial neural network based air conditioning control system for energy efficiency improvement," *Energy and Buildings*, vol. 43, no. 9, pp. 2202-2209, 2011.
- [16] J. Chen, S. Li, and Q. Zhang, "Model predictive control-based air conditioning control system for energy efficiency improvement," *Energy and Buildings*, vol. 119, pp. 57-65, 2016.
- [17] Y. Zhang et al., "Reinforcement learning-based air conditioning control for energy efficiency and user comfort," *Energy and Buildings*, vol. 190, pp. 22-32, 2019.
- [18] Z. Liu, X. Zhang, W. Cai and C. Cui, "An Adaptive Distributed Consensus Control for Air Balancing of HVAC Systems," *IECON 2020 The 46th Annual Conference of the IEEE Industrial Electronics Society*, Singapore, 2020, pp. 4794-4798, doi: 10.1109/IECON43393.2020.9255035.
- [19] W. Tumin, M. M. Olama and S. M. Djouadi, "Adaptive Control for Residential HVAC Systems to Support Grid Services," *2021 IEEE Power & Energy Society Innovative Smart Grid Technologies Conference (ISGT)*, Washington, DC, USA, 2021, pp. 01-05, doi: 10.1109/ISGT49243.2021.9372229.
- [20] C. Dai, Y. -z. Liu, H. -s. Sun, L. Jie and C. -q. Wang, "Research on Fault-tolerant Control for SRM Air Gap Eccentricity Fault," *2018 IEEE CSAA Guidance, Navigation and Control Conference (CGNCC)*, Xiamen, China, 2018, pp. 1-6, doi: 10.1109/GNCC42960.2018.9018954.
- [21] F. B. Islam, C. Ifeanyi Nwakanma, D.-S. Kim, and J.-M. Lee, "IoT-Based HVAC Monitoring System for Smart Factory," in *2020 International Conference on Information and Communication Technology Convergence (ICTC)*, Oct. 2020, pp. 701–704, doi: 10.1109/ICTC49870.2020.9289249.
- [22] Z., Chen, O'Neill, Z., Wen, J., Pradhan, O., Yang, T., Lu, X., ... & Herr, T. (2023). A review of data-driven fault detection and diagnostics for building HVAC systems. *Applied Energy*, 339, 121030.
- [23] G., Barone, Buonomano, A., Forzano, C., Giuzio, G. F., Palombo, A., & Russo, G. (2023). A new thermal comfort model based on physiological parameters for the smart design and control of energy-efficient HVAC systems. *Renewable and Sustainable Energy Reviews*, 173, 113015.
- [24] D., Zhuang, Gan, V. J., Tekler, Z. D., Chong, A., Tian, S., & Shi, X. (2023). Data-driven predictive control for smart HVAC system in IoT-integrated buildings with time-series forecasting and reinforcement learning. *Applied Energy*, 338, 120936.
- [25] P., Movahed, Taheri, S., & Razban, A. (2023). A bi-level data-driven framework for fault-detection and diagnosis of HVAC systems. *Applied Energy*, 339, 120948.

Vibration Assignment, B3pw91 Calculation and Conformational Analysis of Antimicrobial 5-Amino -3-(Methylthio)-1-(1,3,4-Thiadiazol -2-Yl)-1H-Pyrazole-4-Carbonitrile.

Medhat Mohamed El-Moselhy¹, Usama. A. Soliman^{1*}, H. G. Mohamedbagr¹, Mohamed S. Thabet¹, Mahmoud M. Abdelall², Ali M. Hassan²

¹Department of Physical Sciences, Chemistry Division, College of Science, Jazan University, P.O. Box. 114, Jazan 45142, Kingdom of Saudi Arabia

²Department of Chemistry, College of Science, Al-Azhar University (Men's Campus), Nasr City 11884, Cairo, Egypt.

Abstract: In this study, we conducted infrared spectroscopy measurements on solid 5-amino-3-(methylthio)-1-(1,3,4-thiadiazol-2-yl)-1H-pyrazole-4-carbonitrile (AMTDPC, C₇H₆N₆S₂). The spectra were obtained at a resolution of 4 cm⁻¹ and 0.5 cm⁻¹, within the spectrum region of 4000–200 cm⁻¹. Furthermore, the observation of NMR spectra for ¹H and ¹³C has been documented. Nine rotational isomerisms, consisting of nine Cs and one C1 symmetry, are postulated for the AMTDPC molecule due to internal rotation occurring around C–N and/or C–S bonds. The isomers are finally characterized by two conformers (1-2) with energies below 1000 cm⁻¹, as determined through quantum mechanical calculations utilizing RHF and DFT/B3PW91. Based on forecasts, conformer 1, which is the rotamer with the lowest energy and produces real frequencies, is expected to have a stability order of 1 > 2. The spectrum modeling provides complete support for Conformer 1, making it the preferred option based on the recorded infrared (IR), ¹H, and ¹³C spectral data. The chemical shifts at the B3PW91/6-31G level were successfully determined using the Polarizable Continuum Model (PCM) and the Gauge-Invariant Atomic Orbitals (GIAO) technique, regardless of the presence or absence of the solvent. The results of the NMR studies provided indications of both constrained and unconstrained internal rotation of NH₂ around C-N bonds. In order to propose a comprehensive and reliable vibrational assignment for each of the foundations of AMTDPC, potential energy distributions and normal coordinate analysis have been employed. Additionally, supplementary investigations were carried out to examine the torsional obstacles encountered during the internal rotation of the NH₂, CH₃, CH₃S, and thiadiazole ring. Based on spectrum measurements that exhibited a high level of concurrence with the anticipated values, it may be concluded that conformer 1 emerged as the isomer with the highest stability. Also there are small differences between the calculated bond distances and the x-ray readings for comprised compounds.

Keywords: Conformational durability, vibrational categorization, NMR profiles, standard coordinate assessment, obstacles to inner rotation, and computational estimations using DFT.

***Corresponding author:**

Assistant Professor, Department of Physical Sciences, Chemistry Division, College of Science, Jazan University, P.O. Box. 114, Jazan 45142, Kingdom of Saudi Arabia, Tel: +966-535092495; e-mail: usoliman@jazanu.edu.sa

تخصيص الاهتزاز، حساب B3PW91 وتحليل الهيكل لمضادات الميكروبات 5- أمينو-3-(ميثيلثيو)-1-(3،4)-ثياديازول-2-إيل)-1-H-بيرازول-4- كربونائتريل.

المخلص: تم قياس الطيف الأشعة تحت الحمراء للمركب الصلب 5-أمينو-3-(ميثيلثيو)-1-(3،4)-ثياديازول-2-إيل)-1-H-بيرازول-4-كربونائتريل (AMTDPC)، (C7H6N6S2) في نطاق الطيف من 4000 إلى 200 سم⁻¹ بدقة 4 و 0.5 سم⁻¹ على التوالي. وقد تم أيضاً تسجيل طيفي الرنين النووي المغناطيسي البروتوني (1H) والكربوني-13 (13C). نتيجة للدوران الداخلي حول روابط C-N و/أو C-S، تم اقتراح تسعة من الأيزومريات الدورية لجزيء (AMTDPC) بتناظر Cs وتناظر (C1) باستخدام حسابات الكم RHF و DFT/B3PW91، تم التوصل إلى وجود تلك الأيزومريات على شكل تآلفين (1-2) بطاقات طاقة أقل من 1000 سم⁻¹. تم التنبؤ بترتيب الاستقرار ليكون 1 > 2 > لصالح الكونفورمر 1، وهو الروتامر ذو الطاقة الأقل الذي ينتج ترددات حقيقية. تؤيد القياسات الطيفية المسجلة للأشعة تحت الحمراء والرنين النووي المغناطيسي البروتوني والكربوني-13 الكونفورمر 1، والذي يتم دعمه بشكل كامل من خلال المحاكاة الطيفية. تم الحصول على التحولات الكيميائية المتوقعة عند مستوى B3PW91/6-31G باستخدام طريقة الأوربتال الذرية غير المتأثرة بالمقياس (GIAO) مع وبدون استخدام نموذج الوسط المستمر القطبي (PCM). تم اكتشاف دلائل على دوران النيتروجين الداخلي الحر والمقيد حول روابط C-N من قياسات الرنين النووي المغناطيسي. باستخدام تحليل الإحداثيات الطبيعية وتوزيعات الطاقة الكامنة، تم اقتراح تخصيص اهتزازية كاملة ومؤكدة لجميع الأساسيات لجزيء AMTDPC. تمت إجراء دراسات مكملة حول حواجز الدوران الداخلي للحلقات CH3 و CH3S و NH2 و ثياديازول. استناداً إلى قياسات الطيف التي أظهرت مستوى عالياً من التطابق مع القيم المتوقعة، يمكن استنتاج أن المطابق 1 ظهر باعتباره الأيزومر ذو أعلى استقرار. كما توجد اختلافات بسيطة بين مسافات الروابط المحسوبة وقراءات الأشعة السينية للمركبات المقارنة.

الكلمات المفتاحية: استقرار الشكل، تخصيص اهتزازي، طيف الرنين النووي المغناطيسي، تحليل الإحداثيات الطبيعية، حواجز الدوران الداخلي، وحسابات DFT.

1. Introduction

Pyrazoles are frequently employed in the pharmaceutical industry for the synthesis of biologically active derivatives [1], [2], [3]. This approach has also been explored by other researchers [4], [5], [6], [7], [8]. [9], these compounds function as analgesics, anti-inflammatory agents, antibacterial agents, and antidepressants. A recent study conducted by [10] revealed that derivatives of aminopyrazoles exhibit potential in mitigating brain-protein aggregation, a critical early step in the progression of Alzheimer's disease. There is a scarcity of information regarding the vibrational spectra and configuration of substituted pyrazoles, particularly in relation to N-substituted pyrazoles [11]. [12], [13], [14].

Previous studies have examined the vibrational assignment of pyrazoles. The subject of this study, (AMTDPC, $C_7H_6N_6S_2$), exhibits several structural characteristics, such as linear $-C\equiv N$ (sp), planar $-NH_2$ (sp²), and tetrahedral $-CH_3$ (sp³) moieties, in addition to the pyrazole and thiadiazol rings. As far as we know, there has been no previous investigation into the structural stability, vibrational characteristics, ¹H and ¹³C NMR spectra, or obstacles to internal rotation for AMTDPC, either in theoretical or experimental studies. Furthermore, the molecular geometry and structural parameters (SPs) of AMTDPC have not been examined using any of the microwave, x-ray, electron, or neutron diffraction techniques. In the realm of vibrational spectroscopy, the significance of ab initio calculations, including Density Functional Theory (DFT) approaches and Restricted Hartree-Fock (RHF) calculations, has increased [10], [15], [16], [17], [18], [19]. In recent years, the utilization of DFT simulations using the B3PW91 method has gained recognition as a reliable approach for monitoring the molecular geometry and conformational stability of compounds of medium and large size, encompassing up to 26 atoms [20], [21], [22]. In addition, the utilization of GIAO NMR DFT-B3PW91 calculations has become prevalent in the field of interpreting chemical shifts of ¹H and ¹³C [23], [24], [25], [26], [27], [28], [29], [30], [31]. Hence, this study presents a comprehensive investigation into the vibrational assignments and structural stability of AMTDPC through the utilization of infrared (IR) and nuclear magnetic resonance (NMR) spectroscopy. Additionally, theoretical predictions based on B3PW91 are incorporated, encompassing base sets up to 6-311G(d) [15], [32], [18], [19]. In order to gain insight into the intricate conformational changes inside the molecule being investigated, potential surface scans (PSS) were performed on the CH₃, CH₃S, NH₂ groups, and thiadiazol ring. Our research on barriers to internal rotations of methyl and NH₂ [33], [34], [35] was enhanced by the inclusion of these investigations.

2. Experimental

The chemical substances used in this study were obtained from Aldrich Chemical Company, ensuring a minimum purity level of 98%. The materials employed in NMR and IR analysis exhibited spectroscopic characteristics. The solid sample was examined using the CsI pellet technique while IR dye was connected to a vacuum pump. The Fourier transform infrared spectrum (FT-IR) of the solid sample was recorded from 4000 to 200 cm^{-1} using a Spectrum 100 Perkin Elmer spectrophotometer equipped with Spectrum RX software. To obtain a satisfactory signal-to-noise ratio, forty scans were collected at 1.0 cm resolution with baseline correction and automatic smoothing features. In accordance with the methodology outlined by S.M. Hassan et al. [36]. The solid sample of AMTDPC was synthesized by Hassan et al. (2001) through the reaction of ketene with a hydrazine derivative. AMTDPC in DMSO- d_6 was analyzed using Top Spin 1.3 software and a Bruker Avance 400 MHz spectrometer fitted with a Magnex superconducting magnet to get the ^1H and ^{13}C NMR spectra (Figures 1 and 2). The material was first dissolved in methanol and then diluted in a 50/50 (v/v) acetonitrile/water solution in a serial manner. The samples were injected into the mass spectrometer using a Harvard syringe pump (Harvard, CA, USA) at a flow rate of 10 μL per minute.

3. Results and Discussion

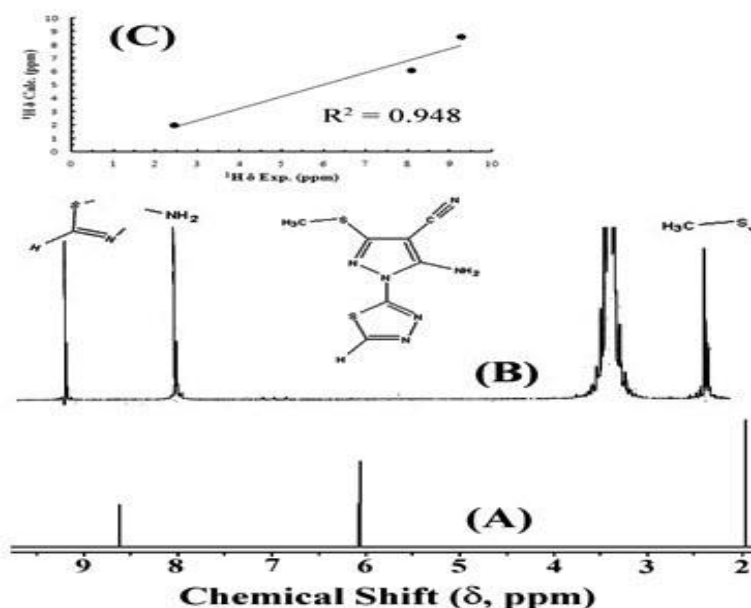


Figure 1: The ^1H NMR spectrum of AMTDPC, wherein the chemical shifts are recorded in parts per million (ppm). (A) The spectrum obtained for conformer 1 is computed using the GIAO method. (B) The experimental spectrum is presented, with peak assignments assigned to both spectra to highlight their differences.

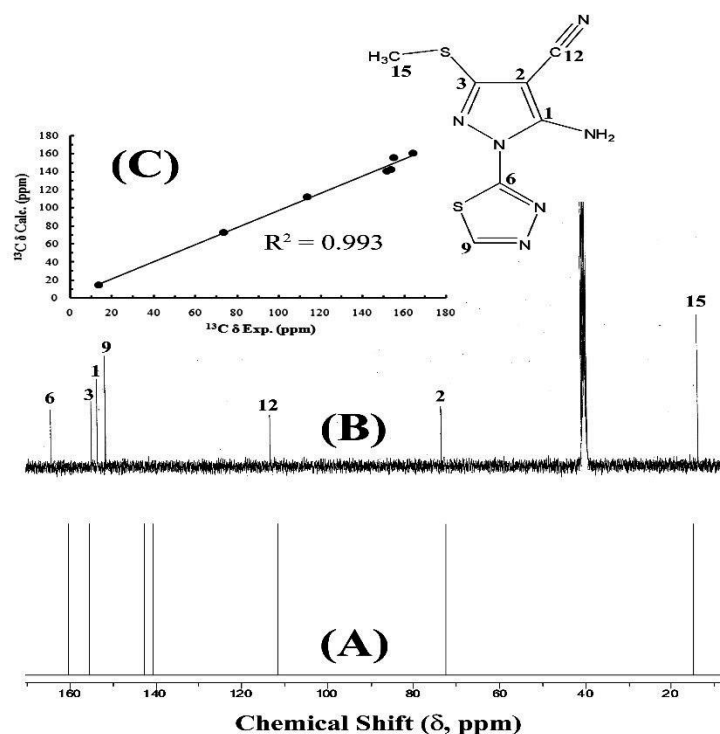


Figure 2: The ^{13}C NMR spectrum of AMTDPC, represented by chemical shifts measured in parts per million (ppm). (A) The spectrum obtained for conformer 1 using the GIAO method; (B) The experimental spectrum, with peak assignments given for both spectra to highlight their differences; (C) The correlation between the calculated (x-axis) and experimental peak positions.

3.1 *Ab initio* calculations

The Linear Combination Atomic Orbitals - Molecular Orbitals - Self Consistent Field (LCAO-MO-SCF) quantum mechanical Gaussian 09 computations were developed using the RHF and DFT methodologies [17]. Due to a lack of computer resources, frequency calculations were only conducted using B3PW91/6-31G(d) [15], [16], [18], [19], [32]

3.2 *Rotational isomerism*

The rotational isomerism of AMTDPC is relatively complex due to the presence of a thiadiazole ring and planar moieties CH_3 , CH_3S , and NH_2 connected by single bonds. These moieties have the ability to spin and generate a total of 9 possible isomers that adhere to the C_s and C_1 point group, as depicted in Figure 3. In conformer 1, the N_4 position of the pyrazole ring and the N_7 position of the thiadiazole ring are first connected in a trans configuration.

The methyl group undergoes a 180° rotation along the C₁₅–S₁₄, leading to the formation of planar NH₂ groups through sp² hybridization, resulting in Structure 2. The formation of Structure 3 involves a 180° rotation of the CH₃S moiety around the C₃–S₁₄, with CH₁₈ eclipsing the bond. The formation of Structure 4 involves a second rotation of the CH₃ group by 180° around C₃–S₁₄, where CH₁₈ is staggered in relation to the two lone pair electrons on sulfur. As a result, the internal rotation around the C₁₅–S₁₄ and/or C₃–S₁₄ bonds suggests the presence of four structures 1-4, wherein the N₇ of the thiadiazole ring and the N₄ of the pyrazole ring are in close proximity to each other. In each of these structures, the NH₂ group exhibits trigonal planar (sp²) symmetry. Structures 5-8 are formed when the N₄ and N₇ of the pyrazole and thiadiazole rings are connected in a cis configuration. Structure 9 has trigonal planar (sp²) symmetry in the NH₂ group, whereas the thiadiazole ring is oriented perpendicular to the plan.

3.3 Optimization and computational analysis of frequencies.

The gradient approach proposed by [37] is employed to concurrently facilitate the relaxation of all geometric parameters, with the ultimate goal of attaining the ideal structural parameters (SPs). The vibrational frequencies were subsequently quantified by employing computed spin perovskites (SPs) with 6-31G* basis sets, as well as the RHF and DFT-B3PW91 methodologies. The primary software utilized for doing the quantum mechanical (QM) calculations mentioned before [17], [32] was the Gaussian 09 program.

The results of the study indicated that conformer (1) displayed the minimum energy, whereas conformer (2) exhibited the maximum energy, reaching up to 1500 cm⁻¹. Notably, conformer 1, which exhibits the lowest energy structure with a trigonal planar NH₂ group and trans to each other N₇ of the thiadiazole ring and N₄ of the pyrazole ring, yielded all 57 real frequencies during full optimization. This observation suggests that the AMTDPC structure is entirely planar. The expected surface areas (SPs) for conformer 1 are compared with x-ray data for substituted pyrazoles [38] to offer contextual information. Refer to Figure 3, as well as Tables 1 and 2)

TABLE (1) RHF energies in Hartrees of AMTDPC conformers 1-9.

6-31G(d) basi set	RHF level	ΔE^b (cm ⁻¹)	ΔE^b (kcal/mol)
Structure-1	-1390.2192908	0.0	0.0
Structure-2	-1390.2160118	720	2.1
Structure-3	-1390.2091144	2234	6.4
Structure-4	-1390.2089367	2272	6.5
Structure-5	-1390.1937991	5595	16.0
Structure-6	-1390.1908846	6234	17.8
Structure-7	-1390.1868164	7127	20.4
Structure-8	-1390.1817386	8242	23.6
Structure-9	-1390.200491	4126	11.8

^aΔE denotes the disparity in energy between conformer 1 (minimum energy) and conformers 2-9 at the RHF level.

TABLE (2) B3PW91 and RHF structural parameters^a for AMTDPC utilizing 6-31G(d) basis sets.

Parameters	Ref [46]	<u>RHF for Structure(I)</u>	<u>B3PW91 for Structure(I)</u>
		6-31G(d)	6-31G(d)
r(C ₁ C ₂)	1.379 (9)	1.383	1.397
r(C ₂ C ₃)	1.405 (5)	1.428	1.434
r(C ₃ N ₄)	1.305 (5)	1.288	1.317
r(N ₄ N ₅)	1.388(5)	1.379	1.383
r(N ₅ C ₁)	1.348 (5)	1.356	1.374
r(N ₅ C ₆)		1.373	1.372
r(C ₁ N ₁₁)	1.358 (4)	1.331	1.340
r(C ₂ C ₁₂)	1.408 (7)	1.419	1.408
r(C ₁₂ N ₁₃)	1.139 (7)	1.139	1.166
r(C ₅ S ₁₄)		1.751	1.754
r(S ₁₄ C ₁₅)		1.810	1.814
r(C ₆ N ₇)		1.275	1.308
r(N ₇ N ₈)		1.365	1.362
r(N ₈ C ₉)		1.268	1.296
r(C ₉ S ₁₀)		1.735	1.743
r(S ₁₀ C ₆)		1.730	1.737
r(C ₉ H ₂₁)		1.071	1.083
r(N ₁₁ H ₁₆)		0.997	1.008
r(N ₁₁ H ₁₇)		0.994	1.016
r(C ₁₅ H ₁₈)		1.082	1.093
r(C ₁₅ H ₁₉)		1.080	1.092
r(C ₁₅ H ₂₀)		1.080	1.092
r(N ₇ ...H ₁₆)		2.158	2.058
r(N ₄ ...H ₂₀)		2.803	2.775
∠(C ₁ C ₂ C ₃)		104.9	104.8
∠(C ₂ C ₃ N ₄)	112.2 (4)	112.0	112.4
∠(C ₃ N ₄ N ₅)	104.4 (3)	105.1	104.4
∠(N ₄ N ₅ C ₁)	111.8 (3)	112.3	112.8
∠(N ₅ C ₁ C ₂)	106.2 (3)	105.7	105.8
∠(N ₅ C ₆ N ₇)		123.6	123.4
∠(N ₅ C ₆ S ₁₀)		121.5	121.6
∠(C ₆ N ₇ N ₈)		112.5	112.2
∠(N ₇ N ₈ C ₉)		112.6	112.4
∠(N ₈ N ₉ S ₁₀)		115.0	115.3
∠(C ₉ S ₁₀ C ₆)		85.0	85.0
∠(N ₈ C ₉ H ₂₁)		122.8	123.0
∠(S ₁₀ C ₉ H ₂₁)		122.2	121.7
∠(C ₆ N ₅ C ₁)	129.4 (3)	128.7	127.5
∠(C ₆ N ₅ N ₄)	118.7 (3)	119.1	119.6
∠(C ₁ N ₁₁ H ₁₆)		120.4	119.0
∠(C ₁ N ₁₁ H ₁₇)		119.3	119.5

$\angle(\text{H}_{16}\text{N}_{11}\text{H}_{17})$		120.3	121.5
$\angle(\text{N}_{11}\text{C}_1\text{C}_2)$	130.5 (3)	130.3	131.4
$\angle(\text{N}_{11}\text{C}_1\text{C}_5)$	123.2 (3)	124.0	123.0
$\angle(\text{C}_{12}\text{C}_2\text{C}_1)$	127.3 (4)	125.3	125.3
$\angle(\text{C}_{12}\text{C}_2\text{C}_3)$	127.4 (4)	129.8	129.9
$\angle(\text{N}_{13}\text{C}_{12}\text{C}_2)$	179.6 (6)	177.8	178.0
$\angle(\text{C}_2\text{C}_{15}\text{S}_{14})$		124.6	124.4
$\angle(\text{S}_{14}\text{C}_3\text{N}_4)$		123.4	123.1
$\angle(\text{C}_3\text{S}_{14}\text{C}_{15})$		100.8	100.1
$\angle(\text{H}_{18}\text{C}_{15}\text{S}_{14})$		105.9	105.9
$\angle(\text{H}_{19}\text{C}_{15}\text{S}_{14})$		110.8	110.8
$\angle(\text{H}_{20}\text{C}_{15}\text{S}_{14})$		110.8	110.8
$\angle(\text{H}_{18}\text{C}_{15}\text{H}_{19})$		109.7	109.8
$\angle(\text{H}_{18}\text{C}_{15}\text{H}_{20})$		109.7	109.8
$\angle(\text{H}_{19}\text{C}_{15}\text{H}_{20})$		109.9	109.7
$\tau\text{C}_3\text{S}_{10}\text{C}_{11}\text{H}_{22}$		61.1	61.0
A, MHz		817	814
B, MHz		343	339
C, MHz		242	240
μ_{tot} , Debye		5.574	5.173

^a Bond distances are expressed in angstroms (Å), while bond and dihedral angles are denoted in degrees. Rotational constants A, B, and C are measured in megahertz (MHz), and the total dipole moment (μ_{tot}) is quantified in Debye

3.5 Structural parameters

The C-N distances for C₁-N₁₁ and C₆-N₅ are approximately 0.03-0.09 Å shorter than those reported for AP (1.429 Å), ATP (1.370 Å), and adenine (1.357 Å) (Mohamed et al., 2008, 2009; Soliman et al., 2007). The calculated SPs (refer to Table 2) for AMTDPC highlight the double-bond nature of these bonds (see atom numbering in Figure 7). Furthermore, it is anticipated that the distances between C₆-N₅ and C₁-N₅ will be shorter than those between C₁-N₁₁ by approximately 0.043 Å, suggesting a greater level of double-bond nature for C₆-N₅ and C₁-N₅ in comparison to C₁-N₁₁. The aforementioned projection is consistent with the calculated rotational barriers of NH₂, the detection of distinct N-H bonds based on NMR findings, and the observed stretching bands of NH₂. The following sections will explore these findings in greater detail.

In contrast to 2-aminophenol (2AP) and 2-aminothiophenol (2ATP), the SPs for AMTDPC exhibit a preference for trigonal planar (sp^2 ; NH_2) NH_2 groups rather than trigonal pyramidal (sp^3 ; NH_2) NH_2 groups. It is worth mentioning that the angles of $N_5C_1C_2$ and $C_{12}C_2C_1$ are estimated to fall within a range of 0.4-2.5 Å when compared to the values derived from x-ray crystallographic data [38], [39], [40]. On the other hand, there are small differences (0.01-0.04 Å) between the calculated bond distances and the x-ray readings. The x-ray crystallographic data of 3-amino-4,5-dicyano-1-methylpyrazole [38]

and 5-amino-4-cyano-1-phenylpyrazole (Zukerman-Schpector et al., 1994) reveal variations in bond lengths and bond angles, with values ranging from 0.3-5.0% and 2.0-4.0%, respectively.

The N...H bond lengths for AMTDPC have been calculated to range from 2.06 to 2.80 Å, with the combined Van der Waal radii of the hydrogen and nitrogen atoms being 2.75 Å [41], [42]. Therefore, in addition to the anticipated intermolecular hydrogen interactions in AMTDPC, it is expected that there would be moderate intramolecular hydrogen bonding interactions between N7...H16 and N4...H20, as seen in Table 2.

3.6. Simulated infrared Spectra

The projected intertwining of the predicted infrared (IR) normal modes is expected to exhibit a reasonably high amount of interaction, particularly for bigger molecules. As a result, the utilization of projected infrared spectra has been proposed by [20], [43] as a valuable method for conducting vibrational studies on organic molecules. Simulated vibrational spectra can be generated by utilizing both infrared (IR) intensities and Raman activity, along with their polarizability and dipole moment derivatives.

The frequencies and infrared intensities of the single conformer (1) were simulated using the B3PW91 density functional theory (DFT) approach, in conjunction with a 6-31G(d) basis set. The IR spectrum seen in Figure 4 was constructed using the dipole moment derivatives, as described in the entire technique outlined in Reference [44]. The agreement between the estimated and observed frequencies, as shown in Table 3, provides strong support for the vibrational assignments. Nevertheless, the calculated infrared (IR) intensities denoted as w, m, and s below 1000 cm^{-1} do not correspond with the solid's IR spectrum, which exhibits strong to extremely strong intensities.

In spite of the significant spectral overlap observed in the recorded infrared (IR) spectrum, it is worth mentioning that the projected IR intensities exhibited superior performance compared to the anticipated Raman activity inside the CH stretching region.

3.7 Simulated NMR spectra

Previous studies have shown that chemical shifts (δ , ppm) for small isolated molecules can be accurately predicted using DFT NMR calculations with the Gauge-invariant atomic orbitals (GIAO) model [15], [24], [29], [30], [31]. In recent years, there has been an increase in the popularity of these calculations [27]. The preference for DFT predictions over the RHF technique has been shown in certain studies [30], [45]. However, it is crucial to note that the accuracy of NMR theoretical predictions is primarily influenced by two key factors: the optimized structural parameters and the implemented basis set. The simulated spectra were computed using the B3LYP/6-31G(d) structural parameters for conformer 1 in this particular instance. Chemical shifts were predicted at the B3LYP/6-311+G(2d,p) level using the Gauge-invariant atomic orbitals (GIAO) method, as described by Chesnut and Phung in 1989. These predictions were then compared to the calculated chemical shifts obtained through the use of the same technology, namely TMS. The GIAO calculations were conducted using the Polarizable Continuum Model (PCM) implicit solvation approach [46], [47], considering both the solvent's impact and not. The NMR prediction also incorporated the solvent. The results presented in Figures 1 and 2 pertain to individuals who employed the phase change material (PCM) due to its observed ability to improve the concordance between experimental and calculated outcomes.

4. Vibrational assignments

In the infrared and Raman spectra of AMTDPC, fifty-seven fundamentals are anticipated, and all of them are Raman and IR active. In addition to the $\nu_{C\equiv N}$ stretch around 2300 cm^{-1} , six vibrations were anticipated in the high frequency region 2900-3500 cm^{-1} (ν_{1-5} and ν_{39}). Below 200 cm^{-1} , which is beyond the range of our instrumental detection capabilities, nine fundamentals are expected. As a result, 41 bands between 1700 and 200 cm^{-1} had to be assigned. Vibrational assignments were compounded by the vast number of basics and occasionally the substantial mixing. The infrared frequencies presented in the subsequent sections are extracted from the solid sample's spectrum within a CsI matrix, as seen in Table 3.

4.1 NH_2 Fundamentals vibrations.

Hydrogen bonding interactions do not appear to significantly alter or affect the N-H stretching fundamentals. The recorded infrared spectrum exhibits distinct and well-defined bands, consistent with the estimated infrared intensity (Figure 4). The infrared (IR) bands seen at 3376 and 3295 cm^{-1} (ν_s) were confirmed to correspond to two distinct stretching modes of NH_2 , namely ν_1 and ν_2 . The measured stretching modes of NH are shifted towards lower frequencies by approximately 200 cm^{-1} as a result of inter- and intramolecular hydrogen bonding. Furthermore, the empirical relationship of $\nu_s = 345.5 + 0.876 \nu_{as}$ [48], where s and as are in wavenumbers, is not followed by the ν_s and ν_{as} NH_2 stretches. This finding implies that the amino groups' N-H bonds are not interchangeable.

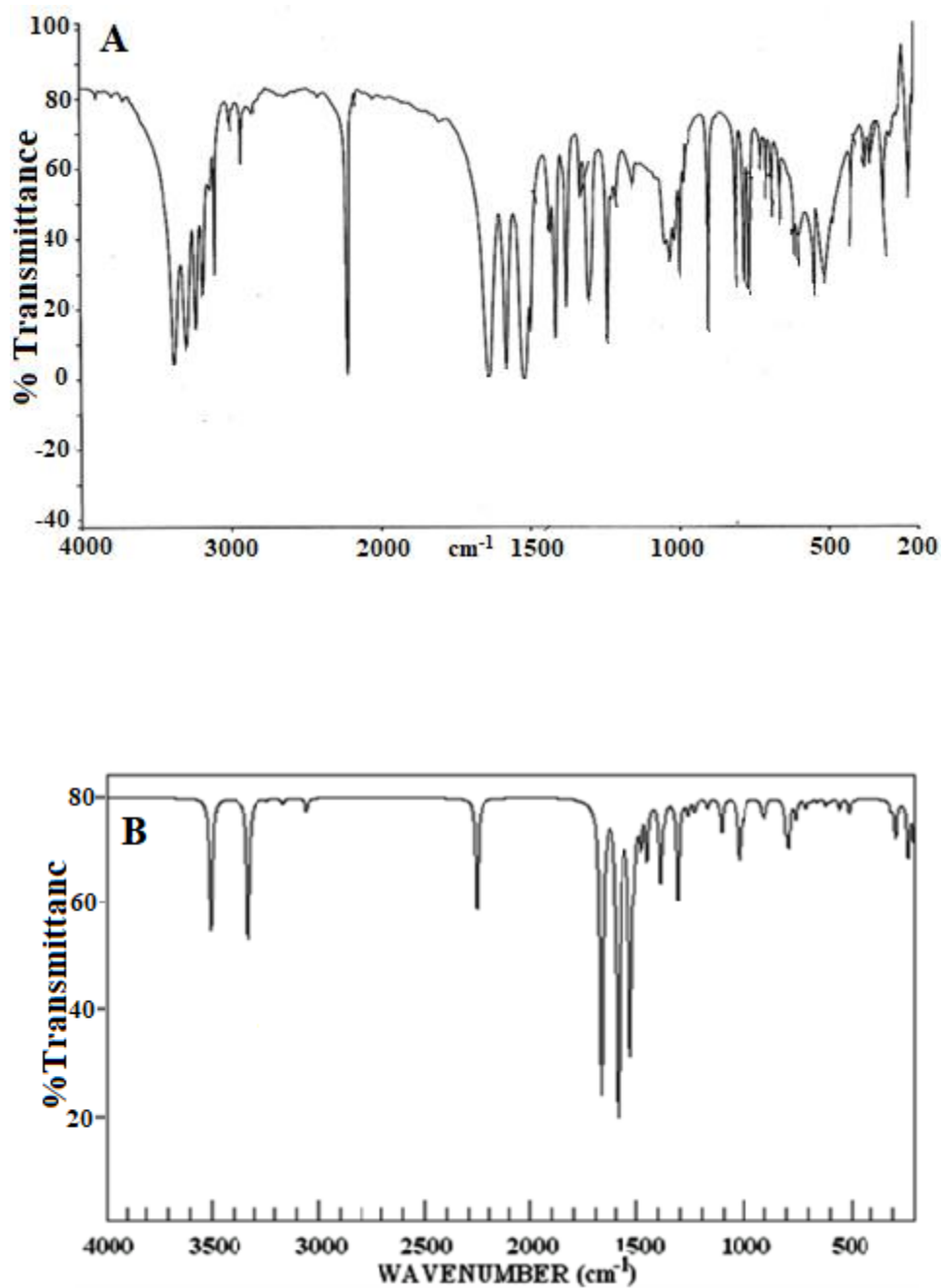


Figure 4: Experimental (A) and Calculated (B) Infrared spectrum of AMTDPC.

Table 3: B3PW91/6-31G(d) calculated and observed frequencies for AMTDPC.

Species	Calculated				Observed	Assignment
	Unscaled	Scaled	IR Int.	Raman act.	IR	
A'	3717	3508	126.6	54.4	3376 vs	ν_{as} NH ₂
A'	3526	3330	136.7	100.2	3295 vs	ν_s NH ₂
A'	3277	3240	1.5	192.9	3231 s	ν C ₉ H ₂₁ (Thiadiazole ring)

A'	3190	3165	2.8	96.2	3184s	ν_{as} CH ₃
A'	3088	3055	10.9	128.0	3105 w	ν_s CH ₃
A'	2342	2260	102.9	385.6	2218 vs	ν C \equiv N
A'	1703	1675	417.7	9.1	1637 s	$\delta_{scissor}$ NH ₂
A'	1625	1590	487.1	102.6	1577 s	ν CC (Pyrazole ring)
A'	1573	1530	306.0	435.7	1517s	ν N ₅ C ₆ (bridge)
A'	1557	1510	40.2	18.1	1496m	ν CN (Pyrazole ring)
A'	1507	1498	5.8	32.4	1490 sh	ν CN (Thiadiazole ring)
A'	1499	1480	30.8	5.2	1472 w	δ_{as} CH ₃
A'	1471	1452	36.1	95.8	1412 s	ν CN (Pyrazole ring)
A'	1421	1390	70.4	15.0	1388 wsh	δ_s CH ₃ (Umbrella mode)
A'	1384	1370	11.0	15.1	1375 s	ν C—N
A'	1336	1310	90.3	41.9	1329 w	ν CC (Pyrazole ring)
A'	1280	1265	12.1	72.8	1301m	δ_{ip} C ₉ H ₂₁ (Thiadiazole ring)
A'	1249	1233	11.1	16.0	1238 s	ν C ₂ C ₁₂ (exocyclic C—C)
A'	1207	1175	7.1	31.5	1152 w	ν N—N (Pyrazole ring)
A'	1111	1111	28.1	5.8	1081 w	ν N—N (Thiadiazole ring)
A'	1054	1025	14.8	0.3	1046 wsh	ρ NH ₂
A'	1032	1019	41.3	8.3	1028 wsh	ν C ₃ S ₁₄ (exocyclic C—S)
A'	1012	1000	8.4	8.1	1013 wsh	δ_{as} CH ₃
A'	912	900	15.3	22.8	900 vs	δ_{ip} NNC (Thiadiazole ring)
A'	799	788	36.4	26.3	779 m	Ring breathing (Pyrazole ring)
A'	765	755	16.0	4.3	763 m	ν C—S (Thiadiazole ring)
A'	733	720	0.9	7.4	722 w	ν S ₁₄ —C ₁₅ (S—CH ₃)
A'	697	688	2.4	2.8	686 w	Ring breathing (Thiadiazole ring)
A'	672	660	2.6	8.3	659 w	δ_{ip} C ₂ C ₁₂ (exocyclic C—C)
A'	617	600	2.9	13.9	598 w	δ_{ip} CSC (Thiadiazole ring)
A'	483	477	1.8	2.0	482 wsh	δ_{ip} C—C \equiv N
A'	424	420	0.7	2.8	419 w	δ_{ip} (Pyrazole ring)
A'	361	355	0.4	1.6	357 w	δ_{ip} N ₅ C ₆ (bridge)
A'	306	305	7.7	6.1	312 m	δ_{ip} C ₃ —S ₁₄ —C ₁₅ (C—S—CH ₃)
A'	287	287	9.5	1.3	264 w	δ_{ip} C ₁ —N ₁₁ (C—NH ₂)
A'	196	196	18.2	2.4	211 wsh	δ_{ip} N ₅ C ₆ S ₁₀ + δ_{ip} N ₄ C ₃ S ₁₄
A'	100	100	1.5	5.9	—	δ_{ip} C \equiv N
A'	95	95	2.9	0.8	—	δ_{ip} (Pyrazole ring)
A''	3189	3159	2.5	36.0	3120 w	ν_{as} CH ₃
A''	1483	1450	11.4	22.1	1430 w	δ_{as} CH ₃
A''	998	998	5.2	4.7	995 m	ρ CH ₃
A''	801	801	21.6	1.7	807 m	δ_{wag} C ₉ H ₂₁ (Thiadiazole ring)
A''	723	710	6.8	1.1	705 w	Pyrazole ring Torsion
A''	639	619	5.3	0.4	616 vw	Pyrazole ring Torsion
A''	625	910	5.6	0.3	611 wsh	Thiadiazole ring Torsion
A''	577	557	8.7	0.6	544 m	δ_{twist} NH ₂
A''	549	519	0.1	0.3	(509 wbr)	Thiadiazole ring Torsion
A''	528	511	12.7	5.5	(509 wbr)	δ_{wag} C ₂ C ₁₂ (exocyclic C—C)
A''	376	376	0.2	0.1	373 w	Pyrazole ring Torsion
A''	281	281	25.8	0.7	289 w	Ring Torsion
A''	225	225	44.7	2.5	227 m	Ring Torsion (Butter fly)
A''	182	182	163.5	0.02	—	δ_{wagg} NH ₂
A''	154	154	2.0	0.4	—	CH ₃ Torsion
A''	114	114	0.5	0.4	—	NH ₂ Torsion
A''	61	61	0.1	0.04	—	δ_{wagg} S ₁₄ —C ₁₅ (S—CH ₃)
A''	45	45	0.1	0.4	—	Ring Torsion
A''	35	35	8.5	0.5	—	Ring Torsion

Based on the findings of Jesson

(1958), Soliman et al. (2007), Mohamed et al. (2008), and Mohamed et al. (2009), it has been observed that the NH₂ scissoring frequency falls within the spectral range of 1950-1650 cm⁻¹. According to Table 3, there are two predicted bending modes of A' NH₂ at 1703 (ν_7) and 1054 (ν_{21}) cm⁻¹. Therefore, the unscaled NH₂ scissor mode, κ_7 at 1703 cm⁻¹, aligns with the previously documented highly intense infrared bands observed at 1637 cm⁻¹ [34], [35], [49]. On the other hand, the NH₂ rock (ν_{21}) is associated with the faint infrared band detected at 1046 cm⁻¹ (predicted at 1054 cm⁻¹).

4.2 CH and CH₃ fundamental vibrations

The C₉-H₂₁ stretching of the thiadiazole ring is associated with the conspicuous infrared band observed at 3231(ν_3), which is calculated to be 3240 cm⁻¹. In addition, the C-H bending mode (ν_{17}), which is calculated at a wavenumber of 1280 cm⁻¹, is associated with the medium-infrared band found at 1301.

The weak band at 3105 cm⁻¹ fit the A' stretch species (ν_5), while the two methyl C- stretches (A' and A'') are attributed to the detected IR bands at 3184 (ν_4) and 3120 (ν_{39}) cm⁻¹, respectively. Between 980 and 1500 cm⁻¹ there are predicted to be five vibrational modes (CH₃ bending and rocking) (3A'; ν_{12} , ν_{14} and ν_{23} and 2A''; ν_{40} and ν_{41}). As a result, the IR bands that are detected at 1472 and 1430 cm⁻¹ are attributed to ν_{12} and ν_{40} , which are 42 cm⁻¹ apart (estimated at 1499 and 1483 cm⁻¹), respectively.

Furthermore, the measured shoulders at 1388 cm⁻¹ in the IR spectrum are consistent with the umbrella modes (ν_{14}). While the second methyl rock (ν_{23}) was attributed to the measured IR band at 1013 cm⁻¹ reported earlier at 1013 cm⁻¹, the first methyl rock (ρ CH₃; ν_{41}) is predicted/seen at 998/995 cm⁻¹ in the IR spectra [49]. It was attributed to the faint Calc IR at 154 cm⁻¹ due to the methyl torsion mode's extremely low IR intensity (ν_{53}). However, due to the Rayleigh scattering background below 100 cm⁻¹, the CH₃S torsion (ν_{55}) was not visible (Figure 4).

4.3 Heavy atom stretching fundamentals

The C \equiv N bond (ν_6) exhibited a direct correlation with the highly intense infrared band seen at 2218 cm⁻¹. The C=C stretch (ν_8) is observed at a wavenumber of 1577 (s, IR) cm⁻¹, which aligns well with the calculated infrared intensity of 487.1 kcal/mol. The presence of a prominent infrared band at 1517 cm⁻¹ can be ascribed to the C \equiv N (ν_9) group of the pyrazole ring, as evidenced by the substantial intermixing of the three C \equiv N stretching vibrations (ν_9 , ν_{10} , and ν_{11}). This corresponds to the infrared intensity band at 1573 cm⁻¹, which has been determined to be high.

In addition, the calculated infrared intensities of the three C≡N stretching modes (ν_{13} , ν_{15} , and ν_{24}) exhibit a rather moderate level of intensity, which contradicts the observed bands. These modes can be considered as being inherently mixed. These C were allocated to the identified infrared bands at 1412 (s), 1375 (s), and 900 (vs) cm^{-1} .

The C₂–C₃ (ν_{16}) and C₂–C₁₂ (ν_{18}) segments in the infrared spectrum were predicted to have high and low intensities, respectively. The infrared bands at 1329/1336 and 1238/1249 cm^{-1} were assigned to (ν_{16}) and (ν_{18}) respectively, within the spectral range of N-methylpyrazole, as determined by Orza et al. (1997). Moreover, it is expected that $\nu_{\text{N-N}}$ (ν_{19} and ν_{20}) will either be prohibited or significantly diminished in the infrared spectrum. Consequently, when comparing the medium band observed at 1056 cm^{-1} with the weak infrared (IR) bands discovered at 1152 and 1081 cm^{-1} , respectively, it is possible that these bands correspond to the $\nu_{\text{N-N}}$ stretches, as suggested by Durig et al. (1992).

The AMTDPC molecule consists of two rings, namely pyrazole and thiadiazole. These rings enable the observation of the A' ring bending modes (ν_{28} and ν_{30}) in the infrared (IR) spectra at approximately 686 and 598 cm^{-1} , respectively. In contrast, the IR spectra at 419(w) cm^{-1} and out of ray light revealed the other two ring bending modes (ν_{32} and ν_{38}), respectively.

Due to the expected occurrence of the out-of-plane ring bending modes (ν_{56} and ν_{57}) below 100 cm^{-1} , they cannot be observed experimentally. According to the computed frequencies, the C₆S₁₀ (25 cm^{-1}) and C₉S₁₀ (26 cm^{-1}) segments were found to be separated by 34 cm^{-1} . This separation aligns with the observed infrared bands at 779 cm^{-1} and 763 cm^{-1} , respectively. Similarly, the infrared (IR) bands detected at 1028/1032 cm^{-1} and 722/733 cm^{-1} were assigned to the C₃S₁₄ (ν_{22}) and C₁₅S₁₄ (ν_{27}) strains, respectively. The δ_{ip} C–S (ν_{35}) could potentially be linked to CCS bending, as evidenced by the presence of a poorly resolved weak at 312 cm^{-1} (estimated at 306 cm^{-1}) in the infrared spectra.

5. NMR spectral interpretations

The simulated and experimental ¹H and ¹³C NMR spectra showed a remarkably high level of agreement, as shown in Figures 1 and 2. This confirms the established structural properties of AMTDPC's conformer 1. According to the prediction made by Chesnut and Phung in 1989, the signal observed at 1.96 ppm is attributed to three protons belonging to the CH₃ group, which are located at 2.44 ppm. This is achieved by calculating the average chemical shifts of similar hydrogen atoms. The GIAO prediction also yields positive signals for NH₂ protons. The measured spectrum has a wide singlet peak at 8.09 ppm, which corresponds to two protons of the NH₂ group. These protons are estimated to be located at 6.06 ppm. The singlet observed at 9.26 ppm can be attributed to the CH proton of the thiadiazole ring, which was determined to be 8.61 ppm.

6. Barriers to internal rotation.

Figure 1C demonstrates a robust correlation between the theoretical and experimental chemical changes, as evidenced by the high R2 value of 0.948. Moreover, the correlation between the theoretical and experimental chemical shifts resulting from the ^{13}C NMR GIAO prediction is clearly demonstrated in Figure 2C, where R2 is equivalent to 0.993 (Chesnut and Phung 1989). The signals seen at 164.43, 155.09, 153.72, and 151.8 ppm were assigned to the carbons C6, C3, C1, and C9, respectively, as indicated in Tables 4, 5, and Figure 2. Furthermore, the observed signals at 113.64, 73.72, and 13.70 ppm were ascribed to the remaining three carbon atoms, namely C12, C2, and C15. The obtained results exhibit a high level of concurrence with the computed values depicted in Figure 2. The restricted photosystem simulations (PSS) were performed using the optimized spin perovskites (SPs) of conformer 1, which were computed at the B3LYP/6-31G(d) level. The critical structure for internal rotations around C is believed to be Conformer 1, which is considered the global minimum for internal rotations around CS, CN, and CC single bonds. After rotating the CH_3 , CH_3S , NH_2 groups, and thiadiazole ring, conformer 1's symmetry shifts from Cs to C1, where the methyl hydrogens are no longer equal. As a result, neither the NH_2 moiety nor the methyl group are longer C_2V symmetry rotors.

Table 4 Theoretical and experimental ^1H NMR chemical shift values expressed in parts per million (ppm) for AMTDPC.

	Chem draw	DFT, B3PW91/6-311G(d)		Experimental (DMSO- d_6)
		Without solvent	With solvent (DMSO- d_6)	
H ₁₆	6.51	5.36	6.06	8.09
H ₁₇	6.51	5.36	6.06	8.09
H ₁₈	2.53	1.7	1.96	2.44
H ₁₉	2.53	1.7	1.96	2.44
H ₂₀	2.53	1.7	1.96	2.44
H ₂₁	9.00	7.56	8.61	9.26

Table 5 Theoretical and experimental ^{13}C NMR chemical shift values expressed in parts per million (ppm) for AMTDPC.

	Chem draw	DFT, B3PW91/6-311G(d)		Experimental (CDCl ₃)
		Without solvent	With solvent (CDCl ₃)	
C ₁	159.0	139.75	142.6	153.72
C ₂	92	70.28	72.47	73.72
C ₃	132	151.14	155.43	155.09
C ₆	162.7	156.84	160.42	164.43
C ₉	152.1	137.99	140.79	151.80
C ₁₂	117.0	98.51	111.81	113.64
C ₁₅	12.8	13.45	14.76	13.70

6.1 CH₃ Barriers to internal rotation

Conformer 1 from Table 2 SPs was used to create the PSS curve shown in Figure 5, as stated earlier. When the dihedral angle (H₁₈C₁₅S₁₄C₃) is rotated in 10° increments, the estimated energy of conformer 1 in B3LYP/6-31G(d) increases until it reaches its maximum value at 60-70° (2). The energy barrier for conformer 1 is 643 cm⁻¹. The emergence of Structure 1' occurs at around 120-130 degrees as the dihedral angle undergoes further rotation. The structure of 1' (C1) closely matches that of 1 (Cs), with the exception of the non-equivalence of the out-of-plane hydrogens (H₁₈ and H₁₉). A 356 cm⁻¹ barrier is located between 1' and 2. Following the complete optimization of structure 2 and structure 1, calculations were performed to determine the energies and harmonic vibrational frequencies. In both instances, the presence of an imaginary frequency signifies the occurrence of transitional periods for the two structures.

The calculated values of 689 cm⁻¹ for trimethyldisilane[50], as well as the average values of 703 cm⁻¹ for trans,trans-2,4-hexadiene[51], 448 cm⁻¹ for 1,1,1-trifluoro-propane-2-thione[52], and 392 cm⁻¹ for 1,1,1-trifluoroacetone [49], seem to be in line with the estimated methyl barriers of 643 and 356 cm⁻¹ for AMTDPC. According to Mohamed and Abo Aly (2004), the theoretical values of 493±21 cm⁻¹, obtained from the far infrared spectrum of trans,trans-2,4-hexadiene, exhibit a strong correlation with the experimental results of 727±3.5 cm⁻¹ (FIR) for propene[53] and 773 cm⁻¹ for isobutene[54]. Therefore, the values of the methyl barrier to internal rotation, as reported by Durig and Church (1980), Durig et al. (1989, 1977), Mohamed (2003), Mohamed and Abo Aly (2004), and Mohamed and Farag (2005), exhibit a strong concurrence between theoretical and experimental data.

6.2 CH₃S barriers to internal rotation

In accordance with conformer 1, the CH₃S group exhibited rotational movements around the C-S bond in increments of 10°, akin to the methyl moiety. The CH₃ group is orientated towards the C-N moiety at (N₄C₃S₁₀C₁₁) approximately 130°, resulting in a local minimum at C1. This occurs after a peak in energy, where the CH₃ moiety is nearly perpendicular to the pyrazole ring (C1 symmetry). The energy of the CH₃ component rises as it reaches C N at around 180°. According to the information shown in Figure 6, the CH₃S barriers are seen to be 1170, 1330, and 3874 cm⁻¹, indicating a preference for conformer 1 at a dihedral angle of zero degrees.

After conducting comprehensive geometry relaxation and frequency calculations, it has been ascertained that the C1 conformer exhibits an imaginary frequency transition state at a position of 130 degrees. Based on the results obtained, it can be concluded that conformer 1 is the only AMTDPC conformer. Although there is no existing literature on experimental CH₃S rotation barriers, it is clear that the CH₃S barriers calculated in this study are 1.5–2 times higher than the previously described CH₃ barrier. This proposition is deemed rational given the comparative dimensions of the carbon and sulfur atoms.

It is important to mention that the expected CH₃ barriers for ethylsilane[22], [55] and chloroethylsilane[44] were found to be between 1071 and 1483 cm⁻¹, which aligns closely with the experimental results of 1348 cm⁻¹ (far infrared) and 918±3.6 cm⁻¹ (MW), respectively.

6.3 Planar NH₂ barriers to internal rotation

Figure 7 illustrates the impact of NH₂ groups on internal rotation. When the NH₂ groups are perpendicular to the plane of AMTDPC, they exhibit extreme positions. Conversely, when the NH₂ groups are positioned at shallow angles to the ring, there are less energy structures. The calculated rotational barriers for NH₂ are 6251 cm⁻¹. According to Badawi (2005) and Van Dyck et al. (2018), it is important to highlight that the NH₂ barriers for CH₂=CH–NH₂, O=C=CH–NH₂, and CH₃–CH₂–NH₂ often fall within the range of 1.0–3.3 kcal/mole (350–1154 cm⁻¹). The calculated obstacles are deemed excessively substantial to justify additional scrutiny of these formations. Nevertheless, it is important to recognize that the existing NH₂ barriers are merely approximations due to the absence of a comprehensive optimization at the maximum sites. However, according to the NMR observations and computational findings, it is evident that the NH₂ barriers are significant, even when taking into account the double bond (π) nature of the NH₂ group.

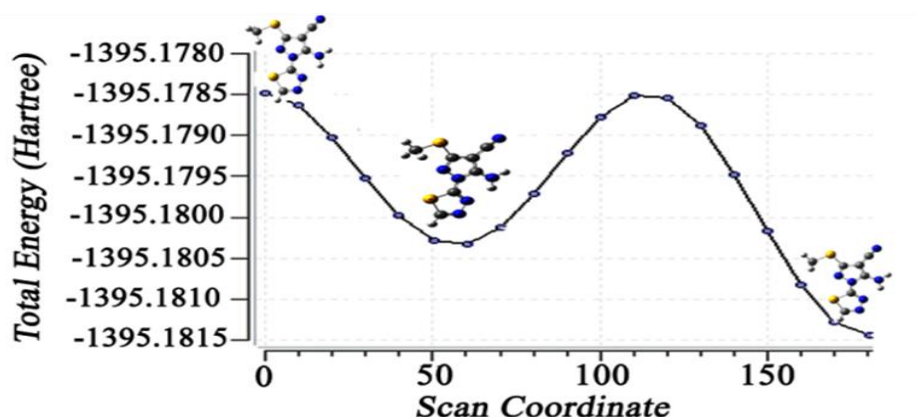


Figure 5: The barriers to internal rotation of the CH₃ group in AMTDPC, obtained through a potential surface scan using the B3PW91/6-31G(d) method.

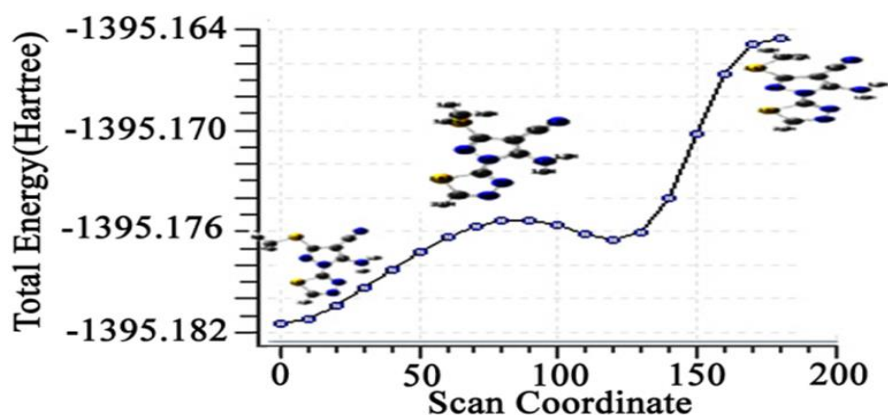


Figure 6: The barriers to internal rotation of the CH₃S group in AMTDPC, obtained through a potential surface scan using the B3PW91/6-31G(d) method.

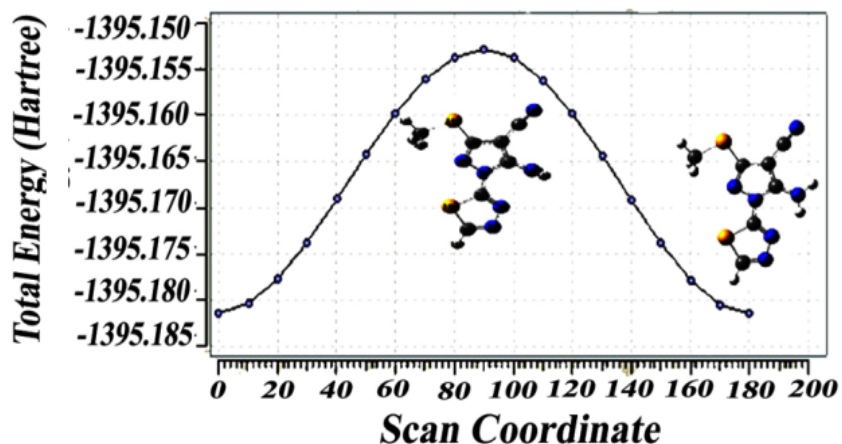


Figure 7: The barriers to internal rotation of the NH₂ group in AMTDPC, obtained through a potential surface scan using the B3PW91/6-31G(d) method.

6.4 Thiadiazole ring barriers to internal rotation

A stiff potential surface scan (PSS) was conducted using the optimized SPs obtained from B3PW91/6-31G(d) methods in order to examine the possible presence of a non-planar arrangement of the thiadiazole ring. The present study focused on the manipulation of the dihedral angle τ (N₄N₅C₆S₁₀), which is known to have a significant role in the structural interconversions.

As depicted in Figure 8, the thiadiazole ring exhibits maximum at a perpendicular orientation to the AMTDPC plane, namely at 4958 cm^{-1} , and a lower energy structure at 4945 cm^{-1} when the angular separation ($\text{N}_4\text{N}_5\text{C}_6\text{S}_{10}$) is around 130° . Subsequently, as depicted in Figure 8, the energy exhibits a steady rise until it reaches its peak magnitude, culminating in structure 5 and an energy barrier of 7634 cm^{-1} .

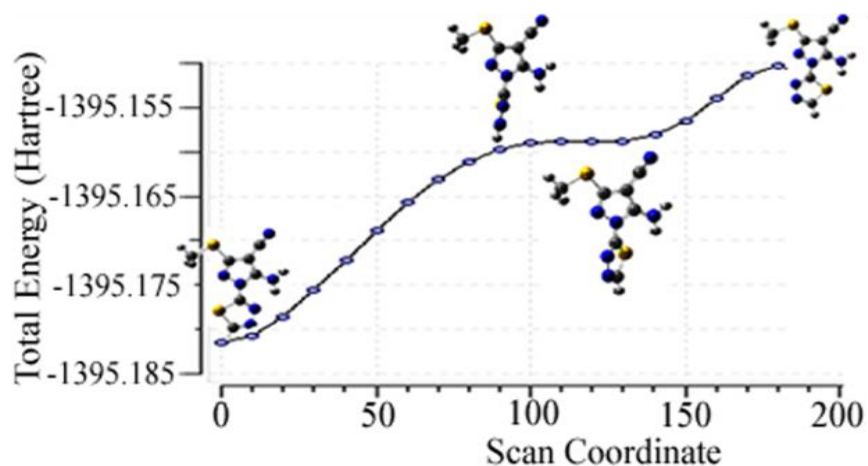


Figure 8: Barriers to internal rotations within the rings of AMTDPC, derived from a potential surface scan utilizing the B3PW91/6-31G(d) method.

7. Conclusion

The compound (AMTDPC, C₇H₆N₆S₂) has undergone extensive spectroscopic investigation, resulting in significant findings about its dynamic characteristics and structural attributes. The utilization of ¹H and ¹³C nuclear magnetic resonance (NMR) spectra, along with infrared spectra within the 4000–200 cm⁻¹ range, has played a pivotal role in elucidating the molecular intricacies of AMTDPC. The research of rotational isomerisms induced by internal rotation around C–N and/or C–S bonds led to the identification of nine isomers. Quantum mechanical simulations employing the RHF and DFT/B3PW91 techniques enhanced our comprehension, ultimately uncovering two conformers (1-2) with energies below 1000 cm⁻¹. Based on spectrum measurements that exhibited a high level of concurrence with the anticipated values, it may be concluded that conformer 1 emerged as the isomer with the highest stability. Furthermore, the chemical shifts predicted using the GIAO approach, both with and without solvent inclusion (PCM), provided confirmation for our spectroscopic findings. By comparing our results with those of related chemicals, we were able to provide more support and context to our conclusions. Our NMR findings provided clarification on the dynamic nature of AMTDPC, revealing evidence of both restricted and free NH₂ internal rotation around C-N bonds. A reliable vibrational assignment was achieved for all observable fundamentals by the utilization of potential energy distributions and study of normal coordinates. The extensive investigation on the torsional barriers to internal rotation of CH₃, CH₃S, NH₂, and the thiadiazole ring has significantly improved our understanding. This research has provided crucial insights into the dynamic behavior of AMTDPC. The combination of experimental data and quantum mechanical simulations has for a comprehensive examination of the molecular structure, conformational dynamics, and vibrational properties of AMTDPC. The aforementioned finding serves as a fundamental basis for subsequent inquiries in the domains of molecular spectroscopy and structural analysis, thereby enhancing our comprehension of associated compounds.

References

- [1] M. H. Baren, S. A. Ibrahim, M. M. Al-Rooqi, S. A. Ahmed, M. M. El-Gamil, and H. A. Hekal, "A new class of anticancer activity with computational studies for a novel bioactive aminophosphonates based on pyrazole moiety," *Scientific Reports*, vol. 13, no. 1, p. 14680, 2023.
- [2] P. Mahesh *et al.*, "Antiproliferative Activity of New Pyrazole-4-sulfonamide Derivatives: Synthesis and Biological Evaluation," *ACS Omega*, vol. 8, no. 29, pp. 25698–25709, Jul. 2023, doi: 10.1021/acsomega.2c07539.
- [3] M. Mantzanidou, E. Pontiki, and D. Hadjipavlou-Litina, "Pyrazoles and pyrazolines as anti-inflammatory agents," *Molecules*, vol. 26, no. 11, p. 3439, 2021.
- [4] K. R. Jyothikumari, K. N. Rajasekharan, and K. Dhevendran, "Synthesis of Some New Pyrazolo³, 4-d-pyrimidine Derivatives and their Antibacterial Activity," *Journal of the Indian Chemical Society*, vol. 68, no. 10, pp. 578–580, 1991.
- [5] T. A. Mohamed, A. M. Hassan, U. A. Soliman, W. M. Zoghaib, J. Husband, and M. M. Abdelall, "Infrared, Raman and NMR spectra, conformational stability, normal coordinate analysis and B3LYP calculations of 5-amino-4-cyano-3-(methylthio)-1H-pyrazole-1-carbothioamide," *Journal of molecular structure*, vol. 985, no. 2–3, pp. 277–291, 2011.
- [6] T. A. Mohamed, A. M. Hassan, U. A. Soliman, W. M. Zoghaib, J. Husband, and M. M. Abdelall, "Infrared, Raman and NMR spectra, conformational stability, normal coordinate analysis and B3LYP calculations of 5-amino-4-cyano-3-(methylthio)-1H-pyrazole-1-carbothioamide," *Journal of molecular structure*, vol. 985, no. 2–3, pp. 277–291, 2011.
- [7] V. J. Ram, U. K. Singha, and P. Y. Guru, "Chemotherapeutic agents XI: synthesis of pyrimidines and azolopyrimidines as leishmanicides.," *European Journal of Medicinal Chemistry*, vol. 25, no. 6, pp. 533–538, 1990.
- [8] R. K. Robins, "Potential Purine Antagonists. I. Synthesis of Some 4,6-Substituted Pyrazolo [3,4-d] pyrimidines ¹," *J. Am. Chem. Soc.*, vol. 78, no. 4, pp. 784–790, Feb. 1956, doi: 10.1021/ja01585a023.
- [9] A.-R. Farghaly, S. A. Ahmed, K. S. Ismail, D. Ibrahim, N. Amri, and S. Elgogary, "Synthesis, antitumor activity, antimicrobial evaluation and molecular docking studies of some hydrazone, 1, 3, 4-oxadiazole, 1, 2, 4-triazole and pyrazole derivatives bearing nicotinoyl moiety," *Results in Chemistry*, vol. 7, p. 101474, 2024.

- [10] P. Rzepecki, M. Wehner, O. Molt, R. Zadmand, K. Harms, and T. Schrader, "Aminopyrazole Oligomers for β -Sheet Stabilization of Peptides," *Synthesis*, no. 12, pp. 1815–1826, 2003, doi: 10.1055/s-2003-41031.
- [11] O. Ebenezer, M. Shapi, and J. A. Tuszynski, "A review of the recent development in the synthesis and biological evaluations of pyrazole derivatives," *Biomedicines*, vol. 10, no. 5, p. 1124, 2022.
- [12] W. Abisha, D. A. Dhas, S. Balachandran, and I. H. Joe, "Synthesis, Structural, and Quantum Chemical Spectroscopic, Hydrogen Bonding, and Molecular Docking Investigation of Antifungal Compound Pyrazole-Pyrazolium Picrate," *Polycyclic Aromatic Compounds*, vol. 43, no. 9, pp. 8455–8481, Oct. 2023, doi: 10.1080/10406638.2022.2149571.
- [13] K. Karrouchi *et al.*, "Synthesis, X-ray structure, vibrational spectroscopy, DFT, biological evaluation and molecular docking studies of (E)-N'-(4-(dimethylamino)benzylidene)-5-methyl-1H-pyrazole-3-carbohydrazide," *Journal of Molecular Structure*, vol. 1219, p. 128541, 2020.
- [14] P. Rejnhardt and M. Daszkiewicz, "Crystal structure and vibrational spectra of salts of 1H-pyrazole-1-carboxamide and its protonation route," *Struct Chem*, vol. 32, no. 2, pp. 539–551, Apr. 2021, doi: 10.1007/s11224-020-01671-0.
- [15] A. D. Becke, "Density-functional exchange-energy approximation with correct asymptotic behavior," *Phys. Rev. A*, vol. 38, no. 6, pp. 3098–3100, Sep. 1988, doi: 10.1103/PhysRevA.38.3098.
- [16] A. D. Becke, "Density-functional thermochemistry. I. The effect of the exchange-only gradient correction," *The Journal of chemical physics*, vol. 96, no. 3, pp. 2155–2160, 1992.
- [17] M. J. Frisch *et al.*, "Uranyl extraction by N, N-dialkylamide ligands studied by static and dynamic DFT simulations," *Gaussian*, vol. 9, p. 227, 2009.
- [18] C. Lee, W. Yang, and R. G. Parr, "Development of the Colle-Salvetti correlation-energy formula into a functional of the electron density," *Phys. Rev. B*, vol. 37, no. 2, pp. 785–789, Jan. 1988, doi: 10.1103/PhysRevB.37.785.
- [19] Chr. Møller and M. S. Plesset, "Note on an Approximation Treatment for Many-Electron Systems," *Phys. Rev.*, vol. 46, no. 7, pp. 618–622, Oct. 1934, doi: 10.1103/PhysRev.46.618.

- [20] J. R. Durig, G. A. Guirgis, C. Zheng, and T. A. Mohamed, "Spectra and structure of silicon-containing compounds.: Part XXXVIII: Infrared and Raman spectra, vibrational assignment, conformational stability, and ab initio calculations of vinyl difluorosilane," *Spectrochimica Acta Part A: Molecular and Biomolecular Spectroscopy*, vol. 59, no. 9, pp. 2099–2114, 2003.
- [21] H. Lampert, W. Mikenda, and A. Karpfen, "Molecular Geometries and Vibrational Spectra of Phenol, Benzaldehyde, and Salicylaldehyde: Experimental versus Quantum Chemical Data," *J. Phys. Chem. A*, vol. 101, no. 12, pp. 2254–2263, Mar. 1997, doi: 10.1021/jp962933g.
- [22] A. Nasser, M. A. Migahed, N. M. EL Basiony, H. M. Abd-El-Bary, and T. A. Mohamed, "Raman and Infrared Spectral Analysis, Normal Coordinate Analysis, DFT calculations of Novel Schiff Base Containing di-imine moieties," *Egyptian Journal of Chemistry*, vol. 66, no. 9, pp. 271–291, 2023.
- [23] A. Asensio, N. Kobko, and J. J. Dannenberg, "Cooperative Hydrogen-Bonding in Adenine–Thymine and Guanine–Cytosine Base Pairs. Density Functional Theory and Møller–Plesset Molecular Orbital Study," *J. Phys. Chem. A*, vol. 107, no. 33, pp. 6441–6443, Aug. 2003, doi: 10.1021/jp0344646.
- [24] D. B. Chesnut and C. G. Phung, "Nuclear magnetic resonance chemical shifts using optimized geometries," *The Journal of chemical physics*, vol. 91, no. 10, pp. 6238–6245, 1989.
- [25] V. Chiş, "Molecular and vibrational structure of 2, 4-dinitrophenol: FT-IR, FT-Raman and quantum chemical calculations," *Chemical physics*, vol. 300, no. 1–3, pp. 1–11, 2004.
- [26] P. K. Chowdhury, "Infrared depletion spectroscopy of the hydrogen-bonded aniline-diethylamine (C₆H₅-NH₂ center dot center dot center dot NHC₄H₁₀) complex produced in supersonic jet," *Journal of Physical Chemistry A*, vol. 107, no. 30, pp. 5692–5696, 2003.
- [27] R. Ditchfield, "Self-consistent perturbation theory of diamagnetism: I. A gauge-invariant LCAO method for N.M.R. chemical shifts," *Molecular Physics*, vol. 27, no. 4, pp. 789–807, Apr. 1974, doi: 10.1080/00268977400100711.
- [28] H.-G. Korth, M. I. De Heer, and P. Mulder, "A DFT Study on Intramolecular Hydrogen Bonding in 2-Substituted Phenols: Conformations, Enthalpies, and Correlation with Solute Parameters," *J. Phys. Chem. A*, vol. 106, no. 37, pp. 8779–8789, Sep. 2002, doi: 10.1021/jp025713d.

- [29] T. Kupka, G. Pasterna, P. Lodowski, and W. Szeja, "GIAO-DFT prediction of accurate NMR parameters in selected glucose derivatives," *Magn. Reson. Chem.*, vol. 37, no. 6, pp. 421–426, Jun. 1999, doi: 10.1002/(SICI)1097-458X(199906)37:6<421::AID-MRC479>3.0.CO;2-W.
- [30] T. Kupka, M. Kołaski, G. Pasterna, and K. Ruud, "Towards more reliable prediction of formaldehyde multinuclear NMR parameters and harmonic vibrations in the gas phase and solution," *Journal of Molecular Structure: THEOCHEM*, vol. 467, no. 1, pp. 63–78, 1999.
- [31] V. G. Malkin, O. L. Malkina, M. E. Casida, and D. R. Salahub, "Nuclear Magnetic Resonance Shielding Tensors Calculated with a Sum-over-States Density Functional Perturbation Theory," *J. Am. Chem. Soc.*, vol. 116, no. 13, pp. 5898–5908, Jun. 1994, doi: 10.1021/ja00092a046.
- [32] W. J. Hehre, "Ab initio molecular orbital theory," *Acc. Chem. Res.*, vol. 9, no. 11, pp. 399–406, Nov. 1976, doi: 10.1021/ar50107a003.
- [33] T. A. Mohamed, U. A. Soliman, A. I. Hanafy, and A. M. Hassan, "Conformational stability, barriers to internal rotation of 2-aminothiophenol (d0 and d3): A combined vibrational and theoretical approach," *Journal of Molecular Structure: THEOCHEM*, vol. 865, no. 1–3, pp. 14–24, 2008.
- [34] T. A. Mohamed, I. A. Shabaan, W. M. Zoghaib, J. Husband, R. S. Farag, and A. E.-N. M. Alajhaz, "Tautomerism, normal coordinate analysis, vibrational assignments, calculated IR, Raman and NMR spectra of adenine," *Journal of Molecular Structure*, vol. 938, no. 1–3, pp. 263–276, 2009.
- [35] U. A. Soliman, A. M. Hassan, and T. A. Mohamed, "Conformational stability, vibrational assignments, barriers to internal rotations and ab initio calculations of 2-aminophenol (d0 and d3)," *Spectrochimica Acta Part A: Molecular and Biomolecular Spectroscopy*, vol. 68, no. 3, pp. 688–700, 2007.
- [36] S. M. Hassan, H. A. Emam, and M. M. Abdelall, "Heteroaromatization with Ketene Dithioacetals: Part II. Synthesis of Some Novel 5-Aminopyrazole-3-Carbonitrile, 3-Carboxamide and Pyrazolo [3, 4-d] Pyrimidin-4-One Derivatives as Antimicrobial Agents," *Phosphorus, Sulfur, and Silicon and the Related Elements*, vol. 175, no. 1, pp. 109–127, 2001.
- [37] P. Pulay, "Ab initio calculation of force constants and equilibrium geometries in polyatomic molecules: I. Theory," *Molecular Physics*, vol. 17, no. 2, pp. 197–204, 1969.

- [38] J. Zukerman-Schpector, E. J. Barreiro, and A. C. C. Freitas, "Structures of pyrazole derivatives. III. 5-Amino-4-cyano-1-phenylpyrazole," *Acta Crystallographica Section C: Crystal Structure Communications*, vol. 50, no. 12, pp. 2095–2096, 1994.
- [39] P. Prusiner, M. Sundaralingam, T. Ito, and T. Sakurai, "The crystal and molecular structure of 3-amino-4, 5-dicyano-1-methylpyrazole," *Acta Crystallographica Section B: Structural Crystallography and Crystal Chemistry*, vol. 32, no. 3, pp. 853–856, 1976.
- [40] J. Zukerman-Schpector, E. E. Castellano, G. Oliva, A. C. Massabni, and A. D. Pinto, "Hydrogen bonding in the crystal structures of the adducts between 1-phenyl-3, 5-dimethylpyrazole with oxalic and perchloric acids," *Canadian Journal of Chemistry*, vol. 62, no. 4, pp. 725–728, 1984.
- [41] A. van Bondi, "van der Waals volumes and radii," *The Journal of physical chemistry*, vol. 68, no. 3, pp. 441–451, 1964.
- [42] J. E. Huheey, E. A. Keiter, R. L. Keiter, and O. K. Medhi, *Inorganic chemistry: principles of structure and reactivity*. Pearson Education India, 2006.
- [43] H. Lampert, W. Mikenda, and A. Karpfen, "Molecular geometries and vibrational spectra of phenol, benzaldehyde, and salicylaldehyde: experimental versus quantum chemical data," *The Journal of Physical Chemistry A*, vol. 101, no. 12, pp. 2254–2263, 1997.
- [44] T. A. Mohamed, G. A. Guirgis, Y. E. Nashed, and J. R. Durig, "Spectra and structure of silicon containing compounds: Part XXXIV. Raman and infrared spectra, vibrational assignment, barriers to internal rotation, and ab initio calculations of 1-chloroethylsilane," *Vibrational spectroscopy*, vol. 30, no. 2, pp. 111–120, 2002.
- [45] T. Kupka, G. Pasterna, P. Lodowski, and W. Szeja, "GIAO-DFT prediction of accurate NMR parameters in selected glucose derivatives," *Magn. Reson. Chem.*, vol. 37, no. 6, pp. 421–426, Jun. 1999, doi: 10.1002/(SICI)1097-458X(199906)37:6<421::AID-MRC479>3.0.CO;2-W.
- [46] V. Barone, M. Cossi, and J. Tomasi, "A new definition of cavities for the computation of solvation free energies by the polarizable continuum model," *The Journal of chemical physics*, vol. 107, no. 8, pp. 3210–3221, 1997.
- [47] J. Tomasi and M. Persico, "Molecular interactions in solution: an overview of methods based on continuous distributions of the solvent," *Chemical Reviews*, vol. 94, no. 7, pp. 2027–2094, 1994.
- [48] L. J. Bellamy and R. L. Williams, "The NH stretching frequencies of primary amines," *Spectrochimica Acta*, vol. 9, no. 4, pp. 341–345, 1957.

- [49] J. Swaminathan, M. Ramalingam, and N. Sundaraganesan, "Molecular structure and vibrational spectra of 3-amino-5-hydroxypyrazole by density functional method," *Spectrochimica Acta Part A: Molecular and Biomolecular Spectroscopy*, vol. 71, no. 5, pp. 1776–1782, 2009.
- [50] T. A. Mohamed, "Structural parameters, barriers to internal rotation, normal coordinate analysis and quantum mechanics calculations of 1, 1, 1-trimethyldisilane," *Journal of Molecular Structure: THEOCHEM*, vol. 635, no. 1–3, pp. 161–172, 2003.
- [51] T. A. Mohamed and M. M. Abo Aly, "Vibrational analysis, conformational stability, force constants, barriers to internal rotations, RHF, MP2 and DFT calculations of trans, trans-2, 4-hexadiene," *Journal of Raman Spectroscopy*, vol. 35, no. 10, pp. 869–878, 2004.
- [52] T. A. Mohamed and R. S. Farag, "Raman spectrum, conformational stability, barriers to internal rotations and DFT calculations of 1, 1, 1-trifluoro-propane-2-thione with double-internal-symmetric rotor," *Spectrochimica Acta Part A: Molecular and Biomolecular Spectroscopy*, vol. 62, no. 4–5, pp. 800–807, 2005.
- [53] J. R. Durig, G. A. Guirgis, and S. Bell, "Torsional spectrum and ab initio calculations for propene," *The Journal of Physical Chemistry*, vol. 93, no. 9, pp. 3487–3491, 1989.
- [54] J. R. Durig, W. J. Natter, and P. Groner, "Analysis of torsional spectra of molecules with two internal C 3 V rotors. IX. The torsional potential functions of isobutene-d and-d 6," *The Journal of Chemical Physics*, vol. 67, no. 11, pp. 4948–4951, 1977.
- [55] R. t Schwendeman and G. D. Jacobs, "Molecular structure of ethyl chloride," *The Journal of Chemical Physics*, vol. 36, no. 5, pp. 1245–1250, 1962.

Multiple sources of big data are used to create a method for protecting computer networks

Mohammad Eid Alzahrani

**Department of Computer Science, Faculty of Computing & Information
Al-Baha University, Al-Baha, Saudi Arabia
meid@bu.edu.sa**

Abstract: The purpose of this article is to present a model for the cybersecurity defense of computer networks that makes use of big data from multiple sources. The purpose of this endeavor is to improve the overall security of computer networks by addressing the limitations of the defense systems that are currently in place. A comprehensive analysis of the current state of network security is carried out, with a particular emphasis placed on the difficulties that are encountered in this field. After that, the concept of big data that comes from multiple sources is presented as a potential solution. A definition of big data and an analysis of the multisource big data model are presented in this article. An information system network security framework is presented that can be found in this article. The model illustrates the connection between network operations, potential security risks, attacks on networks, and the defense provided by security devices. For the purpose of developing a defense system measurement and optimization system, the network security system measurement and optimization scheme is utilized. Real-world scenarios are skillfully incorporated into the application analysis that is being conducted for the project. The purpose of this article is to demonstrate the usefulness and efficiency of the proposed network security defense system evaluation and optimization scheme. This is accomplished by evaluating and enhancing the security defense system through the utilization of conventional methods.

Keywords: *Big data, Multiple Sources, Computer Network Security, Cyberattacks, Network Protection.*

استخدام مصادر متعددة للبيانات الضخمة لإنشاء طريقة لحماية شبكات الكمبيوتر

الملخص: الهدف من هذه الورقة العلمية هو تقديم نموذج لتعزيز الامن السيبراني لشبكات الحاسب وذلك بالاستفادة واستخدام البيانات الضخمة من مصادر متعددة. والغرض من هذا المسعى هو تحسين الأمان العام لشبكات الكمبيوتر من خلال معالجة القيود الموجودة في أنظمة التعزيز الامني الحالية. يتم إجراء تحليل شامل للحالة الحالية لأمن الشبكات، مع التركيز بشكل خاص على الصعوبات التي يتم مواجهتها في هذا المجال. بعد ذلك، يتم طرح مفهوم البيانات الضخمة القادمة من مصادر متعددة كحل محتمل. تستعرض الورقة تعريف للبيانات الضخمة وتحليل لنموذج البيانات الضخمة متعدد المصادر. يتم عرض إطار عمل لأمن شبكة نظم المعلومات يمكن العثور عليه من خلال هذا البحث. النموذج يوضح العلاقة بين عمليات الشبكة، المخاطر الأمنية المحتملة، الهجمات على الشبكات، والتعزيز الأمني التي توفرها أجهزة الخاصة بالأمان. ومن أجل تطوير نظام قياس وتحسين التعزيز الأمني، يتم استخدام مخطط قياس وتحسين نظام الأمان للشبكات الحاسوبية وذلك من خلال دمج السيناريوهات الواقعية بشكل فعال في تحليل التطبيق الذي يتم إجراؤه للمشروع. الغرض من هذا المقال هو إظهار فائدة وكفاءة خطة تقييم وتحسين نظام التعزيز الأمني المقترحة. يتم تحقيق ذلك من خلال تقييم وتعزيز نظام الحماية الأمني باستخدام الطرق التقليدية.

1. Introduction

Recently, there has been a significant increase in the progress of emerging technologies such as blockchain (Zhou, Z. 2022), the Internet of Things (IoT), cloud computing resources (Zarei S.M., 2021), and big data. The integration of computer networks as the underlying framework for information construction has had a significant influence on both economic progress and human ways of life (Prvan, M, 2020).

The number of connected devices and generated content are growing rapidly on the internet. While networks offer various conveniences, the possibility of attacks can give rise to security apprehensions (Nour, B, 2021). The complete utilization of multi-source and large data resources can be achieved through the mining of explorer travel rules and the acquisition of trip information through big data advancement (A. Ju, 2020). Additionally, monstrous learning benefits from the consistent absorption of vast quantities of test data and the separation of sporadic, unsteady, and exceptionally dubious data ascribes. Additionally, it can provide state-of-the-art development and advancement to address the accuracy of explorer stream assumption in various environments in metropolitan rail travel voyager stream assumption data support. While considering the impact of social and monetary components, temporary and spatial factors, and various emergencies on explorer stream changes, these variables can be considered continuously and exhaustively (Bhat, 2021).

In the contemporary mechanical and associated world, it is imperative to protect computer networks from a variety of cyber threats. A significant instrument for reinforcing these networks has emerged as a result of the remarkable development of data generated from a variety of sources: big data. The utilization of various big data sources, which are areas of strength, can be employed to establish a comprehensive strategy for safeguarding computer networks from emerging cyber threats (C. Zhou, 2021). Network traffic is a significant source of big data. The identification of unusual behaviors that are indicative of potential hazards can be facilitated by the examination of significant surges in network sections, which can be used to establish standard examples of conduct.

Additionally, network device, server, and application logs provide valuable insights into organizational practices by facilitating the identification of unauthorized access attempts and questionable behavior (D. Wang, 2020). In essence, organizations have the ability to implement a variety of strategies to protect computer networks by leveraging a limited number of large data sources. By integrating network traffic analysis, structure logs, threat knowledge, and IoT data, this approach establishes a comprehensive security system.

This concept aids organizations in maintaining a competitive edge over cyber adversaries and safeguarding their critical high-level assets by means of continuous monitoring, analysis, and proactive risk mitigation (Fadhil, 2021).

2. Literature review

The network produces a daily volume of 2.5 exabytes of data, which is substantial, diverse, and generated quickly (R. Vinayakumar, 2017). As big data is collected and analyzed more efficiently, the significant value that is concealed within the data is gradually being uncovered. Network operators can optimize network performance and enhance network revenue by leveraging big data (H. Sun, 2021). The article by Gupta (2020) provides a meticulous logical categorization and risk assessment for artificial intelligence models used in secure data analysis. The paper resolves the central inquiry of guaranteeing data security and protection in the period of artificial intelligence driven examination. The creators order the different man-made intelligence models utilized in data examination through a careful survey of past writing, and afterward recommend a risk model to recognize possible weaknesses. The review gives significant experiences to specialists and experts to foster solid security apparatuses for data examination structures via cautiously arranging simulated intelligence models and related gambles.

This paper conducts a deliberate examination that focuses on the intersection of IoT advancements and big data in clever settings (Hajjaji, 2021). In particular, the review examines the intersection of IoT applications and big data analysis, particularly in relation to smart metropolitan regions, medical care, transportation, and energy for Presidents. The creators provide pieces of information regarding the current state of craftsmanship, challenges, and future prospects in this thriving region by combining findings from a variety of investigations. The deliberate review showcases the diverse applications of big data and IoT advancements, ranging from continuous observation and vision investigation to custom-made services and resource enhancement. In addition, the review emphasizes the necessity of addressing critical issues such as data security, adaptability, and interoperability in order to gain a comprehensive understanding of the potential impact of big data and IoT on the development of sharp ecosystems.

Data fusion brought a fresh approach for the identification of heterogeneous intrusions (Jeyepalan and Kirubakaran, 2019). (Essid and Jemili, 2016) proposed using Hadoop and MapReduce the integration of two heterogeneous data sources. Combining intrusion detection datasets—including the NSL-KDD, Mawilab, and DARPA'99 datasets—Ben Fekih and Jemili, 2018 put forth a method They built and assessed the detection model using the Naïve Bayes algorithm. In order to suggest an approach for the discovery of temporal patterns, (Radhakrishna V et al., 2019) presented the idea of data fusion in respect to the temporal pattern tree. Every timeslot generates a tree; the trees acquired for one timeslot are combined or fused to produce the total tree for the whole dataset. Effective and proactive pruning of elements during the pattern mining process depends much on the idea of tree-based data fusion. By means of principal component analysis (PCA), (Om Prakash Singh et al., 2022) sought the suitable coefficients for data fusion. Look at how computational information approaches are utilized in numerous spaces for big data examination (Iqbal, 2020).

The review gives a complete outline of a few computational experiences, like brain networks, hereditary calculations, fluffy rationale, and multiverse information, among others. The creators outline the adequacy of these strategies in tending to perplexing difficulties related with large data examination, for example, data pre-taking care of, feature determination, and model affirmation, through relevant investigations and true applications.

The study by J. Hu (2021) provides a methodology for predicting problems associated with vehicle travel by utilizing data from various sources. The survey focuses on accurately predicting protests by utilizing various data inputs, such as GPS data, traffic patterns, and real-time travel information. The recommended approach aims to enhance the accuracy of genuine assumption by integrating diverse data sources and implementing artificial intelligence techniques. This has significant implications for efficient urban driving, navigation systems, and transportation planning. This examination aims to enhance intelligent transportation systems by limiting the capacity of multi-source data analysis for advanced research.

The study conducted by Khang and colleagues in 2024 Examine the potential applications of big data in resolving challenges within the pharmaceutical industry (Khang, 2024). Utilizing a vast amount of patient data, clinical records, and genetic information, big data research enables medical professionals to identify significant new discoveries, customize treatments, and focus on long-term outcomes. This segment showcases the profound impact of big data on shaping the future of medicine and introduces several applications, such as drug discovery, precision medicine, and predictive market analysis. This examination contributes to the growing body of literature on the application of data-driven approaches to enhance clinical development and healthcare practices.

Wang et al. (2020) propose a pre-impact fall area framework for a CNN enterprise that incorporates multiple sources (L. Wang, 2020). The survey addresses the primary requirement for accurate fall detection, particularly in vulnerable populations such as the elderly. The proposed framework achieves precise and robust fall detection prior to impact by integrating data from multiple sensors, such as depth cameras, gyroscopes, and accelerometers.

The dress showcase strategy by Tehrani et al. (2019) predicts tropical woodland fire weakness spatially. Forest fires pose significant financial and environmental risks in tropical regions, so the audit addresses the growing need for precise assessment. With the Logit Lift computer-based intelligence classifier and many geospatial data sources, the designers created an impressive prescient model that can identify forest fire-prone areas. The study improves proactive fire fighting and early warning systems, reducing the harm caused by wildfires. Sanden and Neideck (2021) examine how connected data resources can improve multi-source public region tirelessness. The survey uses public data sources to create complete, connected data resources for evidence-based policymaking, program assessment, and organization delivery. The examination promotes data executive techniques and government organization cooperation to make data an incentive for social benefit.

The cybersecurity improvements at specific southwest Nigerian schools are examined by Oluwafunmilayo (2019). The review evaluates academic institutions' cybersecurity measures to protect sensitive data and cyber threats. The findings highlight the importance of cybersecurity availability and protecting stakes in strong security measures to reduce cyber risks. Analyse large data using data science and computerized reasoning (Pramanik, 2023). This section describes big data research's challenges and opportunities. The authors explain big data analysis's origins and potential for independent direction, progress, and social change by examining various keen strategies, instruments, and application spaces. The examination improves big data strategy understanding and multidisciplinary collaborative efforts to maximize big data's potential in many areas.

An proposed method for intrusion detection focuses on combining data from different sources, like user behavior, system logs, and network traffic (Anjum, N. et al., 2021). This method is specifically made to make intrusion detection more accurate. Aleroud and Karabatis (2017) suggested a context-aware data fusion method that makes intrusion detection more accurate by taking into account things like the time and location of the intrusion.

3. Design of a multisource big data based computer network security defence system

3.1. Building Multisource Big Data Models

Providing clients with information regarding data plan and various perspectives through a unified perspective is the primary objective of the multisource big data organizing stage. Consequently, the data availability process is further developed by enhancing the data organizing cycle's instinct.

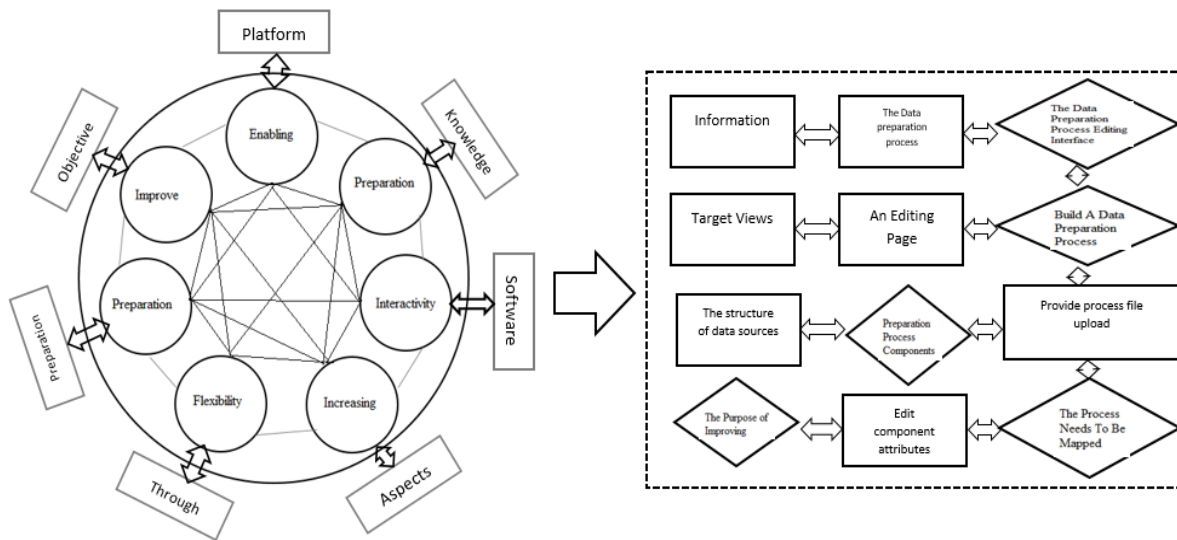


Figure 1: Process of the platform functional analysis system.

Information regarding the development of data sources and target views must be accumulated in order to achieve the objective of disseminating a unified perspective. It is also necessary to provide a modifying page that allows clients to select specific sections of the data availability cycle and modify the credit allocations in the data organizing process by adjusting the association point. Finally, to satisfy the justification for managing the versatility of the data organization process, a data organization process for multisource big data must be established, as well as process record move and age capabilities provided. The cycle should be developed and demonstrated after the framework is established, and it is typically employed to finalize the client-depicted strategy. Each step toward the client-represented data game plan process should be executed with adaptability and efficiency (Q. Guo, 2020). It is imperative to enhance the estimation and strategy for addressing missing data. The bit by bit advantageous assessment system approach is illustrated in Figure 1.

Figure 2 shows the multisource big data flowchart. Extra-assembled analysis of multisource security events generates anomaly alerts using security semantics. Though assault examinations can be fooled, anomaly alerts provide only low-level security. Relationship analysis will link these spots to a more serious attack scenario using semantic security data from firewalls, antivirus software, and intrusion detection systems (Ragazou, 2023).

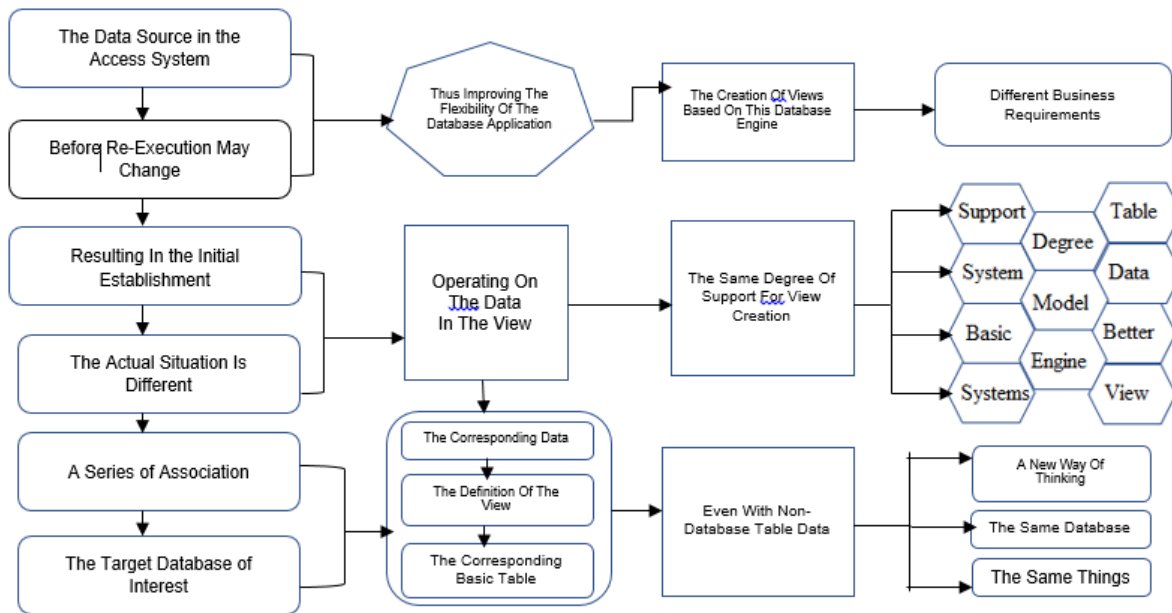


Figure 2: Big data flowchart with multiple sources.

3.2. System Model Design is Defined by Computer Network Security

The goal of the quantitative evaluation of defense systems during the arrangement stage is to help security staff figure out if security threats are built into the system and, if so, which threats the system is meant to protect against. It also wants to find any holes in the defense system or threats that the system might not be able to stop well enough (S. S. Harsha, 2019).

(1) Figure out the possible security risks and set up a framework for the evaluation subject's network security. There is a suggested network security model for the information system that shows the network topology of the information infrastructure.

Not all of the device hubs that the information structure goes through are completely safe, which makes it less safe (Tao, 2020).

(2) The degree of risk associated with security threats is used to assess the system's evolutionary stage. Various research procedures are employed to assess the severity of a security risk. Information systems may be vulnerable to upcoming challenges, such as security risks. When information systems are threatened by attacks, security personnel counteract these threats by deploying security devices to neutralize or eliminate them (Ullah, 2023). This suggests that the degree of probability that the information system assesses can be employed as a quantitative indicator to measure the protective capability of the shield structure. This article examines the dynamic relationship between the type of danger and the actual level of risk. It utilizes various reviewed studies to assess the level of risk associated with a specific situation. Aggressors interpret dangers as clear attacks and achieve their goals by employing hostile behaviors to deliver threats to their intended targets. Risks associated with security encompass data leakage, data aggregation, data manipulation, and lack of managerial accessibility. Specific hazards present distinct security opportunities and vary in the level of risk they pose to a security threat T at a device hub within a data infrastructure (Vasa, 2023). Using SDNA design, a hypervisor is put between each network hub. This gives each hub a unique look while still being essential for the computer's OS, different applications, and end consumers.

$$\sum_{i=1}^n tw(n-1) = \frac{\sqrt{n-1}}{n+1} \quad (1)$$

(3) Utilize the network security model to decide how to safeguard the information structure's security gadgets against dangers to the gadget centers. There is a security risk since it is normal that the contraction center point is gadget 1. T , device1's network danger is $addr1$, the assailant's network address is $addr2$, and the security gadget's defensive impact is contraction against the danger in the shield system. DT_j ($dj1, dj2, \dots, djn$), dji with t_i adjusted correspondence, addresses T . Clients will work with computer information systems for a lot of time consistently (Wu, 2020). Bosses frequently start with a model setup of the security of the computer system, which safeguards the computer information structure:

$$S = \sum_{i=1}^n (r_i + tw_{i-1}) - TW^T. \quad (2)$$

(4) Decide if the watchman design is suitable for general protection. Considering that the information structure has m resources, the resources' genuine monetary worth is utilized to decide their significance (X. Chen, 2019).

The asset importance weight is communicated as AW (aw_1, \dots, aw_2), where $aw_1: aw_2: \dots: aw_m v_1: v_2: \dots: v_m$, where v addresses the genuine money related worth of each buy, and $j_1 aw_j$, the equation for deciding the protection effect of the all-out information structure is acquired:

$$S_1 = \sum_{j=1}^m aw_j + \sum_{i=1}^m tw_i. \quad (3)$$

The data sources can be recognized, recognized, and dealt with fittingly by the security protect engineering in view of the aftereffects of data coordinating.

Figure 3 shows the security defend system's design. The planning module, the disclosure module, the actually take a look at module, and the database storing system make up the shield part. The structure will initially gather a large measure of data (T1, T2, TN, and so forth) in the planning module. It will then pre-process the data, store the pre-dealt with data in the readiness set database, set up the pre-taken care of planning set utilizing the mind net, and store the got features the component library (Zhang, 2021).

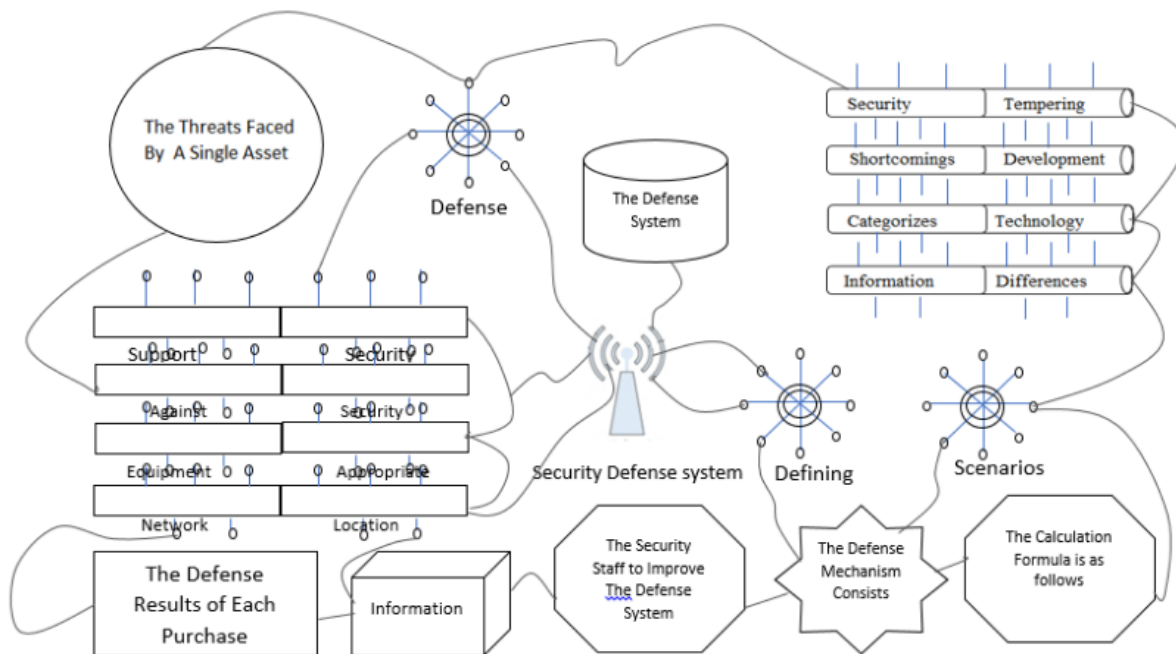


Figure 3: The security defense system's design.

At last, two situational points of view are analyzed in line with their reasonable relevance. The first is RE, the general reaction impact of the protection system against the hazards that gadget 1 poses in the resources; $re_1 0$ shows that gadget 1 is covered by the defend range of the protection structure. All security devices cannot differentiate the danger presented by attacks; hence, none of the security devices covered by the defense system (gadget 1) can prevent attacks linked with hazards; moreover, none of the security gadgets covered by the protect structure (gadget 3) can prevent attacks linked with hazards. Therefore, assuming each of the four credits of gadget 1 are available, no security element can protect against the risk presented by $re_4 0$.

The next one is Bij, Bij, the reaction system of the security devices to protect the resources against the risk gadget 1. Though every value device 1 has a similar significance as the others, Bij, or the actual response to hazards that every remarkable security gadget generates, really counts (Z. Xiong, 2021).

3.3 Potential Situations anomaly notifications using security semantics

Anomaly correction for data quality is essential for improving datasets' accuracy, reliability, and usability across all domains and use cases. We will highlight the most important areas where our framework can improve data quality in the sections that follow.

Personal details: The accuracy of sensitive data can be compromised due to human error, incomplete or missing data, inconsistent data formats or types, misspellings, and other human error-related issues. There is hope that the proposed framework can improve data quality. Customer profiling, targeted marketing, and personalized services are all at risk when data is inaccurate or unreliable due to quality anomalies. Some methods for dealing with these problems include finding correlated features, choosing comparable records, and filling in missing values, fixing inconsistencies, and fixing data entry mistakes with machine learning models like XGBoost. Think about a scenario where the date of birth field has some blanks. To improve the data quality and make accurate predictions of date of birth values, the framework can use correlated features like name, address, and age. (Elouataoui Widad, 2023).

Cybersecurity : When it comes to cybersecurity, data quality correction is absolutely crucial. In order to effectively detect threats, respond to incidents, and manage risks, trustworthy cybersecurity data is essential. Our dependence on digital systems and the ever-changing threat landscape make this a top priority (Gahi, Y., 2019). When it comes to cybersecurity, poor data quality can be caused by things like missing or incomplete log entries, incorrect timestamps, inconsistent data formats, and intrusion detection systems that produce false positives or false negatives. The cybersecurity dataset data quality could be improved by the framework.

Healthcare: Inaccurate patient records, inconsistent or missing diagnoses, and treatment discrepancies are some causes of poor data quality in healthcare information systems. The reliability of medical research, decisions, and patient care can all be severely compromised by these anomalies. These problems can be handled by the framework by selecting related features like patient IDs, medical diagnoses, and treatment histories.

Trasportation: Anomalies in data quality can occur in transportation networks due to things like incorrect vehicle identification numbers, missing route information, inconsistent timestamps, and inaccurate location data. Errors can make it harder to find the best route, predict delays, and control traffic.

These problems can be handled by the framework by picking out related features like location coordinates, timestamps, and vehicle attributes. Banking : In the banking industry, inconsistent transaction records, erroneous customer information, missing account details, and inconsistencies in financial statements can all result from poor data quality. Problems with noncompliance, ill-informed decisions, and financial losses can all stem from aberrations. To solve these problems, the framework can identify and examine interrelated client identifiers, account details, and transaction types. By using anomaly detection and filling in missing or inconsistent data, the framework can validate financial datasets, fix transaction errors, and reconcile account information. Financial institutions, transportation companies, healthcare providers, online retailers, and personal information managers can all benefit from the data quality anomaly correction framework.

4. Results analysis

4.1 Examination Analysis of a comprehensive data model using multiple sources

The system optimizes and expands standard processes to address issues in multisource significant data unification, taking into account the data preparation requirements of multisource analysis and centralization management. The solution pertains to the establishment of the view, the definition of data preparation process components, and their organization. Computer networks provide convenience and enhanced office efficiency; however, they also present security risks, including software vulnerabilities, hacker attacks, malicious codes, and protocol vulnerabilities. These threats have the potential to inflict varying degrees of damage on computers.

The multisource human data platform's data preparation results are saved and supported for analysis and centralized management tasks. Enabling unified big data management from access to output and displays, the e-platform integrates human data access, editing process management, and execution. Data is saved as part of the data preparation process to facilitate subsequent tasks and increase flexibility in multisource big data. The attacker is presented with a significant obstacle by the weakest attack link, as they are required to generate events at various stages of the attack chain in order to accomplish their goal.

However, attack independence implies that there is little chance of attack chain related events happening in the absence of an attack. Thus, it follows that the coincidence of multiple events in an attack chain is implied. On the other hand, analysts can reconstruct the attack scenario by using the association between these events. This article also focuses on using different source events for association analysis. The analysis presented suggests that studies concentrating on network attack chains have a clear advantage when it comes to characterizing attack scenarios and improving comprehension. Furthermore, it is possible to recognize crucial phases in the attack implementation process and quickly intercept them during defense by using forwarding mapping and reverse reasoning of attack chains.

The analysis and detection of Advanced Persistent Threats (APTs) frequently lag behind the actual attack due to the slowness of defense mechanisms. The dynamic security model suggests that there may be a longer lag between the time an attack is discovered and successfully carried out. $E_t - D_t + R_t - P_t > 0$. is the equation. Only when P_t is greater than $D_t + R_t$ can the system be guaranteed to be secure.

The MCKC network attack chain model can be used to decrease the time it takes to detect an attack, thereby increasing system security. The relationship's description cannot exist without the keyword. The variable $n(t, R)$ indicates how frequently it occurs in R . The following is the equation to calculate $P(t|\theta_{ees})$. To create a single, cohesive viewpoint, information about the target views' and data sources' structures must be gathered.

The flexibility of the data preparation process should be increased by including an editing page that is easy to use. On this page, users will be able to choose which components of the data preparation process to edit and change the properties of those components. In addition, functions for uploading and generating process files should be included in a data preparation process that can handle multiple big data sources.

The MCKC model improves on earlier techniques in most metrics. The lightweight model retains a recursive structure to faithfully represent the lateral movement within the internal network while condensing the attack process into five stages. Because the bidirectional analysis method supports both cyclic iterative analysis and metadata analysis, it is more akin to human analytical cognition.

One advantage of the proposed MCKC model is that it can help analysts who analyze and comprehend complex attack events in large enterprise networks by reducing their cognitive load. This is achieved by applying a reasoning process that is similar to that of a human analyst and merging data from multiple sources. In order to address the scalability issue during the analysis process, this approach also makes it easier to integrate additional attack processes and creative probes into traditional network environments (Zhou, Z, 2022). Nevertheless, a crucial aspect of APT attack research is quantitative analysis, which the MCKC model lacks. Attack operations need to use tactics that make their actions difficult for defenders to detect.

4.2 Solution Implementation is Defined by Computer Network Security

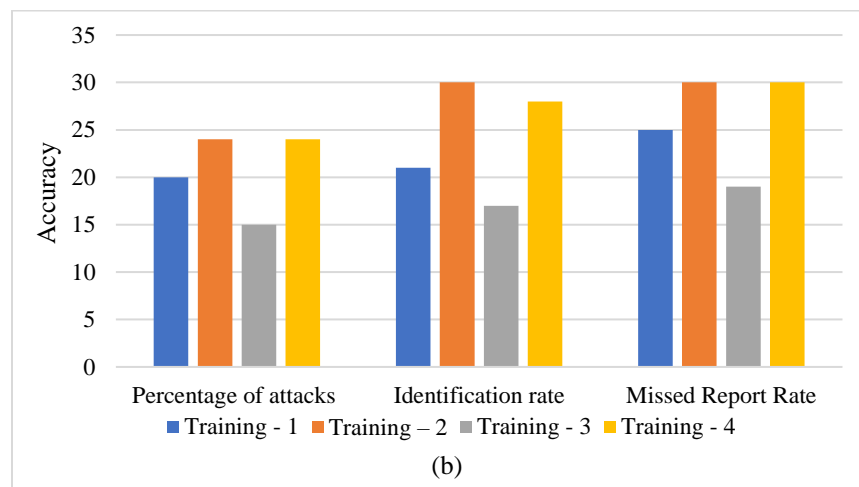
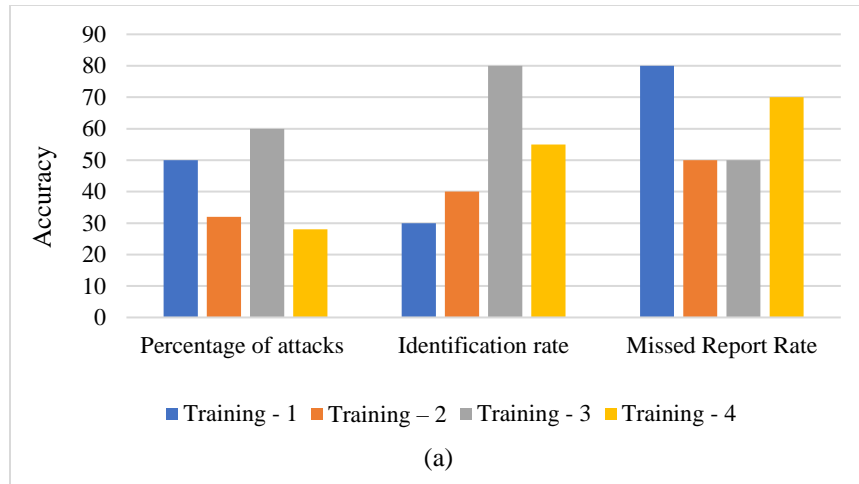
Many methods, including encryption, authentication, identification, and access control, are included in security defense systems. Management is the methodical application of particular security resources to achieve a specific goal.

A security defense system's management involves a variety of activities, including risk assessment, planning, the acquisition of systems and services, authentication, maintenance, and the establishment of policies, standards, and procedures. The information assurance program is significantly influenced by the contributions of individuals, and security defense systems encompass both personnel security and security personnel.

Individuals must possess a high level of security consciousness, knowledge, and proficiency in safety protocols in order to properly design, implement, and supervise security measures. Computer administrators frequently perpetrate specific attacks that originate within the organization. Consequently, it is imperative to possess a comprehensive comprehension of security defense systems. The computer information systems will be frequently used and the users will engage in prolonged operation. In computer systems, administrators typically commence with a model configuration of the system's security, which offers a specific level of protection for the computer information system. Nevertheless, the computer system is unable to accurately identify and prevent malicious attacks, spamming, SQL injection, and improper user operations.

The administration of the system is significantly impeded by these malevolent operations. Based on four critical factors: spamming, SQL injection, user behavior analysis, and access address, we offer a thorough evaluation and analysis. Figure 4 illustrates the degree of user accuracy variability.

Comparative tests were used to assess the impact of the number of iterations on the training set's accuracy, the validation set's accuracy difference, the training set's loss function value change, and the validation set's loss function value change. Additionally, each dataset's various classifications' accuracy, recall, and f1-score were assessed and examined. The experiments compare and assess the conventional approaches to classification: multilayer perceptrons, recurrent neural networks, and basic Bayesian techniques.



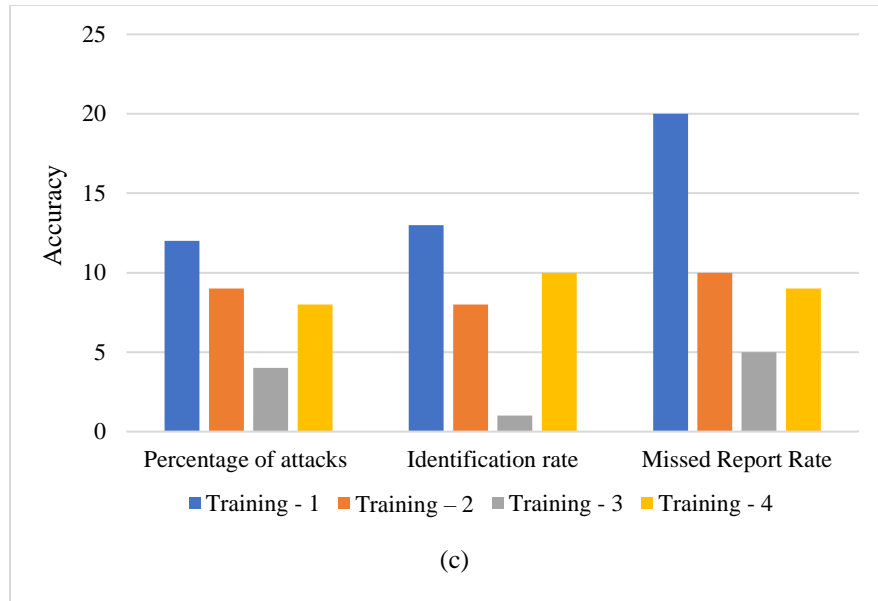


Figure 4: User behaviour accuracy.

Comparative tests were conducted on the exploratory data to adjust the precision of the preparation set in relation to the number of emphasis, the exactness of the approval set in relation to the number of cycles, the worth of misfortune capability of the preparation set in relation to the number of cycles, and the worth of misfortune capability of the approval set in relation to the number of cycles. A correlation of the security defense framework examination findings is illustrated in Figure 5.

Table 1: Security defense system results in the comparison analysis.

Business Continuity (BC), Access Control (AC), Common Criteria (CC), Corporate Governance (CG)

	BC/AC	CC/BC	CG/CC
User behavior	30%	59%	15%
SQL Injection	44%	32%	27%
Spam	55%	31%	17%
Access Address	14%	31%	58%

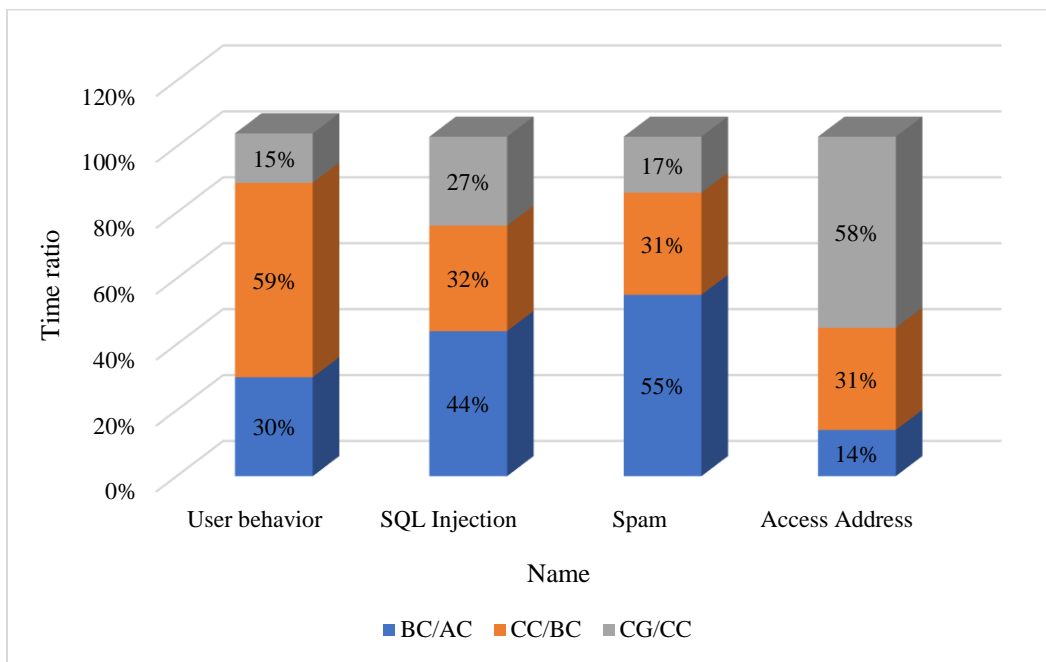


Figure 5: Security defence system findings in the comparative analysis.

A comprehensive overview of the virtual machine preliminary stage of the cautious structure's improvement is provided. The virtual machine's configuration and the associated writing computer programs are thoroughly examined to determine the anticipated reasonable environment for the preliminary stages of the distinctive protective system. The unique defense framework's strength and reasonableness were evaluated in a LAN environment that had been developed. The trial results revealed that the network hosts of one or two types of assigned exercises that were protected by the unique defense framework were generally able to transmit without feeling immediately alert and with minimal impact on the underlying network structure's performance. When an aggressor examines the network protected by the distinctive defense design and endeavors to determine its geographic location, they are unable to view the actual IP address information of the LAN. In fact, the extraordinary defense framework can thwart the aggressor's sifting checks, thereby increasing the attack cost

5. Conclusion and future scope

Quantitative evaluation research and cybersecurity are the topics that are discussed in this article. Following this, the current state of research in the areas of cybersecurity modeling and quantitative assessment is revealed. Lastly, it evaluates the degree to which there are gaps in the research. Comprehensive findings have been obtained through the application of optimization techniques, the measurement of network security defense systems, and the modeling of information system network security. These findings are supported by the fact that the proposed solutions have been demonstrated to be effective in practice. A rule-based algorithm that systematically investigates security device deployment configurations and enables configuration modification is proposed in this article. The goal of the algorithm is to improve and optimize network security defense systems. For the purpose of determining the significance of security devices and differentiated optimization, this foundation is utilized. For the purpose of determining the most effective approach to putting in place a network security defense system, an optimization solution is developed. The implementation of a measurement scheme is a solution to the problem of redundant stacking of security device functions as well as inefficient deployment. For the purpose of developing an effective defense system measurement and optimization system, the proposed network security defense system measurement and optimization scheme is utilized. The system is comprised of modules that are responsible for data entry, defense system evaluation, traversal of deployment methods, and optimization. Defense system evaluation and optimization are both within the realm of possibility. The proposed method for measuring and optimizing the network security defense system in applications that are actual in the real world. The effectiveness of the network security defense system scheme that is described in this article has been demonstrated through the results of optimization and measurement.

When it comes to our future work, one of the most important components will be the enhancement of the framework for anomaly correction. In order to meet the ever-increasing demand for real-time data processing, the framework will be modified to include real-time monitoring of the quality of the data. This includes the investigation of methods for correcting anomalies and monitoring the quality of data in real time.

References

- [1] Zarei, S.M.; Fotohi, R. Defense against flooding attacks using probabilistic thresholds in the internet of things ecosystem. *Secur. Priv.* 2021, 4, e152.
- [2] Zhou, Z.; Tian, Y.; Xiong, J.; Ma, J.; Peng, C. Blockchain-enabled Secure and Trusted Federated Data Sharing in IIoT. *IEEE Trans. Ind. Inform.* 2022; Early Access.
- [3] Prvan, M.; Ožegović, J. Methods in Teaching Computer Networks: A Literature Review. *ACM Trans. Comput. Educ.* 2020, 20, 1–35.
- [4] Nour, B.; Mastorakis, S.; Ullah, R.; Stergiou, N. Information-Centric Networking in Wireless Environments: Security Risks and Challenges. *IEEE Wirel. Commun.* 2021, 28, 121–127
- [5] A. Ju, Y. Guo, and T. Li, “MCKC: a modified cyber kill chain model for cognitive APTs analysis within Enterprise multimedia network,” *Multimedia Tools and Applications*, vol. 79, no. 39-40, pp. 29923–29949, 2020.
- [6] Bhat, S. A., & Huang, N. F. (2021). Big data and ai revolution in precision agriculture: Survey and challenges. *Ieee Access*, 9, 110209-110222.
- [7] C. Zhou, H. Wang, C. Wang et al., “Geoscience knowledge graph in the big data era,” *Science China Earth Sciences*, vol. 64, no. 7, pp. 1105–1114, 2021.
- [8] D. Wang, J. Yu, B. Liu, C. Long, P. Chen, and Z. Chong, “Integrated energy efficiency evaluation of a multi-source multi-load desalination micro-energy network,” *Global Energy Interconnection*, vol. 3, no. 2, pp. 128–139, 2020.
- [9] R. Vinayakumar, K. P. Soman, P. Poornachandran, “Applying convolutional neural network for network intrusion detection,” In *2017 International Conference on Advances in Computing, Communications and Informatics (ICACCI)*, IEEE, 2017, September, pp. 1222–1228.
- [10] H. Sun, Z. Yao, and Q. Miao, “Design of macroeconomic growth prediction algorithm based on data mining,” *Mob. Inf. Syst.*, vol. 2021, no. 7, pp. 1–8, 2021.
- [11] Jeyepalan, D. P., & Kirubakaran, E. (2019). High performance network intrusion detection model using graph databases. *International journal of computational intelligence and information security* December 2019.
- [12] Essid, M., & Jemili, F. (2016). Combining intrusion detection datasets using MapReduce. *proceedings of the International Conference on Systems, Man, and Cybernetics*.

- [13] Ben Fekih, R., & Jemili, F. (2018). Distributed architecture of an Intrusion detection system based on cloud computing and big data techniques. 8th International Conference on Sciences of Electronics, Technologies of Information and Telecommunications (SETIT 2018).
- [14] Radhakrishna, V., Aljawarneh, S., Kumar, P. V., Janaki, V., & Cheruvu, A. (2019). Tree based data fusion approach for mining temporal patterns. Proceedings of the 5th international conference on engineering and MIS (ICEMIS '19). association for computing machinery, New York, NY, USA.
- [15] Singh, O. P., Singh, A. K., & Zhou, H. (2022). Multimodal fusion-based image hiding algorithm for secure healthcare system. *IEEE Intelligent Systems*.
- [16] Fadhil, S. A., Lubna, E. K., & Sayl, G. A. (2021). Protection measurements of computer network information security for big data. *Journal of Discrete Mathematical Sciences and Cryptography*, 24(7), 1959–1965. doi:10.1080/09720529.2021.1959996
- [17] Gupta, R., Tanwar, S., Tyagi, S., & Kumar, N. (2020). Machine learning models for secure data analytics: A taxonomy and threat model. *Computer Communications*, 153, 406-440.
- [18] Hajjaji, Y., Boulila, W., Farah, I. R., Romdhani, I., & Hussain, A. (2021). Big data and IoT-based applications in smart environments: A systematic review. *Computer Science Review*, 39, 100318.
- [19] Iqbal, R., Doctor, F., More, B., Mahmud, S., & Yousuf, U. (2020). Big data analytics: Computational intelligence techniques and application areas. *Technological Forecasting and Social Change*, 153, 119253.
- [20] J. Hu, S. Cai, T. Huang et al., "Vehicle travel destination prediction method based on multi-source data," *Automotive Innovation*, vol. 4, no. 3, pp. 315–327, 2021.
- [21] Khang, A., Abdullayev, V., Ali, R. N., Bali, S. Y., Mammadaga, G. M., & Hafiz, M. K. (2024). Using Big Data to Solve Problems in the Field of Medicine. In *Computer Vision and AI-Integrated IoT Technologies in the Medical Ecosystem* (pp. 407-418). CRC Press.
- [22] L. Wang, M. Peng, and Q. Zhou, "Pre-impact fall detection based on multi-source CNN ensemble," *IEEE Sensors Journal*, vol. 20, no. 10, pp. 5442–5451, 2020.
- [23] M. S. Tehrani, S. Jones, F. Shabani, F. Mart´inez-Alvarez, and ´ D. Tien Bui, "A novel ensemble modeling approach for the spatial prediction of tropical forest fire susceptibility

using Logit Boost machine learning classifier and multi-source geospatial data,” *Theoretical and Applied Climatology*, vol. 137, no. 1-2, pp. 637–653, 2019.

- [24] N. Sanden and G. Neideck, “Learnings from the development of public sector multi-source enduring linked data assets,” *Australian Journal of Social Issues*, vol. 56, no. 2, pp. 288–300, 2021.
- [25] Oluwafunmilayo G . An Assessment of Cybersecurity Technologies in the Selected Universities in Southwestern Nigeria[J]. *International Journal of Computer Applications*; 2019; 178(50):11-18.
- [26] Pramanik, S., & Bandyopadhyay, S. K. (2023). Analysis of big data. In *Encyclopedia of data science and machine learning* (pp. 97-115). IGI Global.
- [27] Anjum, N., Latif, Z., Lee, C., Shoukat, I. A., & Iqbal, U. (2021). MIND: A multi-source data fusion scheme for intrusion detection in networks. *Sensors*, 21(14), 494.
- [28] Aleroud, A., & Karabatis, G. (2017). Contextual information fusion for intrusion detection: a survey and taxonomy. *Knowledge and Information Systems*, 52(3), 563–619.
- [29] Q. Guo, S. Jin, M. Li et al., “Application of deep learning in ecological resource research: theories, methods, and challenges,” *Science China Earth Sciences*, vol. 63, no. 10, pp. 1457–1474, 2020.
- [30] Ragazou, K., Passas, I., Garefalakis, A., Galariotis, E., & Zopounidis, C. (2023). Big data analytics applications in information management driving operational efficiencies and decision-making: mapping the field of knowledge with bibliometric analysis using R. *Big Data and Cognitive Computing*, 7(1), 13.
- [31] S. S. Harsha, H. Simhadri, and K. Raghu, “Distinctly trained multi-source CNN for multi camera based vehicle tracking system,” *International Journal of Recent Technology and Engineering*, vol. 8, no. 2, pp. 624–634, 2019.
- [32] Tao, D., Yang, P., & Feng, H. (2020). Utilization of text mining as a big data analysis tool for food science and nutrition. *Comprehensive reviews in food science and food safety*, 19(2), 875-894.
- [33] Ullah, F., Salam, A., Abrar, M., & Amin, F. (2023). Brain tumor segmentation using a patch-based convolutional neural network: A big data analysis approach. *Mathematics*, 11(7), 1635.

- [34] Widad Elouataoui, Saida El Mendili, and Youssef Gahi, “An Automated Big Data Quality Anomaly Correction Framework Using Predictive Analysis” *Journal Data*, MDPI, December 2023.
- [35] Gahi, Y.; El Alaoui, I. A Secure Multi-User Database-as-a-Service Approach for Cloud Computing Privacy. *Procedia Comput. Sci.* 2019, 160, 811–818.
- [36] Vasa, J., & Thakkar, A. (2023). Deep learning: Differential privacy preservation in the era of big data. *Journal of Computer Information Systems*, 63(3), 608-631.
- [37] Wu, J., Wang, J., Nicholas, S., Maitland, E., & Fan, Q. (2020). Application of big data technology for COVID-19 prevention and control in China: lessons and recommendations. *Journal of medical Internet research*, 22(10), e21980.
- [38] X. Chen, D. Zhao, W. Zhong, and Y. Jiufeng, “Research on information sharing technology of mental health alliance based on multi-source heterogeneous data fusion algorithms,” *Academic Journal of Computing & Information Science*, vol. 2, no. 1, pp. 74–80, 2019.
- [39] Y. Xiong and F. Zhang, “Effect of human settlements on urban thermal environment and factor analysis based on multisource data: a case study of Changsha city,” *Journal of Geographical Sciences*, vol. 31, no. 6, pp. 819–838, 2021.
- [40] Z. Xiong, H. Xu, W. Li, and Z. Cai, “Multi-source adversarial sample attack on autonomous vehicles,” *IEEE Transactions on Vehicular Technology*, vol. 70, no. 3, pp. 2822–2835, 2021.

Separation of yttrium y(iii) from rubidium rb(i) using poly hydroxamic acid

Aly A. A. Soliman^{1*}, Khalid F. Hassan¹, Hossameldin G. Mohamedbagr¹, Mohamed S. Thabet¹, Zeinhom H. Mohamed¹, Medhat M. El-Moselhy¹

¹Department of Physical Sciences, Chemistry Division, College of Science, Jazan University, P.O. Box. 114, Jazan 45142, Kingdom of Saudi Arabia

Abstract: The polyhydroxamic acid PHA performed better when used as a simulation mode for the single-step separation of ⁸⁶Y from Rb. While Polyacrylamide (PAAm) was modified with hydroxylamine to create (PHA) resin. Acrylamide monomers were polymerized using a γ - ray method to create polyacrylamide. PHA was utilized for the way to simulate obtaining ⁸⁶, ⁸⁷, and ⁸⁸Y from Rb. In relationship to pH, the yttrium and rubidium adsorption behaviors on the produced PHA under various environments, including, acetate and citrate buffer solutions as well as HCl, have been investigated. In the present investigation, we found that Y(III) and Rb(I) were separated using PAH resin at pH 5.5, where Rb passed through the column while Y was retained. Y was totally eluted using 2 M HCl.

Keywords: PHA Resin, Polyacrylamide, Gamma Rays, Separation, Y, Rb.

***Corresponding author:**

Assistant Professor, Department of Physical Sciences, Chemistry Division, College of Science, Jazan University, P.O. Box. 114, Jazan 45142, Kingdom of Saudi Arabia, Tel: +966-569091433; e-mail address: asoliman@jazanu.edu.sa.

فصل اليتريوم Y(III) من الروبيديوم Rb(I) باستخدام حمض البولي هيدروكساميك

الملخص: أظهر حمض البولي هيدروكساميك PHA أداءً أفضل عند استخدامه كنمط محاكاة للفصل نظير Y86 من Rb. بينما تم تعديل بولي أكريلاميد (PAAm) باستخدام هيدروكسيل أمين لإنشاء راتينج (PHA). تم بلمرة مونومرات الأكريلاميد باستخدام طريقة أشعة جاما لإنشاء بولي أكريلاميد. تم استخدام PHA لطريقة محاكاة لإنتاج نظائر Y 88,87,86 من Rb. تم دراسة سلوكيات امتصاص اليتريوم والروبيديوم على PHA المنتج في بيئات مختلفة حسب قيمة pH، بما في ذلك المحاليل المنظمة كالأسيات والسترات بالإضافة إلى حمض الهيدروكلوريك. وجد أن Y (III) و Rb (I) تم فصلهما باستخدام راتينج PAH عند درجة حموضة 5.5، حيث مر Rb عبر العمود بينما تم الاحتفاظ بـ Y. تم غسل Y تمامًا باستخدام 2 مولار حمض الهيدروكلوريك.

الكلمات المفتاحية: راتنج PHA، بولي أكريلاميد، أشعة جاما، فصل، Y، Rb.

1. Introduction

The labeled molecules with the indexes of $^{86g,87g,88g}Y$ isotopes have been used in medical diagnostics procedure, tumor therapy, biological tracers or detector calibration. The extraction of radioactive substances from their surrounding substrate constitutes one of the fundamental activities performed in radiochemical labs. β^+ emitters radionuclides with medicinal applications were created (Qaim, 2011). β^+ emitters, ^{86}Y ($T_{1/2} = 14.7$ h), have been made in one of two ways: either by irradiating strontium with proton or by irradiating rubidium (Vértes et al., 2003) with 3He (Abdollah Khorshidi, 2023). For the radiochemical separation of yttrium from rubidium in earlier study, solvent extraction and ion-exchange chromatography were utilized. (Agarwal et al., 2003; Garmestani et al., 2002; Mitra, A. et al., 2021; S. Kandil et al., 2009; S. A. Kandil et al., 2007; Kettern et al., 2002; Pal et al., 2006; Abdollah Khorshidi, 2023). For the purpose of this work, PAAm was modified to generate (PHA) resin, which was then employed as an emulator approach to separate $^{86, 87, \text{ and } 88} Y$ from its parent Rb.

Since more than 40 years ago, hydroxamic acid (HA) groups were discovered in chelating ion-exchange resins, and numerous analytical uses for these polymers have been researched. Numerous heavy metal ions derivatives and the HA groups are known to produce stable chelates. (Cao et al., 2020; Hosseini, 2011; Johann et al., 2019; Li & Yamamoto, 2013; Mzinyane et al., 2021; Singha & Pal, 2020). HA, with the general formula R-CO-NHOH, is regarded as the compounds that result from the hydrogen that is bonded to nitrogen in the HA molecules.

By polymerizing poly(ethylacrylate-divinylbenzene) and then reacting with NH_2OH , (PHA) resins were created (Lee & Hong, 1994). Using copoly(acrylamide-divinylbenzene) and NH_2OH hydrochloride under the influence of KOH, as well as acrylhydroxamic acid and divinylbenzene and free radical solution polymerization, (PHA) chelating ion-exchange resins were created. For the sorption of the ions Fe^{3+} , Cu^{2+} , Co^{2+} , and Pb^{2+} , the generated resins were applied (Khodadadi, R. et al., 1995). By reacting ethylacrylate/acrylonitrile/divinylbenzene copolymer with NH_2OH under the influence of sodium ethoxylate, Using amidoxime and hydroxamic groups, a novel ion-exchanger was developed (Lee et al., 2001).

Ethylacrylate and divinylbenzene have been utilized to create (PHA) resin Cu^{2+} and Fe^{3+} metal ions were complexed with the ready resins. A coordination complex was created by the ligand between a metal ion and an oxygen atom from a carbonyl group (Neagu et al., 2003). Through modification of (PAAm), which was originally produced by employing γ rays as an initiator to polymerize acrylamide monomers, The PHA has been created. NH_2OH is used to treat (PAAm) and change the amide group into a hydroxamic group. Y^{3+} and Sr^{2+} were isolated from Zr^{6+} using (PHA) resin (Hassan et al., 2011). Sago starch that had been modified with poly(methylacrylate) was utilized to create a new polymer with HA functional group using hydroxylamine in an alkaline solution (Lutfor et al., 2001)

2. Experimental

2.1. Reagents and chemicals.

Acrylamide was purchased from Merck for this investigation (Darmstadt, Germany). The crosslinking agent employed was N,N-methylene-bis-acrylamide (NMBA), which was purchased from Sigma-Aldrich (St. Louis, MO, USA). To change the pH of the medium, sodium hydroxide and hydrochloric acid were purchased from Merck, hydroxylamine hydrochloride from Fluka (Buchs, Switzerland). Y_2O_3 99.97% from Cambridge, England's Koch-Light Laboratories Ltd; RbCl 98% (from Aldrich).

2.2. Instrumentation.

With the aid of the ULTIMA2 ICP instrument from Jobin Yvon S. A., France, the composition of the separated material was examined using inductively coupled plasma optical emission spectrometry (ICP-OES).

2.3. Gamma Cell

The irradiation source was a ^{60}Co gamma cell of the Russian type MC-20, with a dosage rate of 2 kGy h^{-1} , it contains two 5-liter chambers.

2.4. FT-IR Analysis.

The FT-IR spectrometer (Bomen, Hartman & Borunz spectrometer, Model MB 157) was used to collect the infrared spectra of polymer samples that contained KBr pellets.

2.5. SEM

The morphology of the resin was determined by scanning electron microscopy (SEM) (Mira3, Tescan, Brno, Czech Republic).

2.6. Preparation of (PHA).

When acrylamide monomers in an aqueous solution are polymerized by radiation, NMBA is used as an agent to crosslink the monomers, resulting in crosslinked polyacrylamide (PAAm) (Park et al., 2004). A solution of 10 g acrylamide and 1 g NMBA was prepared using 100 cc of distilled water. After putting the mixture into glass ampoules, air was removed from the ampoules using nitrogen gas. Before being exposed to ^{60}Co radiation at a dosage rate of 2 kGy h^{-1} , the ampoules were sealed. The fragmented irradiation crosslinked polymers were then cleaned with acetone and water to remove any lingering monomers, dried, and stored. The conversion percentage, which was calculated by gravimetric analysis and was found to be roughly 90%, was determined.

PHA in hydrogen form was created by adding a determined amount of sodium hydroxide and hydroxylamine hydrochloride solutions to a slurry of dry crosslinked PAAm (Siyam, 2001). After that, the mixture was agitated at room temperature for five minutes. After six hours at 70 °C, the response was maintained. H⁺ was released as a byproduct of the process. Following a thorough wet, the generated (PHA) was filtered out of the combination. Next, for a minimum of five minutes, the resin was immersed in a 3 M HCl solution. The resin underwent filtration and many water washes to remove any remaining chlorine, and it was then dried at 50 °C until its weight remained consistent.

2.7. Experiment in batches.

The distribution coefficient must be determined to distinguish between Y and Rb. A stock solution of 5000 mg/L Y and Rb was prepared. The mixture was heated up until almost dry, and the remaining material was dissolved in 100 cc of double-distilled water.

50 mg of sorbent and 100 µl of stock solution were combined. Then, 4.9 ml of various HCl concentrations or an alternate medium, like 0.1 M citrate buffer or 0.1 M acetate buffer at various pH were supplied in 100mm x 15 mm ampoule. The ingredients were stirred to reach equilibrium for two hours. Using the following equation, the distribution coefficient (K_d) was determined (Saraydin et al., 2001) .

$$K_d = \frac{C_{ads}}{C_{unads}} \times \frac{v}{m}$$

where v is the volume of the aqueous phase in milliliters, m is the amount of the resin in grams, C_{ads} is the concentration that has been sorbed on the resin, and C_{unads} is the concentration that is still in solution.

To measure the quantities of yttrium and rubidium in each batch experiment, ICP-OES will be used.

2.8. Cation-Exchange Column Chromatography.

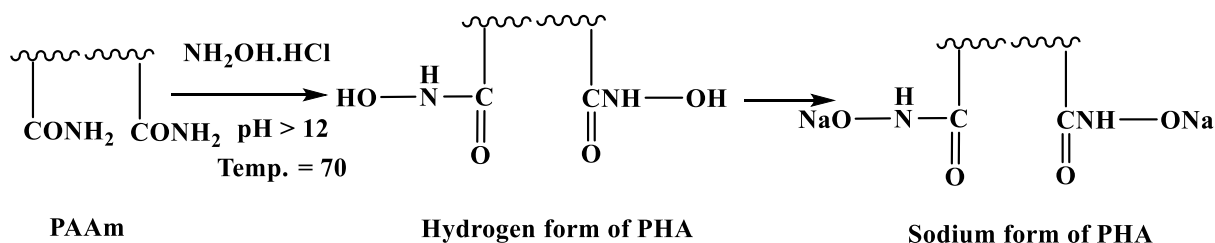
This work involved a thorough investigation of the separation of Y from Rb utilizing PHA resin and 2 M HCl. A100 ml solution containing 100 ppm of Y and Rb dissolved in acetate buffer pH 5.5 was loaded onto a 22 cm long x 1.5 cm diameter column packed with PAH at a depth of 2 cm. Quartz wool was positioned at the top exchanger to prevent the adsorbent particles from being disturbed during solution addition and to regulate the flow of solutions through the column. A 1 ml stock sample was retained as a control. During this phase, load samples were collected to look for breakthrough. The load samples' ICP analysis confirmed that there was no Y column breakout. A further 50 cc of acetate buffer pH 5.5 was used to wash the column.

The resin was completely adsorbed by yttrium whereas rubidium passed through the column. To elute Y, 135 ml of 2 M HCl were used. Nine samples, totaling approximately 15 milliliters, were gathered and put through an ICP analysis. Below are the specifics of the separating process.

3. Results and Discussion

3.1. The Resin's preparation.

PHA resin is created when sodium hydroxide and hydroxylamine hydrochloride combine with comparable crosslinked PAAm (Siyam 2001). The sodium form of PHA and hydrogen are produced in a hypothetical reaction between PAAm, sodium hydroxide, and hydroxylamine hydrochloride, as schematically shown in Scheme 1.

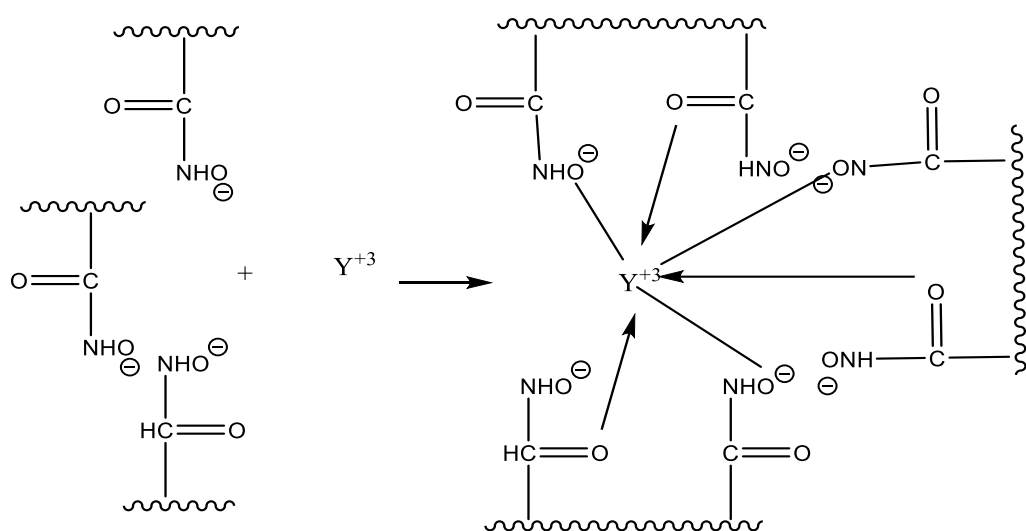


Sch. (1): Preparation of PHA from PAAm.

3.2. Analysis using FT-IR.

The polyacrylamide (PAAm), polyhydroxamic acid (PHA), and metal-loaded PHA samples' infrared spectra are displayed in Figure 1. The crosslinked PAAm's infrared spectra exhibits absorption bands for carbonyl groups, amide (N-H), and CH₂ stretching at 3401, 2998, and 1649 cm⁻¹, respectively. PHA resin exhibited discrete absorption bands at 3200, 3444, 1670, and 930 cm⁻¹, corresponding to hydroxamic (O-H), amide (N-H), carbonyl, and (N-O) groups. The absorption band at 2862 cm⁻¹ is connected to the C=N group in hydroxamic acid's enol form. By comparing the spectra of the PHA sample and the metal ion loaded PHA sample, it is possible to see that the N-O band shifts in the metal ion loaded sample from 930 to 775 cm⁻¹ as a result of the interaction of homologous groups with metal ions.

The N-O group of the sorbent exhibits lower stretching frequency due to the stronger M-O bond, which is indicative of a significant interaction between metal ions and the N-O group. The O-M-O stretching vibrations' additional peaks, which are visible at a wavelength of about 700 cm⁻¹, can also be identified. In Scheme 2, it is depicted how metal ions might interact with PHA polymers (Tompkins & Mayer, 1947)



Sch. (2): Yttrium ion interactions with PHA resin.

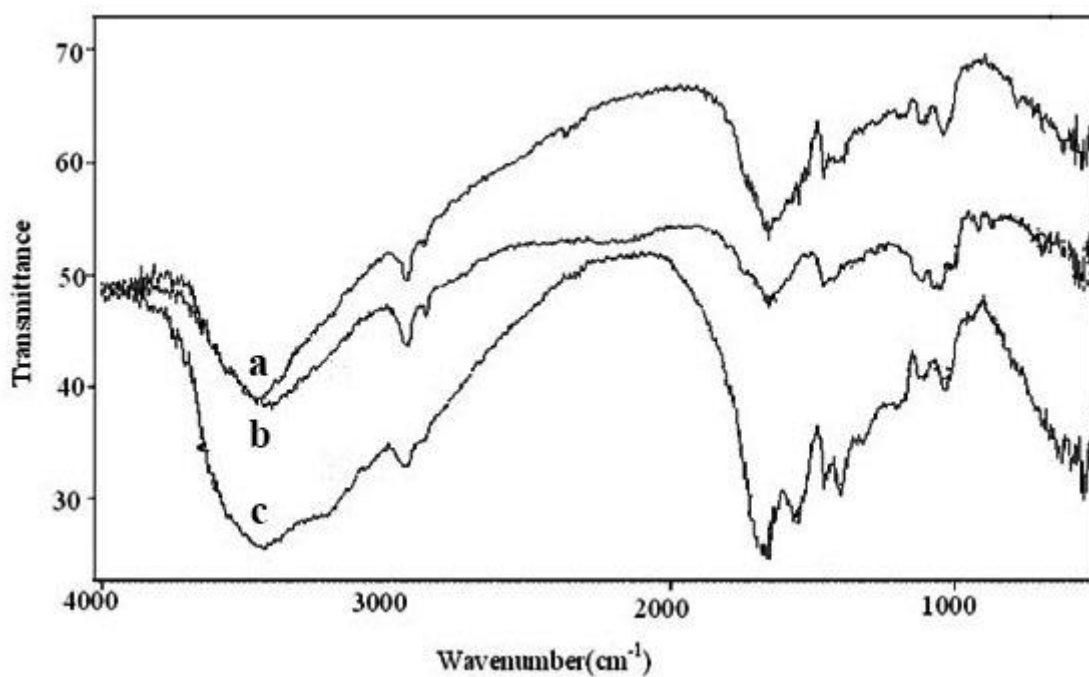


Fig. (1) : FTIR spectra of a) The polyacrylamide (PAAm), b) polyhydroxamic acid (PHA), and c) metal-loaded PHA

3.3. SEM

SEM analysis is a productive way to view morphology. Figure 2 shows the morphologies of the poly (hydroxamic acid) both before and after yttrium Y(III) ions were adsorbed. The presence of coarse pore structures and surface on the resin could have had a role in the adsorption of metal ions. The morphological surfaces changed after adsorption. The resin's porosity and structure altered, and its surface developed a metallic sheen. We reach the conclusion that yttrium Y(III) ions adsorbed on the resin's surface. The outcomes showed that the resin's porous structure is primarily mesoporous.

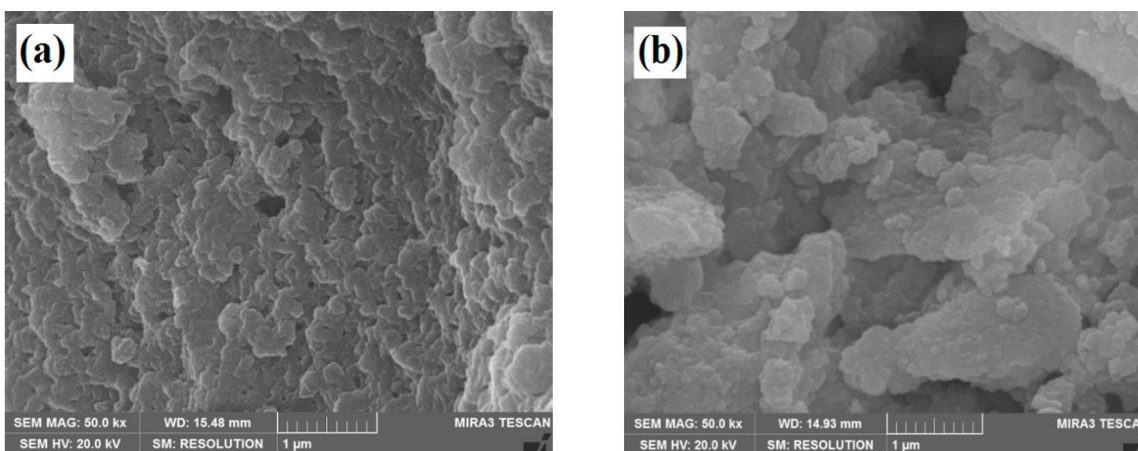


Fig. (2): SEM images of the resin before (a) and after (b) adsorption.

3.4 Behaviors of Y and Rb Adsorption on Cation Exchangers.

Specifically HCl, acetate buffer, and citrate buffer were used to study the yttrium and rubidium adsorption behaviours on the synthetic PHA resin. However, batch mode research has examined the effects of equilibration time based on Y and Rb uptake, finding that equilibrium was attained after two hours of shake.

3.4.1. Hydrochloric Acid.

The effect of pH solution is a significant factor that affects the adsorbent's ability to bind metal ions (Yang, K.Y, et al.2020]. Figure 3 illustrates how pH affects resin adsorption for Y(III). Since yttrium tends to hydrolyze above pH 6, higher pH ranges were avoided for study.

The K_d -values of Rb and Y increased from 10^{-5} to 10^{-3} mol/L, and then they decrease as acidity increased to 0.1 mol/L as a result of a change in PHA resin charge. This can be explained as follows: as pH increases, amide, carboxylic, and amidoxime groups dissociate more readily, creating more binding sites for the adsorption of metal ions. Low levels of metal ion adsorption were observed under more acidic concentration, or low pH values of roughly 2.0–3.0. This is explained by the competition between metal ions and H^+ ions for the active sites. The surface layer of the adsorbent surface may shrink as a result of hydrogen bonds forming between its active sites. This surface layer acts as a barrier slowing down the adsorption of metal ions.

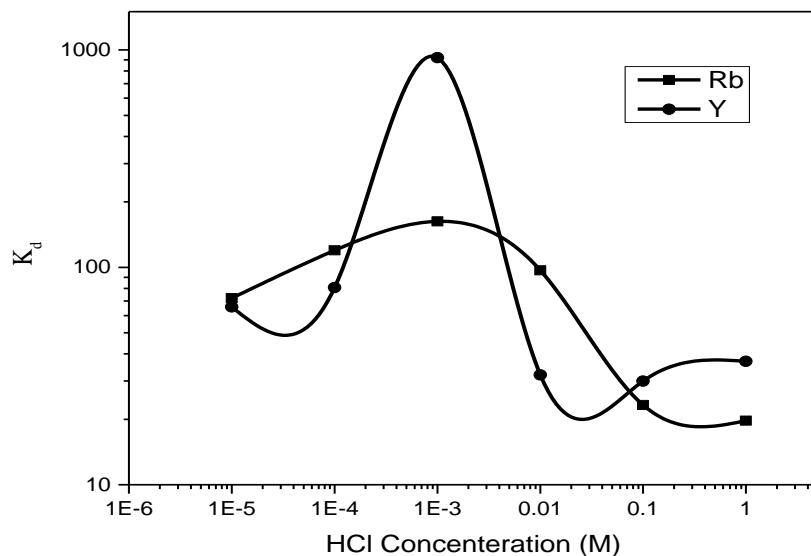


Fig. (3) : Y(III) and Rb(I) distribution coefficients on PHA resin as a function of HCl concentration, with a 2-hour shaking period.

3.4.2. 0.1M Acetate Buffer.

Figure (4) depicts the K_d -values of Rb and Y in 0.1 mol/L acetate buffer over the pH range of 3 to 5.5. As the pH value rises, the K_d -values of Y gradually rise as well. The K_d -values for Rb remain unchanged. Additionally, it has been found that Y is more adsorbable than Rb.

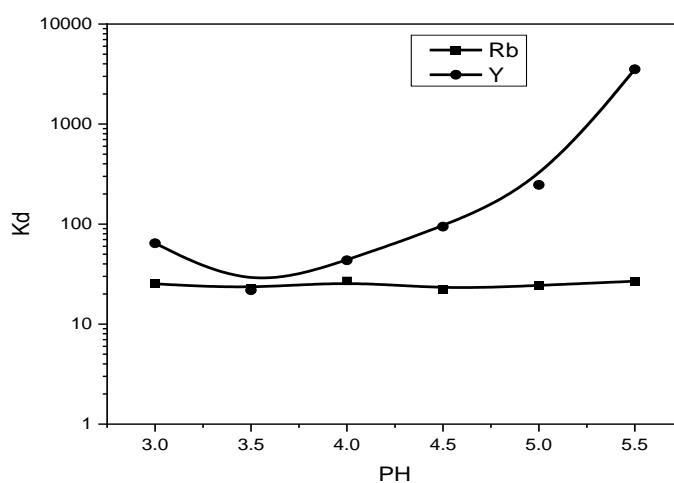


Fig. (4): Y(III) and Rb(I) distribution coefficients on PHA resin with a 2-hour shaking period as a function of pH in 0.1 M acetate buffers.

3.4.3. 0.1 M Citrate Buffer

On the PHA increase, Y and Rb behaviors in 0.1 mol/L citrate buffer at pH values ranging from 3 to 5.5 were examined (Fig. 5). Their modest and largely stable adsorbabilities over the pH range of 3 to 5.5 were demonstrated by the findings.

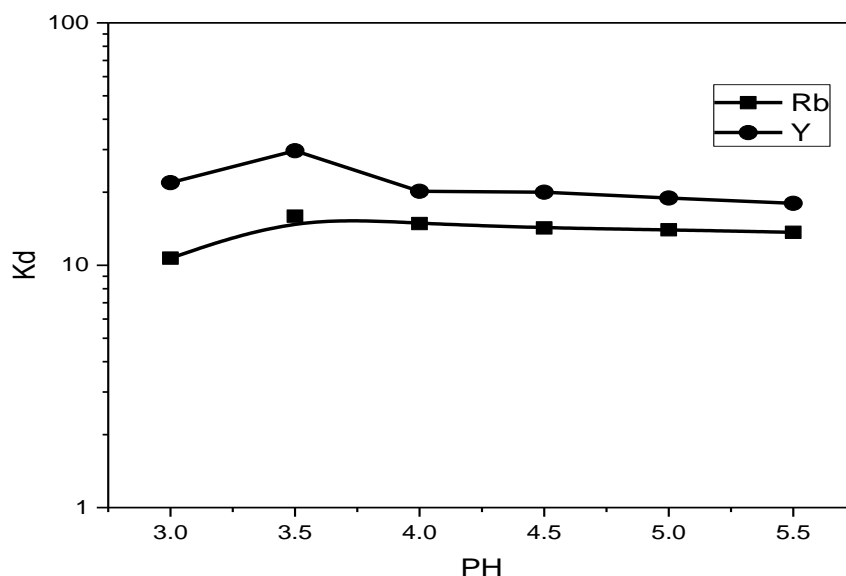


Fig. (5) : Rb(I) and Y(III), distribution coefficients on PHA resin as a function of pH of 0.1 M citrate buffers, shaking period of two hours.

3.5. Effect of Contact Time

The effects of contact time on the adsorption of the (PHA) for Y (III) was investigated and the results are shown in Figure 6. It is clear that the adsorption capacity of Y (III) increased with increases in contact time, reached equilibrium after around two h, and remained steady the rest of the time. Remarkably, the amount of adsorption was obviously faster at the initial stage, potentially because, initially, the adsorbent site was vacant and the solute concentration gradient was high. Thus, it appeared that the adsorption capacity of Y (III) on the resin was a rapid process, with equilibrium reached in two hours (Li, C.X, et al.2015). Therefore, the contact time of three hours was considered appropriate in the following experiments.

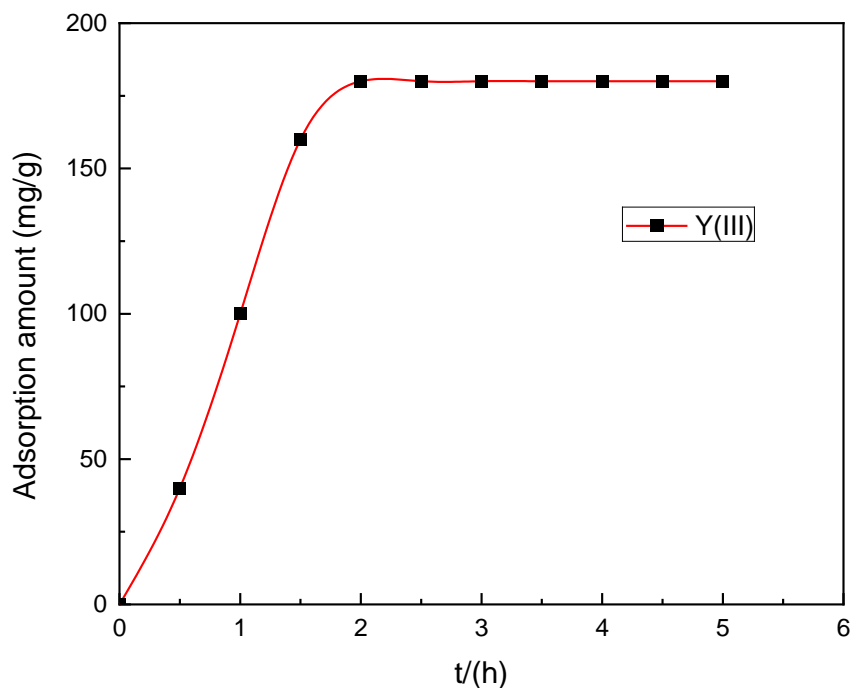


Fig. (6): Effect of contact time on the adsorption (adsorption rate) of Y(III) metal ions onto (PHA) resin.

3.6. Rb(I) and Y(III) separation by PHA-Column Chromatography

The ideal conditions for separating Y from Rb were discovered in batch mode and applied in column mode. Practically, from all of the data on PHA in batch mode that were provided, these components showed a considerable variation that might help separate Y from Rb. Additionally, in column mode, the effective parameter is the flow rate correlated with time. However, 100 ml were supplied at a flow rate of 1.5 ml/min during the loading process. All of the yttrium during loading was adsorbed on the resin, while rubidium went through the column. This indicates that Rb has separated and that Y elution has begun. The elution profile for separating Y from the column was detailed in Fig (7). As previously indicated, a 100 mL stock solution containing 100 ppm of each Rb and Y diluted in 0.1 M acetate buffer pH 5.5 was put into a glass column that measured 22 cm long by 1.5 cm in diameter and 2 cm deep in PHA. Rb displayed low K_d in the 0.1 M acetate buffer at this pH. (3). Rb thus traversed the column with a percentage of 100% of the starting value. No Rb passed through the column after additional washing with 0.1 M acetate buffer pH 5.5, but yttrium was still present (Fig. 4; its K_d -values are fairly high). Y was completely eluted with 2mol/L HCl, and the full amount of yttrium was collected in 135 mL.

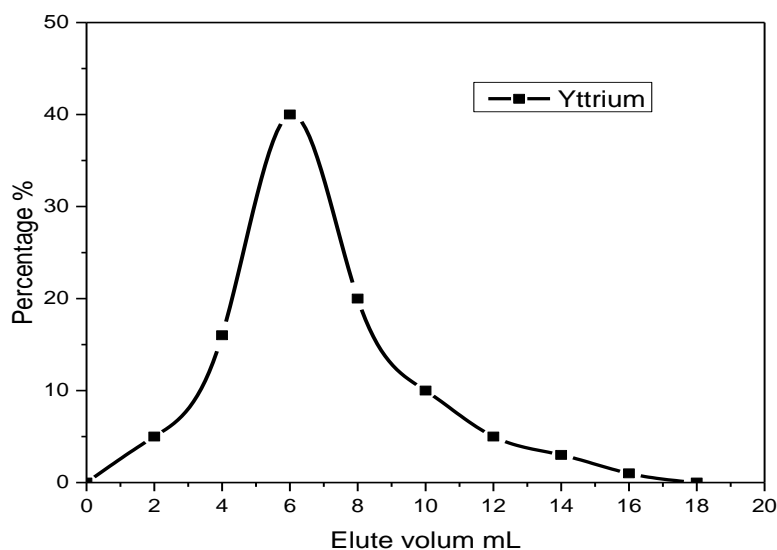


Fig. (7): Y(III) elution profile from a PHA resin-packed column. 15 milliliters is the fraction volume.

4. Conclusion

In this paper, we reported that Poly (hydroxamic acid) PHA resin was prepared by modification of polyacrylamide (PAAm) using hydroxylamine. Polyacrylamide was prepared by polymerization of acrylamide monomers by gamma rays technique. PHA was used for the separation of Y(III) from Rb(I) as a simulation mode for the separation of $^{86,87,88}\text{Y}$ from its parent (Rb). Based on our systematic characterizations and batch adsorption experimental results, the obtained polymer shows that Y(III) and Rb(I) were separated using PAH resin at pH 5.5, where Rb passed through the column while Y was retained. Y was totally eluted using 2 M HCl.

5. Conflicts of interest

“There are no conflicts to declare”.

References

- [1] Agarwal, A., Bhardwaj, M. K., Rizvi, I. A., & Chaubey, A. K. (2003). Measurement and analysis of excitation functions for alpha induced reactions with rubidium. Retrieved from <https://nopr.niscpr.res.in/handle/123456789/25254>
- [2] Baren, M. H., Ibrahim, S. A., Al-Rooqi, M. M., Ahmed, S. A., El-Gamil, M. M., & Hekal, H. A. (2023). A new class of anticancer activity with computational studies for a novel bioactive aminophosphonates based on pyrazole moiety. *Scientific Reports*, 13(1), 14680.
- [3] Cao, X., Zhou, C., Wang, S., & Man, R. (2020). Adsorption Properties for La (III), Ce (III), and Y (III) with Poly (6-acryloylamino-hexyl hydroxamic acid) Resin. *Polymers*, 13(1), 3.
- [4] Garmestani, K., Milenic, D. E., Plascjak, P. S., & Brechbiel, M. W. (2002). A new and convenient method for purification of ^{86}Y using a Sr (II) selective resin and comparison of biodistribution of ^{86}Y and ^{111}In labeled HerceptinTM. *Nuclear Medicine and Biology*, 29(5), 599–606.
- [5] Hassan, K. F., Kandil, S. A., Abdel-Aziz, H. M., & Siyam, T. (2011). Preparation of poly (hydroxamic acid) for separation of Zr/Y, Sr system. *Chromatography Research International*, 2011. Retrieved from <https://downloads.hindawi.com/archive/2011/638090.pdf>
- [6] Hosseini, S. H. (2011). Detection of arsenic agents by polyhydroxamic acid. *Journal of Applied Polymer Science*, 121(4), 2338–2343. <https://doi.org/10.1002/app.30541>
- [7] Johann, T., Keth, J., Bros, M., & Frey, H. (2019). A general concept for the introduction of hydroxamic acids into polymers. *Chemical Science*, 10(29), 7009–7022.
- [8] Kandil, S. A., Spahn, I., Scholten, B., Saleh, Z. A., Saad, S. M. M., Coenen, H. H., & Qaim, S. M. (2007). Excitation functions of (α , xn) reactions on natRb and natSr from threshold up to 26 MeV: Possibility of production of ^{87}Y , ^{88}Y and ^{89}Zr . *Applied Radiation and Isotopes*, 65(5), 561–568.
- [9] Kandil, S., Scholten, B., Hassan, K., Hanafi, H., & Qaim, S. (2009). A comparative study on the separation of radioyttrium from Sr-and Rb-targets via ion-exchange and solvent extraction techniques, with special reference to the production of no-carrier-added ^{86}Y , ^{87}Y and ^{88}Y using a cyclotron. *Journal of Radioanalytical and Nuclear Chemistry*, 279(3), 823–832.

- [10] Kettern, K., Linse, K.-H., Spellerberg, S., Coenen, H. H., & Qaim, S. M. (2002). Radiochemical studies relevant to the production of ^{86}Y and ^{88}Y at a small-sized cyclotron. *Radiochimica Acta*, 90(12), 845–849.
https://doi.org/10.1524/ract.2002.90.12_2002.845
- [11] Khodadadi, R., Fakhri, S. A., & Entezami, A. A. (1995). Poly (hydroxamic acid) chelating resin: The synthesis and uses. *Iranian Journal of Polymer Science and Technology Vol*, 4(4), 11995.
- [12] Khorshidi, A. (2023). Nano Yttrium-90 and Rhenium-188 production through medium medical cyclotron and research reactor for therapeutic usages: A Simulation study, *Nuclear Engineering and Technology*, 55, 5, , 1871-1877,
<https://doi.org/10.1016/j.net.2023.02.013>
- [13] Lee, T. S., & Hong, S. (1994). Synthesis of porous poly(hydroxamic acid) from poly(ethyl acrylate-co-divinylbenzene). *Polymer Bulletin*, 32(3), 273–279.
<https://doi.org/10.1007/BF00308537>
- [14] Lee, T. S., Jeon, D. W., Kim, J. K., & Hong, S. I. (2001). Formation of metal complex in a poly(hydroxamic acid) resin bead. *Fibers and Polymers*, 2(1), 13–17.
<https://doi.org/10.1007/BF02875221>
- [15] Li, C.X.; Zhong, H.; Wang, S.; Xue, J.R.; Zhang, Z.Y. (2015)Removal of basic dye (methylene blue) from aqueous solution using zeolite synthesized from electrolytic manganese residue. *J. Ind. Eng. Chem.*, 23, 344–352.
- [16] Li, Z., & Yamamoto, H. (2013). Hydroxamic Acids in Asymmetric Synthesis. *Accounts of Chemical Research*, 46(2), 506–518. <https://doi.org/10.1021/ar300216r>
- [17] Lutfor, M. R., Sidik, S., Yunus, W. W., Ab Rahman, M. Z., Mansoor, A., & Jelas, H. (2001). Preparation and swelling of polymeric absorbent containing hydroxamic acid group from polymer grafted sago starch. *Carbohydrate Polymers*, 45(1), 95–100.
- [18] Mahesh, P., Akshinthala, P., Katari, N. K., Gupta, L. K., Panwar, D., Sharma, M. K., ... Gundla, R. (2023). Antiproliferative Activity of New Pyrazole-4-sulfonamide Derivatives: Synthesis and Biological Evaluation. *ACS Omega*, 8(29), 25698–25709.
<https://doi.org/10.1021/acsomega.2c07539>
- [19] Mantzanidou, M., Pontiki, E., & Hadjipavlou-Litina, D. (2021). Pyrazoles and pyrazolines as anti-inflammatory agents. *Molecules*, 26(11), 3439.

- [20] Mitra, A., Chakraborty, A., Gaikwad, S., Tawate, M., Upadhye, T., Lad, S., Sahoo, S., Jagesia, P., Parghane, R., Menon, S., Basu, S., Dhami, P., and Banerjee, S., (2021). On the Separation of Yttrium-90 from High-Level Liquid Waste: Purification to Clinical-Grade Radiochemical Precursor, Clinical Translation in Formulation of 90Y-DOTATATE Patient Dose, *Cancer Biotherapy & Radiopharmaceuticals*, 36, 2.
- [21] <https://doi.org/10.1089/cbr.2020.4092>
- [22] Mzinyane, N. N., Ofomaja, A. E., & Naidoo, E. B. (2021). Synthesis of poly (hydroxamic acid) ligand for removal of Cu (II) and Fe (II) ions in a single component aqueous solution. *South African Journal of Chemical Engineering*, 35, 137–152. <https://doi.org/10.1016/j.sajce.2020.09.002>
- [23] Neagu, V., Bunia, I., Plesca, I., & Popa, M. (2003). Synthesis of new chelating ion exchange resin with hydroxamic and amidoxime groups and study of its metal binding property. *Journal of Applied Polymer Science*, 88(13), 2956–2962. <https://doi.org/10.1002/app.12062>
- [24] Pal, S., Chattopadhyay, S., Das, M. K., & Sudersanan, M. (2006). Production and separation of no-carrier-added radioactive tracers of yttrium, strontium and rubidium from heavy-ion irradiated germanium target: Applicability to the standardization of a separation technique for production of positron-emitting radionuclide 86Y. *Applied Radiation and Isotopes*, 64(12), 1521–1527.
- [25] Park, L. S., Szajek, L. P., Wong, K. J., Plascjak, P. S., Garmestani, K., Googins, S., ... Paik, C. H. (2004). Semi-automated 86Y purification using a three-column system. *Nuclear Medicine and Biology*, 31(2), 297–301.
- [26] Qaim, S. M. (2011). Cyclotron production of medical radionuclides. *Handbook of Nuclear Chemistry*, 1903.
- [27] Rösch, F., Qaim, S. M., & Stöcklin, G. (1993a). Nuclear Data Relevant to the Production of the Positron Emitting Radioisotope ⁸⁶Y via the ⁸⁶Sr(p,n)- and ^{nat}Rb(³He,xn)-Processes. *Ract*, 61(1), 1–8. <https://doi.org/10.1524/ract.1993.61.1.1>
- [28] Rösch, F., Qaim, S. M., & Stöcklin, G. (1993b). Production of the positron emitting radioisotope 86Y for nuclear medical application. *Applied Radiation and Isotopes*, 44(4), 677–681.
- [29] Saraydin, D., Isikver, Y., & Sahiner, N. (2001). Uranyl ion binding properties of poly(hydroxamic acid) hydrogels. *Polymer Bulletin*, 47(1), 81–89. <https://doi.org/10.1007/s002890170024>

- [30] Singha, M., & Pal, S. (2020). Removal of toxic metals using a novel PHA resin-fixed bed column performance study. *Journal of Radioanalytical and Nuclear Chemistry*, 326(2), 1193–1198. <https://doi.org/10.1007/s10967-020-07407-y>
- [31] Siyam, T. (2001). Development of acrylamide polymers for the treatment of waste water. *Designed Monomers and Polymers*, 4(2), 107–168. <https://doi.org/10.1163/156855500300203377>
- [32] Tompkins, E. R., & Mayer, S. W. (1947). Ion Exchange as a Separations Method. III. Equilibrium Studies of the Reactions of Rare Earth Complexes with Synthetic Ion Exchange Resins ¹. *Journal of the American Chemical Society*, 69(11), 2859–2865. <https://doi.org/10.1021/ja01203a068>
- [33] Vértes, A., Nagy, S., & Klencsár, Z. (2003). *Handbook of nuclear chemistry* (Vol. 2). Springer Science & Business Media. Retrieved from [https://books.google.com/books?hl=ar&lr=&id=fvoId6Fv5xQC&oi=fnd&pg=PR9&dq=14.%09Vertes+A,+Nagy+S,+Klencsarn+Z,+Kluwer,+Handbook+of+nuclear+chemistry,+volumes+1%E2%80%9335,+Academic+Publishers,+Dordrecht,+47+\(2003\).&ots=rTfqlD7evF&sig=IMzXVu-5ivqBi6CG8tfoWXi6qrU](https://books.google.com/books?hl=ar&lr=&id=fvoId6Fv5xQC&oi=fnd&pg=PR9&dq=14.%09Vertes+A,+Nagy+S,+Klencsarn+Z,+Kluwer,+Handbook+of+nuclear+chemistry,+volumes+1%E2%80%9335,+Academic+Publishers,+Dordrecht,+47+(2003).&ots=rTfqlD7evF&sig=IMzXVu-5ivqBi6CG8tfoWXi6qrU)
- [34] Yang, K.Y.; Xing, J.C.; Xu, P.P.; Chang, J.M.; Zhang, Q.F.; Usman, K.M. (2020) Activated carbon microspheres from sodium lignosulfonate for Cr(VI) adsorption evaluation in wastewater treatment. *Polymers*, 12, 236.

Investigation of levels and human health risk of heavy metals in tea samples marketed in Jazan, Saudi Arabia

Zeinhom H. Mohamed^{1*}, Mustafa S. Elhassan², Mukul sharma³, Medhat Mohamed El-Moselhy⁴, Khaled F. Hassan⁵, Hossameldin G. Mohamedbaker⁶, Emad M. Masoud⁷, and Yasser M. Riyad⁸

¹ Department of Physical Sciences, Chemistry Division, College of Science, Jazan University, P.O. Box. 114, Jazan 45142, Kingdom of Saudi Arabia; zmohamed@jazanu.edu.sa

² Department of Physical Sciences, Chemistry Division, College of Science, Jazan University, P.O. Box. 114, Jazan 45142, Kingdom of Saudi Arabia; Melsebty@jazanu.edu.sa

³ Environment and Nature Research Centre, Jazan University, Jazan 45142, P.O. Box 114, Saudi Arabia; mukulsh77@gmail.com

⁴ Department of Physical Sciences, Chemistry Division, College of Science, Jazan University, P.O. Box. 114, Jazan 45142, Kingdom of Saudi Arabia; mlailah@jazanu.edu.sa

⁵ Department of Physical Sciences, Chemistry Division, College of Science, Jazan University, P.O. Box. 114, Jazan 45142, Kingdom of Saudi Arabia; kferieg@jazanu.edu.sa

⁶ Department of Physical Sciences, Chemistry Division, College of Science, Jazan University, P.O. Box. 114, Jazan 45142, Kingdom of Saudi Arabia; hmohamedbaker@jazanu.edu.sa

⁷ Department of Chemistry, Faculty of Science, Islamic University of Madinah, Madinah 42351, Saudi Arabia; emad.youssef@iu.edu.sa

⁸ Department of Chemistry, Faculty of Science, Islamic University of Madinah, Madinah 42351, Saudi Arabia; yasser.riyad@iu.edu.sa

* Correspondence: zmohamed@jazanu.edu.sa

Abstract: Following water, tea is the most widely used beverage. Tea is regarded as a healthful beverage because of its relationship with a decreased risk of stroke, metabolic syndrome, obesity, and events related to cardiovascular disease. Tea contains a variety of trace minerals and elements that are good for human health, but if they are present in high enough amounts, some of them can be hazardous and cause cancer. This work stands out due to its thorough evaluation of heavy metal levels, and conducting a risk assessment for tea consumers in Jazan region southern of Saudi Arabia. The present research examined the content of 6 different heavy metals in 11 samples of black tea gathered from local markets in Jazan, southern Saudi Arabia: cadmium (Cd), lead (Pb), chromium (Cr), zinc (Zn), copper (Cu), iron (Fe), and zinc (Zn).

Flame atomic absorption spectroscopy (FAAS) was employed to detect heavy metals in tea samples. The Target Hazard Quotient (THQ) and combined hazard index (HI) for heavy metals in tea samples were employed for assessing the health risks to tea consumers. The study found that the median content of Cd, Pb, Cr, Zn, Cu, and Fe in the investigated samples is 1.31, 2.33, 16.07, 27.88, 5.52, and 120.4 $\mu\text{g/g}$, respectively. We compared the concentration of heavy metals in the samples under examination to the World Health Organization's (WHO) maximum allowable levels. The findings demonstrated that the mean levels of Cu, Fe, Pb, Cd, and Zn in tea samples were significantly below the maximum permitted values. Conversely, Cr level in tea samples exceeded the maximum allowable values. THQ mean values were 0.003, 0.05, 0.16, 0.19, 0.69, and 0.8 for Cr, Fe, Zn, Pb, Cu, and Cd, respectively. The THQ values of all metals under investigation were found to be below the permitted limits (less than one). These data show that the individual heavy metals present in the investigated samples do not pose any carcinogenic health concerns. In contrast, the HI value for various heavy metals was determined to be greater than one (1.91) indicating that regular tracking of the levels of heavy metals in black tea samples is required.

Keywords: Evaluation; Heavy metals levels; Tea; Non-carcinogenic health risk

دراسة مستويات ومخاطر المعادن الثقيلة على صحة الإنسان في عينات الشاي المسوقة في جازان، السعودية

الملخص: بعد الماء، يعد الشاي هو المشروب الأكثر استخدامًا. يعتبر الشاي مشروبًا صحيًا بسبب علاقته بانخفاض خطر الإصابة بالسكتة الدماغية ومتلازمة التمثيل الغذائي والسمنة والأحداث المرتبطة بأمراض القلب والأوعية الدموية. يحتوي الشاي على مجموعة متنوعة من المعادن النادرة والعناصر المفيدة لصحة الإنسان، ولكن إذا كانت موجودة بكميات عالية بما فيه الكفاية، فقد يكون بعضها خطيرًا ويسبب السرطان. يبرز هذا العمل بسبب تقييمه الشامل لمستويات المعادن الثقيلة، وإجراء تقييم المخاطر لمستهلكي الشاي في منطقة جازان جنوب المملكة العربية السعودية. تناول البحث الحالي محتوى 6 معادن ثقيلة مختلفة في 11 عينة من الشاي الأسود التي تم جمعها من الأسواق المحلية في منطقة جازان، جنوب المملكة العربية السعودية: الكاديوم (Cd)، الرصاص (Pb)، الكروم (Cr)، الزنك (Zn)، النحاس (النحاس)، والحديد (Fe)، والزنك (Zn).

تم استخدام مطيافية الامتصاص الذري باللهب (FAAS) للكشف عن المعادن الثقيلة في عينات الشاي. تم استخدام حاصل الخطر المستهدف (THQ) ومؤشر الخطر المشترك (HI) للمعادن الثقيلة في عينات الشاي لتقييم المخاطر الصحية على مستهلكي الشاي. وجدت الدراسة أن متوسط محتوى الكاديوم والرصاص والكروم والزنك والنحاس والحديد في العينات التي تم فحصها هو 1.31، 2.33، 16.07، 27.88، 5.52، و120.4 ميكروجرام/جرام، على التوالي. قمنا بمقارنة تركيز المعادن الثقيلة في العينات قيد الفحص بالمستويات القصوى المسموح بها من قبل منظمة الصحة العالمية. وأظهرت النتائج أن متوسط مستويات النحاس والحديد والرصاص والكاديوم والزنك في عينات الشاي كانت أقل بكثير من القيم القصوى المسموح بها. وعلى العكس من ذلك، تجاوز مستوى الكروم في عينات الشاي الحد الأقصى للقيم المسموح بها. كانت القيم المتوسطة لـ THQ هي 0.003 و0.05 و0.16 و0.19 و0.69 و0.8 لكل من Cr وFe وZn وPb وCu وCd على التوالي. تبين أن قيم THQ لجميع المعادن قيد التحقيق أقل من الحدود المسموح بها (أقل من واحد). تظهر هذه البيانات أن المعادن الثقيلة الفردية الموجودة في العينات التي تم فحصها لا تشكل أي مخاوف صحية مسرطنة. في المقابل، تم تحديد قيمة HI لمختلف المعادن الثقيلة لتكون أكبر من واحد (1.91) مما يشير إلى أن التتبع المنتظم لمستويات المعادن الثقيلة في عينات الشاي الأسود مطلوب.

1. Introduction

Drinking tea is almost as common as drinking water throughout the world. Every day, almost 18 billion teacups are drunk worldwide [1-3]. Arabian adults usually have three or four cups of tea a day. Tea can be categorized as black, white, green, oolong, dark, or yellow tea depending on the method of fermentation and the mix of flavor characteristics [4]. The most common forms of tea are green and black types [5]. Black tea is created by fermentation but green tea is created by drying and roasting. Numerous studies have demonstrated the link between reasonable tea drinking and reduced blood cholesterol, the prevention of LDL oxidation, Skin cancer, Parkinson's disorder, infarction of the heart, heart attack, and stroke, and a decreased risk of cardiovascular and cancer diseases [6-8]. This is so because a variety of chemicals, such as heavy metals, polyphenols, caffeine, and fluorides, are beneficial to the human body [9]. Several studies have demonstrated that the tea plant is contaminated with a variety of dangerous heavy metals, such as nickel, lead, cadmium, mercury, chromium, and others which affect the tea quality [10-15]. There are several reasons why heavy metals naturally accumulate into tea leaves, including contaminated soil, the use of pesticides and fertilizers, the environment in which the tea is grown, mining, agricultural runoff, contaminated irrigation water, the provenance of the tea, and the manufacturing processes [16-20]. Some heavy metals are harmful and carcinogenic, however acceptable quantities of Cr, Fe, Co, Ni, and Zn are necessary for organism growth and may be used as a treatment for a variety of diseases [21-24]. Chromium, for instance, reduces fat and cholesterol and regulates insulin and blood sugar levels; however, prolonged contact with elevated chromium concentrations causes lung cancer [25]. Moreover, lead and cadmium pose a serious risk to human health, especially to the neurological urinary systems, which can lead to troubles with the kidneys, hearts, bones, and nervous systems [26]. All of these minerals can be released by tea leaves into the infusion. [17]. One key biological feature of heavy metals is their potential to bioaccumulate. This makes bioaccumulation an essential component of hazard evaluation methods. Thus, excessive consumption of heavy metals can lead to a number of illnesses, including weakening nails, oily skin, pigmentation, skin discoloration, hyperactivity in autistic children, and hair loss, particularly in women. They may potentially result in toxicity, hyposmia, coma, or even death [27-29]. For these reasons, determining the concentration of heavy metals in tea is vital to human health and ought to be done regularly. Several studies were conducted to determine the hazardous metal content in various samples of tea leaves. Many investigations have been conducted in Asia to evaluate the content of hazardous elements in tea samples. Wu, Xiaoling, et al. [30] examined the health problems associated with tea drinking in China and the presence of heavy metals in tea leaves. An additional study [31] found that 30 distinct Chinese teas had Pb contents ranging from 0.26 to 3.2 mg kg⁻¹, and Cd contents ranging from 0.0059 to 0.085 mg kg⁻¹. Another study [32] discovered that various heavy metal concentrations (Al, Pb, Cd, Hg, and As) were near the upper levels published by (WHO).[33]. Pourramezani et al.[23] concluded that drinking tea posed no danger of heavy metal exposure because the hazard index of Indian and Sri Lanka teas was non-significant for tea consumers.

Moreover, Pb and Cd contents in tea brands in Saudi Arabia ranging from 0.3–2.2 to 0.32–2.17 $\mu\text{g g}^{-1}$, correspondingly, according to Ashraf and Mian [5]. According to WHO-acceptable standards, these levels are safe for ingestion by humans.

Analytical techniques such as anodic stripping voltammetry (ASV), graphite furnace atomic absorption spectrometry (GFAAS), and inductively coupled plasma-mass spectrometry (ICP-MS) are employed for assessing the concentration of heavy metals [34-36] but these instruments are expensive. However, Flame Atomic Absorption Spectrometry (FAAS) is more widely available and reasonably priced. This work stands out due to its thorough evaluation of both individual and multiple heavy metal levels, comparing them with international standards and conducting a risk assessment for tea consumers in Jazan region southern of Saudi Arabia. The goal of this research aimed to measure the heavy metals content, particularly Cd, Pb, Cr, Zn, Cu, and Fe, in 11 samples of black tea using FAAS. The study examined the potential health risks associated with heavy metals in Saudi tea consumers, utilizing the HQ and HI to calculate human health hazards.

2. Materials and methods

2.1. Reagents and materials

Standard solutions and tea samples were prepared using ultrapure deionized water generated by a Milli-Q purification system. Tea sample preparation for analysis was done using HPLC-grade nitric acid, which was purchased from Sigma-Aldrich. Typical stock solutions of Zinc, Cu, Fe, Pb, Cd, and Cr were purchased from Analytik Jena in Germany at a concentration of 1000 mg/L in 0.5% (v/v) HNO_3 . Every day, a specific volume of stock solution was dissolved in MilliQ water to prepare fresh working standards solutions within the appropriate concentration range for each element. All of the glassware used in the standard solution preparation was thoroughly cleaned with MilliQ water, allowed to air dry, and then immersed in 10% nitric acid for an entire night before being used.

2.2. Apparatus

The content of heavy metals in tea samples was determined using FAAS novAA 350, Analytik Jena, Germany. Table 1 shows the measuring conditions for each heavy metal.

Table 1. Operating conditions for measuring each heavy metal with an atomic absorption spectrophotometer.

	Cu	Fe	Pb	Cd	Zn	Cr
λ (nm)	324.8	248.3	283	228	213.9	357.9
Slit (nm)	1.4	0.2	1.4	1.4	0.5	0.2
Lamp current (mA)	2	4	2	2	2	4
Flame	Air- C_2H_2					

2.3. Tea samples, collection, preparation, and analysis

Eleven of the most popular tea samples were randomly selected from supermarkets in the Saudi Arabian southern city of Jazan. Samples were prepared for chemical analysis using the standard protocol outlined in the Association of Official Agriculture Chemists [37]. The samples were easily dried at 100°C, then ignited at 450°C for 10 hours till white ashes formed. After adding five milliliters of 6M HCl, the sample was allowed to evaporate until completely dried. The remaining substance was dissolved with 0.1 M nitric acid. The same protocol was applied to blanks. FAAS was used to assess the diluted digested samples. First, use the device software to choose the desired elements for analysis as well as a suitable wavelength for the selected element. Calibrate the instrument by inserting a blank and standards, creating a standard curve, and then analyzing the unknown samples.

2.4. Characterization of the health risks

An important metric for evaluating the risks to long-term health is the metals daily intake determination which can be calculated using the equation (1) in Table S1[38]. On the other hand, the prospective risk implications of different metals can be statistically assessed via the target hazard quotient. equation (2) in Table S1 is used to compute the target hazard quotient [39, 40]. In this study, the total risk potential of non-carcinogenic effects of being exposed to a combination of heavy metals was evaluated using (HI) using equation (3) in Table S1 [13, 38]. The cumulative non-carcinogenic health risk of several heavy metals is determined using Equation 3 [41]. It was considered that the non-carcinogenic risk would be tolerable if the THQ value was less than one. Greater THQ levels correspond to more risk [42]. On the other hand, if the HI is less than one, there is no risk of cancer from the exposure dose. Heavy metal exposure doses that are harmful to human health are highly likely to occur if the HI is greater than one. When the HI value exceeds 10.0, there is a prolonged harmful impact on human health [43].

3. Results and discussion

Stock solutions of 1000 mg/L for each of the selected heavy metals were diluted using 0.5% (v/v) HNO₃ solution to create a series of standard solutions for establishing the calibration curves for the metals. Figure 1 illustrates the obtained calibration curves for the heavy metals under investigation. The correlation coefficient (R^2) was used to assess the calibration curves' linearity. The calibration curves for all heavy metals under consideration were found to have good linearity within their concentration range.

3.1. Heavy metal concentrations in tea samples

Figure 2 indicates the concentrations of the heavy metals Cu, Fe, Zn, Pb, Cd, and Cr in the tea samples under investigation. The ability of this plant to accumulate Tea's capacity for gathering metals is demonstrated by the overall levels of metals evaluated in tea samples.

Based on the average metal content in tea samples, the metals can be ranked as follows: Fe > Zn > Cr > Cu > Pb > Cd. Cu levels in the samples investigated varied from 1.9 to 14.5 µg/g, with a mean of 5.52 µg/g. Our findings are consistent with the average Cu concentration (5.5 µg/g) obtained by Kilicel F.[44].

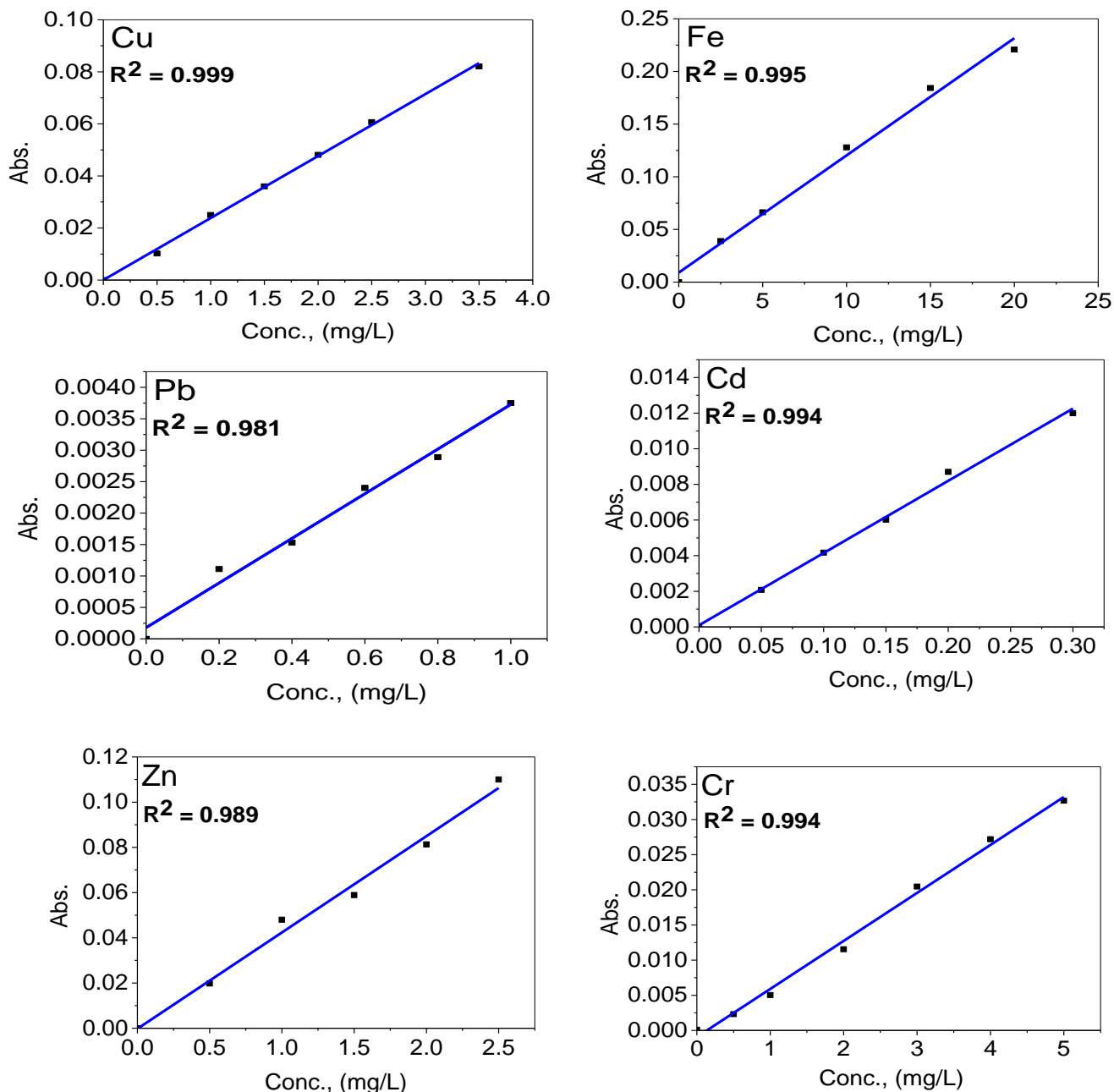


Figure 1: Standard curves for Cu, Fe, Pb, Cd, Zn, and Cr.

The average concentration of Cu in tea samples in the current study was lower than the upper limits established by the World Health Organization (10 µg/g) [43, 44] and several other countries, such as China (60 µg/g), Japan (100 µg/g), and the United States (150 µg/g) [44]. Our findings showed good agreement with values reported in the literature for tea samples from Turkey, China, Japan, India, and the United States. [3, 19, 34, 36, 45] Furthermore, the level of Cu identified in the tea samples under investigation agrees with the results of Abdallah A. Shaltout et al. [46] who stated that samples taken from Saudi Arabia had Cu levels ranging from 7.5 to 28.3 µg/g. The wide range in Cu concentration seen in the teas may be explained by the various types and quality levels, Cu pollution comes from fungicides and growing regions of the teas [47].

The first element detected at the greatest level in the samples of black tea that were being examined was iron. The iron content ranged widely between 53.5 to 223.9 µg/g in the various tea samples, with an average of 120.4 µg/g. All tea samples had an acceptable level of Fe, even if it was below the allowable threshold of 450 µg/g. [48]. The Fe level in the samples under investigation was found to be consistent with the findings of Al-Othman et al. [49] who found that the levels of Fe in the examined samples were 46 and 348 µg/g, respectively. On the other hand, Waqar Ashraf and Atiq A. Mian [5] have observed that the mean value of Fe was 250.5 µg/g, with levels ranging from 88.7–946.7 µg/g. Additionally, Fe levels in the investigated samples varied from 74 and 1,000 µg/g, according to Pedro et al.[2]

Zinc concentrations fluctuated between 6.7 and 46.8 µg/g, averaging 27.88 µg/g. When the zinc content is below the 50 µg/g allowable limit, all tea samples are considered acceptable.[48, 50]. Our findings matched with those of Federico et al. [49], who found that samples of black tea had an average Zn concentration of 29 µg/g. [51]. POPOVIĆ, Slađana, et al. obtained similar results, determining that the Zn level varied between 19.06 and 43.97µg/g.[52]. Furthermore, Kilicel F. [44] discovered that samples of black tea had an average Zn concentration of 31.99 µg/g.

Concentrations of Pb were 0.01 to 12.5 µg/g, averaging 2.33 µg/g. This is consistent with Al-Oud, S. [53], who observed that Pb levels in Saudi Arabia tea samples varied between 0.03 and 14.84 µg/g. According to a different study, the mean Pb content is 3.04 µg/g [54]. Except for the T11 sample, all samples had acceptable Pb levels that were below the WHO-permitted standard of 10 µg/g [33] as well as other countries including China (5 µg/g), India (10 µg/g), and Thailand (10 µg/g). This rise could be attributable to commercial flavor and color additives containing different amounts of various heavy metals. [55]. Previous investigations have shown that Pb levels ranged from 0.03 to 14.84 µg/g, 0.198 to 6.345 µg/g, and 0.26 to 0.83 µg/g [18, 53, 56]. The primary sources of Lead in tea are the growing mediums, such as soil. Pb contamination in soil is frequently related to industrial operations, agricultural activities (application of pesticides), and urban activities (the burning of gasoline). Pb is more accessible for tea root intake in extremely acidic soils. Another way that Pb can contaminate tea is through deposits from the contaminated air into the plant's leaves [47].

Cadmium levels in black tea samples varied between 0.92 and 3.98 $\mu\text{g/g}$, having a mean value of 1.31 $\mu\text{g/g}$. This was considered acceptable since the amount was below the WHO-recommended threshold of 3 $\mu\text{g/g}$. [33]. All of our findings on Cd in samples other than T3 are consistent with those of Alwan W. [55] who found that Cd concentrations ranged from 0.18 to 2.43 $\mu\text{g/g}$. Furthermore, our results for Cd in all samples except T3 are consistent with those of POPOVIĆ, Slađana, et al. [52] who discovered that the range of Cd concentrations was 0.077 to 0.92 $\mu\text{g/g}$. Franklin et al. [57] She stated that phosphatic fertilizers had 4.9–5.5 $\mu\text{g/g}$ of Cd and zinc sources contained 11.8–50.9 $\mu\text{g/g}$. It seems that the sources of the lead in tea came from phosphatic and zinc fertilizers.

Chromium (Cr) is extremely harmful to human health, causing severe damage to the kidneys and lungs. All of the black tea samples had chromium contents ranging from 5.6 to 40.2 $\mu\text{g/g}$, with an average of 16.07 $\mu\text{g/g}$. Every tea sample had an unacceptable level of Cr, defined as one where the level exceeds the allowable limit of 1.3 $\mu\text{g/g}$. [48]. The results we got were consistent with those of Falahi, E. [58] who reported a mean concentration of Cr of 15.9 $\mu\text{g/g}$. The nine commercial teas that were gathered from different countries had a Cr level that ranged from 19.8 to 129.1 $\mu\text{g/g}$ [17]. According to Ferrara et al., black tea samples had chromium levels between 17.9 to 115.4 $\mu\text{g/g}$, which is in line with the Cr level found in our investigation [59]. On the other hand, Mandiwana et al. [60] discovered that the chromium concentration in samples of black tea varied from 0.28 to 14.0 $\mu\text{g g}^{-1}$. Additionally, maximum Cr was discovered in Turkish tea samples by Narin et al. [36] at 16.9 $\mu\text{g/g}$. Cr is mostly introduced into the black tea manufacturing process through the CTC rollers, where it is regarded as a local contaminant [56]. According to Seenivasan et al., the sharpening of crush, tear, and curl rollers employed in the production of tea was mostly associated with the Cr content of tea. [17]. Moreover, it has been noted that Cr speciation in soil determines whether plants are contaminated with Cr [61]. The variation in Cr concentration across tea from different production sites may help to explain this in part.

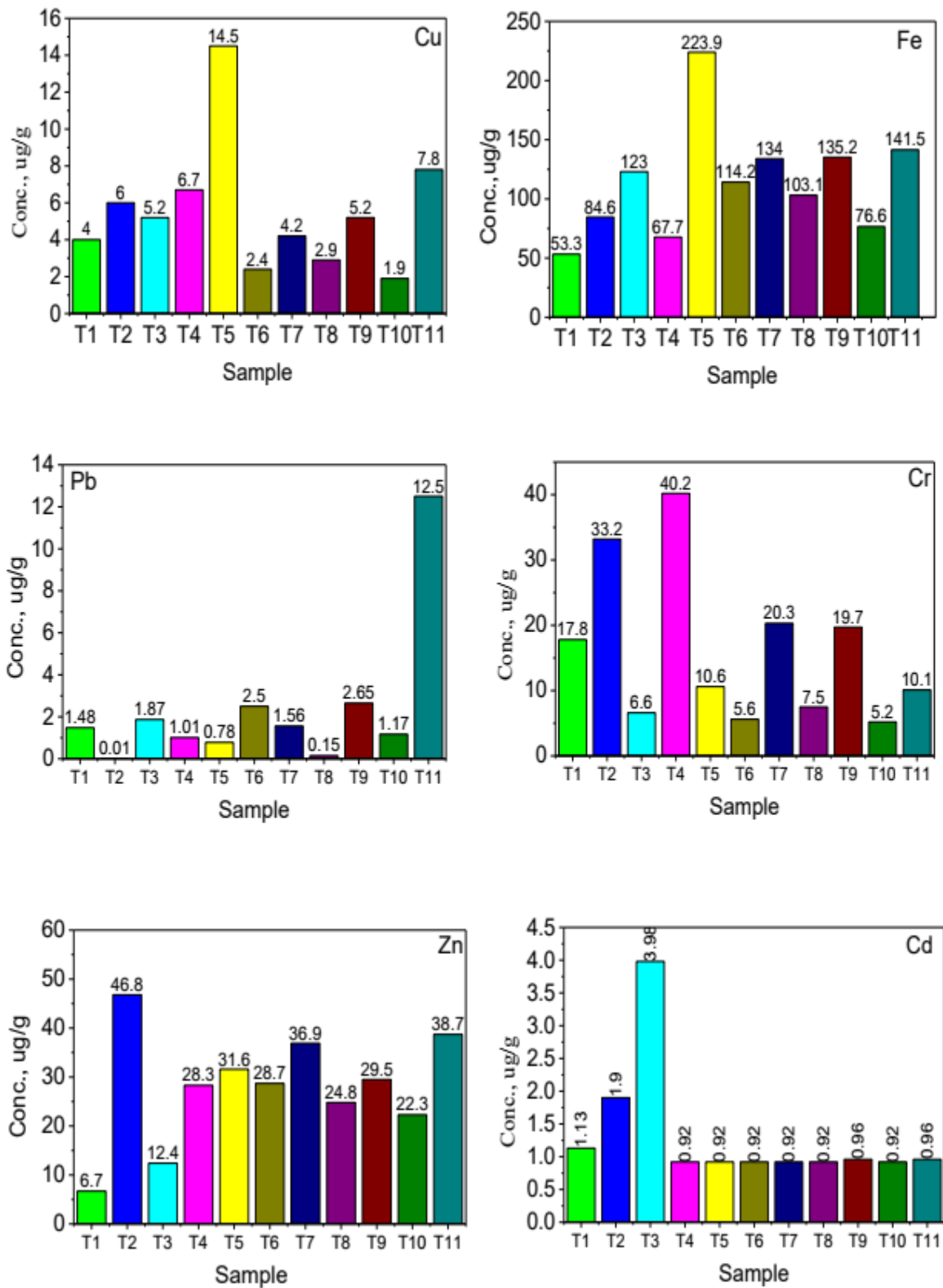


Figure 2. Concentration of Cu, Fe, Pb, Cd, Zn, and Cr in tea samples ($\mu\text{g/g}$)

3.2. Assessment of health risk

3.2.1. Singular heavy metal risk

The target hazard quotient (THQ) values for each heavy metal in each sample under investigation are estimated to evaluate non-cancer health risks. The target hazard quotient (THQ) evaluates the possibility of being exposed to a trace element with known negative impacts on humans [62]. Figure 3 depicts the THQ values for every heavy metal in each sample and the mean THQ values. The order of the mean THQ values after consuming prepared tea was $Cd > Cu > Pb > Zn > Fe > Cr$. The THQ values for each heavy metal in all samples under investigation ranged from 0.002 to 0.051 averaging 0.003, 0.02 to 0.1 averaging 0.05, 0.04 to 0.27 averaging 0.16, 0.001 to 1.05 averaging 0.19, 0.16 to 1.17 averaging 0.69 and 0.56 to 2.42 averaging 0.8 in case of Cr, Fe, Zn, Pb, Cu, and Cd, respectively. For all heavy metals in all of the samples under evaluation, THQ mean values were found to be less than 1 ($THQ < 1$). However, the THQ values were 1.1 and 2.42 in the T₂ copper sample and T₃ cadmium sample. The THQ values for Cu, Cd, Fe, and Zn in tea samples were less than 1, which is consistent with the findings of Gogoi b. et al [63]. Similar results showed that drinking tea does not expose people to heavy metal hazards [13, 64]. Additionally, comparable findings were made by S. Wali Alwan [55], who showed that the THQ values for Pb and Cd were less than 1. Moreover, THQ values for Cd and Cr were less than 1, according to Sahar G. et al [65]. According to these results, it is unlikely that consuming tea leaves regularly would hurt a Consumer's health.

3.2.2 Accumulated hazard of several heavy metals

The HI values for different metals can be used to express their accumulated non-carcinogenic effects. Figure 4a indicates the hazard index scores of all metals that were examined through the consumption of tea samples. Figure 4b shows the mean THQ values for the investigated heavy metals and their corresponding HI value. It was indicated that the HI values in both cases were greater than 1. As shown in Figure 4a, HI was ranged from 1.04 in T₁ to 3.02 in T₃ samples. Our findings concurred with those of previous studies [13, 20, 66] which revealed that the HI value was greater than 1. Moreover, S. Wali Alwan [55] reported comparable results, determining that the HI values for Cd, Pb, and Ni in tea samples varied from 0.34 to 23.4. Additionally, HI values for Cu, Zn, Ni, Cr, Cd, Pb, As, Hg, and Al in tea samples ranged from 0.16 to 1.7, according to another investigation [13]. These findings suggest that there are non-carcinogenic health risks linked with the multiple heavy metals found in the examined samples.

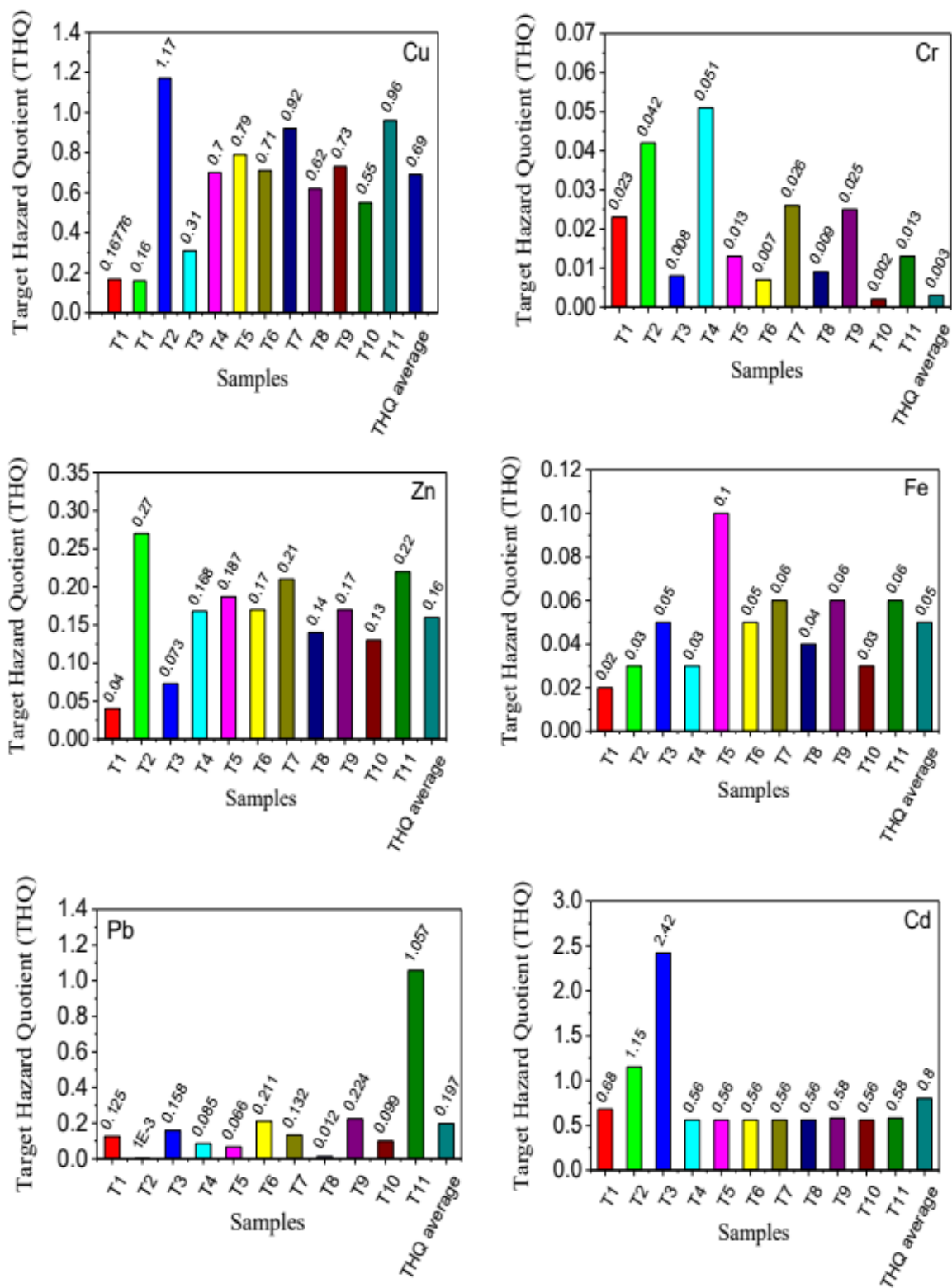


Figure 3. Target Hazard Quotient and its average for the selected heavy metals; Cu, Fe, Pb, Cd, Zn, and Cr in the examined samp

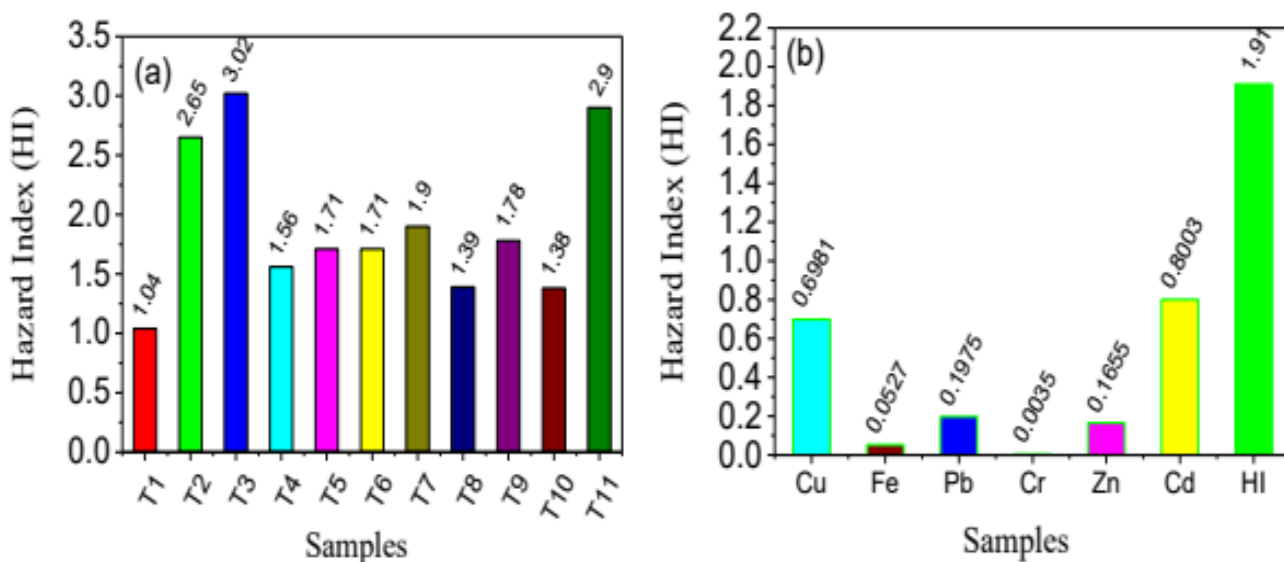


Fig.4. a) Hazard Index, and b) THQ average and corresponding HI for; Cu, Fe, Pb, Cd, Zn, and Cr.

4. Conclusion

This study monitored the level of several heavy metals, including Cu, Fe, Pb, Cd, Zn, and Cr, in tea samples gathered from Jazan local markets in southern Saudi Arabia. According to the findings, the average level of the heavy metals in tea samples under investigation Cu, Fe, Pb, Cd, and Zn was found to be below the maximum allowable limit. Conversely, the mean concentration of Cr exceeds the maximum permitted thresholds, and it is crucial to keep an eye on its level in tea brands. Furthermore, THQ mean values were 0.003, 0.05, 0.16, 0.19, 0.69, and 0.8 for Cr, Fe, Zn, Pb, Cu, and Cd, respectively accordingly. The THQ values of every metal under investigation were found to be below the allowable limits (less than one) in all samples indicating the individual heavy metals have no health risk to tea consumers. Conversely, the HI value was found to be higher than the allowable limits (less than 1). These findings suggest that the different heavy metals found in the investigated samples can carry non-carcinogenic health risks and highlight the importance of regularly monitoring the concentration of heavy metals in tea samples.

References

- [1] M. T. Soomro, E. Zahir, S. Mohiuddin, A. N. Khan, and I. Naqvi, "Quantitative assessment of metals in local brands of tea in Pakistan," *Pakistan journal of biological sciences: PJBS*, vol. 11, no. 2, pp. 285-289, 2008.
- [2] P. L. Fernández-Cáceres, M. J. Martín, F. Pablos, and A. G. González, "Differentiation of tea (*Camellia sinensis*) varieties and their geographical origin according to their metal content," *Journal of agricultural and food chemistry*, vol. 49, no. 10, pp. 4775-4779, 2001.
- [3] A. Kumar, A. Nair, A. Reddy, and A. Garg, "Availability of essential elements in Indian and US tea brands," *Food Chemistry*, vol. 89, no. 3, pp. 441-448, 2005.
- [4] V. S. P. Chaturvedula and I. Prakash, "The aroma, taste, color and bioactive constituents of tea," *Journal of Medicinal Plants Research*, vol. 5, no. 11, pp. 2110-2124, 2011.
- [5] W. Ashraf and A. A. Mian, "Levels of selected heavy metals in black tea varieties consumed in Saudi Arabia," *Bulletin of environmental contamination and toxicology*, vol. 81, pp. 101-104, 2008.
- [6] F.-L. Chung, J. Schwartz, C. R. Herzog, and Y.-M. Yang, "Tea and cancer prevention: studies in animals and humans," *The Journal of nutrition*, vol. 133, no. 10, pp. 3268S-3274S, 2003.
- [7] A. Mehra, P. Lynch, S. Saikat, and L. Chan, "Trace elements in tea (*Camellia sinensis*) and their bioavailability," *Tea in Health and Disease Prevention*, vol. 257274, 2013.
- [8] F. Zaman *et al.*, "Natural variation of main biochemical components, morphological and yield traits among a panel of 87 tea [*Camellia sinensis* (L.) O. Kuntze] cultivars," *Horticultural Plant Journal*, vol. 9, no. 3, pp. 563-576, 2023.
- [9] C. Cabrera, R. Giménez, and M. C. López, "Determination of tea components with antioxidant activity," *Journal of agricultural and food chemistry*, vol. 51, no. 15, pp. 4427-4435, 2003.
- [10] L. Li, Q.-L. Fu, V. Achal, and Y. Liu, "A comparison of the potential health risk of aluminum and heavy metals in tea leaves and tea infusion of commercially available green tea in Jiangxi, China," *Environmental monitoring and assessment*, vol. 187, pp. 1-12, 2015.
- [11] L. M. de Oliveira *et al.*, "Metal concentrations in traditional and herbal teas and their potential risks to human health," *Science of the total environment*, vol. 633, pp. 649-657, 2018.

- [12] J. Sun, G. Hu, K. Liu, R. Yu, Q. Lu, and Y. Zhang, "Potential exposure to metals and health risks of metal intake from Tieguanyin tea production in Anxi, China," *Environmental geochemistry and health*, vol. 41, pp. 1291-1302, 2019.
- [13] J. Zhang, R. Yang, R. Chen, Y. Peng, X. Wen, and L. Gao, "Accumulation of heavy metals in tea leaves and potential health risk assessment: a case study from Puan County, Guizhou Province, China," *International Journal of Environmental Research and Public Health*, vol. 15, no. 1, p. 133, 2018.
- [14] J. Zhang, R. Yang, R. Chen, Y. C. Li, Y. Peng, and C. Liu, "Multielemental analysis associated with chemometric techniques for geographical origin discrimination of tea leaves (*Camelia sinensis*) in Guizhou Province, SW China," *Molecules*, vol. 23, no. 11, p. 3013, 2018.
- [15] B. Yang *et al.*, "Distribution of trace metals in a soil–tea leaves–tea infusion system: characteristics, translocation and health risk assessment," *Environmental Geochemistry and Health*, vol. 44, no. 12, pp. 4631-4645, 2022.
- [16] A. Ebadi, S. Zare, M. Mahdavi, and M. Babae, "Study and measurement of Pb, Cd, Cr and Zn in green leaf of tea cultivated in Gillan province of Iran," *Pak J Nutr*, vol. 4, no. 4, pp. 270-2, 2005.
- [17] T. Karak and R. Bhagat, "Trace elements in tea leaves, made tea and tea infusion: A review," *Food research international*, vol. 43, no. 9, pp. 2234-2252, 2010.
- [18] F. a. Qin and W. Chen, "Lead and copper levels in tea samples marketed in Beijing, China," *Bulletin of environmental contamination and toxicology*, vol. 78, pp. 128-131, 2007.
- [19] G. Karimi *et al.*, "Concentrations and health risk of heavy metals in tea samples marketed in Iran," *Pharmacology*, vol. 3, no. 1, pp. 164-174, 2008.
- [20] M. A. Nkansah, F. Opoku, and A. A. Ackumey, "Risk assessment of mineral and heavy metal content of selected tea products from the Ghanaian market," *Environmental monitoring and assessment*, vol. 188, pp. 1-11, 2016.
- [21] V. Shukla, M. Dhankhar, J. Prakash, and K. Sastry, "Bioaccumulation of Zn, Cu and cd in *Channa punctatus*," *Journal of Environmental Biology*, vol. 28, no. 2, p. 395, 2007.
- [22] M. Dambiec, L. Polechońska, and A. Klink, "Levels of essential and non-essential elements in black teas commercialized in Poland and their transfer to tea infusion," *Journal of Food Composition and Analysis*, vol. 31, no. 1, pp. 62-66, 2013.
- [23] A. C. Achudume and D. Owoeye, "Quantitative assessment of heavy metals in some tea marketed in Nigeria," *Health*, vol. 2, no. 9, pp. 1097-1100, 2010.
- [24] J. J. Bower, S. S. Leonard, and X. Shi, "Conference overview: molecular mechanisms of metal toxicity and carcinogenesis," *Molecular and cellular biochemistry*, vol. 279, pp. 3-15, 2005.

- [25] F. Pourramezani, F. Akrami Mohajeri, M. H. Salmani, A. Dehghani Tafti, and E. Khalili Sadrabad, "Evaluation of heavy metal concentration in imported black tea in Iran and consumer risk assessments," *Food Science & Nutrition*, vol. 7, no. 12, pp. 4021-4026, 2019.
- [26] L. Järup, "Hazards of heavy metal contamination," *British medical bulletin*, vol. 68, no. 1, pp. 167-182, 2003.
- [27] E. A. Abu Bakar, "Determination of heavy metals (cadmium, chromium, copper, lead and nickel) in slimming teas by using atomic absorption spectroscopy," Faculty of Applied Sciences, 2008.
- [28] O. O. Dosumu, O. O. Oluwaniyi, V. G. Awolola, and O. A. Ogunkunle, "Toxicity assessment of some tea labels from supermarkets in Ilorin, Nigeria using brine shrimp(*Artemia salina*) lethality assay," *African Journal of Food Science*, vol. 4, no. 5, pp. 282-285, 2010.
- [29] L. Mahan, S. Escott-Stump, and J. Raymond, "Krause's food & the nutrition care process,(Krause's Food & Nutrition Therapy)," *Saunders Elsevier*, pp. 165-169, 2012.
- [30] X. Wu, D. Zhang, F. Wang, L. Luo, Y. Chen, and S. Lu, "Risk assessment of metal (loid) s in tea from seven producing provinces in China," *Science of The Total Environment*, vol. 856, p. 159140, 2023.
- [31] P. Ning, C. Gong, Y. Zhang, K. Guo, and J. Bai, "Lead, cadmium, arsenic, mercury and copper levels in Chinese Yunnan Pu'er tea," *Food Additives and Contaminants*, vol. 4, no. 1, pp. 28-33, 2011.
- [32] M. Parviz, N. Eshghi, S. Asadi, H. Teimoory, and M. Rezaei, "Investigation of heavy metal contents in infusion tea samples of Iran," *Toxin Reviews*, vol. 34, no. 3, pp. 157-160, 2015.
- [33] W. H. Organization, "Department of technical cooperation for essential drugs and traditional medicine," *Guidelines for assessing quality of herbal medicines with reference to contaminants and residues, Geneva, Switzerland*, 2007.
- [34] H. Matsuura, A. Hokura, F. Katsuki, A. Itoh, and H. Haraguchi, "Multielement determination and speciation of major-to-trace elements in black tea leaves by ICP-AES and ICP-MS with the aid of size exclusion chromatography," *Analytical sciences*, vol. 17, no. 3, pp. 391-398, 2001.
- [35] H. Lixin and L. Ran, "Determination of minerals and trace elements in various tea by ICP-AES," *Guang pu xue yu Guang pu fen xi= Guang pu*, vol. 22, no. 2, pp. 304-306, 2002.
- [36] I. Narin, H. Colak, O. Turkoglu, M. Soylak, and M. Dogan, "Heavy metals in black tea samples produced in Turkey," 2004.
- [37] L. Jorhem and C. A. G. C. G. D. H. G. K. H. G. J. K. K. K. L. B. L. J. M. M. O. A. P. S. S. B. U. B. W. T, "Determination of metals in foods by atomic

- absorption spectrometry after dry ashing: NMKL1 collaborative study," *Journal of AOAC International*, vol. 83, no. 5, pp. 1204-1211, 2000.
- [38] U. S. E. P. A. O. o. Emergency and R. Response, *Risk Assessment Guidance for Superfund: pt. A. Human health evaluation manual*. Office of Emergency and Remedial Response, US Environmental Protection Agency, 1989.
- [39] X. Wu, "Studies on maximum residue limits for pesticides in tea and relative risk assessment," ed: Anhui Agricultural University Hefei, China, 2007.
- [40] S. De Flora, A. Camoirano, M. Bagnasco, C. Bennicelli, G. Corbett, and B. Kerger, "Estimates of the chromium (VI) reducing capacity in human body compartments as a mechanism for attenuating its potential toxicity and carcinogenicity," *Carcinogenesis*, vol. 18, no. 3, pp. 531-537, 1997.
- [41] H. Cao, L. Qiao, H. Zhang, and J. Chen, "Exposure and risk assessment for aluminium and heavy metals in Puerh tea," *Science of the Total Environment*, vol. 408, no. 14, pp. 2777-2784, 2010.
- [42] Q. Yao, M. Huang, Y. Zheng, M. Chen, C. Huang, and Q. Lin, "Prediction and health risk assessment of copper, lead, cadmium, chromium, and nickel in Tieguanyin tea: A case study from Fujian, China," *Foods*, vol. 11, no. 11, p. 1593, 2022.
- [43] R.-Z. Li, C.-R. Pan, J.-J. Xu, J. Chen, and Y.-M. Jiang, "Contamination and health risk for heavy metals via consumption of vegetables grown in fragmentary vegetable plots from a typical nonferrous metals mine city," *Huan jing ke xue= Huanjing kexue*, vol. 34, no. 3, pp. 1076-1085, 2013.
- [44] F. Kilicel, H. S. Karapinar, and A. Uğuz, "Determination of some heavy metal concentrations of sage tea with FAAS," *International Journal of Secondary Metabolite*, vol. 4, no. 3, Special Issue 2, pp. 391-399, 2017.
- [45] C.-F. Wang, C.-H. Ke, and J.-Y. Yang, "Determination of trace elements in drinking tea by various analytical techniques," *Journal of Radioanalytical and Nuclear Chemistry*, vol. 173, pp. 195-203, 1993.
- [46] A. A. Shaltout, M. S. Abdel-Aal, B. Welz, and I. N. Castilho, "Determination of Cd, Cu, Ni, and Pb in black tea from Saudi Arabia using graphite furnace atomic absorption spectrometry after microwave-assisted acid digestion," *Analytical Letters*, vol. 46, no. 13, pp. 2089-2100, 2013.
- [47] H. W. Han WenYan, L. Y. Liang YueRong, Y. Y. Yang YaJun, S. Y. Shi YuanZhi, M. L. Ma LiFeng, and R. J. Ruan JianYun, "Effect of processing on the Pb and Cu pollution of tea," 2006.
- [48] I. Duka, S. Shallari, A. Maçi, Z. Rada, and J. Shehu, "Heavy Metals Accumulation by Aromatic Plant *Salvia Officinalis* Irrigated with Treated Wastewater," *ANGLISTICUM. Journal of the Association-Institute for English Language and American Studies*, vol. 4, no. 10, pp. 86-92, 2015.

- [49] Z. A. Al-Othman, E. Yilmaz, H. M. Sumayli, and M. Soylak, "Evaluation of trace metals in tea samples from Jeddah and Jazan, Saudi Arabia by atomic absorption spectrometry," *Bulletin of environmental contamination and toxicology*, vol. 89, pp. 1216-1219, 2012.
- [50] R. Nazir *et al.*, "Accumulation of heavy metals (Ni, Cu, Cd, Cr, Pb, Zn, Fe) in the soil, water and plants and analysis of physico-chemical parameters of soil and water collected from Tanda Dam Kohat," *Journal of pharmaceutical sciences and research*, vol. 7, no. 3, p. 89, 2015.
- [51] F. Girolametti, A. Annibaldi, S. Illuminati, E. Damiani, P. Carloni, and C. Truzzi, "Essential and potentially toxic elements (PTEs) content in European tea (*Camellia sinensis*) leaves: Risk assessment for consumers," *Molecules*, vol. 28, no. 9, p. 3802, 2023.
- [52] S. Popović, A. Pantelić, Ž. Milovanović, J. Milinkov, and M. Vidović, "Analysis of tea for metals by flame and graphite furnace atomic absorption spectrometry with multivariate analysis," *Analytical Letters*, vol. 50, no. 16, pp. 2619-2633, 2017.
- [53] S. Al-Oud, "Heavy metal contents in tea and herb leaves," *Pakistan Journal of Biological Sciences (Pakistan)*, vol. 6, no. 3, 2003.
- [54] W.-S. Zhong, T. Ren, and L.-J. Zhao, "Determination of Pb (Lead), Cd (Cadmium), Cr (Chromium), Cu (Copper), and Ni (Nickel) in Chinese tea with high-resolution continuum source graphite furnace atomic absorption spectrometry," *Journal of food and drug analysis*, vol. 24, no. 1, pp. 46-55, 2016.
- [55] S. Wali Alwan, "Potential human health risk of some heavy metals in the commercially tea leaves and tea infusion," *Caspian Journal of Environmental Sciences*, vol. 20, no. 3, pp. 629-635, 2022.
- [56] S. Seenivasan, N. Manikandan, N. N. Muraleedharan, and R. Selvasundaram, "Heavy metal content of black teas from south India," *Food control*, vol. 19, no. 8, pp. 746-749, 2008.
- [57] R. Franklin, L. Duis, R. Brown, and T. Kemp, "Trace element content of selected fertilizers and micronutrient source materials," *Communications in soil science and plant analysis*, vol. 36, no. 11-12, pp. 1591-1609, 2005.
- [58] E. Falahi and R. Hedaiati, "Heavy metal content of black teas consumed in Iran," *Food Additives & Contaminants: Part B*, vol. 6, no. 2, pp. 123-126, 2013.
- [59] L. Ferrara, D. Montesano, and A. Senatore, "The distribution of minerals and flavonoids in the tea plant (*Camellia sinensis*)," *Il farmaco*, vol. 56, no. 5-7, pp. 397-401, 2001.
- [60] K. L. Mandiwana, N. Panichev, and S. Panicheva, "Determination of chromium (VI) in black, green and herbal teas," *Food Chemistry*, vol. 129, no. 4, pp. 1839-1843, 2011.

- [61] J. Gardea-Torresdey, J. Peralta-Videa, M. Montes, G. De la Rosa, and B. Corral-Diaz, "Bioaccumulation of cadmium, chromium and copper by *Convolvulus arvensis* L.: impact on plant growth and uptake of nutritional elements," *Bioresource technology*, vol. 92, no. 3, pp. 229-235, 2004.
- [62] E. Ubuoh, F. Nwogu, and C. Oporuiche, "Evaluation of nutrients, toxicity and hazard quotient associates of artificially ripened humid tropical banana (*musa. spp*)," *Food Chemistry Advances*, vol. 1, p. 100045, 2022.
- [63] B. B. Gogoi *et al.*, "The level of selected metals in made tea and tea infusion from the roadside tea plants and health risk assessment," *Biological Trace Element Research*, pp. 1-21, 2023.
- [64] C. y. Peng *et al.*, "Aluminum and heavy metal accumulation in tea leaves: an interplay of environmental and plant factors and an assessment of exposure risks to consumers," *Journal of food science*, vol. 83, no. 4, pp. 1165-1172, 2018.
- [65] S. Ghale Askari, V. Oskoei, F. Abedi, P. Motahhari Far, A. Naimabadi, and S. Javan, "Evaluation of heavy metal concentrations in black tea and infusions in Neyshabur city and estimating health risk to consumers," *International Journal of Environmental Analytical Chemistry*, vol. 102, no. 19, pp. 7928-7937, 2022.
- [66] N. SeyyediBidgoli, G. R. Mostafaii, H. Akbari, M. Mohammadzadeh, M. Hesami Arani, and M. B. Miranzadeh, "Determination of the concentration of heavy metals in infused teas and their assessment of potential health risk in Kashan, Iran," *International Journal of Environmental Analytical Chemistry*, vol. 102, no. 19, pp. 7673-7683, 2022.

Design And Development of a Feeding Unit for Medical Devices Implanted Inside Human Body Using Artificial Intelligence Theories

Abdulkarim Almuhammad*, Mohanad Alrasheed*

*Computer Engineering Dept., Faculty of Informatic, Ittihad Private University, Aleppo, Syria.

Abstract: In this research paper, we present the design and development of a power unit for medical devices that are implanted inside the human body. It uses a micro-electromagnetic generator to generate electrical energy by taking advantage of natural vibrations to generate electrical energy in order to supply these applications that need electrical supply for a long period without human intervention. We used a direct lever rectifier switch. Direct AC-DC Step Up Converter for low voltage amplitude to reach a value suitable for the application in the open loop. The voltage in the closed loop was then regulated using a fuzzy controller based on digital signal processing chips, which allowed improving the performance of the converter. To calculate the fuzzy controller, we used the Fuzzy Logic tool of MATLAB. Interconnection circuits were proposed to adapt low-level signals to control circuits and power switches. We performed a simulation of the entire system, represented by the control circuit based on digital signal processing chips, the fuzzy control algorithm, and the switcher using the Proteus program in the open and closed loop, and then we compared and discussed the results.

Keywords: Micro-electromagnetic, Direct AC-DC Step Up Converter, dsPIC, Biomedical Implants, micro-generator, Artificial Intelligence Theories.

تصميم وتطوير وحدة تغذية للأجهزة الطبية المزروعة داخل جسم الانسان باستخدام نظريات الذكاء الصناعي

المخلص: نقدم في هذه الورقة البحثية تصميماً وتطويراً لوحدة تغذية للأجهزة الطبية التي تزرع داخل جسم الانسان تستخدم المولد الكهرومغناطيسي الميكروي لتوليد الطاقة الكهربائية بالاستفادة من الاهتزازات الطبيعية لتوليد الطاقة الكهربائية بغية تغذية هذه التطبيقات التي تحتاج للتغذية الكهربائية لفترة طويلة وبدون التدخل البشري، وقمنا باستخدام مبدلة مقومة رافعة المباشرة Direct AC-DC Step Up Converter للجهد المنخفض المطال للوصول إلى قيمة مناسبة للتطبيق في الحلقة المفتوحة، تم بعد ذلك تنظيم الجهد في الحلقة المغلقة باستخدام المتحكم الضبابي اعتماداً على شرائح معالجة الإشارة الرقمية مما سمح بتحسين أداء المبدلة.

استخدمنا من أجل حساب المتحكم الضبابي أداة المنطق الضبابي لبرنامج MATLAB.

تم اقتراح دارات ربط لملائمة الإشارات ذات المستوى المنخفض مع دارات التحكم والمبدلة الاستطاعية أجرينا عملية محاكاة للنظام كاملاً ممثلاً بدارة التحكم المعتمدة على شرائح معالجة الإشارة الرقمية وخوارزمية التحكم الضبابي والمبدلة باستخدام برنامج Proteus في الحلقة المفتوحة والمغلقة ومن ثم قمنا بمقارنة النتائج ومناقشتها.

1. Introduction

The idea has recently emerged of using internal resources such as vibration, pressure and heat available in places where medical equipment is installed to obtain the electrical energy needed to operate them.

The Micro Electromagnetic Generator is one of the proposed solutions for generating electrical energy, as the vibration resulting from movement is converted into low electrical energy of the order of tens of millivolts, which can be used to charge a small battery [1].

One of the problems with these microgenerators is that they produce an alternating voltage with low amplitude and insufficient to operate electronic circuits on the one hand, and cannot be rectified using traditional rectifier circuits on the other hand. Therefore, it is necessary to use circuits that can raise and rectify the voltage with high efficiency, allowing to overcome problems arising from a weak voltage signal. Among the proposed circuits that perform this purpose, Direct AC-DC Step Up Converters stand out strongly[2].

In the research [4], a design was made for a micro electromagnetic generator to generate electrical energy, but the generated voltage was weak, of the order of millivolts, insufficient to benefit from it. To solve this problem, the researchers proposed in the research [1] the use of a closed-loop lever switch in order to obtain a voltage from Voltage arrangement, considering the input voltage as constant. Then the researchers in the research [2] simulated this system using MATLAB. Many researchers have presented different designs for the voltage raising system. The most prominent of these researches is the research [11] that designed a design to improve the efficiency using classical control methods, and the researcher [12] improved the design of the Micro Electromagnetic Generator, but the main problem in the previous proposals was the poor efficiency and low voltage. Unregulated variable output due to variations in the micro generator output.

2. The importance of the research and its objectives

The importance of the research lies in finding a practical design for a power unit for medical devices that are implanted inside the human body. The digital signal processor (DSP) is used to control the Direct AC-DC Step Up Converter in terms of regulating the output voltage of the switch within the closed loop, and proposing a simplified working method for generating control pulses. With electronic breakers in the switch using PWM (Pulse Width Modulation) technology.

In this research, we also took advantage of the DSP digital signal processor to implement an advanced real-time control algorithm based on Fuzzy Logic, where we were able to increase the output and response speed of the AC-DC Step Up Converter, which made it possible to make the most of the energy generated by the microgenerator.

In this research, a simulation model of the Fuzzy Controller was also built using Matlab, so that this model will be the nucleus for practical applications in future research.

3. Search method

This research was based in its stages on the following topics:

1. Study the working principle and components of the microelectromagnetic generator.
2. Study and analyze the operation of the AC-DC Step Up Converter Direct
3. Design and simulation of the Fuzzy Controller.
4. Design a circuit to generate control pulses for the open-loop switch.
5. Design the switch control circuit using a closed-loop DSP controller.
6. Results and discussion.
7. Practical recommendations and proposals.

4. Working principle of the microelectromagnetic generator

The Micro-electromagnetic generator (Figure 1) consists of a permanent magnet, a damping element, a spring, and a primary coil, where the permanent magnet is fixed at one end by the spring to the generator body and free to move at the other end within the primary coil [1].

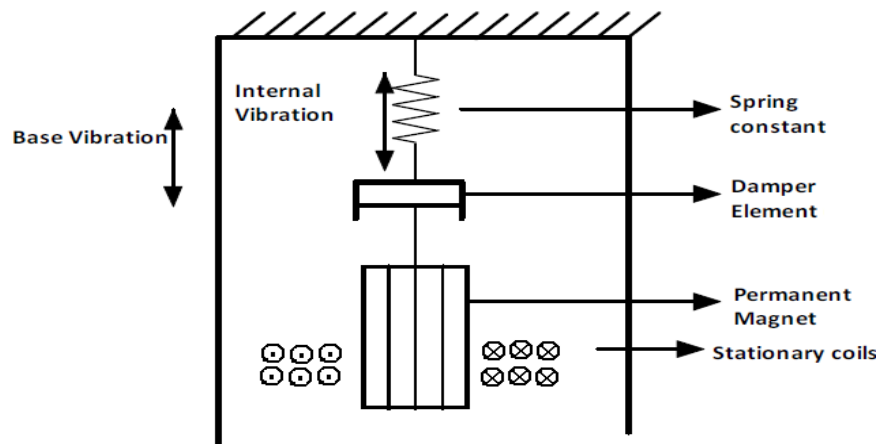


Figure (1): Micro-electromagnetic generator

When the generator is exposed to vibration, the permanent magnet within the coil vibrates, which, according to Faraday's law, generates an alternating voltage between the two ends of the coil. Its value depends on the number of turns of the coil, the magnetism of the permanent magnet, and the intensity of the vibration. The generated voltage is usually sinusoidal and has a low amplitude of the order of tens of millivolts and cannot be used directly to supply electrical equipment.

5. Study and analyze the work of the AC-DC Step Up Direct Converter

This converter, one of whose structures we show in Figure (2), performs the processes of raising and rectifying the low alternating voltage at the same time. The converter consists of a boost converter containing the elements (L1, T1, D1) in parallel with a buck-boost converter containing the elements (L2, T2, D2). Capacitor C acts as a filter to smooth the output voltage [3].

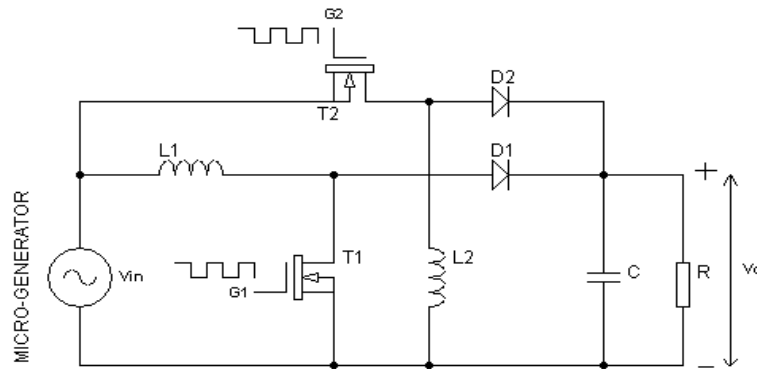


Figure (2): AC-DC Step Up Direct Converter

Transistors T1 and T2 are used as electronic circuit breakers whose passing and cutting are controlled using PWM pulse width modulation technology, where T1 works in the positive part of the input voltage and T2 in the negative part of the input voltage [4]. The voltage generated by the micro-electric generator is expressed in terms of V_{in} . The work of the switch can be divided into four stages [8]:

- The first phase (Figure 3-A): Transistor T1 is switched through the positive part of the input voltage V_{in} , which leads to charging the coil L1.
- Second phase (Figure 3-B): The control voltage of transistor T1 is canceled through the positive part of the input voltage V_{in} , which leads to the current stored in coil L1 being discharged into the load by D1.
- The third phase (Figure 3-C): The transistor T2 is switched through the negative part of the input voltage V_{in} , which leads to the coil L2 being charged with current by T2.
- Fourth phase (Figure 3-D): The control voltage of the transistor T2 is canceled through the negative portion of the input voltage V_{in} which results in the current stored in coil L2 being discharged into the load by D2.

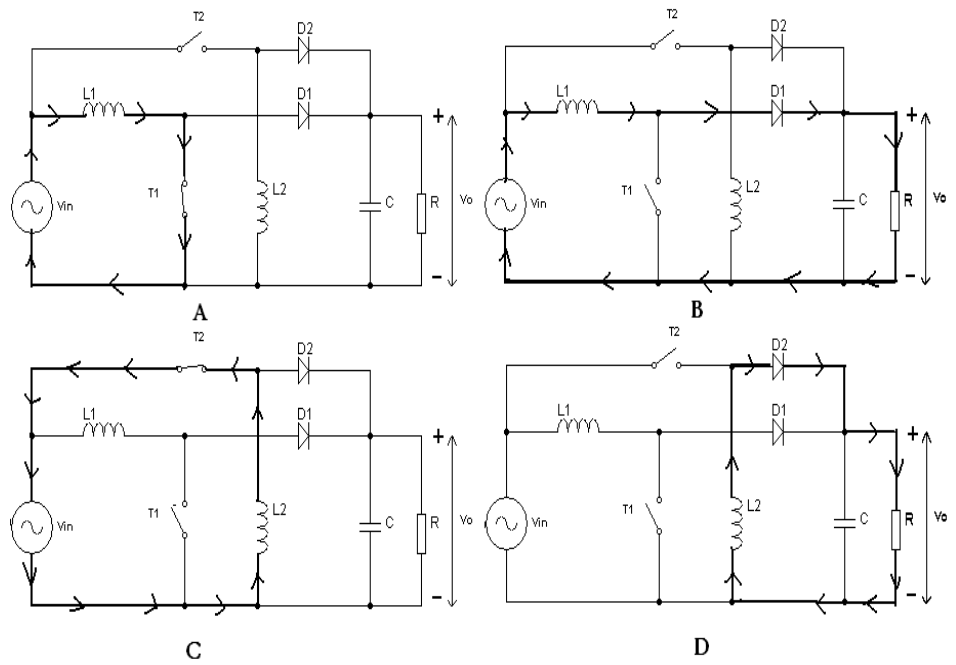


Figure (3): AC-DC Step Up Converter operating phases

Figure (4) shows the input voltage, the pulses applied to the gates G1 and G2, the currents passing through L1 and L2 for the four phases, and the output voltage.

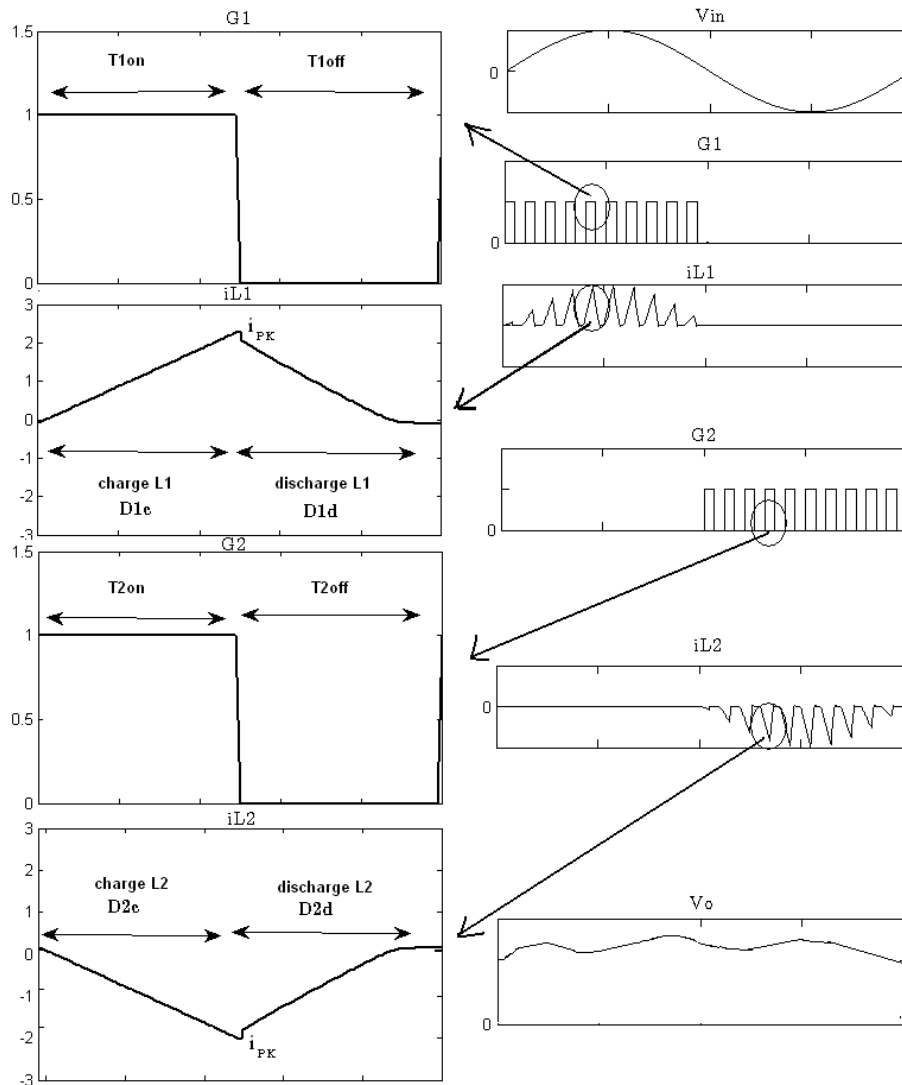


Figure (4): The pulses applied to the gates G1 and G2 and the currents passing through L1 and L2 in the lever rectifier switch

6. Design and simulation of the Fuzzy Controller:

Intelligent control algorithms are sometimes resorted to when the model of the system to be controlled is difficult to deduce mathematically or is simply unknown. Fuzzy control is one of the high-performance methods used in these cases, as it is used to avoid mathematical complexity in designing the control system [5].

Since our system to be controlled, which is the lever rectifier switch, contains several modes of operation, which complicates the mathematical model and thus the design of the controller, in this research a fuzzy controller was used to control this system according to the box diagram shown in Figure (5).

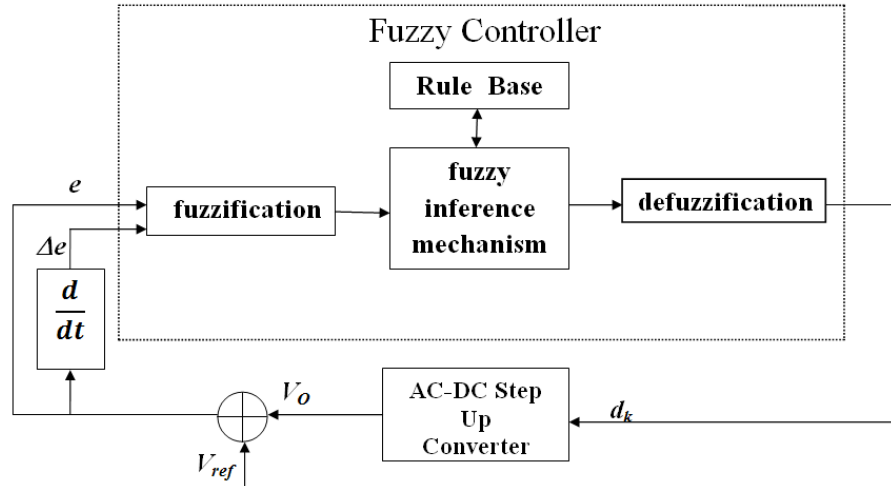


Figure (5): Block diagram for controlling AC-DC Step Up Converter using a fuzzy controller

The control system based on fuzzy logic is divided into several parts:

Fuzzification - rule base - fuzzy inference mechanism - defuzzification.

The fuzzy controller has two inputs, one for the error e and for the error change Δe , which are defined as follows [2]:

$$e = v_o - v_{ref} \quad (1)$$

$$\Delta e = e_k - e_{k-1} \quad (2)$$

Where V_o [volt], V_{ref} [volt] are respectively the switch output voltage and the reference voltage to be reached, taking into account the cut-off frequency of 10KHz.

The fuzzy controller output is expressed as the change Δd_k in the duty cycle at sample k , and thus the duty cycle relationship for the PWM control signal at sample k is given by the following relationship [2]:

$$d_k = d_{k-1} + n \cdot \Delta d_k \quad (3)$$

Where n is a calibratorable quantity called the gain of the fuzzy controller.

The fuzzification process determines the degree to which the error values e and the error change values Δe belong to the fuzzy membership functions shown in Table (1):

Table (1): Table of fuzzy affiliation functions for the fuzzy controller

PB	PS	ZE	NS	NB
Positive Big	Positive Small	Zero	Negative Small	Negative Big

Figure (6) shows the functions used in the fuzzification process for e and Δe .

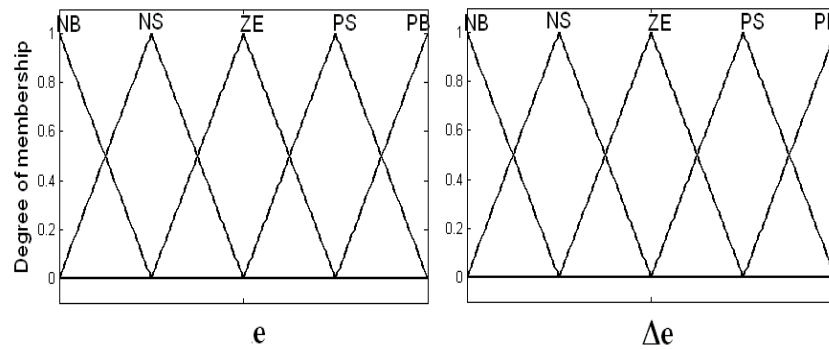


Figure 6: membership functions for e and Δe

The rules of fuzzy control are derived from human experience and expertise [9], and the design of the fuzzy controller was based on the following criteria:

- 1- When there is a large difference between the converter output value and the required output value, the duty cycle change Δdk of the PWM must be large in order to quickly reach the required value.
- 2- When the converter output value approaches the required value, the duty cycle change Δdk of the PWM should be small.
- 3- When the converter output value is close to the required value and is approaching quickly, the duty cycle must not change in order to prevent exceeding the required value.
- 4- When the required output value is reached and the output is still changing, the duty cycle must be changed slightly to prevent deviation from the required value.
- 5- When the required output value is reached and the output is constant, the duty cycle remains unchanged.
- 6- When the converter output value is greater than the required value, the duty cycle change Δdk for the PWM must be negative, and vice versa.

Based on the previous criteria, the following table of conditional rules was derived:

Table (2): Table of conditional rules for the fuzzy controller

$\Delta e \backslash e$	NB	NS	ZE	PS	PB
NB	NB	NB	NB	NB	ZE
NS	NB	NS	NS	ZE	NS
ZE	NB	NS	ZE	PS	PB
PS	NB	EZ	PS	PS	PB
PB	NB	NS	ZE	PS	PB

The table of conditional rules is expressed using Fuzzy If-Then. Considering that C is the fuzzy output of a single conditional rule, we get the following relationships:

Rule1: If e is NB and Δe is NB then C1 is NB.

Rule2: If e is NS and Δe is NB then C2 is NB.

.

.

Rule25: If e is PB and Δe is PB then C25 is PB.

We note that the conditional link And is used in the previous conditional rules only, where the min method was used and the Sugeno inference engine methodology was used to express the previous condition according to the following [7]:

$$Z_i = \min\{\mu(e_i), \mu(\Delta e_i)\} \quad (4)$$

Where

$\mu(e_i)$ The degree of membership e_i to fuzzy membership functions.

$\mu(\Delta e_i)$ Degree of membership Δe_i to fuzzy membership functions.

Z_i The result of the conditional rule And.

Using the weighted average method, which depends on the average of the sum of the output values of the conditional rules in the defuzzification process, we obtain the fuzzy controller output relationship as follows [7]:

$$WA = \Delta d_k = \frac{\sum_{i=1}^{25} z_i c_i}{\sum_{i=1}^{25} z_i} \quad (5)$$

The fuzzy controller was designed and simulated using MATLAB's Fuzzy ToolBox[6]. We show in Figure 7 the membership functions used in this research paper, which are of the triangle type, where we determined the input values of the fuzzy controller within the domain [-3.5V , +3.5V] Considering that we preset the switch output voltage to 3.5V.

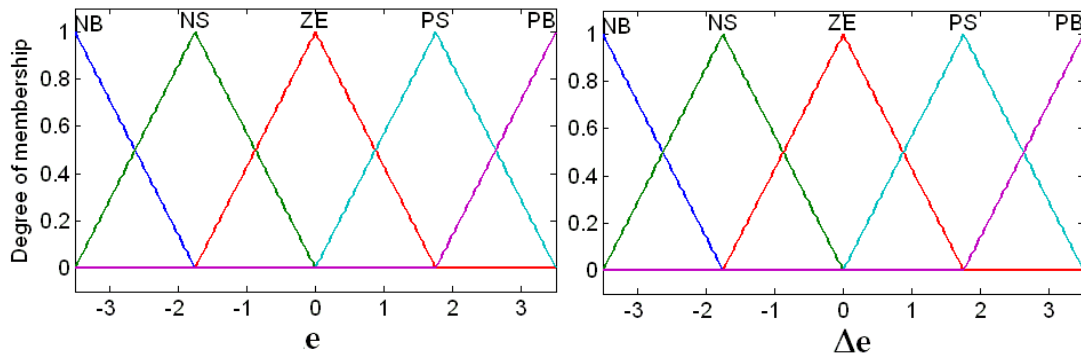


Figure (7): Triangle membership functions within the domain [-3.5V, +3.5V]

Considering that the output membership function takes fixed values for C according to Table (3)

Table (3): Values of the output membership function

NB	NS	ZE	PS	PB
0%	25%	50%	75%	100%

Using the conditional rules table (2) to construct the Fuzzy If-Then conditional rules, then the relationship of the fuzzy controller's output with respect to its two inputs, the error e and the error change Δe , is according to Figure (8), which represents the simulation [10].

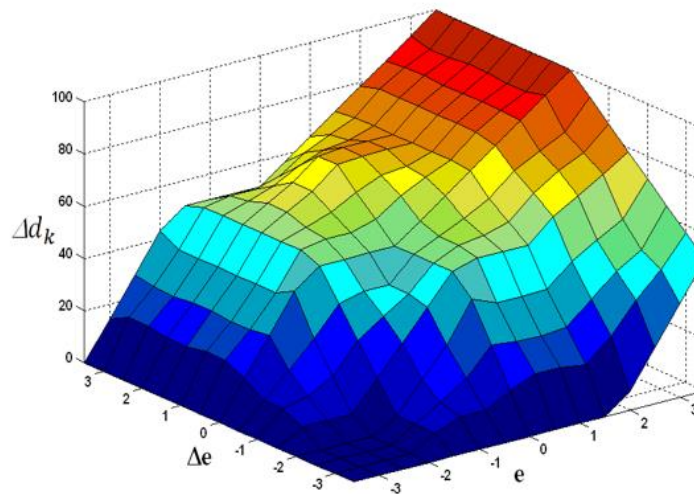


Figure (8): The relationship of the fuzzy controller output with respect to its input error e and the error change Δe

7. Design of a circuit for generating switch control pulses in an open circuit

In this research, an appropriate circuit was proposed that passes control pulses to the switch, as shown in Figure (9). This circuit consists of two comparators (OP1, OP2) to determine the positive and negative part of the alternating input voltage generated by the micro-generator and two logic gates (AND1, AND2) that act as pass switches for the PWM signal.

The work of the converter control pulse generation circuit can be divided into two parts:

- 1- At the positive part of the input voltage, the positive input voltage of the comparator OP1 becomes greater than the negative input voltage, then the output of this comparator becomes Logic 1. Thus, the AND1 gate passes the PWM pulses to the G1 gate, while the output of the comparator OP2 becomes Logic 0, and thus the AND2 gate blocks the signal. PWM for G2 gate.

- 2- At the negative part of the input voltage, the positive input voltage of the comparator OP2 becomes greater than the negative input voltage. Then the output of this comparator becomes in the Logic 1 state, and thus the AND2 gate passes the PWM pulses to the G2 gate. As for the comparator OP1, its output is in the Logic 0 state, so the AND1 gate blocks PWM signal from gate G1.

In this way, the boost converter works on the positive part of the AC input voltage, while the buck-boost converter works on the negative part of the input voltage.

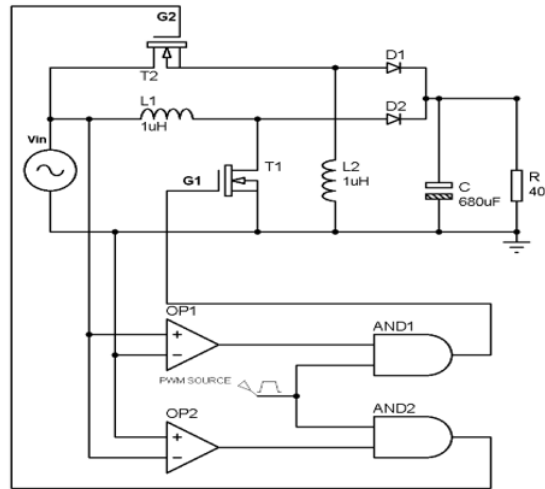


Figure (9): Circuit for generating control pulses and AC-DC Step Up Direct Converter in an open circuit

We simulated the circuit using the Proteus program, which is a simulation program for electronic circuits and microcontrollers that runs in real time. We assumed the values of the elements as shown in Figure (9). We also assumed that the frequency of the PWM signal is 2 kHz with duty cycle = 0.18, and assuming the load current changes within The range of [8.75-93.3] mA, which corresponds to a change in the load resistance [8.75-93.3] Ω At VODC output voltage=3.5V and using the ANALOGUE ANALYSIS tool to analyze the transient and steady state as follows:

Initially, an ohmic load of $R = 400 \Omega$ was used. The average value of the steady-state output voltage was $V_{ODC} = 3.503V$, with a peak-to-peak fluctuation of 0.15V. While the circuit was running, we changed the value of the load so that it became $R = 375\Omega$, so the average value of the output voltage in the steady state was $V_{ODC} = 3.398V$, with a peak-to-peak fluctuation of 0.17 V. We notice from the voltage curve shown in Figure 10 that the value of the output voltage in the open loop is affected by the change in the value of the load. We also notice that the time for the output voltage to reach the final state from zero to the final state took about 600ms.

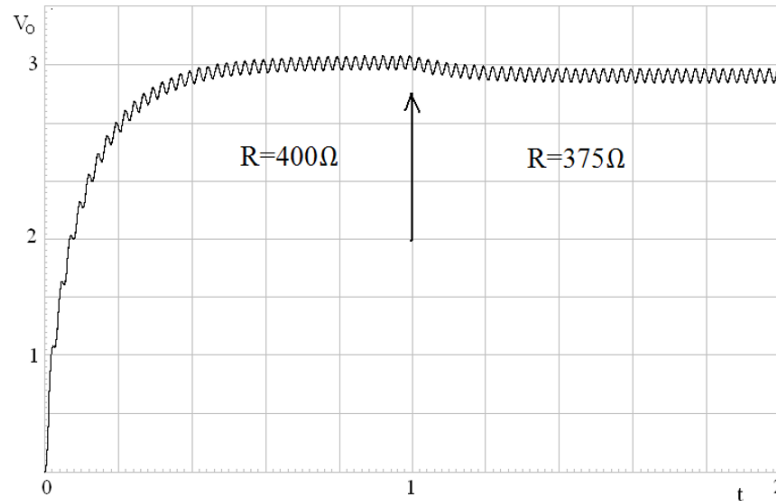


Figure (10): The effect of the open-loop Converter output signal when switching the load value from 400 Ω to 375 Ω

8. Design of the Converter control circuit using a closed-loop DSP controller

We show in Figure (11) the practical implementation of the closed-loop switch circuit. The fuzzy switch control algorithm was applied using the DSPIC33FJ12MC202 chip from MICROCHIP. This chip is distinguished by its DSP core and high processing speed of up to 40 MIPS. It can also operate at a low supply voltage of 2.5V and draws a working current of the order of milliamps, which is suitable for applications that use small electronic equipment, including our application.

From this chip, we used the 10-bit ANO terminal to measure the output voltage of the switch. The PWM1L1 terminal was also used to generate the work pulses applied via the trapping circuit to the transistor gates.

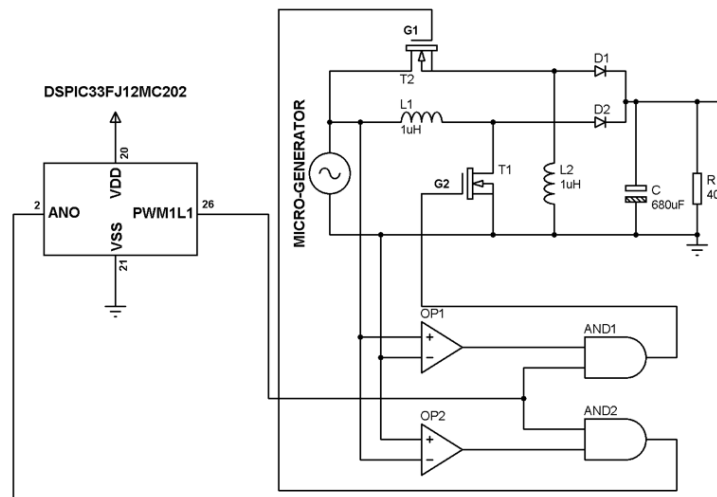


Figure (11): Ring Converter circuit using a DSP controller

The processor was programmed in C language using the mikroC PRO for dsPIC compiler in an optimal way so that the DSP instructions for the control algorithm worked in real time.

At a sampling frequency equal to 0.1 ms, the time required to implement the control algorithm took 0.891 ms. Below we show the program steps during one programming cycle:

- 1- Measure a sample of the converter's output voltage V_O and convert the analog value V_O into a digital value.
- 2- Calculate the error e and the error Δe changes depending on the previous sample.
- 3- Determine the degree of membership to e and Δe according to the functions of membership (fuzzification) in Figure (8).
- 4- Apply fuzzy control rules to fuzzy inputs using the Sugeno inference engine according to Table (2).
- 5- Calculating the change in the duty cycle (Δdk) according to the Weighted average (defuzzification) method.
- 6- Calculate the new duty cycle Δdk and update the value of the pulse width control register.
- 7- Return to step 1.

Another advantage of this chip is that it is available within the Proteus libraries, which enabled us to repeat the simulation as we explained in Section 7 using the closed-loop fuzzy control algorithm as follows:

Initially, an ohmic load of $R = 400 \Omega$ was used, so the average value of the output voltage in the steady state was $V_{ODC} = 3.509 \text{ V}$, with a peak-to-peak fluctuation of 0.13 V.

Later we changed the load value to $R=375 \Omega$, so the average value of the continuous output voltage was $V_{ODC}=3.507\text{V}$, with a peak-to-peak fluctuation of 0.14V.

We show in Figure (12) the output voltage curve, where it is clear that placing the system within a closed loop and using fuzzy control to regulate the voltage has led to an improvement in the shape of the output voltage compared to the open loop, as this voltage maintained its constant value despite the change in the load value.

On the other hand, we notice an improvement in the time for the output voltage to reach the final state, as it took about 100ms.

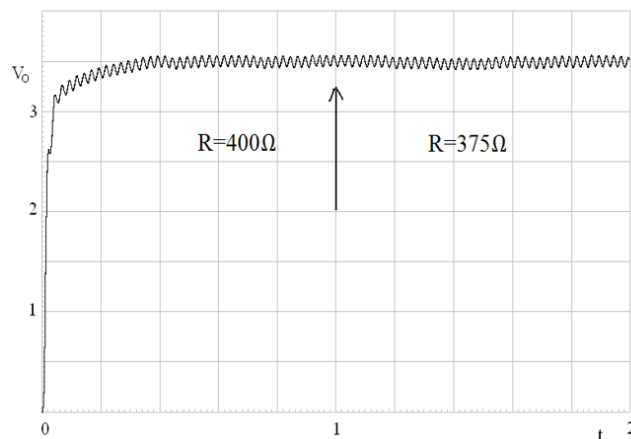


Figure (12): Output signal shape of the closed-loop converter at load $R=400\Omega$ and $R=375\Omega$

9. Results and discussion

It is clear to us through this theoretical study and the simulation results presented in this research paper that the use of a digital signal processor (DSP) and a fuzzy control algorithm to regulate the output voltage of a closed-loop AC-DC Step Up Converter Direct is characterized by the following:

- The response time of the switch improved from 600ms in the open loop to 100ms in the proposed method, which leads to an increase in the performance of the feeder system (converter, micro-generator), especially when the micro-generator operates intermittently Compared to search [2] which ranks 1 second.
- The proposed control method provides better regulation of the switch's output voltage, and reduces the fluctuation of the output voltage Compared to the open-loop circuit, the rate reaches 97 percent, compared to research [1], which had a high rate of 76 percent.
- Better stability of the output voltage at the required value when the load changes in the closed loop (the proposed method) compared to the circuit in the open loop .

This research presented an integrated system for a feeding unit with sustainable energy, unlike previous research that provided improvement in certain stages, such as research [1], [2], [3], [4].

10. Practical recommendations and proposals

This design can be used to implement a practical product in medical engineering, and in many other fields such as studying animal behavior and collecting data. It can also be greatly benefited from in industrial fields.

References

- [1] G. Ashok1, K. B. Madhu Sahu, Ch. Krishna Rao, **Closed Loop Operation of High Efficiency Ac-Dc Step-Up Converter Using Fuzzy Logic Controller**, *Journal of Engineering Research and Applications*, Vol. 3, Issue 6, Nov-Dec 2013.
- [2] H. Susan, K.Dhayalini, **Design and Simulation of AC to DC Low Voltage Energy Harvesting Converters**, *Journal of Scientific & Engineering Research*, Volume 4, Issue 8, August 2013.
- [3] S .Dwari ,L. Parsa, **An Efficient AC/DC Step Up Converter for Low Voltage Energy Harvesting**, *IEEE Trans On Power Electronics* VOL .25,NO.8, Aug 2010.
- [4] B. H. Stark, P. D. Mitcheson, M. Peng, T. C. Green, E. Yeatman, A. S. Holmes, **Converter circuit design, semiconductor device selection and analysis of**

- parasitics for micropower electrostatic generators**, *IEEE Trans. Power Electron.*, vol. 21, no. 1, pp. 27–37, Jan. 2006.
- [5] M .N. Cirstea, A. Dinu, J.G. Khor, M. McCormick; **Neural and Fuzzy Logic Control of Drives and Power Systems**; India. ISBN 07506 55585.2002.
- [6] S. N. Sivanandam, S. Sumathi ,S. N. Deepa; **Introduction to Fuzzy Logic using MATLAB**; New York. Springer,2007.
- [7] J. Ross; **FUZZY LOGIC WITH ENGINEERING APPLICATIONS**; USA. University of New Mexico,2010.
- [8] V. Dinavahi,N. Lin ; **DC-DC Converters**; USA. IEEE 2021.
- [9] G. Nandi; **Fuzzy Computing**; USA. IEEE 2024.
- [10] A.Puryaev, A.Puryaev ; **Fuzzy Logic Toolbox in Evaluating the Effectiveness of Projects in the Matlab Program**; IEEE . International Multi-Conference on Industrial Engineering and Modern Technologies (FarEastCon), 06-09 October 2020.
- [11]R. C. H. Chang et al., **A high-performance AC-DC rectifier with fully actively controlled switches for vibration energy harvesting**; Proceedings of IEEE WPTC, pp. 1-4, 2017.
- [12]A. Shin et al., **A MEMS Magnetic-Based Vibration Energy Harvester**; IEEE PowerMEMS, Nov. 2017.

Investigating Artificial Intelligence Systems Through the Use of Constrained Deep Neural Networks

**Mohammed Yahya Alghamdi ^a, Mohammed M. Abbassy ^b, Ayman Abo-Alnadr ^c, Emad Elabd ^{d,e},
Sayed Saber ^f, Waleed Ead ^{b,g*}**

^aDepartment of Computer Science, Faculty of Computing & Information, Al-Baha University, Al-Baha, Saudi Arabia.

^bFaculty of computers and artificial intelligence, Beni-Suef university, Egypt

^cInformation system Dept., Higher Institute of management and information technology, Kafr el Shekh, Egypt

^dFaculty of Computers and Information, Menoufia University, Shebin El Kom, Egypt

^eDepartment of Computer, Deanship of Educational Services, Qassim University, Buraydah, Saudi Arabia.

^fDepartment of Mathematics and Computer Science, Faculty of Science, Beni-Suef University, Egypt.

^gEgypt-Japan university of science and Technology (E-JUST), Alexandria, Egypt

Abstract: Deep neural networks have significantly advanced the field of image and text categorization, pushing the boundaries of machine learning. However, designing efficient neural network architectures remains a challenge, often requiring complex and costly methods to find optimal configurations. This paper introduces a novel approach to architectural design through a restricted search method, focusing on creating networks that are both cost-effective and fast, suitable for AI systems with strict memory and time limitations, particularly in near-sensor applications. Neural networks now surpass traditional machine learning techniques in various computational perception tasks. Despite their success, deploying these advanced models on mobile and IoT devices is computationally challenging, leading to reliance on cloud-based solutions. Such dependence increases communication costs and potential system inoperability during connectivity outages. Our method addresses these issues, offering a viable solution for efficient, local deployment of advanced neural networks in resource-constrained environments. We propose a conceptual framework that leverages a Deep neural networks (DNN) approach to decide whether data should be processed locally or sent to the cloud, optimizing both computational resources and performance. Our findings suggest that this method requires sending only 52% of test data to the server, achieving an overall system accuracy of 48%. This significantly enhances the efficiency of client-server models and supports the implementation of AI capabilities on local devices.

By employing a strategic search for computational models based on content extraction, we improve the efficiency and speed of AI operations. Our experiments demonstrate the practicality and effectiveness of this approach, which has also been tested on actual hardware, offering a promising direction for enhancing AI applications in resource-constrained environments.

Keywords: Efficiency, Query Issues, Branch Scanning, Metrics, Retrieval Phase, Perception, Networks, Sensor Fusion, Developing Artificial Intelligence, Simulation, Techniques, Convolutional Networks Layout

دراسة أنظمة الذكاء الاصطناعي من خلال استخدام الشبكات العصبية العميقة المقيدة

المخلص: لقد ساهمت الشبكات العصبية العميقة في تطوير مجال تصنيف الصور والنصوص بشكل كبير، مما دفع حدود التعلم الآلي إلى الأمام. ومع ذلك، لا يزال تصميم بنيات الشبكات العصبية الفعالة يمثل تحديًا، وغالبًا ما يتطلب أساليب معقدة ومكلفة للعثور على التكوينات المثالية. تقدم هذه الورقة نهجًا جديدًا للتصميم المعماري من خلال طريقة بحث مقيدة، مع التركيز على إنشاء شبكات فعالة من حيث التكلفة وسريعة، ومناسبة لأنظمة الذكاء الاصطناعي ذات القيود الصارمة على الذاكرة والوقت، وخاصة في تطبيقات أجهزة الاستشعار القريبة. تتفوق الشبكات العصبية الآن على تقنيات التعلم الآلي التقليدية في مهام الإدراك الحسابي المختلفة. وعلى الرغم من نجاحها، فإن نشر هذه النماذج المتقدمة على الأجهزة المحمولة وأجهزة إنترنت الأشياء يمثل تحديًا حسابيًا، مما يؤدي إلى الاعتماد على الحلول المستندة إلى السحابة. يؤدي هذا الاعتماد إلى زيادة تكاليف الاتصال واحتمال عدم تشغيل النظام أثناء انقطاع الاتصال. تعالج طريقتنا هذه المشكلات، وتقدم حلاً قابلاً للتطبيق للنشر المحلي الفعال للشبكات العصبية المتقدمة في البيئات المحدودة الموارد. نقترح إطارًا مفاهيميًا يعزز نهج الشبكات العصبية العميقة (DNN) لتحديد ما إذا كان يجب معالجة البيانات محليًا أو إرسالها إلى السحابة، مما يؤدي إلى تحسين الموارد الحسابية والأداء. تشير النتائج التي توصلنا إليها إلى أن هذه الطريقة تتطلب إرسال 52% فقط من بيانات الاختبار إلى الخادم، مما يحقق دقة إجمالية للنظام تبلغ 48%. وهذا يعزز بشكل كبير كفاءة نماذج خادم العميل ويدعم تنفيذ قدرات الذكاء الاصطناعي على الأجهزة المحلية. من خلال توظيف البحث الاستراتيجي عن النماذج الحسابية القائمة على استخراج المحتوى، نقوم بتحسين كفاءة وسرعة عمليات الذكاء الاصطناعي. وتُظهر تجاربنا مدى التطبيق العملي لهذا النهج وفعالته، والذي تم اختباره أيضًا على أجهزة فعلية، مما يوفر اتجاهًا واعدًا لتعزيز تطبيقات الذكاء الاصطناعي في البيئات المحدودة الموارد.

1. Introduction

The rapid development of artificial intelligence (AI) has led to an increase in complex tasks that require efficient and effective splitting. Premature exiting, an early termination of certain operations, can be a vital strategy for optimizing performance in real-time applications. This paper delves into using neural network search techniques to optimize this process. Artificial Intelligence (AI) has experienced monumental growth over the past few decades, evolving from rudimentary algorithms to sophisticated systems that can perform tasks previously believed to be exclusive to human intelligence. One area of AI that has been gaining traction is the ability to effectively split tasks, a crucial aspect for improving efficiency, especially in large-scale applications. This process, known as AI splitting, allows systems to divide complex tasks into more manageable sub-tasks. But with the rise of real-time applications, there has been a pressing need to ensure not just effective splitting, but also timely response. Enter the concept of premature exiting—a strategy that allows an AI system to terminate certain operations early, ensuring faster results, albeit at the potential cost of some accuracy, see [1], [2], [3], [4], [5].

Premature exiting is rooted in the understanding that in many scenarios, waiting for a complete and thorough computation might be less optimal than obtaining a quicker, albeit slightly less accurate result. For instance, in real-time object detection, it might be more beneficial to identify a potential threat quickly rather than wait for a thorough analysis that confirms the nature of every object in a scene. The challenge, however, lies in determining the optimal point at which to exit prematurely without compromising the integrity of the result excessively. This is where neural network search techniques come into play. Neural networks, inspired by the human brain's architecture, have been at the forefront of many recent AI advancements. These networks consist of interconnected nodes (neurons) that process and transmit information. The depth and complexity of these networks can be vast, allowing them to model intricate patterns and relationships in data. But this depth is a double-edged sword: while it provides the network with its powerful modeling capability, it also means that processing can be lengthy, especially in deeper architectures, see [6], [7], [8], [9].

Neural network search techniques aim to find the most efficient pathways or configurations within these expansive networks. By employing these techniques, one can optimize a network to recognize when it has gathered "enough" information to decide, allowing it to exit prematurely and deliver a result. Essentially, instead of traversing the entire depth of the network, the system can determine an exit point where the prediction's confidence surpasses a predetermined threshold. This is analogous to a student answering a question once they're reasonably sure of the answer, rather than pondering all possible solutions [10], [11], [12], [13], [14].

But how does one determine these exit points? The answer lies in the training process. When training a neural network, we typically feed it vast amounts of data, adjusting its internal parameters to minimize the difference between its predictions and the actual outcomes. By integrating premature exiting into this training paradigm, we can simultaneously optimize accuracy and speed. The neural network is trained not only to recognize patterns in data but also to gauge its own confidence in its predictions. When this confidence reaches a level deemed satisfactory, the network can opt for a premature exit, thereby speeding up the response time [15], [16], [17], [18]. It's worth noting that the balance between speed and accuracy is a delicate one. If a network exists too early, it risks producing results that are too inaccurate to be useful. Conversely, if it waits too long, it might negate the benefits of premature exiting. This balance becomes even more critical in applications where stakes are high, such as medical diagnoses or autonomous vehicle navigation. Also, the integration of neural network search techniques into AI splitting, combined with the strategy of premature exiting, holds significant promise for the future of real-time AI applications. By allowing systems to intelligently determine when they have enough information to make a decision, we can achieve a harmonious blend of speed and accuracy. As the demand for real-time AI continues to grow, strategies like these will be indispensable in ensuring that our systems are both swift and reliable. As with all technological advancements, continuous research and refinement are essential, but the foundations laid by these techniques are undeniably robust and promising for the future landscape of AI.

2. Research Background

In the realm of artificial intelligence (AI), the ability to efficiently split tasks is paramount. This process, often referred to as task decomposition, involves breaking down complex problems into smaller, more manageable sub-tasks [1], [2], [4], [5]. Such division not only makes problem-solving more tractable but also allows for parallel processing, speeding up computations. For instance, in the field of robotics, a task like "cleaning a room" might be split into sub-tasks like "picking up objects," "vacuuming the floor," and "dusting surfaces" ([12], [17]). Each sub-task can then be tackled using specialized algorithms or models. Similarly, in natural language processing, understanding a paragraph might involve tasks such as sentence segmentation, word tokenization, syntactic parsing, and semantic analysis [2].

By splitting these tasks, AI researchers can focus on optimizing individual components, which collectively leads to improved overall performance. Furthermore, task splitting is pivotal in collaborative AI systems, where multiple agents work together [7]. Each agent can be assigned a specific sub-task, fostering cooperation and efficiency. In essence, splitting tasks in AI not only simplifies complex challenges but also harnesses the power of specialization and collaboration, pushing the boundaries of what AI systems can achieve.

Premature exiting, in the context of deep learning and neural networks, refers to the practice of allowing a model to make early predictions before processing through all its layers. Typically, deep models, especially those like deep convolutional neural networks, process input data through multiple layers to derive a final prediction. However, with premature exiting, if the model is confident enough in its prediction at an earlier stage, it can bypass the remaining layers and provide an immediate output ([1], [10], [11]). The primary benefit of this approach is efficiency [12]. As deep learning models have grown deeper and more complex, their computational demands have increased exponentially. By allowing for early exits, the computational cost can be significantly reduced, especially when the model is dealing with simpler inputs that don't necessitate full processing. This results in faster predictions and saves valuable resources, making it particularly beneficial for real-time applications or devices with limited computational power. Moreover, premature exiting can also aid in preventing overfitting [13]. By not always relying on the deeper layers, which are more prone to fitting noise in the data, models can sometimes generalize better to unseen data. However, implementing premature exiting comes with its set of challenges [14]. The first is determining the criteria for an early exit. The model must be equipped with a mechanism to gauge its confidence in a prediction. This often involves auxiliary classifiers placed at various stages of the network, adding to the model's complexity. Furthermore, training such a model requires careful consideration. Traditional training methods might not be directly applicable, and new strategies, such as staged training or specialized loss functions, might be necessary. Another challenge is ensuring that the premature exit does not compromise the accuracy of the model. While the idea is to exit early for simpler inputs, there is always a risk that the model might make an incorrect early prediction, especially in borderline cases. Balancing speed and accuracy is crucial ([15], [16], [18]). Finally, premature exiting offers a promising avenue to enhance the efficiency of deep learning models, making them more adaptable to diverse applications and constraints. While the benefits in terms of speed and potential generalization are apparent, the challenges in training and implementation necessitate thorough research and careful design. As AI continues to integrate more deeply into real-world applications, strategies like premature exiting will play a pivotal role in bridging the gap between computational demand and available resources.

The quest to optimize neural network architectures has been a central theme in the evolution of deep learning. Historically, the design of these networks was largely based on human intuition, experimentation, and manual tweaking ([6], [7], [8], [9]). Researchers would adjust layers, nodes, and other hyperparameters based on heuristic insights, often informed by previous successes and failures. Pioneering architectures like LeNet, AlexNet, and VGG were products of this manual design process. However, as the complexities of tasks and datasets grew, so did the architectures, making manual exploration increasingly infeasible.

Enter the era of automated neural architecture search (NAS) ([1], [2], [4], [5], [19]). NAS algorithms aim to automatically discover optimal or near-optimal network architectures [20], alleviating the need for human-led trial and error. The seminal work in this space used reinforcement learning, where a controller network proposed architectures and was rewarded based on the performance of the resultant networks [21]. While effective, early NAS methods were computationally expensive, often requiring thousands of GPU hours.

Recent advancements have addressed these inefficiencies. One significant leap is weight-sharing methods, where different architectures share weights, enabling a faster evaluation of multiple architectures without training each one from scratch ([10], [11], [12], [13], [14], [22]). Techniques like DARTS represent this category, allowing for more efficient search processes. Another advancement is the use of evolutionary algorithms, inspired by natural selection, to evolve optimal network designs [23]. Furthermore, the rise of transfer learning, where pretrained models on large datasets are fine-tuned for specific tasks, has also influenced NAS, leading to methods that search for optimal fine-tuning strategies ([10], [24]). In reflection, the journey from manual design to automated neural network search encapsulates the broader evolution of AI: from relying heavily on human expertise to developing self-optimizing systems. As the field continues to progress, the boundary between designer and design is poised to blur further, with AI systems playing an increasingly active role in their own evolution.

While existing NAS methods have achieved remarkable results, they often focus on maximizing accuracy without sufficient consideration of deployment constraints on edge devices. Our approach distinguishes itself by explicitly incorporating a restricted search method aimed at optimizing both cost-effectiveness and speed, making it highly suitable for near-sensor applications with stringent memory and time limitations. In comparison to methods like BranchyNet and SACT, which introduce early-exit strategies to improve inference speed, our method integrates these strategies within the NAS framework to ensure that the resulting architectures are inherently designed for efficient early exits. This allows for a more seamless and effective balance between performance and computational efficiency.

3. Methodology

3.1. Neural Network Architecture: Details of the neural architecture employed.

The neural architecture employed in this context utilizes a deep convolutional neural network (CNN) designed for image classification tasks. This network architecture is specifically tailored to process and analyze visual data, making it suitable for a wide range of computer vision applications. CNN consists of multiple layers, including convolutional layers, pooling layers, and fully connected layers. The convolutional layers are responsible for learning spatial features from the input image through a series of convolution operations, effectively detecting patterns and edges. These layers are typically followed by pooling layers, which reduce the spatial dimensions of the feature maps while retaining essential information. This process is repeated multiple times to extract increasingly abstract and complex features from the image.

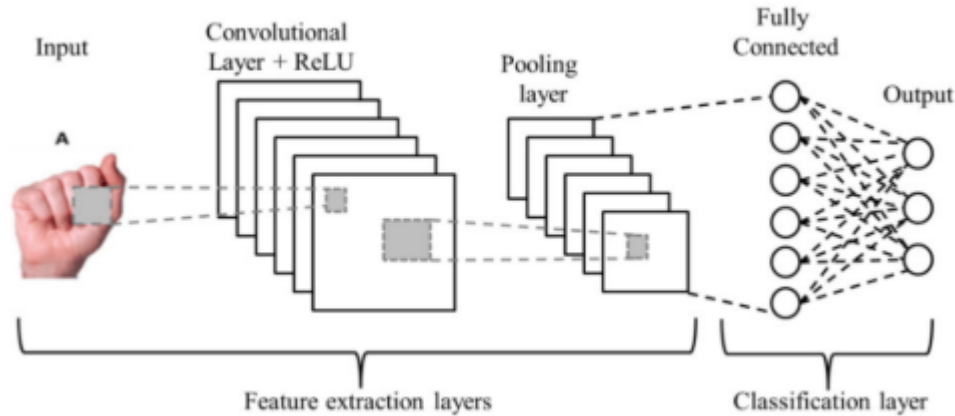


Figure 1. Information Flow through the layers of the neural network

The extracted features are then passed through one or more fully connected layers, which act as a classifier to make predictions. These layers learn to associate the extracted features with specific classes or categories, enabling the network to identify and classify objects within the input image. Tree diagram for artificial intelligence is given by figure 1. In this diagram, you can see the flow of information through the layers of the neural network, illustrating how the input image is processed to make predictions about its content. This neural architecture, with its convolutional layers, pooling layers, and fully connected layers, forms the foundation for many successful image recognition and classification tasks in the field of deep learning.

3.2. Training Procedure: Information on hyperparameters, training iterations, and evaluation metrics.

The training procedure of a machine learning model is a critical aspect of its development, as it directly influences the model's performance and capabilities. It involves several key components, including the selection of hyperparameters, determining the number of training iterations, and establishing evaluation metrics to assess the model's performance. Hyperparameters are parameters that are set prior to the training process and cannot be learned from the data. They significantly impact the model's behavior and generalization ability. Examples of hyperparameters include learning rates, batch sizes, and the architecture of neural networks. Choosing appropriate hyperparameters is often done through experimentation and tuning, as finding the right combination can significantly impact the model's performance. Training iterations refer to the number of times the model's weights are updated using the training data. More iterations can lead to better convergence, but it can also risk overfitting the model to the training data. Balancing this trade-off is crucial. Additionally, techniques like early stopping can be employed to halt training when performance on a validation set plateaus, preventing overfitting.

Architecture diagram for restrictive deep neural network is given by Figure 2. A restrictive deep neural network architecture is designed to be efficient in terms of computational resources, making it suitable for deployment on devices with limited memory and processing power, such as mobile and IoT devices.

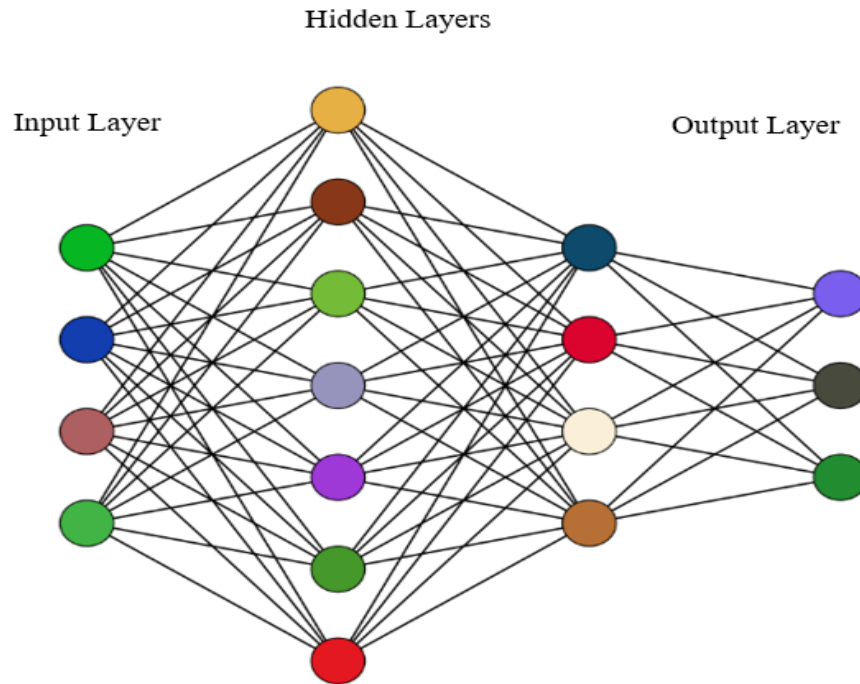


Figure 2. Architecture diagram for restrictive deep neural network

Evaluation metrics are used to quantitatively assess how well the model performs on a specific task. The choice of metrics depends on the problem at hand. For classification tasks, metrics like accuracy, precision, recall, and F1-score are commonly used. In regression tasks, metrics like mean squared error (MSE) or mean absolute error (MAE) are employed. The choice of metrics should align with the project's objectives and provide a comprehensive understanding of the model's performance. Furthermore, it's important to establish a robust evaluation protocol that includes cross-validation, or a separate validation set to ensure the model's performance generalizes well to unseen data. So, the training procedure of a machine learning model involves making informed decisions about hyperparameters, determining the appropriate number of training iterations, and defining relevant evaluation metrics. These components collectively shape the model's effectiveness and its ability to solve real-world problems. A well-designed training procedure is essential for building models that can make accurate predictions and drive meaningful insights from data. As depicted in the following Algorithm 1.

Algorithm 1

1. **Start:** Begin the algorithm.
2. **Input Constraints:** Define the input constraints, including memory limits, processing time, and accuracy requirements.
3. **Initialize Search Space:** Initialize the search space with a set of possible network architectures.
4. **Evaluate Initial Population:** Evaluate the initial population of architectures against the defined constraints using a performance metric (e.g., accuracy).
5. **Selection:** Select architectures that best meet the constraints for further exploration.
6. **Generate Variants:** For each selected architecture, generate variants by altering layers, nodes, or connections.
7. **Evaluate Variants:** Evaluate the new variants against the constraints.
8. **Check Improvement:** Check if there is an improvement in the performance metric within the constraints.
 - **If Yes:** Update the selection with better-performing architectures.
 - **If No:** Proceed to termination criteria.
9. **Termination Criteria:** Determine if the search has met the termination criteria (e.g., maximum iterations or no further improvement).
 - **If Not Met:** Go back to step 5 (Selection).
 - **If Met:** Proceed to the final step.
10. **Output Optimal Architecture:** Output the architecture(s) that best meet the constraints and performance metric.
11. **End:** End of the algorithm.

3.3. Objectives and Motivation

The primary objective of this research is to address the significant challenges associated with the design and implementation of artificial intelligence (AI) systems, particularly those employing deep neural networks (DNNs), under stringent resource constraints. These challenges include high computational demands, extensive memory requirements, and the need for rapid processing speeds, which are critical for AI applications in near-sensor environments and on edge devices. The motivation behind this work is twofold:

1. Efficiency in Design: Despite the proven capabilities of DNNs in various domains, such as image and text categorization, the design of these networks remains a labor-intensive and complex task. Traditional methods for finding optimal network architectures are often prohibitively expensive and time-consuming. There is a pressing need for a streamlined approach that can discover efficient architecture more rapidly and at a lower cost.

2. Operational Constraints: Many AI applications are intended for deployment in environments with limited computational resources, such as mobile and Internet of Things (IoT) devices. These environments necessitate models that not only perform well but also adhere to strict memory and processing time limitations. Furthermore, reliance on cloud-based processing introduces issues related to connectivity dependence, data privacy, and operational costs.

To address these challenges, this work proposes a novel, constrained architectural search methodology that aims to identify efficient DNN architectures that can operate within the specific limitations of near-sensor AI systems. By doing so, this research seeks to broaden the applicability of AI technologies, enabling their deployment in a wider range of settings, including those where computational resources are scarce. The goal is to enhance the performance and accessibility of AI systems, making them more adaptable to various operational constraints while maintaining high levels of accuracy and efficiency. Our methodology focuses on designing a restricted neural architecture search framework that optimizes for both cost-effectiveness and speed, making it suitable for deployment on resource-constrained devices such as mobile phones and IoT devices. To further enhance computational efficiency, we incorporate early-exit strategies into the NAS framework. These strategies allow the network to make intermediate predictions, which can significantly reduce inference time and resource usage for simpler inputs. By incorporating early-exit strategies within a restricted NAS framework, our methodology addresses the key challenges of deploying efficient neural networks on resource-constrained devices as shown in algorithm 1. The proposed approach not only improves computational efficiency but also ensures high performance, making it highly suitable for near-sensor AI applications.

4. Proposed Approach

In our study on premature exiting in machine learning models, we devised an experimental set comprising various datasets and model architectures to assess the efficacy of our tailored objective function. By integrating validation metrics and convergence criteria into the objective function, we aimed to determine the optimal point for halting the training process. Our experimental setup involved dividing datasets into training, validation, and test segments, with models subjected to training under controlled conditions. Performance metrics such as accuracy, precision, and recall were monitored across epochs.

To validate the performance and efficiency of premature exiting, we implemented a systematic comparison against traditional training methods. This involved tracking the computational resources consumed and the time taken to reach peak performance.

The results were obtained through rigorous testing, where each model was trained multiple times to ensure consistency and reliability of the outcomes. Our analysis focused on identifying patterns of performance plateauing and degradation, using these insights to refine the premature exiting criteria. The innovative aspect of our approach lies in the dynamic adjustment of the training process based on real-time performance evaluation, ensuring models do not overfit or waste computational resources. This methodology has shown promise in significantly reducing training times while maintaining or even enhancing model performance, marking a substantial improvement over traditional extended training method. Our findings underscore the importance of a well-crafted objective function in optimizing machine learning workflows, especially in resource-constrained scenarios.

4.1. Neural Search Strategy: Explanation of the search strategy used to explore possible split points.

In the realm of neural networks and machine learning, the neural search strategy refers to a systematic approach for exploring and identifying optimal split points or decision boundaries within data. This strategy plays a pivotal role in various applications such as decision trees, gradient boosting, and neural network architectures, particularly when dealing with classification tasks.

The primary objective of a neural search strategy is to efficiently navigate through the feature space and identify the points at which the model can separate data into different classes or categories most effectively. To achieve this, it often employs algorithms like gradient descent, backpropagation, or evolutionary optimization techniques. In decision trees, for example, the search strategy evaluates different features and their thresholds to split data into subsets that are as pure as possible in terms of class labels. Gradient boosting algorithms iteratively optimize the choice of split points to minimize the residual errors. In neural networks, the search strategy involves adjusting the weights and biases of neurons to minimize the loss function, effectively learning the optimal decision boundaries.

The choice of a search strategy depends on the problem complexity, dataset size, and computational resources available. More sophisticated strategies may involve random sampling, genetic algorithms, or Bayesian optimization to efficiently explore the vast feature space. Ultimately, an effective neural search strategy is crucial for training accurate models that can generalize well to unseen data. It enables models to learn intricate patterns and relationships within the data, leading to improved performance and predictive capabilities across various machine learning tasks.

The restricted NAS framework operates within a constrained search space to ensure that the resulting architectures are computationally feasible for edge devices.

The key components of the NAS framework are:

- **Search Space Definition:** Our search space includes various types of layers (e.g., convolutional, pooling, and fully connected layers), with constraints on their size and complexity to ensure efficiency.
- **Search Strategy:** We utilize a modified evolutionary algorithm that focuses on optimizing both accuracy and computational efficiency. The evolutionary process involves selection, crossover, and mutation operations tailored to our constraints.
- **Evaluation Metric:** We introduce a composite metric that combines accuracy and computational cost to guide the search process towards efficient architectures. Algorithm 2 demonstrate such explanation.

4.2. Exit Criteria: Conditions for premature exiting.

Exit criteria in the context of machine learning and optimization refer to the conditions or thresholds that determine when a specific process, such as training a model or conducting an experiment, should be prematurely terminated. These criteria are essential for preventing unnecessary computational expenses and ensuring the efficient allocation of resources. Common exit criteria include reaching a predefined level of performance (e.g., accuracy or loss), achieving convergence (i.e., minimal improvement in the objective function), exceeding a time or resource limit, or detecting signs of overfitting. By establishing clear and appropriate exit criteria, practitioners can strike a balance between obtaining desirable results and conserving valuable time and resources.

As shown in algorithm 3 , Early-exit strategies allow the network to make intermediate predictions, thus reducing inference time and computational load for simpler inputs. We integrate early-exit branches at various depths of the network, enabling a flexible trade-off between accuracy and efficiency.

- **Design of Early-Exit Branches:** Each early-exit branch consists of a few layers (e.g., convolutional layers followed by a classifier) designed to provide accurate predictions with minimal computation.
- **Optimization of Early-Exit Criteria:** We optimize the criteria for early-exit (e.g., confidence thresholds) during the training process to ensure that the network exits early whenever possible without compromising overall performance.

Algorithm 2: Restricted NAS Framework

- 1: Initialize the population with random architectures within the constrained search space
- 2: for each generation do
- 3: Evaluate each architecture using the composite metric (accuracy and computational cost)
- 4: Select the top-performing architectures based on the composite metric
- 5: Apply crossover and mutation to generate new candidate architectures
- 6: Incorporate early-exit branches into candidate architectures
- 7: Re-evaluate architectures with early-exit branches using the composite metric
- 8: Select the final set of architectures for the next generation
- 9: end for
- 10: Return the best-performing architecture

Algorithm 3: Early-Exit Branch Optimization

- 1: Initialize the network with early-exit branches at predefined depths
- 2: for each training epoch do
- 3: for each input sample do
- 4: Compute intermediate predictions at each earlyexit branch
- 5: Evaluate the confidence of each intermediate prediction
- 6: If confidence exceeds the threshold, use the intermediate prediction
- 7: Else, pass the input to the next layer
- 8: end for
- 9: Update the network parameters and confidence thresholds based on loss and accuracy
- 10: end for
- 11: Return the optimized network with early-exit branches

5. Results

Benchmarking is a fundamental practice in the field of artificial intelligence (AI) that involves comparing a proposed approach against traditional methods to assess its effectiveness and efficiency. In the context of splitting data effectively with premature exiting using neural network search, benchmarking plays a pivotal role in evaluating the novelty and performance of the proposed methodology in comparison to established AI techniques. Traditional methods for splitting data and implementing premature exiting in AI encompass a range of strategies, including decision trees, random forests, gradient boosting, and various heuristic approaches. These methods often rely on handcrafted rules, feature engineering, or statistical techniques to make data partitioning decisions and halt the training process when necessary. They have been widely used in machine learning for classification tasks and have proven to be effective in many domains. Activation function and Forward propagation in a layer is given by (1) and (2).

$$\sigma(z) = \frac{1}{1+e^z}, \tag{1}$$

$$a^{[l]} = g^{[l]}(z^{[l]}), \tag{2}$$

where $z^{[l]} = w^{[l]}a^{[l-1]} + b^{[l]}$ and $g^{[l]}$ is the activation function for layer l .

We conduct experiments on standard image classification datasets, including CIFAR-10 and ImageNet, which are widely used benchmarks for evaluating neural network performance. For hardware configuration, We use an NVIDIA Tesla V100 GPU for training and evaluation, with 32GB of memory. For edge device simulations, we utilize a Raspberry Pi 4 Model B with 4GB RAM. For the software configuration, the experiments are conducted using PyTorch 1.7 as the deep learning framework. We implement our NAS framework and early-exit strategies within this environment.

The proposed approach, on the other hand, involves utilizing neural network-based search strategies to automatically discover optimal data splitting points and exit criteria. This methodology leverages the power of deep learning and neural networks to learn intricate patterns and relationships within the data, adaptively adjusting splitting decisions during training. It seeks to combine the flexibility and representation learning capabilities of neural networks with the efficiency of premature exiting, potentially leading to more accurate and efficient models. Benchmarking these two approaches involves several key aspects:

- **Performance Metrics:** To assess the effectiveness of both methods, various performance metrics are considered, such as accuracy, precision, recall, F1-score, and computational efficiency. These metrics provide a comprehensive view of how well each approach splits data and makes premature exit decisions.
- **Data Diversity:** A diverse dataset comprising different types of data, including structured, unstructured, and real-world data, is used to test the robustness and generalization ability of the methods. This ensures that the benchmarking results are applicable across various domains and scenarios.
- **Computational Resources:** Benchmarking includes evaluating the computational resources required for both approaches. This involves measuring the training time, memory usage, and hardware requirements, allowing practitioners to make informed decisions based on available resources.
- **Hyperparameter Tuning:** The benchmarking process may also involve hyperparameter tuning for both methods to ensure that they are operating at their optimal configurations. This helps to avoid any potential bias in the comparison due to suboptimal parameter settings.
- **Statistical Significance:** To draw meaningful conclusions, statistical significance tests are often applied to assess whether observed differences in performance are statistically significant or could have occurred by random chance.
- Ultimately, benchmarking serves as a critical step in the evaluation and validation of the proposed neural network-based approach for splitting data effectively with premature exiting.

Table-1. Number of layers vs. various metrics

Network Name	Number of Layers	Accuracy (%)	Training Time (hrs)	Number of Parameters (millions)
NetA	5	85	1.5	2
NetB	10	90	2	4
NetC	15	92	3	8
NetD	20	93	4	16
NetE	25	94	5	32

It allows researchers and practitioners to determine whether the new methodology provides a substantial improvement over traditional AI methods in terms of accuracy, efficiency, and adaptability to various data types. Additionally, benchmarking can help identify scenarios where the neural network-based approach excels and where traditional methods may still have their place, facilitating informed decision-making in AI model development and deployment. Number of layers with respect to various metrics is given by table 1 and figure 3. It is noticed that while the number of layers increases it affects the accuracy level to be increased on one hand, but we see , it's costly in the time of training. The Cost function and Cross-Entropy cost function for classification is given below:

$$I(W, b) = \frac{1}{2m} \sum (y^{(i)} - \hat{y})^2, \quad (3)$$

$$I(W, b) = -\frac{1}{m} \sum y^{(i)} \log (\hat{y}) + (1 - y^{(i)}) \log (1 - \hat{y}), \quad (4)$$

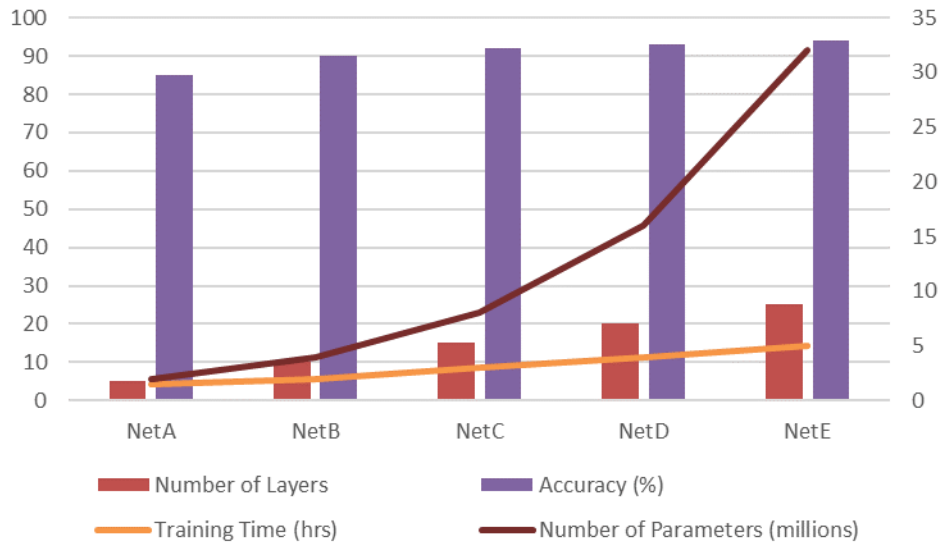


Figure-3. Representation of Number of Layers vs. Various Metrics

5.1. Real-world Application: Demonstrating the performance of the proposed method in real-world scenarios.

Demonstrating the performance of the proposed method for Artificial Intelligence Splitting Effectively with Premature Exiting Using Neural Network Search in real-world scenarios is crucial to validate its practical utility and effectiveness across diverse applications. Such real-world applications showcase the methodology's adaptability and potential impact on addressing practical challenges in fields where AI plays a pivotal role.

One compelling real-world application of this methodology can be found in the realm of medical diagnostics, specifically in the domain of disease classification from medical images. In medical imaging tasks like the detection of lung cancer from CT scans or diabetic retinopathy from retinal images, the accuracy and efficiency of data splitting and model training are of paramount importance. Traditional approaches may require expert-designed heuristics to determine how to split data into training and validation sets and when to halt training, which can be suboptimal and time-consuming.

By applying the proposed method in this context, AI researchers and medical practitioners can potentially benefit from its ability to autonomously discover optimal data splitting strategies and exit criteria.

The neural network-based search can adapt to the nuances of medical image data, such as variations in image quality and patient demographics. Moreover, it can help in identifying the right moment to stop training, preventing overfitting and reducing computational costs.

The methodology's performance can be evaluated using critical metrics like sensitivity, specificity, and AUC-ROC, demonstrating its ability to aid in early and accurate disease diagnosis. Another real-world application lies in autonomous vehicles and their perception systems. Training neural networks to accurately recognize and interpret visual data from cameras, LiDAR, and radar sensors is a complex task and given by table 2 and figure 4. It shows the decreasing in validation error rate while the number in epochs increased. The proposed method can be employed to fine-tune models for various driving scenarios, including lane detection, object recognition, and pedestrian tracking. Neural network search can adaptively determine when to exit training, ensuring that the models achieve a delicate balance between accuracy and computational efficiency. In a safety-critical domain like autonomous driving, where split-second decisions matter, demonstrating the effectiveness of the methodology through real-world testing and validation is essential.

Table 2. Datasets trained vs. various metrics.

Network Name	Datasets Trained	Validation Error (%)	Test Error (%)	Epochs Required
NetA	10	10	12	10
NetB	20	8	10	15
NetC	30	6	8	20
NetD	40	5	7	25
NetE	50	4	5	30

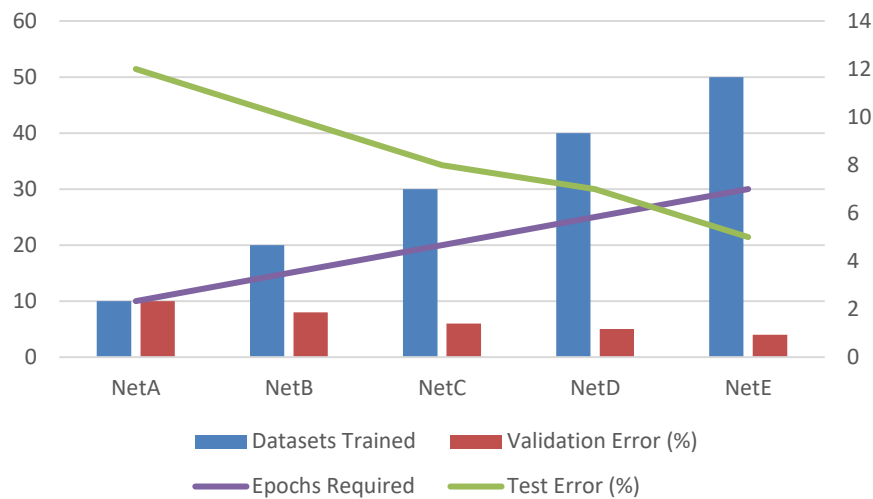


Figure 4. Representation of Number of Layers vs. Various Metrics

Furthermore, in the financial sector, where AI is increasingly utilized for fraud detection, portfolio optimization, and algorithmic trading, the proposed method can be applied to enhance model development. Detecting fraudulent transactions or optimizing trading strategies require models that can adapt quickly to changing market conditions while maintaining high accuracy. By automating the data splitting and training termination decisions, the methodology can help financial institutions improve their models' performance and reduce risks. Real-world testing can involve evaluating the model's performance on historical data and comparing it against traditional methods to showcase its advantages in terms of both accuracy and efficiency. Backpropagation and Dropout regularization (for layer l) is given by (5), (6) and (7) respectively.

$$w^{[l]} = w^{[l]} - \alpha \frac{\partial J}{\partial w^{[l]}}, \quad (5)$$

$$b^{[l]} = b^{[l]} - \alpha \frac{\partial J}{\partial b^{[l]}}, \quad (6)$$

$$d^{[l]} = np.random.rand(a^{[l]}.shape[0], a^{[l]}.shape[1]) < keep_prob, \quad (7)$$

where $d^{[l]}$ is the dropout mask and *keep_prob* is the probability of keeping a neuron active.

In all these real-world applications, the proposed method's performance can be quantified not only in terms of traditional metrics but also in practical benefits such as reduced computational resources, improved model generalization, and faster deployment of AI systems. These real-world demonstrations serve as compelling evidence of the methodology's effectiveness and its potential to transform various industries by making AI model development more efficient, accurate, and adaptable to the challenges of complex and dynamic environments. Such applications validate the practical relevance of the proposed approach and underscore its significance in advancing the field of artificial intelligence.

5.2. Computational Overhead: Analysis of the computational savings achieved.

The analysis of the computational savings achieved through the approach of Splitting Effectively with Premature Exiting Using Neural Network Search is crucial for understanding the practical benefits and efficiency gains that this methodology offers in comparison to traditional methods.

This analysis focuses on quantifying the reduction in computational resources, training time, and associated costs, highlighting the potential impact on various applications. First and foremost, one of the key advantages of this approach is its ability to significantly reduce the computational resources required during the training phase of machine learning models. Traditional methods may involve extensive trial and error in determining optimal splitting criteria and training epochs, often consuming a substantial amount of CPU or GPU time and given by table 3 and figure 5. In contrast, the neural network search approach dynamically adapts these decisions, learning from the data itself.

The savings in computational resources become particularly evident when dealing with large datasets and complex neural network architectures. For instance, in deep learning applications involving massive image datasets or natural language processing tasks, the proposed method can lead to substantial reductions in training time. This not only accelerates the model development cycle but also lowers the operational costs associated with utilizing high-performance computing infrastructure.

Table 3. Network Hyperparameters

Network Name	Learning Rate	Batch Size	Dropout Rate (%)	Regularization Lambda
NetA	0.01	32	5	0.1
NetB	0.005	64	10	0.2
NetC	0.001	128	15	0.3
NetD	0.0005	256	20	0.4
NetE	0.0001	512	25	0.5

Furthermore, the computational savings achieved through premature exiting using neural network search extend beyond just training time. By dynamically deciding when to halt training, the approach prevents overfitting, which is a common issue in machine learning. Overfit models tend to require more computational resources and time to train, and they often perform poorly on unseen data. The methodology's ability to curb overfitting leads to a more efficient allocation of computational resources and a higher likelihood of producing models that generalize well. In addition to the direct computational benefits, there are indirect cost savings associated with this approach. Traditional methods may necessitate extensive hyperparameter tuning and expert intervention to fine-tune the data splitting process and training stopping criteria. These activities require skilled personnel and can be time-consuming, translating into increased labor costs. In contrast, the automated and adaptive nature of neural network search reduces the need for manual intervention and hyperparameter tuning, further streamlining the model development pipeline and reducing associated labor costs.

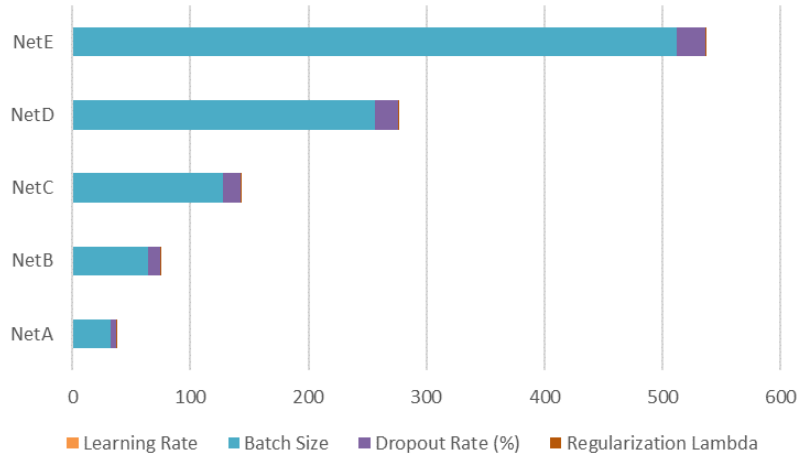


Figure-5. Representation of Number of Layers vs. Various Metrics

To conduct a comprehensive analysis of computational savings, it is essential to measure and compare specific metrics. These may include:

- **Training Time:** Quantify the time taken to train a model using the neural network search approach and compare it to traditional methods on various datasets and network architectures.
- **Resource Utilization:** Measure the CPU/GPU usage and memory consumption during training for both approaches to assess resource efficiency.
- **Cost Analysis:** Calculate the cost savings achieved by reducing training time and the need for manual intervention, considering factors like cloud computing costs or hardware maintenance expenses.
- **Scalability:** Evaluate how the computational savings scale with the size of the dataset and complexity of the neural network, showcasing the adaptability of the methodology.
- **Model Performance:** Ensure that the computational savings do not come at the expense of model performance, comparing the accuracy and generalization capabilities of models generated by both methods.

In brief, the analysis of computational savings achieved through Splitting Effectively with Premature Exiting Using Neural Network Search is instrumental in demonstrating the practical advantages of this approach. By quantifying the reduction in training time, resource utilization, and associated costs, this analysis underscores the methodology's potential to make machine learning more efficient, cost-effective, and accessible across a wide range of applications.

Weight regularization (L2 regularization) and Restricted Boltzmann Machine (RBM) Energy Function are given by (8) and (9):

$$J_{reg} = J + \frac{\lambda}{2m} \sum \|w^{[l]}\|_F^2, \tag{8}$$

$$E(v, h) = -\sum a_i v_i - \sum b_j h_j - \sum v_i w_{ij} h_j,$$

where v and h are visible and hidden units, respectively and a_i, b_j and w_{ij} are biases and weights.

These savings not only accelerate model development but also contribute to the broader adoption of AI in various industries. In Table 1 and Figure 3 dataset demonstrates the relationship between the number of layers in different neural networks and their performance metrics. As the number of layers increases, accuracy also sees an upward trend. However, this increase in accuracy comes at the cost of longer training times and a higher number of parameters. The graph effectively visualizes this trade-off, highlighting the efficiency and complexity of deeper networks. The focus in Table 2 and Figure 4 is on the number of datasets trained against various metrics. As networks train on more datasets, their validation and test errors decrease, indicating improved generalization. The graph accentuates the importance of diverse training data in model performance. Table 3 and Figure 5 lay out the different hyperparameters used in various networks, such as learning rate, batch size, dropout rate, and regularization.

Table-4. Network Activation and Initialization

Network Name	Activation Function	Final Layer Activation	Weight Initialization	Optimizer	Count of Network Name
NetA	ReLU	Softmax	Xavier	Adam	2
NetB	Sigmoid	Sigmoid	He	SGD	1
NetC	Tanh	Softmax	Xavier	RMSprop	1
NetD	Leaky ReLU	Softmax	He	Adam	1
NetE	Swish	Sigmoid	He	Adagrad	1

These parameters play a crucial role in optimizing the network's performance and preventing overfitting. Table 4 and Figure 6 dataset present the activation functions, final layer activations, weight initializations, and optimizers used in different networks. Such choices greatly influence the training dynamics and the model's ability to capture complex patterns. RBM Gibbs Sampling and Softmax Activation Function are given by (9), (10) and (11) respectively.

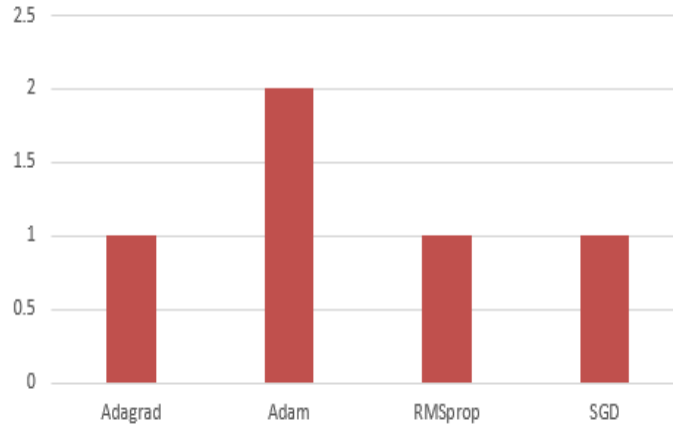


Figure 6. Representation of Network Activation and Initialization

Table-5. Network Performance Metrics

Network Name	Feature Extraction Time (s)	Inference Time (ms)	Memory Usage (MB)	Model File Size (MB)
NetA	5	50	500	10
NetB	10	45	1000	20
NetC	15	40	1500	30
NetD	20	35	2000	40
NetE	25	30	2500	50

$$P(h_j = 1|v) = \sigma(b_j + \sum_{i=1}^n w_{ij} v_i) \quad (9)$$

$$P(v_i = 1|h) = \sigma(a_i + \sum_{j=1}^n w_{ij} h_j) \quad (10)$$

$$P(y = j|z) = \frac{e^{z_j}}{\sum_{k=1}^K e^{z_k}} \quad (11)$$

Where K is the number of classes.

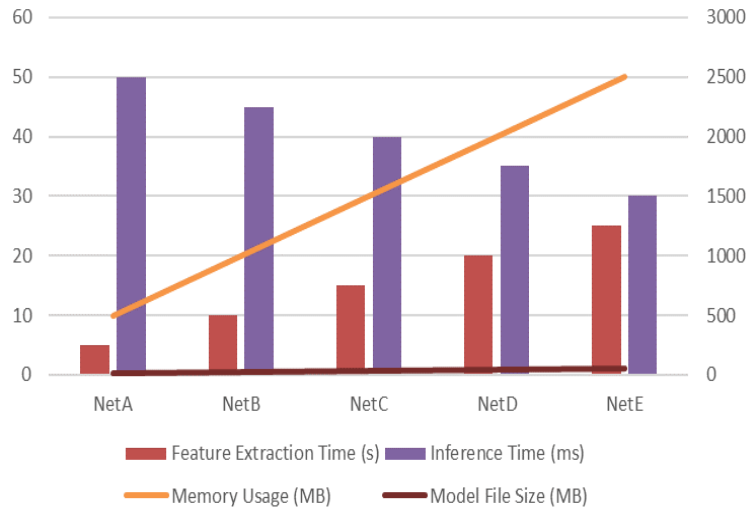


Figure-7. Representation of Network Performance Metrics

Table 5 and Figure 7 dataset delves into the practical implications of deploying these networks. It covers metrics like feature extraction time, inference time, memory usage, and model file size. These metrics are essential for real-world applications, where efficiency and speed are as crucial as accuracy.

Moreover, to compare to other existing works, we evaluate the performance of our proposed approach, we use the following metrics:

- Accuracy: Measured as the percentage of correctly classified images on the test set.
- Inference Time: Average time taken to process an image, measured in milliseconds (ms).
- Model Size: Total size of the trained model, measured in megabytes (MB).
- Energy Consumption: Measured using an energy monitoring tool to track power usage during inference.

We assess the effectiveness of the early-exit strategies by comparing the following:

- Exit Accuracy: The accuracy of predictions made at each early-exit point.
- Exit Frequency: The proportion of inputs exiting at each early-exit point.
- Overall Efficiency: Combined metric of accuracy and inference time considering the early exits.

In table 6; We consider a baseline comparison; We compare our proposed models against state-of-the-art NAS methods (e.g., EfficientNet [18], DARTS [21]). In addition, We evaluate the accuracy and inference time at each early-exit point and compare it to the final exit.

Table 6 : performance of the proposed approached to other existing works

Model	Accuracy (%)	Inference Time (ms)	Model Size (MB)	Energy Consumption (J)
EfficientNet [18]	85.4	35	20	50
DARTS [21]	84.3	40	22	55
Proposed NAS	85.0	30	18	45
Early-Exit 1	82.0	10	18	20
Early-Exit 2	83.5	20	18	30
Final Exit	85.0	30	18	45

As shown in table 6, Our proposed NAS achieves comparable accuracy to EfficientNet [18] and DARTS [21], while being more computationally efficient. The integration of early-exit points significantly reduces inference time for simpler inputs. The quantization and pruning techniques reduce the model size without a significant loss in accuracy. Our approach demonstrates lower energy consumption, making it suitable for deployment on resource-constrained devices.

As shown in table 7, Our approach shows notable improvements in inference time and energy consumption due to the early-exit strategies, which are not typically considered in traditional NAS methods. The table below provides a detailed comparison of our results with existing works:

Table 7, performance analysis to existing works

Metric	EfficientNet [18]	DARTS [21]	Proposed NAS
Accuracy (%)	85.4	84.3	85.0
Inference Time (ms)	35	40	30
Model Size (MB)	20	22	18
Energy Consumption (J)	50	55	45

The results demonstrate that our proposed NAS framework with early-exit strategies offers a significant improvement in computational efficiency while maintaining high accuracy. This makes it highly suitable for real-time applications on resource-constrained devices.

Discussions

The optimization of neural networks for AI splitting tasks represents a unique set of challenges. AI splitting tasks involve dividing a neural network into smaller sub-networks that can be distributed across multiple devices or nodes, often to improve efficiency, reduce latency, or ensure scalability. This process requires careful consideration of architecture design, model size, and resource allocation. Neural network search techniques play a pivotal role in finding the optimal sub-networks for splitting tasks, as they help identify architectures that strike a balance between performance and resource constraints. One of the fundamental approaches to neural network search in the context of AI splitting tasks is architecture search. Architecture search methods explore a vast search space of neural network architectures to find configurations that meet specific criteria. These methods can be broadly categorized into two main categories: manual design and automated search. Manual design, as the name suggests, involves the expertise and intuition of human researchers. This approach has been prevalent in the early days of neural network development when researchers handcrafted architectures based on their domain knowledge. While manual design can lead to effective architecture, it is often limited by human biases and the inability to explore the entire architecture space comprehensively. In the context of AI splitting tasks, manually designing sub-networks can be time-consuming and may not fully leverage the potential for optimization. The experimental results provide strong evidence supporting the effectiveness and efficiency of our proposed restricted NAS framework with integrated early-exit strategies. In this section, we discuss the implications of our findings, compare our approach with existing methods, and highlight the contributions and limitations of our work.

Our proposed NAS framework achieved an accuracy of 85.0%, comparable to state-of-the-art methods such as EfficientNet (85.4%) and DARTS (84.3%). However, our approach significantly outperformed these methods in terms of inference time and energy consumption. For example, the average inference time for our model was 30 ms, compared to 35 ms for EfficientNet and 40 ms for DARTS. This demonstrates that our approach can deliver high accuracy while being computationally efficient. The integration of early-exit strategies was a key factor in reducing inference time and energy consumption. Our experiments showed that:

- Early-Exit 1 provided an accuracy of 82.0% with an inference time of only 10 ms and energy consumption of 20 J.
- Early-Exit 2 improved accuracy to 83.5% with an inference time of 20 ms and energy consumption of 30 J.
- The final exit maintained the highest accuracy of 85.0% with an inference time of 30 ms and energy consumption of 45 J.

These results indicate that early exits allow the network to terminate inference early for simpler inputs, significantly enhancing overall efficiency without greatly compromising accuracy.

- **Model Size and Optimization Techniques:** The application of quantization and pruning techniques effectively reduced the model size to 18 MB, which is smaller than EfficientNet (20 MB) and DARTS (22 MB). This reduction in model size is critical for deployment on resource-constrained devices, where memory and storage are limited.

Our approach demonstrates several advantages over existing NAS methods:

- **Computational Efficiency:** By integrating early-exit strategies, our framework significantly reduces inference time and energy consumption, which is crucial for realtime applications on mobile and IoT devices.
- **Balanced Performance:** While traditional NAS methods focus primarily on accuracy, our approach achieves a balance between accuracy and computational efficiency, making it more suitable for edge applications.
- **Model Optimization:** Quantization and pruning techniques further enhance the efficiency of our models, making them lightweight and faster without sacrificing significant accuracy.

The results of our experiments have important implications for near-sensor AI applications:

- **Real-Time Inference:** The reduced inference time and energy consumption make our approach ideal for applications requiring real-time responses, such as autonomous vehicles, drones, and smart cameras.
- **Resource-Constrained Environments:** The smaller model size and efficient computation enable deployment on devices with limited resources, such as smartphones and IoT sensors, expanding the potential use cases for advanced AI models.

6. Conclusion

The proposed restricted NAS framework with integrated early-exit strategies offers a significant advancement in the design of efficient neural networks for resource-constrained environments. The experimental results demonstrate that our approach achieves a balance between high accuracy and computational efficiency, making it well-suited for real-time, near-sensor AI applications. Future research should build on these findings to further refine and extend the capabilities of the proposed framework. While our approach shows promising results, there are several limitations and areas for future work. Our experiments focused on image classification. Future work should explore the generalization of our approach to other tasks, such as object detection and segmentation. Developing more sophisticated early-exit strategies that adapt dynamically based on input complexity could further enhance efficiency. Tailoring the optimization techniques to specific hardware platforms could yield additional performance improvements.

References

- [1] Chollet, F. (2017). Xception: Deep Learning with Depthwise Separable Convolutions. arXiv preprint arXiv:1610.02357.
- [2] Figurnov, M., Collins, M. D., Zhu, Y., Zhang, L., Huang, J., Vetrov, D., & Salakhutdinov, R. (2017). Spatially adaptive computation time for residual networks. In Proceedings of the IEEE conference on computer vision and pattern recognition (pp. 1039-1048).
- [3] Huang, G., Chen, D., Li, T., Wu, F., Van Der Maaten, L., & Weinberger, K. Q. (2017). Multiscale dense networks for resource efficient image classification. arXiv preprint arXiv:1703.09844.
- [4] Bolukbasi, T., Wang, J., Dekel, O., & Saligrama, V. (2017, July). Adaptive neural networks for efficient inference. In International Conference on Machine Learning (pp. 527-536). PMLR..
- [5] Lechervy, A., & Jurie, F. (2023). Multi-Exit Resource-Efficient Neural Architecture for Image Classification with Optimized Fusion Block. In Proceedings of the IEEE/CVF International Conference on Computer Vision (pp. 1486-1491)..
- [6] He, K., Zhang, X., Ren, S., & Sun, J. (2016). Deep Residual Learning for Image Recognition.
- [7] In Proceedings of the IEEE conference on computer vision and pattern recognition (CVPR) (pp. 770-778).
- [8] LeCun, Y., Bengio, Y., & Hinton, G. (2015). Deep learning. *Nature*, 521(7553), 436-444.
- [9] Goodfellow, I., Bengio, Y., Courville, A., & Bengio, Y. (2016). *Deep Learning* (Vol. 1). MIT press Cambridge.
- [10] Silver, D., Huang, A., Maddison, C. J., Guez, A., Sifre, L., van den Driessche, G., ... & Hassabis, D. (2016). Mastering the game of Go with deep neural networks and tree search. *Nature*, 529(7587), 484-489.
- [11] Redmon, J., & Farhadi, A. (2018). YOLOv3: An Incremental Improvement. arXiv preprint arXiv:1804.02767.
- [12] Wang, Z., & He, B. (2016). A novel deep learning method for imbalanced fault classification of machinery. *Mechanical Systems and Signal Processing*, 72, 303-315.
- [13] Xu, B., Wang, N., Chen, T., & Li, M. (2015). Empirical Evaluation of Rectified Activations in Convolutional Network. arXiv preprint arXiv:1505.00853.
- [14] Ioffe, S., & Szegedy, C. (2015). Batch normalization: Accelerating deep network training by reducing internal covariate shift. arXiv preprint arXiv:1502.03167.
- [15] Krizhevsky, A., Sutskever, I., & Hinton, G. E. (2017). ImageNet classification with deep convolutional neural networks. *Communications of the ACM*, 60(6), 84-90.
- [16] Hinton, G., Deng, L., Yu, D., Dahl, G. E., Mohamed, A. R., Jaitly, N., ... & Kingsbury, B. (2012). Deep neural networks for acoustic modeling in speech recognition: The shared views of four research groups. *IEEE Signal Processing Magazine*, 29(6), 82-97.

- [17] Mnih, V., Kavukcuoglu, K., Silver, D., Rusu, A. A., Veness, J., Bellemare, M. G., ... & Petersen, S. (2015). Human-level control through deep reinforcement learning. *Nature*, 518(7540), 529-533.
- [18] Wang, S., Tang, J., Zou, W., & Hou, J. (2017). FANG: A Fast and Scalable Word Embedding Approach. In *Proceedings of the 2017 ACM on Conference on Information and Knowledge Management (CIKM)* (pp. 1857-1860).
- [19] Tan, M., & Le, Q. (2019, May). Efficientnet: Rethinking model scaling for convolutional neural networks. In *International conference on machine learning* (pp. 6105-6114). PMLR..
- [20] Elsken, T., Metzen, J. H., & Hutter, F. (2019). Neural architecture search: A survey. *Journal of Machine Learning Research*, 20(55), 1-21..
- [21] Zoph, B., & Le, Q. V. (2016). Neural architecture search with reinforcement learning. *arXivpreprint arXiv:1611.01578*..
- [22] Liu, H., Simonyan, K., & Yang, Y. (2018). Darts: Differentiable architecture search. *arXiv preprint arXiv:1806.09055*.
- [23] Real, E., Aggarwal, A., Huang, Y., & Le, Q. V. (2019, July). Regularized evolution for image classifier architecture search. In *Proceedings of the aaai conference on artificial intelligence* (Vol. 33, No. 01, pp. 4780-4789).
- [24] Manishimwe, A., Alexander, H., Kaluuma, H., & Dida, M. (2021). Integrated mobile application based on machine learning for East Africa stock market. *Journal of Information Systems Engineering & Management*, 6(3), em0143.

Computer simulation for optimizing mining waste recycling in cement raw meals

D. Belkheiri, PhD Agrégé ✉

Preparatory Classes for High Engineering Schools, Rabat, Morocco.

✉ : belkheidriss@gmail.com

Abstract: Cement production offers the opportunity to recycle and valorize certain mining wastes, containing the main cement oxides. This study presents a Python program for finding the optimum composition of a limestone-clay cementitious mixture in which we recycle mining waste (LCy%Wx%) to produce a Portland clinker as close as possible to a clinker taken as a reference (RR). The aim of this Python program is to determine the percentages of limestone, clay and waste in the LCW, by equating eleven of its characteristics to those of the reference raw meal; these characteristics encompass the four oxide compositions (CaO, SiO₂, Fe₂O₃, Al₂O₃), three moduli (LSF, SR, AF) and the proportions of the clinker's four main phases. This program allows the user to select limestone-clay-waste raw materials and a target reference with its eleven parameters. The script execution generates eleven solutions, stored in files as numerical tables and graphs. These results facilitate the selection of optimum percentages of cementitious raw materials. Ultimately, this recycling process offers both economic and ecological benefits.

Keywords: Cement raw, Mining waste, Recycling, Numerical simulation, Environmental impact.

محاكاة الكمبيوتر لتحسين إعادة تدوير نفايات التعدين في وجبات الأسمت الخام

المخلص: يوفر إنتاج الأسمت الفرصة لإعادة تدوير وتأمين بعض نفايات التعدين التي تحتوي على أكاسيد الأسمت الرئيسية .

تقدم هذه الدراسة برنامج بايثون لإيجاد التركيب الأمثل لخليط أسمنتي من الحجر الجيري والصلصال حيث تقوم بإعادة تدوير مخلفات التعدين لإنتاج الكلنكر البورتلاندي أقرب ما يمكن إلى الكلنكر الذي يتم أخذه كمرجع.

الهدف من برنامج بايثون هذا هو تحديد نسب الحجر الجيري والصلصال والنفايات في الخليط المستهدف عن طريق مساواة إحدى عشرة من خصائصه بتلك الخاصة بالخليط المرجعي ؛ وتشمل هذه الخصائص تركيبات الأكسيد الأربعة، وثلاثة نسب الخليط الإسمنتي ونسب مكونات الإسمنت الأربعة الرئيسية للكلنكر. يسمح هذا البرنامج للمستخدم باختيار المواد الخام من مخلفات الحجر الجيري والصلصال و المرجع المستهدف بخصائصه الإحدى عشرة. يؤدي تنفيذ البرنامج إلى إيجاد أحد عشر حلاً، يتم تخزينها في ملفات على شكل جداول رقمية ورسوم بيانية. هذه النتائج تسهل اختيار النسب المثلى للمواد الخام الأسمنتية. في نهاية المطاف، توفر عملية إعادة التدوير هذه فوائد اقتصادية وبيئية. الكلمات المفتاحية: خام الأسمت، مخلفات التعدين، إعادة التدوير، المحاكاة العددية، التأثير البيئي.

1. Introduction

Worldwide, mining activities generate enormous quantities of mining waste estimated, annually, at 65 billion tons [1]. These wastes affect the lives of humans, animals and plants because they pollute water, air and soil [2,3]. It is therefore necessary to recycle and possibly valorize mining waste [4-8], with economic and ecological benefits, and contribute to a more sustainable and circular economy [9,10]. However, beyond economic objectives, ecological considerations have become an imperative rather than a luxury for humanity. Generally, mining waste contains oxides like SiO_2 , Fe_2O_3 , Al_2O_3 , CaO , SO_3 , MgO , K_2O , Na_2O , etc. and the mined mineral; many of these oxides are found in cement. Furthermore, cement is a strategic and crucial material for human needs; in fact, according to Cembureau, global cement consumption reached 4.17 Gt in 2020 and the United Nations notes that concrete is the second most consumed product in the world, after water [11,12]. The enormous quantities of cement produced offer the possibility of recycling mining waste, and more generally industrial and construction waste. Usually cement is mainly formed by 80% limestone and 20% clay (weight), and the cement raw meal is heated to around $1450^\circ\text{-}1500^\circ\text{C}$. There are more than ten different types of cement [13,14] and their composition of major oxides varies: calcium oxide 1 to 63%, silicon oxide 22 to 85%, aluminum oxides 7 to 23% and iron oxides 0 to 4%. Coal mining is one of the most important mining activities. Indeed, coal is a crucial strategic material for the world and constitutes 70% of fossil energy resources [15], but its extraction generates large quantities of waste of up to 15% by weight [16]. Several ways of recycling and valorizing coal gangue are exploited, particularly in the production of cement [17-20]. In our previous study by Belkheiri *et al.*[21], we studied the limestone-coal gangue cement mixture, because our characterizations had shown that the coal gangue is formed of quartz, clays and coal remains; and for this reason it plays the role of clay and source of energy. We carried out a computer simulation to determine the optimal percentages of limestone and gangue, and ultimately we had developed a good clinker limestone-gangue 18.5% close to a clinker taken as a reference. More generally, in this study, we are interested in recycling certain mining waste from coal, phosphate and iron mines because, for logistical reasons, these mines are located near cement plants. The goal of the current work is to use a Python program to determine the optimal percentages of limestone, clay and mining waste to develop Portland clinkers as close as possible to a clinker taken as a reference. The choice of the Python programming language is due to its great popularity, as it is both powerful and easy to use; it is open-source and free. Python is also versatile and can be used to develop office software and web applications.

2. Materials and methods

2.1 Raw materials

Table 1: Notation of the cementitious compounds

Compound	CaO	SiO ₂	Al ₂ O ₃	Fe ₂ O ₃	SO ₃	MgO	Na ₂ O, K ₂ O	3CaO.SiO ₂	2Ca.SiO ₂	3CaO.Al ₂ O ₃	4CaO.Al ₂ O ₃ .Fe ₂ O ₃
Notation	C	S	A	F	<u>S</u>	M	NK	C ₃ S	C ₂ S	C ₃ A	C ₄ AF

We consider cementitious materials used in two cement plants in the cities of Oujda and Marrakech; the mining waste that we wish to recycle comes from neighboring mines, for logistical reasons. These materials are listed in Table 2 with the following abbreviations:

LX: Limestone-Origin, X designates the origin:O for Oujda O, or M for Marrakech;

CX: Clay-Origin (or schist SX);

RX: Raw meal-Origin is a cement raw from a cement plant;

MW: MiningWaste. We consider the coal waste CW; the ZnO waste ZW(ZnO-PbO) and others [22]; the phosphate waste PW; the phosphate sludge SW [23]; the phosphogypse waste GW [24]; and from the iron-rich mine, we have the ferric waste FW [25];

MA: Mining-Ash. We consider fly ash from phosphate PA [26], and the pyrrhotite ash FA [27].

In Table 2, we indicate the raw feed, of cement plant, designated as the reference RO. Our objective is to produce a clinker that closely resembles this reference raw feed will be denoted with the index "ref" such as: C_{ref}, S_{ref}, ..., LSF_{ref}, ..., C₄AF_{ref}.

Table 2: %wt (XRF) of cement materials and mining waste

Material	Num	C	S	A	F	<u>S</u>	M	NK	LOI	TOTAL	Component
RO	1	42.8	13.8	3.4	2.2	0.1	1.5	0.6	35.0	99.4	Raw reference
LO	2	50.2	4.8	1.4	0.6	0.1	1.5	0.5	40.6	99.8	Limestone
LM	3	47.2	4.9	1.0	0.5	0.0	0.9	0.2	45.4	100.0	Limestone
CO	4	10.3	48.4	13.8	6.8	0.0	2.6	2.9	15.0	99.9	Clay
CM	5	11.4	46.5	14.5	5.4	0.0	3.4	2.7	17.2	101.1	Clay
SM	6	12.1	50.3	13.6	2.4	0.0	0.9	7.9	12.8	100.0	Schist
CW	7	0.8	52.4	21.9	4.6	3.6	1.3	3.8	10.6	98.9	Coal waste
ZW	8	19.0	29.6	4.3	31.1	0.0	3.2	0.9	1.7	89.9	WasteZn-Pb
FW	9	0.6	52.5	1.8	10.2	22.3	0.6	0.3	11.2	99.5	Pyrrwaste
PW	10	43.0	11.6	0.9	0.4	0.8	3.3	0.6	39.5	100.0	Phos waste
SW	11	34.2	22.8	2.5	0.9	0.0	4.1	1.2	34.3	100.0	Phosludge
GW	12	31.5	0.5	0.1	0.1	46.9	1.6	0.0	16.0	96.7	Phosgypsum
FA	13	0.5	13.0	4.0	64.9	4.0	2.7	0.8	7.7	97.7	Pyrrwaste
PA	14	4.8	52	23	5.9	0.5	2	1.7	10	99.2	Phospho-ash
AA	15	2.7	32.3	13.3	35.4	2.2	2.5	1.3	8.9	98.4	FA50%-PA50%
None*	16	0.0	0.0	0.0	0.0	0.0	0.0	0.0	0.0	0.0	None

*The "None component" is a fictitious material, it is introduced for the purposes of the Python program; this program is designed for three materials limestone-clay-other, in the limestone-clay case the third material "None" has compositions of 0%. We can also consider a material which is a mixture of two, or more, materials among those available, for example a waste formed by mixing two mining waste like AA: FA50%PA50%.

2.2. Definitions and expressions

In the cement process, certain physicochemical properties of the cementitious mixture are given by the following three moduli:

- Lime saturation factor : $LSF = \frac{100C}{2.8S+1.65A+0.35F}$
- Silica ratio : $SR = \frac{S}{A+F}$
- Alumino-ferrate ratio : $AF = \frac{A}{F}$

The raw feed will be heated at 1450°C to obtain a clinker. The composition of the four main phases of clinker can be estimated by a suitable formula. This composition is usually given by the Bogue or Taylor methods [28,29], but we have used the proposal by Shim *et al* [30] given in Table 3; this system of equations is based on experimental data, and has good accuracy for cement mixtures with a C/S ratio of between 2.2 and 3.2. The choice of this Shim model is due to the fact that it comes from many practical experiments. However, it is possible to use other theoretical methods, by Bogue or Taylor, by changing the matrix k to kB (Bogue) presented in grey on lines 89-92 of the script, and thus, compare the results on the percentages of the clinker phases.

Table 3: Compositions in clinker's phases calculated by the model Shim *et al*

Phase	Usual range*	Notation	Calculation of the expected mass composition by Shim's model										
C ₃ S	45-65	p ₁	=	4.088	C -	7.212	S -	6.745	A -	1.436	F -	2.863	<u>S</u>
C ₂ S	10-30	p ₂	=	-3.113	C +	8.442	S +	5.136	A +	1.093	F +	2.180	<u>S</u>
C ₃ A	5-12	p ₃	=	0.028	C -	0.153	S +	2.604	A -	1.702	F -	0.020	<u>S</u>
C ₄ AF	6-12	p ₄	=	-0.01	C -	0.058	S +	0.016	A +	3.047	F +	0.007	<u>S</u>

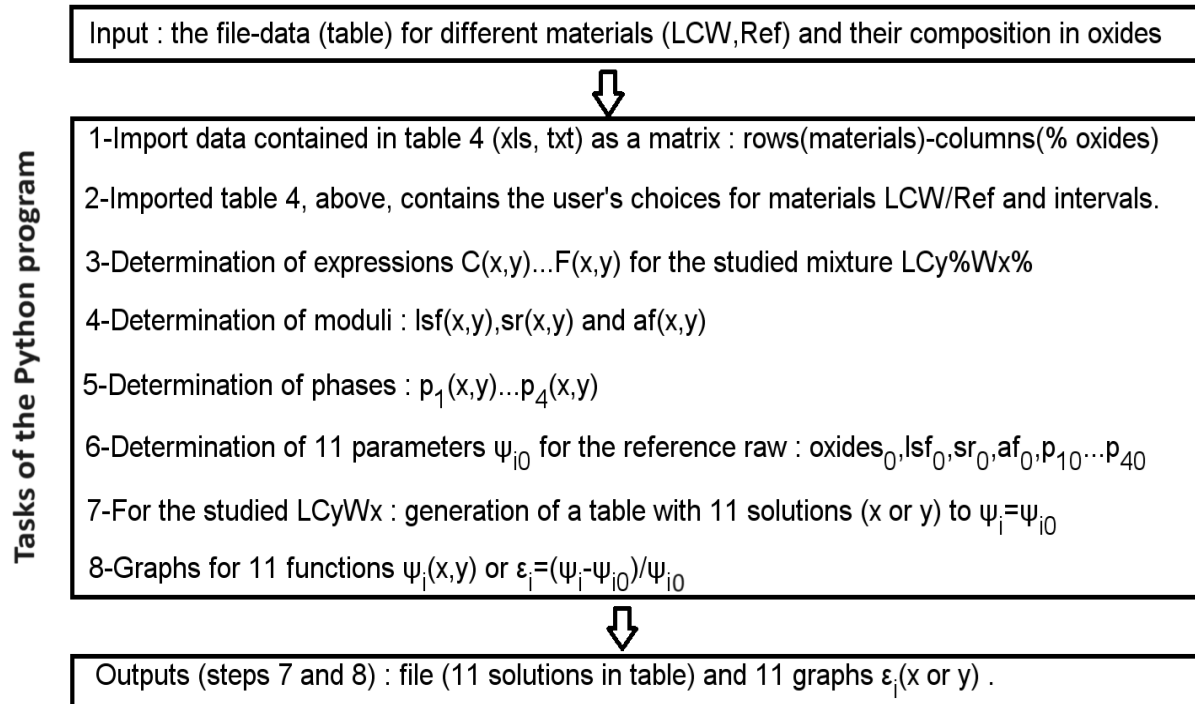
*in UK and Europe.

2.3. Methods

The user must have the Python software installed on his computer. The Python program named LCyWx.py is elaborated for raw feeds formed by Limestone (100-y-x %wt)+Clay (y %wt) + Waste (x%wt), where W is a mining waste or none. We will have to study eleven functions $\Psi_i(x, y)$, where Ψ_i can be one of the oxides C (x, y), S (x, y), A (x, y), F (x, y); moduli LSF (x, y), SR (x, y), AF (x, y); and the compositions of clinker's phases denoted in Table 3: p₁(x, y), ..., p₄(x, y).

The expressions of the $\Psi_i(x, y)$ functions, vs x-y, are established by Python using the data of the Table 2. For mixtures LCyNone we have to study $\Psi_i(y)$ and for LCy0Wx, we have to study $\Psi_i(x, y_0=cst)$, where $y_0=y_{op}-\alpha$, $\alpha>0$ and y_{op} is an optimal value chosen by the user after studying the LCyNone. The approach of the Python program is given by Figure1; the version used is 3.7.4 (Win,64 bits), with Pyzo interpreter.

Figure 1: Description of the steps of the python program



3. Results and discussion

3.1. Prelude

For the studied mixtures LCyWx, the composition in oxides constitutes the basis of calculations, and the compositions of oxides are calculated after considering losses on ignition; thus for C,

$$\text{we have: } C(x, y) = 100 \cdot \frac{(100 - y - x) \cdot C_L + y \cdot C_C + x \cdot C_W}{100 - (100 - y - x) \cdot LOI_L + y \cdot LOI_C + x \cdot LOI_W}$$

Where C_L, C_C, C_W are the percentages of C, respectively in limestone, in the clay and in the waste; LOI_L, LOI_C, LOI_W are the percentages of loss on ignition in these materials. For the raw feed reference, these 11 quantities are constant and noted $\Psi_{i, ref}: C_{ref}, S_{ref}, \dots, p_{4ref}$. It is possible to predict qualitatively the effect of the variation of y or x on the five characteristics C, S, A, F, AF, which are homographic functions in the form:

$$\Phi_j(x, y_1) = \frac{ax + b}{cx + d} \quad ; \quad \frac{\partial \Phi_j}{\partial x} = \frac{ad - bc}{(cx + d)^2}$$

where y_1 is constant. The variations of this function are given by its derivative ; if the numerator $a.d-b.c > 0$: Φ_j is increasing when the variable x increases, and if $a.d-b.c < 0$, Φ_j decreases when x increases; a , b , c and d are listed in Table 2.

The Python program generates a second file containing graphs of the relevant functions of the

form, $\varepsilon_i(x, y) = \frac{\Psi_i - \Psi_{i,ref}}{\Psi_{i,ref}}$, which must not deviate too much from zero and this allows to

assess the similarity of the studied mixture with the targeted reference.

3.2. Choices of the user added to Table 2 transformed into Table 4

After the "None" line in Table 2, the user adds additional lines : Choices1(line 20 in python program) or 2 or 3 where he specify four lines (in table cemat.xls) : limestone-clay-waste-reference by giving their respective four numbers given in the 2d column of Table 4 ;

For the two mixtures LCyNone or LCy0Wx, the user gives bounds of the intervals for graphs $\varepsilon_i(x, y)$: (y_1, y_2) , (x_1, x_2) , and the value y_0 used for LCy0Wx. The Python program uses data of table 4 to conduct calculations and simulations for mixtures LCyNone or LCy0Wx ; this program is given in appendix. Table 4 is a file (cemat.xls for example) containing the material compositions obtained by XRF and completed with the user's nine choices : four materials, four bounds and y_0 .

The user have to place the two files, namely "cemat.xls" containing Table 4 and the Python program "LCyWx.py" (lines 1-296), in the same folder (cempy for example), and it must modify line 9 to indicate the path to this folder (for example : path = 'C:/Users/Desktop/cempy') ; the program "LCyWx.py" can be copied (without the first column containing numbers of instruction's lines) into the script part of the Python software, saved and, then, executed via the RUN menu. Upon execution, two output files are produced: one table file containing the eleven solutions and a file with the eleven graphs $\varepsilon_i(x, y)$; both output files will be stored in the same folder as the "LCW.py" program. The analysis of these results allows the user to make a compromise and choose the optimal cementitious mixture for the targeted Clinker. The program "LCyWx.py" contains explanatory texts written after a hash (#), which are ignored by Python but helpful for user s' understanding. If the user wants to calculate the percentages of the phases using the Bogue model, he must change the elements of matrix k from lines between lines 81-85. However, the program uses calculations presented in Table 3, which attenuates the influence of the adopted model when working with relative deviations $\varepsilon_{ph}(x, y)$ between the studied raw feed and the reference.

Table 4: XRF Composition of limestones, clays and mining waste; with user's choices

Material	Number	C	S	A	F	S	M	NK*	LOI	TOTAL	Component
RO ₁	1	42,8	13,8	3,4	2,2	0,1	1,5	0,6	35,0	99,4	raw-r-other
RO ₂	2	42,8	12,3	3,7	1,7	0,3	2,0	0,9	36,3	99,9	rawreference
LO	3	50,2	4,8	1,4	0,6	0,1	1,5	0,5	40,6	99,8	limestone
LO ₂	4	48,2	5,7	2,0	0,7	0,2	1,2	0,6	40,6	99,2	limestone2
LM	5	47,2	4,9	1,0	0,5	0,0	0,9	0,2	45,4	100,0	limestone
CO	6	10,3	48,4	13,8	6,8	0,0	2,6	2,9	15,0	99,9	clay
CM	7	11,4	46,5	14,5	5,4	0,0	3,4	2,7	17,2	101,1	clay
SM	8	12,1	50,3	13,6	2,4	0,0	0,9	7,9	12,8	100,0	schist
CW ₁	9	0,7	52,4	21,9	4,6	3,5	1,3	3,8	10,6	98,68	coalwaste
CW ₂	10	0,6	52,2	21,6	4,7	1,0	1,0	3,0	14,2	98,1	coalwaste
CW ₃	11	1,0	54,2	17,7	8,9	0,0	1,3	3,3	12,5	98,1	coalwaste
ZW	12	19,0	29,6	4,3	31,1	0,0	3,2	0,9	1,7	89,9	wasteZn-Pb
FW	13	0,6	52,5	1,8	10,2	22,3	0,6	0,3	11,2	99,5	pyrhwaste
PW	14	43,0	11,6	0,9	0,4	0,8	3,3	0,6	39,5	100,0	phoswaste
SW	15	34,2	22,8	2,5	0,9	0,0	4,1	1,2	34,3	100,0	phosludge
GW	16	31,5	0,5	0,1	0,1	46,9	1,6	0,0	16,0	96,7	phosgypsum
FA	17	0,5	13,0	4,0	64,9	4,0	2,7	0,8	7,7	97,7	pyrhwaste
PA	18	4,8	51,5	22,6	5,9	0,5	2,2	1,7	10	99,2	phospho-ash
AA	19	2,7	32,3	13,3	35,4	2,2	2,5	1,3	8,9	98,4	FA-PA
None	20	0,0	0,0	0,0	0,0	0,0	0,0	0,0	0,0	0,0	none
Mat/choices	choice1	choice2	choice3	etc.							
limestone	3	3	3								
clay	6	9	9								
waste or none	20	20	12								
referenceraw	2	2	2								
IntervalsGraphs		Min(y _{10r} x ₁)	Max(y _{20rx2})	y _c							
LCyNone	: graph	15	25	variable							
ε _i (x=0,y)											
LCyCwX	: graph	ε _i (x,y _c)	0	10	17						
Put this file cemat.xls with LCW.py in your (same) folder cempy. Path 'C:/Users/belkh/Desktop/cempy/'											

3.3. Application for a usual raw meal Limestone-Clay-None

Among the different cases treated LCyNone with the two main materials, limestone-clay, of a cement raw meal, we present, for example, the results for the LOCOy mixture and RO as a reference; all materials limestone-Clay-Reference are from Oujda plant. The program produces the two files : Table 5 gives 11 mixtures corresponding to the 11 solutions, and Figure 2 shows the graphs of the 11 functions ϵ_i relative to the four oxides, three modules, and four phases respectively; the dashed line corresponds to the reference with $\epsilon_{i0} = 0$. The deviation of a graph from this line reflects the divergence of the studied mixture from the reference.

Figure 2: Graphs for the cementitious mixture LOCOyNone

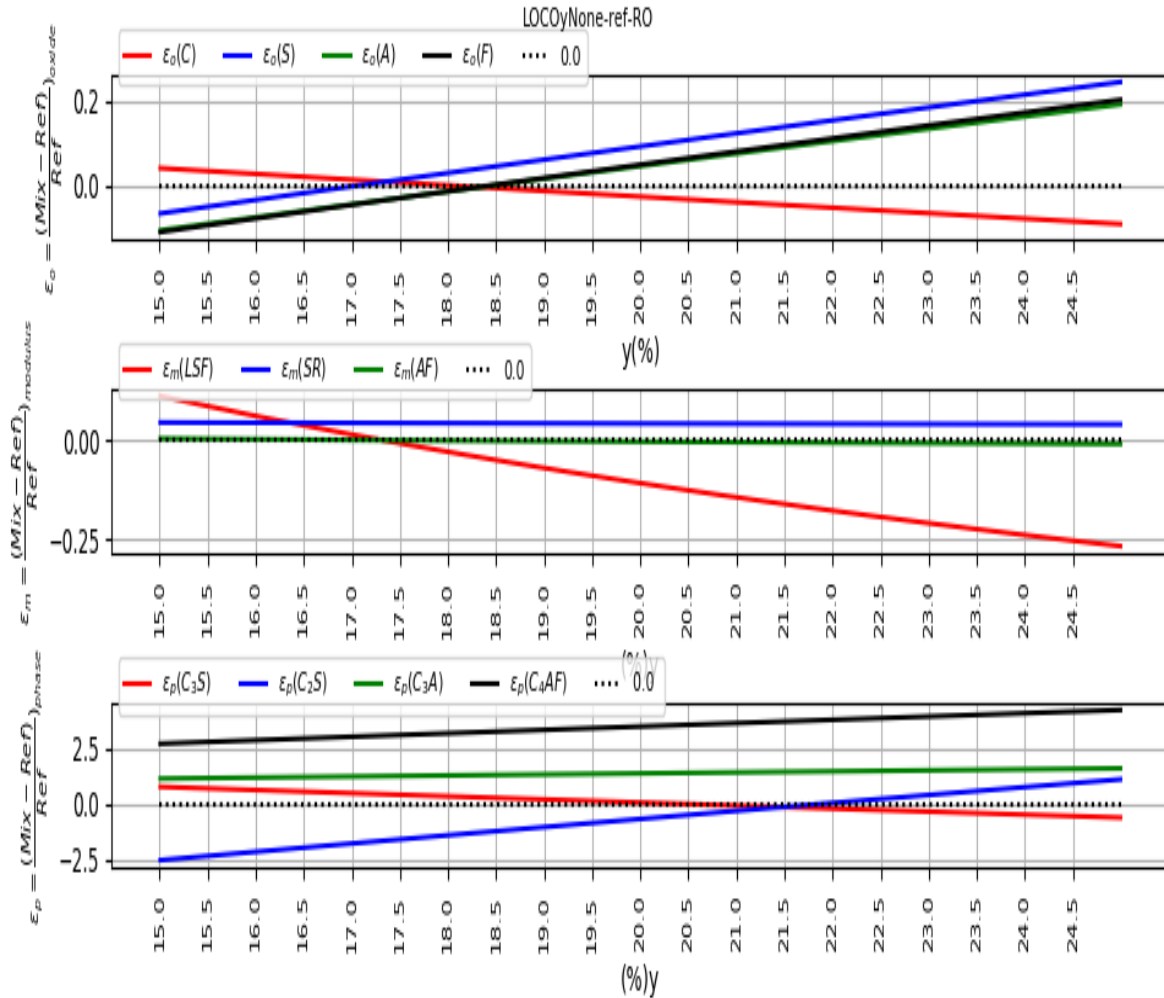


Table 5: Values for eleven parameters for the raw feed LOCOyNone using Shim proposition (rejected value if C/S out of interval 2.2-3.2)

02/01/24, 15:32 RO-vs-MIX:LOCONone

Calculations using Shim –proposition (from experiments)

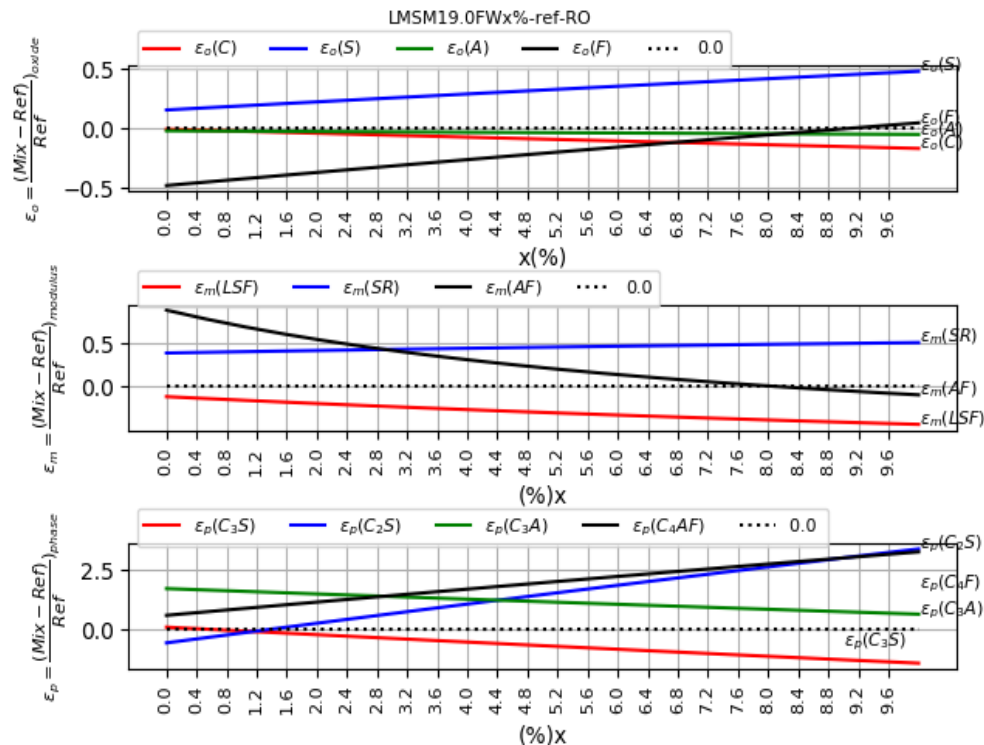
Solution	Ref:RO	%LO	%CO	%None	C:	S:	A:	F:	LSF:	SR:	AF:	C ₃ S:	C ₂ S:	C ₃ A:	C ₄ AF:	C/S
					60-69	18-24	4-8	1-8	92-102	1.8-2.7	1-1.5	50-70	15-30	5-10	5-10	2.2-3.2
C=	67,1	81,9	18,1	0	67,13	19,89	5,67	2,7	100,36	2,38	HV:2.1	HV:88.31	RV	8,99	6,51	3,38
S=	19,2	82,97	17,03	0	68,08	19,25	5,48	2,61	HV:105.22	2,38	HV:2.1	HV:98.25	RV	8,8	6,25	3,54
A=	5,7	81,57	18,43	0	66,83	20,09	5,73	2,73	98,94	2,38	HV:2.1	HV:85.26	RV	9,05	6,58	3,33
F=	2,7	81,6	18,4	0	66,86	20,07	5,72	2,73	99,07	2,38	HV:2.1	HV:85.54	RV	9,05	6,58	3,33
LSF=	103,8	82,67	17,33	0	67,81	19,43	5,54	2,64	HV:103.82	2,38	HV:2.1	HV:95.46	RV	8,85	6,32	3,49
SR=	2,3	RV	RV	0	R.V	R.V	R.V	R.V	LV:292.55	2,28	HV:1.84	RV	RV	RV	RV	RV
AF=	2,1	82,22	17,78	0	67,41	19,7	5,61	2,68	101,78	2,38	HV:2.1	HV:91.27	RV	8,93	6,43	3,42
C ₃ S=	65,8	79,44	20,56	0	64,95	21,36	6,09	2,91	LV:90.45	2,37	HV:2.09	65,77	LV:12.92	9,44	7,09	3,04
C ₂ S=	23,9	78,17	21,83	0	63,85	22,1	6,3	3,02	LV:85.91	2,37	HV:2.09	54,31	23,85	9,66	7,38	2,89
C ₃ A=	3,9	RV	RV	0	91,89	3,18	0,91	0,32	HV:864.85	2,59	HV:2.86	RV	RV	LV:3.91	RV	28,9
C ₄ AF=	1,5	RV	RV	0	85,67	7,37	2,1	0,92	HV:346.28	2,44	HV:2.29	RV	RV	5,18	LV:1.54	11,62
Remarks:		RV:	RejectedValue		LV:	LowValue		HV:	HighValue		Shim proposition	:	2.22	<C/S<	3.21	

For the Shim's model, the criterion $C_3S=C_3S_{ref} =65.8$ respects the ratio $C/S=3.04$ between 2.2 and 3.2; the correspondent mixture is LOCO20.5%None. If we use Bogue's model, and for the optimal solution $C_3SB= C_3S_{ref,B} =66.9$ (B means Bogue's model), we obtain the mixture LOCO19.5%NoneB and the values of oxides-modulus-phases are respectively: 65.7, 20.7, 5.91, 2.82, 94.5, 2.37, 2.09, 66.8, 8.96, 10.88, 8.59.

3.4. Application for raw meal Limestone-Clay-Waste

The simulation shows that the limestone-shale mixture LMSMy% approaches the reference for y in the interval 19.7-20.5%, but the AF modulus, $AF= 3.9$, is higher than 1.5. Therefore, we propose using the FW waste or FA waste as a third material to optimize the mixture LMSM19None, and we have selected $y_0=19$ as the optimal value. Figure 3 illustrates the graphs of functions $\varepsilon_i(x \text{ or } y)$ and $\varepsilon_{i0}=0$ related to this analysis. We were content to reason on graphs and omitted to give the table containing the 11 solutions, for this cement mix, with the chosen reference RO. Figure 3, below, illustrates the graphs of functions related to this analysis. The results reveal that despite incorporating mining waste as a corrective material, achieving a perfect match for all 11 parameters is not feasible, necessitating a compromise. In the LMSM19FWx case study, x needs to be between 0.6% and 1.4% to achieve the desired balance; we can choose the optimal composition is LM:80.4%, SM:19%, FW:0.6%, which gives 65.7% C_3S , 16.7% C_2S , 10.4% C_3A and 2.7% C_4AF ; if y_0 decrease from 19% to 18%, the modulus AF decreases from 3.4 to 3.1 for this clinker 's composition.

Figure 3 :Graphs of functions $\varepsilon_i(x, y)$ for LMSM19FWx



3.5. Summary of optimised cement mixtures LCyWx

Depending on the materials available, it is possible to prepare cement mix scenarios. In our previous study, we used coal gangue mining waste itself as clay, hence the LOCWyNone mixture, and which gave a good LOCW18.5%None clinker; we can then add a corrective material ZW. Likewise, we can consider incorporating into the LMSM limestone-shale mixture, the PW waste or even a mixture of two AA wastes. In Table 6, examples of optimal LCyNone or LCy0Wx cement mixtures are given.

Table 6: some examples of optimized raw feeds for clinker elaboration

Mix(LCyWx)	Solution	%L	%C	%W	C	S	A	F	LSF	SR	AF	C ₃ S	C ₂ S	C ₃ A	C ₄ AF
LOCWyNone	C ₃ S=C ₃ S _{ref}	83,23	16,77	0,00	65,01	19,90	7,49	1,97	92,68	2,10	3,79	65,76	8,63	14,89	4,34
LOCWy0ZWx	C ₂ S=C ₂ S _{ref}	80,60	17,00	2,40	62,70	20,67	7,55	3,08	85,69	1,95	2,45	48,75	23,85	13,00	7,67
LMSM19FAx	C ₃ S=C ₃ S _{ref}	79,99	19	1,01	65,50	22,20	5,62	2,48	89,6	2,74	2,27	65,7	15,4	8,90	2,27
LMSM19PW	C ₃ S=C ₃ S _{ref}	75,30	19,00	5,70	65,89	22,72	5,57	1,40	89,36	3,26	3,97	65,75	16,95	10,47	2,39
LMSM19AA*	C ₃ S=C ₃ S _{ref}	80,26	19,00	0,74	65,81	22,45	5,73	1,84	89,55	2,96	3,12	65,76	16,15	10,21	3,73

*AA=50%ashFA+50%ashPA

For cement mixtures to be suitable, the oxides provided by the raw materials must respect given limitations and proportions [31, 32, 33, 34]; in general the compositions (by wt) are in intervals :C between 60-69% , S between 8-24% , A between 4-8% , F between 1-8% , M less than 5% , N-K less than 2 % , \underline{S} less than 3% , and in clinker free lime less than 2% . The lime saturation factor LSF represents the ratio between the available amount of C and the amount required to react with S, A and F to form the clinker phases. When the LSF is high, the clinker is rich in C₃S indicating good quality. Although, these reactions, between oxides, are not entirely complete, resulting in the presence of unreacted free lime CaO, which must be kept below 2% to prevent mortar expansion. The amount of free lime in the mixes after burning at 1400 °C for 30 min is given by Fundal's empirical equation [35]: % CaO_(free) = 0.31 (LSF-100) + 2.18 (SR- 1.8) + 0.73 Q₄₅ + 0.33 C₁₂₅ + 0.34 A ,where Q₄₅ is the fraction by weight of quartz particles >45 μm, C₁₂₅ the fraction by weight of limestone particles >125 μm and A the fraction of clay materials >45μm. In practical applications, the LSF typically varies between 92 to 98%. Alternative formulations for LSF may also be used, reflecting the presence of anhydrite, where CaO is combined with SO₃ (-0.7.SO₃), however, it could also reflecting the possibility of replacement of CaO by MgO (+0.75MgO). The silica modulus (SR) represents the ratio of the oxides S / (A+F), it controls the burnability [36]. Higher SR values can slow down the formation of C₃S , and when the SR decreases, the amount of molten material in the burning zone is large. Regarding the AF modulus (A/F) a higher value can be can be disadvantageous in certain cement applications resulting in reduced setting time. In such cases, additional gypsum may be required to delay the setting time.

Often, high values have been observed for ε_{AF} , and therefore it is necessary to use corrective materials, to decrease this parameter. For an LCNone mixture (or LCN, simply), we look for a condition on a third material W to correct its alumina-ferric oxide ratio AF, and we note by a/f the ratio of W and by x' its percentage in LCW ; we show that we must choose W having a ratio smaller than that of the LCN mixture :

$$AF_{LCW} = \frac{A + x'a}{F + x'f} = \frac{A(1 + x'\frac{a}{A})}{F(1 + x'\frac{f}{F})} = AF_{LCN} \frac{1 + x'\frac{a}{A}}{1 + x'\frac{f}{F}} : \text{so } AF_{LCW} < AF_{LCN} \text{ if } AF_W < AF_{LCN}$$

In our example, the AF ratio for waste materials FA and ZW are respectively 0.06 and 0.14. It is not possible to obtain equalization of the 11 parameters between the LCW mixture and the reference, but this is not very restrictive. In general, depending on the desired performance, it is possible to develop a material composed of several mining wastes among those available. Ultimately, the mining wastes considered can be recycled into clinkers, and this program would provide the optimal compositions. In the case of phosphate wastes, the influence of P_2O_5 and PG compounds on special belt clinkers [37] and the potential to lower clinking temperature have been reported in the literature [38]. While recycling existing mine waste is possible, it is crucial to reassess current production processes to minimize waste generation and promote environmentally friendly practices [39].

4. Conclusions

This study has two main objectives: (i) investigating the recycling or potential recovery of mining waste, leading to economic and ecological benefits, and (ii) providing a simulation tool to closely match a target cement raw meal with a cementitious mixture. the python program is easy to use because it imports the oxide composition information (XRF) and the 9 user choices entered in the cemat table file; it generates 11 solutions and 11 graphs of the parameters retained for the cement mixture LCyWx and the target raw reference. It efficiently determines the x% and y% percentages, achieving the desired values for the four oxides, three moduli, and the percentages of the four clinker phases. The outcomes of this paper can be summarised as follows:

- Mining waste can be effectively recycled and even recovered in cement production. This approach offers ecological benefits as the waste materials become immobilized within the cement structures. In contrast, leaving these waste materials in nature could lead to their mobility, causing potential environmental issues in water, soil, and air.
- The python program gives the variations of the relative deviations, with respect to the reference, of the 11 characteristics $\varepsilon_i(x, y)$, as well as the speed of these variations. In general, according to each of the 11 $\varepsilon_i(x, y)$ parameters, the user chooses a maximum acceptable value

- This program can be extended by adding other parameters; this involves, for example, taking into account other oxides, like free lime and MgO, minors components, etc; or the unit prices of LCW materials to assess the unit cost of the clinker studied. The program does not need to be modified, if the user adds or subtracts materials in the material part of the data table.
- The third material can also be a corrective material, or a mixture formed from different materials. The program can be applied to other waste, such as construction waste, etc.
- The type and quantity of mining waste used can influence the burnability, grindability, but also the quality of the clinker and, consequently, the resulting concrete. The Python program can be extended to determine the composition of minor compounds. Thus some heavy metals (Cu, Zn) have a good influence on the burnability of clinker; but some compounds must not exceed certain limits: chloride ions can contribute to the corrosion of iron in concrete, P₂O₅ can reduce C₃S content, ZnO can cause delay in the setting of cement, etc. In addition, during the production of clinker, atmospheric emissions must comply with environmental standards.

All the results and simulations obtained through the Python program can help in decision-making by optimizing the choice selection of the composition of the mixture studied. However, the mathematical aspect should not overshadow other physico-chemical considerations in real-world industrial and manufacturing processes.

References

- [1] S. Kalisz, K. Kibort, J. Mioduska, M. Lieder, A. Małachow, Waste management in the mining industry of metals ores, coal, oil and natural gas, A review. *Journal of Environmental Management*. Volume 304, 15 February 2022, 114239.
- [2] J. A. Entwistle, A. S. Hursthouse, M. Reis, A. G. Stewart, (2019), Metalliferous Mine Dust: Human Health Impacts and the Potential Determinants of Disease in Mining Communities, *Current Pollution Reports* 5:pp67–83 <https://doi.org/10.1007/s40726-019-00108-5>.
- [3] T. Karachaliou, V. Protonotarios, D. Kaliampakos, M. Menegaki, (2016), Using Risk Assessment and Management Approaches to Develop Cost-Effective and Sustainable Mine Waste Management Strategies Recycling, *I(3)*, pp328-342.
- [4] L. Li, Z. Yimin, B. Shenxu, and C. Tiejun, (2016), Utilization of Iron Ore Tailings as Raw Material for Portland Cement Clinker Production, *Hindawi Publishing Corporation Advances in Materials Science and Engineering* Volume, Article ID 1596047, 6 pages <http://dx.doi.org/10.1155/2016/1596047>
- [5] M. S. Imbabi, C. Carrigan, S. McKenna, (2012), Trends and developments in green cement and concrete technology, *International Journal of Sustainable Built Environment* pp194-216

- [6] M. Frías, G. Rosario, G. ; R. Vigil de la Villa and M. R. Sagrario, (2016) .Coal Mining Waste as a Future Eco-Efficient Supplementary Cementing Material : Scientific Aspects. *Recycling* 1(2), pp232-241
- [7] P. E. Tsakiridis, S. Agatzini-Leonardou, P. Oustadakis, (2004), Red mud addition in the raw meal for the production of Portland cement clinker, *Journal of Hazardous Materials* B116 pp103-110.
- [8] Y. Taha, (2017), Valorisation des rejets miniers dans la fabrication de briques cuites : évaluations technique et environnementale. 0.13140/RG.2.2.19573.78565.
- [9] S. Singh, L. B. Sukla, S. K. Goyal, (2020), Mine waste & circular economy. *Materials Today: Proceedings*. Vol30, Part2, pp332-339. <https://doi.org/10.1016/j.matpr.2020.01.616>.
- [10] T. K. Maedeh, E. Mansour, C. Glen, and G. Artem, (2019), Re-Thinking Mining Waste through an Integrative Approach Led by Circular Economy Aspirations, *Minerals* 9, 286; doi:10.3390/min9050286.
- [11] A. Atmaca, S. Yumruta, Analysis of the parameters affecting energy consumption of a rotary kiln in cement industry, *Appl. Therm. Eng.* 2014, 66, pp435–444.
- [12] UN environment, (2017), Eco-efficient cements: Potential economically viable solutions for a low-CO₂ cement-based materials industry: p 9,13.
- [13] S. P. Dunuweera, R. M. G. Rajapakse, (2018), Cement Types Composition, Uses and Advantages of Nanocement Environmental Impact on Cement Production and Possible Solutions, *Advances in Materials Science and Engineering* Volume, Article ID 4158682.
- [14] 7th International Congress on the Chemistry of Cement, Volume I, principal reports, p14, PARIS 1980.
- [15] J. Kim, S. Tae, R. Kim, (2018), Theoretical Study on the Production of Environment-Friendly Recycled Cement Using Inorganic Construction Wastes as Secondary Materials in South Korea Sustainability, 4449. <https://doi.org/10.3390/su10124449>.
- [16] A. Franco, A. R. Diaz, (2008), The future challenges for “cleancoaltechnologies”: Joining efficiency increase and pollutant emission control, *in Energy* DOI: 10.1016/j.energy.2008.09.012 , <https://www.researchgate.net/publication/222549604>.
- [17] Y. Jianglong, M. Fanrui, L. Xianchun, T. Arash, (2012), Power generation from coal gangue in China: Current status and development, *Advanced Materials Research* Vols. 550-553 p 443-446.
- [18] L. Yu, Y. Yuan, L. Xiaoming, S. Henghu, N. Wen, (2013), Improvement on pozzolanic reactivity of coal gangue by integrated thermal and chemical activation, *Fuel* Vol 109, Pages 527-533.
- [19] S. X. Zhou, (2009), Study on the reaction degree of calcined coal gangue powder in blended cement by selective solution method. *Procedia Earth and Planetary, The 6th International Conference on Mining Science & Technology*, pp 634-639.
- [20] S. Chhaiba, M. T. Blanco-Varela, M. Teresa, A. Diouri, (2018), Moroccan oil shale and coal waste as alternative raw materials in Portland cement clinker manufacture Clinkerization

- reactions and clinker characterization, *Materiales de Construcción*, vol. 68, no 331, p. 166. <https://doi.org/10.3989/mc.2018.07017>.
- [21] D. Belkheiri, A. Diouri, M. Taibi, O. Sassi, J. Aride, (2015), Recycling of Moroccan coal gangue in the elaboration of a Portland clinker, *J. Mater. Environ. Sci.* 6 (6) 1570-1577 Belkheiri et al. ISSN: 2028-2508 CODEN: JMESCEN.
- [22] R. Moussaoui, S. EL Moudni EL Alami, H. Aouraghe H. (Sept 2019), Characterization of the Zellidja Lead Smelter Slag (Eastern Morocco) in order to their Valorization in Civil Engineering, *Journal of Ecological Engineering*, Volume 20, Issue 8, pages 71–81 <https://doi.org/10.12911/22998993/110812>.
- [23] R. Hakkou, M. Benzaazoua; B. Bussière, (2016), Valorization of phosphate waste rocks and sludge from the Moroccan phosphate mines: Challenges and perspectives. *Procedia Engineering* 138 110 – 118.
- [24] S. Oumnih, N. Bekkouch, E. Gharibi, N. Fage, K. Elhamouti, M. El Ouahabi, (2019). Phosphogypsum waste as additives to lime stabilization of bentonite, *Sustainable Environment Research* 29 -35. <https://doi.org/10.1186/s42834-019-0038-z>.
- [25] R. Hattaf, M. Benchikhi, A. Azzouzi, R. El Ouatib, M. Gomina, A. Samdi, R. Moussa, (2021), Preparation of Cement Clinker from Geopolymer-Based Wastes, *Materials*, 14, 6534. <https://doi.org/10.3390/ma14216534>
- [26] S. Nfissi, Y. Zerhouni, M. Benzaazoua, S. Alikouss, A. Chtaini, R. Hakkou, M. Samir, (Nov 2011), Carcterisation of the tailings of abandoned mines of Kettara and Roc Blanc (Jebilet central, Morocco), *Ann. Soc. Géol. du Nord*.T. 18 (2ème série), p. 43-53.
- [27] M. Achik, A. Oulmekki, M. Ijjaali, H. Benmoussa, N. EL Mouden, S. EL Khattabi, R. EL Khallabi, F. Z. Ahjyayaj, G. Álvaro Gonzalez, F. Rivera Guitian, (2017). Physicochemical characterization of an industrial waste: A case study of the pyrrhotite ash from south west of Morocco, *JMES Vol 8, Issue 8, Pages 2738-2746*, <http://www.jmaterenvironsci.com>
- [28] H. F. Taylor, (1997). *Cement chemistry* (Vol. 2, p. 459), London: Thomas Telford.
- [29] P. Hewlett, , M. Liska, (Eds.), (2019), *Lea's chemistry of cement and concrete*, Butterworth-Heinemann.
- [30] S-H. Shim, T- H. Lee, S- J. Yang, N. B. M. Noor, J- H- J. Kim, (2021). Calculation of Cement Composition Using a New Model Compared to the Bogue Model. *Materials* 14. 4663. <https://doi.org/10.3390/ma14164663>.
- [31] F. Sorrentino, (2011), Chemistry and engineering of the production process: State of the art, *Cement and Concrete Research* 41, 616–623.
- [32] B. J. R. Mungyeke Bisulandu, F. Marias, (2019), Modélisation de la chimie du clinker et de l'ingénierie du processus de fabrication du ciment : État de l'art [Modeling of cement clinker chemistry and engineering of cement manufacturing process : State of the art]. *International Journal of Innovation and Applied Studies*. 528-551.
- [33] B. Kohlhaas, O. Labahn, *Cement Engineers Handbook*, 6th edition, Bauverlag GMBH, Berlin, 1983.

- [34] Y. Tao, W. Zhang, D. Shang, Z. Xia, N. Li, W.Y. Ching, F. Wang, S. Hu, Comprehending the occupying preference of manganese substitution in crystalline cement clinker phases: A theoretical study, *Cem. Concr. Res.* 109 (2018) 19–29.
doi:10.1016/j.cemconres.2018.04.003.
- [35] E. Fundal, (1979), *World Cement Technol.* 10..
- [36] M. A. Aldieb, H. G. Ibrahim, Variation of Feed Chemical Composition and Its Effect on Clinker Formation–Simulation Process Proceedings of the World Congress on Engineering and Computer Science 2010, Vol II WCECS 2010, Oct 20-22, 2010, San Francisco, USA.
- [37] F. Osawa, N. Shirahama, M. Yamashita, H. Tanaka H, (2015). Effects of phosphorus oxide in clinker and cement on the properties of high content belt cement, *Cement Science and Concrete Technology.* VL 69. P 23-28.
- [38] Y. Huang, J. Qian, X. Kang, J. Yu, Y. Fan, Y. Dang, W. Zhang, S. Wang, (2019). Belite-calcium sulfoaluminate cement prepared with phosphogypsum: Influence of P₂O₅ and F on the clinker formation and cement performances, *Construction and Building Materials.* VL203, p432 442.
- [39] Y. Taha, A. Elghali, R. Hakkou, M. Benzaazoua, (2021), Towards Zero Solid Waste in the Sedimentary Phosphate Industry: Challenges and Opportunities, *Minerals* 1250, <https://doi.org/10.3390/min11111250>.

Appendix : the used Python rogram LCW.py (instructions lines 1-296)
 (modify path in line 9, #ignored instruction or text)

```

import numpy as np, numpy.linalg as alg, matplotlib.pyplot as pt
from pylab import *
from sympy import *
import xlrd #import xlrd to read excel data
from xlwt import Workbook

#I-Preamble :raw feed : LCy% Wx% : variable y or x
x,y =symbols('x,y')
path = 'C:/Users/belkh/Desktop/cempy240102/'

#I-1-Import data on compositions (XRF) : sored in an excel file.xls
wb =xlrd.open_workbook(path+'cemat.xls',on_demand=True)
sh = wb.sheet_by_name(u'Feuil1')

#Display row i (or column j), by: rowi = sh.row_values(i),colj=sh.col_values(j)
d=[sh.row_values(p) for p in range(0,len(sh.col_values(0)))]
mat=[sh.col_values(0)[p] for p in range(0,sh.col_values(0).index('None')+1)]

#3 choices of mix limestone-clay-3material(1 or 2 or 3):
choice1=[int(d[s][1]) for s in
range(sh.col_values(0).index('None')+3, sh.col_values(0).index('None')+7)]
choice2=[int(d[s][2]) for s in range(sh.col_values(0).index('None')+3,
sh.col_values(0).index('None')+7)]
choice3=[int(d[s][3]) for s in range(sh.col_values(0).index('None')+3,
sh.col_values(0).index('None')+7)]
l,c,w,r=choice1[0],choice1[1],choice1[2],choice1[3]
#l,c,w,r=choice2[0],choice2[1],choice2[2],choice2[3]
#l,c,w,r=choice3[0],choice3[1],choice3[2],choice3[3]

#4+1 choices:bonds intervals and y0
y1,y2,x1,x2,yc=d[len(mat)+8][1],d[len(mat)+8][2],d[len(mat)+9][1],
d[len(mat)+9][2],d[len(mat)+9][3]
print('intervaly1-y2=',y1,y2,'-intervalx1-x2=',x1,x2,'-yc=',yc)
for p in range(0,6):
    print(d[0][p],',',d[1][p],',',d[c][p],',',d[w][p])
if w==sh.col_values(0).index('None'):
    x=0
    name=d[1][0]+d[c][0]+str(y)+d[w][0]+'-ref'+d[r][0]
else:
    x!=0
    y=yc
    name=d[1][0]+d[c][0]+str(y)+d[w][0]+str(x)+'+'-ref'+d[r][0]
print("The mixture studied is :",name)

#II-Compositions of oxides after loss of ignition(lists: o and o0=refernce
#Mass of raw feed mr=100 kg, after LOI, we get mk mass of clinker

mk=0.01*((100-x-y)*(100-d[1][9])+y*(100-d[c][9])+x*(100-d[w][9]))
o=np.array((((100-x-y)*d[1][q]+y*d[c][q]+x*d[w][q]))/(mk)) for q in
range(2,7))
o0=np.array( ((100*(d[r][q]))/(100-d[r][9]) for q in range(2,7))

#solutions x or y for equation OXi=OXi0:
ox=(solve(o[q]-o0[q]))[0] for q in range(0,4)]

#III-Determination of the 3 modulus (list:m) with hypothesis for
#LSF(A/F<0.64),-0.7*so3 gypsum),SR,AF

if (d[1][4]/d[1][5]<0.64 or d[c][4]/d[c][5]<0.64
or d[r][4]/d[r][5]<0.64):
    lsf=100*(o[0]-0.7*o[4])/ (2.8*o[1]+1.18*o[2]+0.65*o[3])
    lsf0=100*(o0[0]-0.7*o0[4])/(2.8*o0[1]+1.18*o0[2]+0.65*o0[3])
    print('Modify LSF denominator expr to: 2.8S+1.1A+0.65F,in line...')
else:
    lsf=100*(o[0]-0.7*o[4])/(2.8*o[1]+1.65*o[2]+0.63*o[3])
    lsf0=100*(o0[0]-0.7*o0[4])/(2.8*o0[1]+1.65*o0[2]+0.35*o0[3])
    print('keep LSF denominator expr (2.8S+1.65A+0.35F):see line...')

#Verification 0.71<AF<2.27 :LSF ok!\n LSF substract gypsum

sr=o[1]/(o[2]+o[3])
af=o[2]/o[3]
m=[lsf,sr,af]

sr0=o0[1]/(o0[2]+o0[3])
    
```

```

af0=o0[2]/o0[3]
m0=[lsf0,sr0,af0]

#solutions of mod i=mod i,0 :[14.68, 3.835, -0.82]
md=[(solve(m[q]-m0[q]))[0] for q in range(0,3)]

#IV-Determination of % phases in clinker (after LOI);phases noted p1=C3S,p2=C2S,
#p3=C3A,p4=C4AF
#Phases determinated by Shiu (or Bogue orTaylor)model : matrix =k
k=np.array([[4.088,-7.212,-6.745,-1.436,-2.863],[-3.113,8.442,5.136,1.093,2.18],
[0.028,-0.153,2.604,-1.702,-0.020],[-0.01,-0.058,0.016,3.047,0.007 ],
[ 0.006,-0.02,-0.011,-0.002,1.696 ]])
p0 = np.linalg.solve(k, o0)
p = np.dot(k,o)
kB=np.array([ [4.071,-7.600,-6.718,-1.430 ],[-3.072,8.600,5.068,1.079 ],
#[0,0,2.650,-1.692 ],[0,0,0,3.043]])
#p0 = np.linalg.solve(kB, o0[:4])
#p = np.dot(kB,o[:4])
#ph : solutions for equations ph i=phi,0
ph=[(solve(p[q]-p0[q]))[0] for q in range(0,4)]

#V-Results :
#11 solutions for 11 criterions are stored in sol

sol=[float("%.2f" % x) for x in (ox+md+ph)]

#cr=o[:4]+m+p #expressions of 11 parameters vs x or y
cr=[o[0],o[1],o[2],o[3],m[0],m[1],m[2],p[0],p[1],p[2],p[3]]

#st matrix where we replace x or y by its solution from 11 values of
#sol:11 lists, each list have 11elmnts
s0=[['R.V' if (v<0) or (v>100) else v for v in sol]]

if w==sh.col_values(0).index('None'):
    st=[float("%.2f" % cr[q].subs(y,sol[v])) for v in range (0,11)] for q
    in range(0,11)
    solz=[['RV' if (v<0) or (v>100) else 100-v for v in sol]]
    solx=[(0*np.ones(len(sol))),tolist()]
    soly=[['RV' if (v<0) or (v>100) else v for v in sol]]
else :
    st=[float("%.2f" % cr[q].subs(x,sol[v])) for v in range (0,11)] for q
    in range(0,11)
    solz=[['RV' if (v<0) or (v>100) else 100-y-v for v in sol]]
    soly=[(y*np.ones(len(sol))),tolist()]
    solx=[['RV' if (v<0) or (v>100) else v for v in sol]]
#st[0]: values of C for each solution yi,xi

s1=[['RV' if (h<0) or (h>100) else h for h in st[u]] for u in range(0,4)]
#4 oxides in 4 col and 11 rows ; r.v: rejected value

s2 = [ ['LV'+str(t) if (t < 92 and t>0) else 'HV'+str(t) if t>102 else 'RV'
if (t<0) else t for t in st[4]]]

s3 = [ ['LV'+str(t) if (t < 1.8 and t>0) else 'HV'+str(t) if t>2.7 else 'RV'
if (t<0) else t for t in st[5]]]

s4 = [ ['LV'+str(t) if (t < 1 and t>0) else 'HV'+str(t) if t>1.5 else 'RV'
if (t<0) else t for t in st[6]]]

s5=[['LV'+str(t) if (t<45 and t>0) else 'RV' if (t>100 or t<0) else
'HV'+str(t) if (t>65 and t<100) else t for t in st[7] ]]

s6=[['LV'+str(t) if (t<10 and t>0) else 'RV' if (t>100 or t<0) else
'HV'+str(t) if (t>30 and t<100) else t for t in st[8] ]]

s7=[['LV'+str(t) if (t<5 and t>0) else 'RV' if (t>100 or t<0) else
'HV'+str(t) if (t>12 and t<100) else t for t in st[9]]]

s8=[['LV'+str(t) if (t<6 and t>0) else 'RV' if (t>100 or t<0) else
'HV'+str(t) if (t>12 and t<100) else t for t in st[10] ]]

s9=[ [ st[0][i]/st[1][i] for i in range(0,11) ]]

s10=[ [ float("%.2f" % x) for x in s9[0]]]

s11=[ ['RV' if s10[0][i]<0 else s10[0][i] for i in range(0,11) ]]

he=[['C=', 'S=', 'A=', 'F=', 'LSF=', 'SR=',
'AF=', 'C3S=', 'C2S=', 'C3A=', 'C4AF=']]

```

```
rr=[[]+[float("%.1f" % x) for x in o0[:4]] ]+[float("%.1f" % x) for x in m0]
+[float("%.1f" % x) for x in p0[:4]] ]
```

```
#sp=[['p','h','a','s','e','c','l','i','n','k','e','r']]
sp=[ ['l','l','l','l','l','l','l','l','l','l','l']]
tot=he+rr+solz+soly+solx+s1+s2+s3+s4+s5+s6+s7+s8+s11#+sp
```

```
r1=['Solution','Ref:'+d[r][0],%'+d[l][0],%'+d[c][0],%'+d[w][0],
'C:','S:','A:','F:','LSF:','SR:','AF:','C3S:','C2S:','C3A:','C4AF:','C/S']
r2=["","","",""]
'60-69','18-24','4-8','1-8','92-102','1.8-2.7','1-1.5'
', '45-65','10-30','5-12','6-12','2.2-3.2']
```

```
r14=[ 'Remarks:', 'RV:', 'RejectedValue', 'LV:', 'LowValue', 'HV:',
'HighValue', 'Shim', 'proposition', '2.22', '<C/S<', '3.21' ]
```

```
[tot[q].insert(0,r1[q]) for q in range(0,len(r1))]
[tot[q].insert(1,r2[q]) for q in range(0,len(r2))]
[tot[q].insert(14,r14[q]) for q in range(0,len(r14))]
```

#VI-File (xls or txt) with numerics values

```
import xlswriter
from datetime import datetime

workbook =xlswriter.Workbook(path+name+'Bogjan4.xlsx')
worksheet = workbook.add_worksheet(name)

date_time = datetime.now()
worksheet.write_datetime(0, 0, date_time)
date_format = workbook.add_format({'num_format': 'dd/mm/yy, hh:mm'})
worksheet.write_datetime(0, 0, date_time, date_format)
worksheet.write(0,1,'RR:'+d[r][0]+'-vs-')
#worksheet.write(0,1,)
worksheet.write(0,2,d[l][0])
worksheet.write(0,3,d[c][0])
worksheet.write(0,4,d[w][0])
worksheet.write(0,7,'Calculations')
worksheet.write(0,9,'using')
worksheet.write(0,10,'Shim'+ ' '+'-')
worksheet.write(0,11,'proposition')
worksheet.write(0,13,' '(from ')
worksheet.write(0,14,' experiments)')
row = 2

for col, data in enumerate(tot):
    worksheet.write_column(row, col, data)

#worksheet.write(row+len(tot[0]),1,'r.v: rejected value')
```

#VII-Graphs for functions
 #Intervals :without waste y1,y2=15,25;in presence of waste x1,x2=0,10
 #Graphs for Shim model, modify to get graph3phases for Bogue model,etc...

```
if w==sh.col_values(0).index('None'):
    #x1,x2=15,25
    t=np.linspace(y1,y2,20)
    g=np.array([[cr[i].subs({y:q}) for q in t] for i in range(0,11)])
    variable=y
else :
    #x1,x2=0,10
    t=np.linspace(x1,x2,20)
    g=np.array([[cr[i].subs({x:q}) for q in t] for i in range(0,11)])
    variable=x

one=np.ones(len(t))

dc=(g[0])/(o0[0]*one)-one
ds=(g[1])/(o0[1]*one)-one
da=(g[2])/(o0[2]*one)-one
df=(g[3])/(o0[3]*one)-one
mi=min([ min(dc),min(ds),min(ds),min(df)])#min value
ma=max([ max(dc),max(ds),max(ds),max(df)])#max value
#sq=(float(ma)-float(mi))/4
```



```

pt.subplots_adjust(hspace = 0.9,left=0.135, bottom=0.15, right=0.97, top=0.91,
wspace=None)
pt.clf()
pt.subplot(3,1,1)
pt.plot(t,dc,'r',t,ds,'b',t,da,'g',t,df,'k',t,0*one,'k:')
pt.grid()
pt.suptitle(name,fontsize=8)
pt.xlabel('{}'.format(variable)+'(%)')
pt.xticks(np.arange(t.min(),t.max(), step=0.4), fontsize=8,rotation=90)
#pt.yticks(np.arange(y1,y2, step=sp), fontsize=8)
pt.ylabel(r"$\epsilon_{o}=\frac{(Mix-Ref)}{Ref})_{oxide}$", fontsize=8)
pt.text(x2,dc[1:len(t)-1],r"$\epsilon_{o}(C)$", fontsize=8)
pt.text(x2,ds[1:len(t)-1],r"$\epsilon_{o}(S)$", fontsize=8)
pt.text(x2,da[1:len(t)-1],r"$\epsilon_{o}(A)$", fontsize=8)
pt.text(x2,df[1:len(t)-1],r"$\epsilon_{o}(F)$", fontsize=8)
pt.text(x1-0.5,0,' ', fontsize=6)
pt.legend([r"$\epsilon_{o}(C)$",r"$\epsilon_{o}(S)$",r"$\epsilon_{o}(A)$",
r"$\epsilon_{o}(F)$", "0.0"],ncol=5,loc="upper left",bbox_to_anchor=(0,1.35),
fontsize=8)
pt.show()

dlsf=(g[4])/(m0[0]*one)-one
dsr=(g[5])/(m0[1]*one)-one
daf=(g[6])/(m0[2]*one)-one

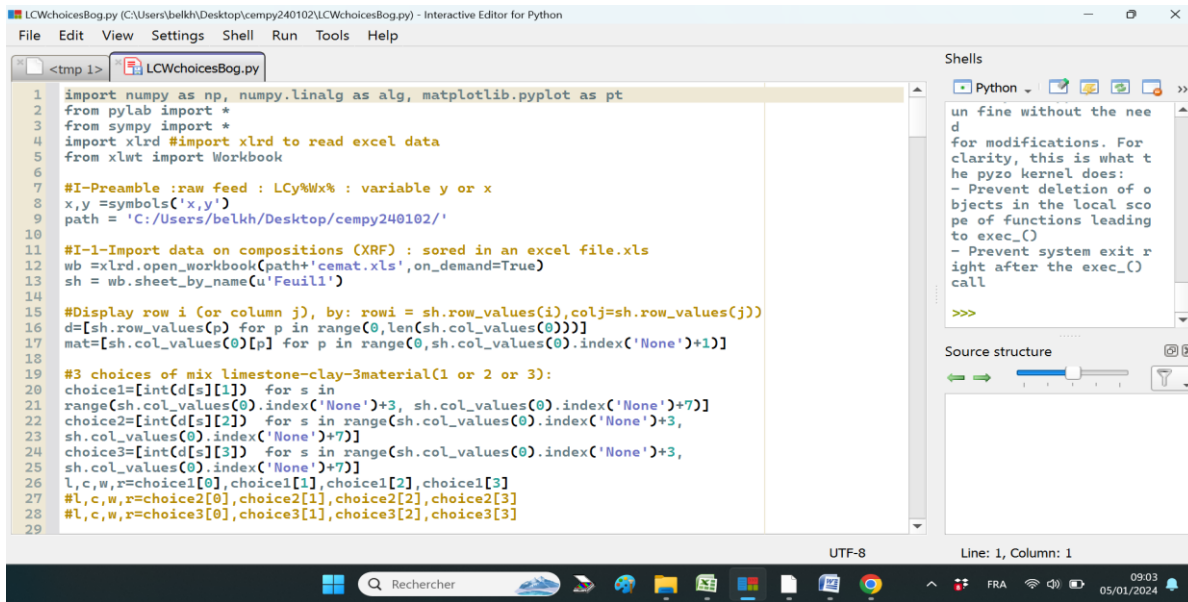
pt.subplot(3,1,2)
pt.plot(t,dlsf,'r',t,dsr,'b',t,daf,'k',t,0*one,'k:')
pt.grid()
pt.suptitle(name,fontsize=8)
pt.xticks(np.arange(t.min(),t.max(), step=0.4), fontsize=8,rotation=90)
pt.xlabel('{}'.format(variable))
pt.ylabel(r"$\epsilon_{m}=\frac{(Mix-Ref)}{Ref})_{modulus}$", fontsize=8)
pt.text(x2,dlsf[1:len(t)-1],r"$\epsilon_{m}(LSF)$", fontsize=8)
pt.text(x2,dsr[1:len(t)-1],r"$\epsilon_{m}(SR)$", fontsize=8)
pt.text(x2,daf[1:len(t)-1],r"$\epsilon_{m}(AF)$", fontsize=8)
pt.text(x1-0.5,0,' ', fontsize=6)
pt.legend([r"$\epsilon_{m}(LSF)$",r"$\epsilon_{m}(SR)$",r"$\epsilon_{m}(AF)$",
"0.0" ],ncol=4, loc="upper left",bbox_to_anchor=(0, 1.35), fontsize=8)
pt.show()

dp1=(g[7])/(p0[0]*one)-one
dp2=(g[8])/(p0[1]*one)-one
dp3=(g[9])/(p0[2]*one)-one
dp4=(g[10])/(p0[3]*one)-one

pt.subplot(3,1,3)
pt.plot(t,dp1,'r',t,dp2,'b',t,dp3,'g',t,dp4,'k',t,0*one,'k:')
pt.grid()
pt.suptitle(name,fontsize=8)
pt.xticks(np.arange(t.min(),t.max(), step=0.4), fontsize=8,rotation=90)
pt.xlabel('{}'.format(variable))
pt.ylabel(r"$\epsilon_{p}=\frac{(Mix-Ref)}{Ref})_{phase}$", fontsize=8)
pt.text(x2-1,dp1[1:len(t)-1]+0.7,r"$\epsilon_{p}(C_{3}S)$", fontsize=8)
pt.text(x2,dp2[1:len(t)-1],r"$\epsilon_{p}(C_{2}S)$", fontsize=8)
pt.text(x2,dp3[1:len(t)-1],r"$\epsilon_{p}(C_{3}A)$", fontsize=8)
pt.text(x2,dp4[1:len(t)-1]-1.5,r"$\epsilon_{p}(C_{4}F)$", fontsize=8)
*pt.legend([r"$\epsilon_{p}(C_{3}S)$",r"$\epsilon_{p}(C_{2}S)$",
r"$\epsilon_{p}(C_{3}A)$",r"$\epsilon_{p}(C_{4}AF)$", "0.0" ],ncol=5,
loc="upper left", bbox_to_anchor=(0, 1.35), fontsize=8)
pt.show()
savefig(path+name+'.png')

```

Figure 4: opening and running the program LCW.py



```
LCWchoicesBog.py (C:\Users\belkh\Desktop\cempy240102\LCWchoicesBog.py) - Interactive Editor for Python
File Edit View Settings Shell Run Tools Help

<tmp 1> LCWchoicesBog.py
1 import numpy as np, numpy.linalg as alg, matplotlib.pyplot as pt
2 from pylab import *
3 from sympy import *
4 import xlrd #import xlrd to read excel data
5 from xlwt import Workbook
6
7 #I-Preamble :raw feed : LCy%Wx% : variable y or x
8 x,y =symbols('x,y')
9 path = 'C:/Users/belkh/Desktop/cempy240102/'
10
11 #I-1-Import data on compositions (XRF) : sored in an excel file.xls
12 wb =xlrd.open_workbook(path+'cemat.xls',on_demand=True)
13 sh = wb.sheet_by_name(u'Feuil1')
14
15 #Display row i (or column j), by: rowi = sh.row_values(i),colj=sh.row_values(j)
16 d=[sh.row_values(p) for p in range(0,len(sh.col_values(0)))]
17 mat=[sh.col_values(0)[p] for p in range(0,sh.col_values(0).index('None')+1)]
18
19 #3 choices of mix limestone-clay-3material(1 or 2 or 3):
20 choice1=[int(d[s][1]) for s in
21 range(sh.col_values(0).index('None')+3, sh.col_values(0).index('None')+7)]
22 choice2=[int(d[s][2]) for s in range(sh.col_values(0).index('None')+3,
23 sh.col_values(0).index('None')+7)]
24 choice3=[int(d[s][3]) for s in range(sh.col_values(0).index('None')+3,
25 sh.col_values(0).index('None')+7)]
26 l,c,w,r=choice1[0],choice1[1],choice1[2],choice1[3]
27 #l,c,w,r=choice2[0],choice2[1],choice2[2],choice2[3]
28 #l,c,w,r=choice3[0],choice3[1],choice3[2],choice3[3]
29
```

Shells

```
Python
un fine without the need
d
for modifications. For
clarity, this is what t
he pyzo kernel does:
- Prevent deletion of o
bjects in the local sco
pe of functions leading
to exec_()
- Prevent system exit r
ight after the exec_()
call
>>>
```

Source structure

UTF-8 Line: 1, Column: 1

09:03 05/01/2024

هيئة التحرير

- أ.د. فضل نور
مدير التحرير
أستاذ علوم وهندسة الحاسب الآلي، بالجامعة الإسلامية بالمدينة المنورة. المملكة العربية السعودية
- أ.د. فايز جبالي
أستاذ، الهندسة الكهربائية وهندسة الحاسبات، جامعة فيكتوريا، فيكتوريا، كولومبيا البريطانية، كندا
- أ.د. محمد معبد بيومي
أستاذ التحليل العددي، جامعة الإمام، الرياض. المملكة العربية السعودية
- أ.د. سعد طلال الحربي
أستاذ علوم الحاسب – التفاعل بين الإنسان والحاسب كلية الحاسبات - جامعة طيبة المملكة العربية السعودية
- أ.د. يزيد بدر السعوي
أستاذ مشارك
كلية الحاسب ونظم المعلومات بالجامعة الإسلامية بالمدينة المنورة، المملكة العربية السعودية
- أ.د. شمس الدين أحمد
أستاذ الهندسة الصناعية، كلية الهندسة بالمدينة المنورة
- أ.د. احمد بدرالدين الخضر
رئيس التحرير
أستاذ علوم الحاسب، الجامعة الإسلامية بالمدينة المنورة، المملكة العربية السعودية
- د. توميتا كنتارو
أستاذ مشارك، قسم علوم وهندسة الكم، كلية الدراسات العليا للهندسة، جامعة هوكايدو، اليابان
- أ.د. رضا الششتاوي
أستاذ الكيمياء العضوية، قسم الكيمياء - كلية العلوم - جامعة الملك عبد العزيز، المملكة العربية السعودية
- أ.د. باسم راشد العمري
أستاذ هندسة القوى الكهربائية جامعة الطائف المملكة العربية السعودية
- أ.د. عصام شعبان حسانين
أستاذ الفيزياء، جامعة الأزهر، فرع أسبوط مصر
- أ.د. عبدالقادر رحيم بهاتي
أستاذ الهندسة المدنية، كلية الهندسة، الجامعة الإسلامية بالمدينة المنورة. المملكة العربية السعودية

سكرتير التحرير: أحمد زياد الزحيلي

الهيئة الاستشارية

- أ.د. حسين مفتاح
أستاذ ، الهندسة الكهربائية وعلوم الكمبيوتر ،
جامعة أوتاوا ، أوتاوا ، أونتاريو ، كندا
كرسي أبحاث كندا في شبكات الاستشعار
اللاسلكية، أستاذ جامعي ، جامعة أوتاوا
- أ.د. ضياء خليل
أستاذ الهندسة الكهربائية ، ووكيل الكلية ، جامعة
عين شمس ، القاهرة ، مصر
- أ.د. سلطان العدوان
أستاذ الكيمياء العضوية ، الأردن
- أ.د. كمال منصور جمبي
أستاذ الحاسب ونظم المعلومات ، جامعة الملك عبد
العزیز ، جدة ، المملكة العربية السعودية
- أ.د. محمد عبدالعاطي
أستاذ دكتور الرياضيات وعلوم المعلومات في جامعة
العلوم والتكنولوجيا ، مصر
- أ.د. عبد الغفور ميمون
أستاذ الهندسة الميكانيكية ، الجامعة الوطنية
للعلوم والتكنولوجيا ، باكستان
- أ.د. أمين فاروق فهمي
أستاذ الكيمياء في جامعة عين شمس
القاهرة ، مصر

قواعد النشر في المجلة

- أن يكون البحث جديداً، ولم يسبق نشره
- أن يتسم بالأصالة والجدة والابتكار والاضافة للمعرفة
- أن لا يكون مستلماً من بحوث سبق نشرها للباحث/للباحثين
- أن تراعى فيه قواعد البحث العلمي الاصيل، ومنهجيته.
- أن يشتمل البحث على:
 - ✓ صفحة عنوان البحث باللغة الانجليزية.
 - ✓ مستخلص البحث باللغة الانجليزية.
 - ✓ صفحة عنوان البحث باللغة الانجليزية.
 - ✓ مستخلص البحث باللغة العربية.
 - ✓ مقدمة.
 - ✓ صلب البحث.
 - ✓ خاتمة تتضمن نتائج وتوصيات.
 - ✓ ثبت المصادر والمراجع.
 - ✓ الملاحق الملزمة (إن وجدت).
- في حال (نشر البحث ورقياً) يمنح الباحث نفسه نسخة من عدد المجلة الذي نشر بحته بها و10 نسخ من بحته بشكل مستقل
- في حال اعتماد نشر البحث تؤول حقوق نشره كافة للمجلة، ولها ان تعيد نشره ورقياً أو إلكترونياً، ويحق لها
- إدراجه في قواعد البيانات المحلية والعالمية- بمقابل أو بدون مقابل -وذلك دون حاجة للإذن الباحث.
- لا يحق للباحث إعادة نشر بحته المقبول للنشر في المجلة- في أي وعاء من أوعية النشر- إلا بعد إذن
- كتابي من رئيس هيئة تحرير المجلة
- نمط التوثيق المعتمد في المجلة هو نمط IEEE

معلومات الإيداع

النسخة الورقية :

تم الإيداع في مكتبة الملك فهد الوطنية برقم 1439/8742 وتاريخ 1439/09/17 هـ

الرقم التسلسلي الدولي للدوريات (ردمد) 1658 – 7936

النسخة الإلكترونية:

تم الإيداع في مكتبة الملك فهد الوطنية برقم 1439/ 4287 تاريخ 1439/9/17 هـ

الرقم التسلسلي الدولي للدوريات (ردمد) 1658 -7944

الموقع الإلكتروني للمجلة:

<https://jesc.iu.edu.sa>

ترسل البحوث باسم رئيس تحرير المجلة إلى البريد الإلكتروني

jesc@iu.edu.sa

الآراء الواردة في البحوث المنشورة تعرب عن وجهة نظر الباحث فقط، ولا تُعرب بالضرورة عن المجلة.

بِسْمِ اللَّهِ الرَّحْمَنِ الرَّحِيمِ



الجامعة الإسلامية بمكة المكرمة
ISLAMIC UNIVERSITY OF MADINAH

مجلة الجامعة الإسلامية للعلوم التطبيقية مجلة علمية دورية محكمة

العدد: السادس الجزء الأول السنة: 1445هـ